Imperial College London

Imperial College London

Department of Physics

Optimal Quantum Control Beyond the Minimal System

Modesto Orozco Ruiz

March 06, 2025

Submitted in part fulfilment of the requirements for the degree of Doctor of Philosophy in Physics of Imperial College London and the Diploma of Imperial College London.

Declaration of Originality

I, Modesto Orozco Ruiz, declare that the work in this thesis is my own. The work of others has been appropriately referenced. A full list of references is given in the bibliography.

Copyright declaration

The copyright of this thesis rests with the author. Unless otherwise indicated, its contents are licensed under a Creative Commons Attribution-NonCommercial 4.0 International Licence (CC BY-NC).

Under this licence, you may copy and redistribute the material in any medium or format. You may also create and distribute modified versions of the work. This is on the condition that: you credit the author and do not use it, or any derivative works, for a commercial purpose.

When reusing or sharing this work, ensure you make the licence terms clear to others by naming the licence and linking to the licence text. Where a work has been adapted, you should indicate that the work has been changed and describe those changes.

Please seek permission from the copyright holder for uses of this work that are not included in this licence or permitted under UK Copyright Law.

Declaration of authorship

I declare that, except where otherwise referenced, all of the work presented in this thesis is my own, and is based on research carried out during my time at Imperial College London, under the supervision of Florian Mintert.

Chapter 5 is based on work first presented in, and reuse assets from,

- Modesto Orozco-Ruiz, Nguyen Le and Florian Mintert "Quantum control without quantum states" PRX Quantum, 5(4), 040346 (2024) [1],

which is published under the Creative Commons Attribution 4.0 International (CC BY 4.0) license.

Chapter 6 is based on work first presented in, and reuse assets from,

- Modesto Orozco-Ruiz, Selwyn Simsek, Sahra A. Kulmiya, Samuel J. Hile, Winfried K. Hensinger and Florian Mintert "Optimal control with a multidimensional quantum invariant" Physical Review A, 108(2), 022601 (2023) [2],

which is published under the Creative Commons Attribution 4.0 International (CC BY 4.0) license.

Chapter 7 is based on work first presented in, and reuse assets from,

- Modesto Orozco-Ruiz, Wasim Rehman and Florian Mintert "Generally noise-resilient quantum gates for trapped-ions" arXiv preprint (2024), submitted to PRX Quantum [3],

which is available on the arXiv under the Creative Commons Attribution 4.0 International (CC BY 4.0) license.

Chapter 8 is based on work to be presented in,

- Modesto Orozco-Ruiz and Florian Mintert "Entangling gates of trapped ions mediated by spectrally crowded modes" (in preparation).

Other works published during my doctoral research not included in this thesis:

- Nguyen H. Le, Modesto Orozco-Ruiz, Sahra A. Kulmiya, James G. Urquhart, Samuel J. Hile, Winfried K. Hensinger and Florian Mintert "Amplitude-noise-resilient entangling gates for trapped ions" arXiv preprint (2024), submitted to Physical Review Letters [4],

which is available on the arXiv under the Creative Commons Attribution 4.0 International (CC BY 4.0) license.

Abstract

Quantum computing holds the potential to transform fields ranging from cryptography to materials science by tackling problems that exceed the reach of classical computation. Yet, moving beyond proof-of-concept demonstrations to practical large-scale quantum systems requires overcoming two major challenges: the exponential increase in control complexity as the number of qubits grows and the inherent fragility of quantum operations in realistic experimental conditions. While high-fidelity control of individual qubits has been demonstrated, scalable architectures demand protocols that maintain precision across thousands of qubits, even in the presence of imperfections.

This thesis addresses these challenges through advances in quantum control and error resilience. First, we introduce a resource-efficient control framework that mitigates the exponential scaling of state-vector representations, enabling precise manipulation of many-qubit systems that were previously beyond reach. This approach supports the development of efficient protocols for state preparation and quantum simulation — both essential for realizing practical quantum technologies. Second, we develop error-mitigation strategies to suppress decoherence in multi-qubit arrays. Key contributions include shuttling protocols for trapped-ion systems that minimize motional heating during transport, noise-robust entangling gates that remain resilient to simultaneous frequency errors, initial motional excitation, and motional heating due to environmental coupling, as well as spectral engineering techniques that remove the need for mode selectivity and resolved sideband requirements in multi-ion operations.

Together, these advances refine the control of large-scale qubit systems and provide concrete steps toward scalable, fault-tolerant quantum processors.

Acknowledgements

To my supervisor, Florian Mintert — thank you for trusting me with this journey and giving me the space to grow as a researcher. Your mentorship has been a masterclass in blending creativity with scientific precision, from endless hours brainstorming on your office whiteboard to pushing me to ask better questions. You kept your promise from day one: *"This thesis is yours — make it something you're proud of"*. And I am! Thank you for never rushing our discussions, for laughing at my *anti-Madridista* complaints, and for showing me that brilliant scientists can still have impeccable taste in football rivalries.

To Nguyen — your constant support and countless discussions on Lie algebras and quantum control were crucial to this thesis — far surpassing the triumphs of Chelsea's latest season (though that's admittedly a low bar, haha!). To my quantum comrades: Gabriele ("Bimbo"), for your boundless energy, debates on the perfect pizza (always *margherita*), the sacred rules of carbonara, and gossip sessions that rivaled quantum entanglement in complexity; Thomas (Man Hei), for your brilliance, your iconic "Thomas diagrams", and rounding out our gossip trio with flair (*ganbeeeei!*); Selwyn, for teaching me how to embrace London life — from avoiding "tourist trap" beers to understanding why football might (or might not) rival Nando's in British hearts; Minjae, for introducing me to *bibimbap*, the... *acquired* taste of soju, and being my partner in crime for Spanish TV shows; Wasim, for demonstrating that physics debates can shake even the most stoic London building; and Hongzheng and Fred, for guiding a nervous newcomer through the labyrinth of early doctoral days. To the ever-changing cast of Floor 12 — Sean, Yuxun, Nick, Lydia, Hadrien, and more — for laughter over tea, shared struggles, and the occasional existential crisis. To Adam and Luca, for turning teatime into therapy sessions, and to Myungshik Kim, for your kindness and making me feel part of your research family. Finally, to Albert Albesa — *por las pausas para "el café", los festines de carbonara con trufa en Crazy for Pasta, las raves en Brixton y las bacon cheeseburgers de Five Guys cuando todo lo demás fallaba.*

To the experimental collaborators at Sussex University and Universal Quantum — Winnie, Sam, Sahra, Martin, Pedro, Iason, Madalina, Falk, Petros, and the entire team — walking into your lab felt like stepping into a sci-fi movie: lasers everywhere, wave generators buzzing, and cables tangled like spaghetti. As a theorist, I was amazed but scared to touch anything (I kept my hands in my pockets, sure I'd break something!). But you taught me how my math could turn into real experiments, trapping ions so precisely it still amazes me. Thanks for your patience, for answering my endless "*Wait, how does this work? And that?*", and for never making fun of my cluelessness. You turned my ideas into something real.

To the scientific "conference families" forged under Lake Como's moonlight, the mountains of Les Diableretes, the coasts of Rhode Island, and the charm of Nessebar — your insights and camaraderie transformed brief encounters into collaborations that profoundly shaped this work.

A mis "amigos de Barcelona" — gracias por ser mi red de apoyo mientras intentaba eso de "ser físico cuántico" en la fría y gris Londres (sí, la ciudad es una pasada... y el clima, bueno, nadie es perfecto). El doctorado fue la excusa perfecta para descubrir pubs, aunque nada como las tapas, el sol y las risas en los bares de casa. Gracias por recibirme con los brazos abiertos cada vez que volvía, por ponerme al día de los últimos cotilleos jugosos, por los partidos de pádel y por recordarme que, al final, lo importante sigue siendo la misma birra fría y las mismas historias de siempre. Y sí, esta vez sí he acabado el doctorado... no como las otras veces, lo juro.

A mi familia política, en especial Ana, Amador y Abuela. Gracias por llenar la mesa de mis platos favoritos cada vez que volvemos, por esos "kits de supervivencia para Londres" repletos de fuet y jamón, y por preguntar siempre, con esa mezcla de curiosidad y cariño: "Como llevas eso del doctorado?".

A mi familia — Mami, gracias por tu sonrisa al otro lado del teléfono ("antes de que el tiempo se acabe"), por mantener el mundo en orden y por ese beso que se siente incluso a la distancia. Papi, gràcies per ser el mirall que em mostra tot el que puc arribar a ser, no només el que sóc ara. Sergi, gràcies per cridar "Això és brutal!" cada vegada que parlo del doctorat... i per recordar-me que després de tantes equacions, el millor sempre són uns nachos amb formatge i un capítol de "Crims".

Finalmente, a Laura, mi compañera de aventuras (Abuela tiene razón: "¡no paramos quietos!"). Gracias por quereme a pesar de mis horas perdidas en fórmulas, por las noches de stand-up comedy en Greenwich, las "citas fancy" en Mayfair y los atardeceres junto al Támesis con Malibú-piña en mano. Por convertir Camden en nuestro patio de mega-burgers, los Cotswolds en una aventura "improvisada", y las mañanas del "Antrillo" en un thriller casero. Y, sobre todo, por fingir que entendías mis teorías cuánticas... hasta que empezaste a corregirme. Eres mi brújula en cada locura. Te quiero más que a cualquier ecuación cuántica.

Contents

List of Figures

List of Tables

Chapter 1

Introduction

> "It was as if the ground had been pulled out from under one, with no firm foundation to be seen anywhere upon which one could have built."
>
> – Albert Einstein, 1949 [5]

The early decades of the 20th century witnessed a profound crisis in classical physics. Established theories, which had long excelled at describing macroscopic phenomena, failed when confronted with atomic and subatomic systems. For example, classical electrodynamics predicted that orbiting electrons would spiral into atomic nuclei within picoseconds due to continuous energy loss — an outcome that directly contradicted the observed stability of matter and the discrete emission spectra of atoms [6]. Similarly, the ultraviolet catastrophe revealed that classical thermodynamics incorrectly predicted infinite energy radiation at short wavelengths [7, 8], a result so unphysical that it threatened the foundations of statistical mechanics. These failures highlighted a fundamental truth: the microscopic world operates according to principles that defy macroscopic intuition, prompting a radical rethinking of physical laws — an intellectual shift that gave rise to the quantum revolution.

Max Planck's 1900 proposal of energy quantization — the radical idea that electromagnetic energy is exchanged in discrete packets called *quanta* — resolved the black-body radiation paradox and ignited a paradigm shift [9]. Einstein's 1905 explanation of the photoelectric effect further cemented the particle-like behavior of light [10], while Bohr's 1913 model of quantized electron orbits bridged atomic stability with spectral observations [11]. By the 1920s, Schrödinger's wave mechanics [12], Heisenberg's matrix mechanics [13], and Dirac's operator formalism [14] converged into the mathematical framework of modern quantum mechanics. This revolution not only explained microscopic phenomena but also catalyzed transformative technologies, from semiconductors [15] and lasers [16] to magnetic resonance imaging (MRI) [17], reshaping modern life.

Today, the legacy of these breakthroughs continues in the pursuit of quantum computing, a field poised to transform domains from cryptography to materials science by tackling problems that lie beyond the reach of classical computation. Unlike classical bits, qubits exploit superposition and entanglement to explore exponentially large solution spaces simultaneously, enabling exponential speedups for specific tasks — such as integer factorization via Shor's algorithm [18] and quantum simulations that promise to revolutionize materials science [19] and drug discovery [20]. For example, quantum phase estimation could elucidate the electronic structure of transition-metal catalysts critical for sustainable energy technologies [21].

However, moving beyond proof-of-concept demonstrations to practical, large-scale quantum systems requires overcoming two major challenges. First, there is the exponential increase in control complexity as the number of qubits grows — today's noisy intermediate-scale quantum (NISQ) devices operate with only hundreds of error-prone qubits [22], while scalable architectures demand protocols that maintain high precision across thousands of qubits even in the presence of imperfections. Second, quantum operations are inherently fragile, with decoherence, crosstalk, and hardware imperfections threatening reliable computation. While theoretical frameworks such as surface codes [23] and topological qubits [24] offer error-correction strategies, their experimental realization remains highly demanding.

Central to overcoming these obstacles is quantum control — the precise engineering of external fields (*e.g.*, laser pulses, microwave signals, or magnetic gradients) to manipulate quantum states while mitigating decoherence and noise [25]. Even minor deviations in control parameters can disrupt quantum superpositions, leading to errors that accumulate over time. Advances in optimal control theory, such as gradient-ascent pulse engineering (GRAPE) [26] and shortcuts to adiabaticity [27], have transformed these challenges into tractable problems, enabling high-fidelity quantum gates across various platforms, including trapped ions [28], superconducting circuits [29], and photonic architectures [30].

Among these platforms, trapped-ion systems stand out for their versatility and exceptional performance. In these systems, atomic ions — confined in ultrahigh vacuum by precisely engineered electromagnetic fields — serve as robust qubits encoded in long-lived electronic states. Laser-induced transitions mediate entanglement by exploiting spin-dependent forces that couple to shared vibrational modes [31], while microwave fields and magnetic field gradients offer alternative control pathways with reduced sensitivity to optical phase noise. These diverse control strategies have yielded record-breaking gate fidelities exceeding 99.9% [28, 32], comparable to the precision of atomic clocks that once validated quantum theory. Nonetheless, scaling trapped-ion architectures to practical, large-scale quantum processors presents significant challenges, including mode crowding, crosstalk in dense ion arrays [33, 34], and the susceptibility of laser frequencies and amplitudes to noise.

This thesis advances scalable quantum computing by addressing fundamental challenges in quantum control and error resilience through novel theoretical approaches. At its core,

we introduce a quantum control framework inspired by the properties of quantum invariants, which circumvents the exponential scaling of state-vector-based methods. Instead of explicitly constructing quantum states, our approach formulates control directly in terms of quantum operators that implicitly encode the system's evolution. The efficiency of this framework stems from the algebraic structure of these operators, which form a closed algebra of small dimension under the action of the Hamiltonian. This structure enables a compact representation of the system's dynamics, allowing us to unify a broad class of control problems and obtain solutions that would otherwise be computationally intractable. We apply this framework to quantum state preparation and quantum simulation, developing efficient protocols for generating highly entangled states, such as cluster states and Greenberger-Horne-Zeilinger (GHZ) states, and simulating complex many-body dynamics.

In parallel, we develop optimized pulse engineering techniques to achieve high-fidelity quantum logic operations in multi-qubit systems. In the context of trapped-ion architectures, we design motional control protocols that minimize excitation, even in fast diabatic processes, ensuring that any transient heating is fully reversed by the end of the evolution. Additionally, we introduce a novel control strategy that enhances error resilience by simultaneously mitigating multiple error sources. Unlike conventional methods, which typically suppress a single dominant error at the risk of amplifying others, our approach systematically accounts for the leading sources of error within a unified optimization process. This capability is crucial for scalability, as it ensures robust performance in the presence of hardware imperfections that inevitably arise in large-scale quantum processors. Moreover, we develop an entanglement generation strategy for multi-ion chains that operates beyond conventional constraints, avoiding the need for mode selectivity or sideband resolution. Instead, it harnesses all accessible motional modes and extends beyond weak-coupling limitations, offering a versatile route to scalable entanglement generation.

By integrating these advances, this thesis contributes to the foundational development of scalable and resilient quantum computing architectures, bridging theoretical quantum control with practical implementation challenges.

1.1 Thesis Outline

This thesis explores the intersection of theoretical quantum physics, advanced control methods, and numerical optimization to tackle key challenges in quantum computing. It is divided into two parts: the first (Chapters 2–4) develops the core theoretical foundations, while the second (Chapters 5–9) introduces new quantum control methodologies, both at a general level and specifically for trapped-ion systems.

Foundational Chapters (2–4)

- **Chapter 2: Mathematical Framework of Quantum Mechanics**
  We establish the mathematical framework of quantum theory, including Hilbert spaces, state vectors, and operators. Key postulates — such as the Born rule and the Schrödinger equation — are formalized, with extensions to *open quantum systems* using density matrices and master equations. A unifying theme is the application of *Lie theory* to characterize symmetries and dynamics, providing tools essential for quantum control.

- **Chapter 3: Optimal Quantum Control**
  At the heart of manipulating quantum systems lies the challenge of balancing precision, speed, and resilience against noise — a challenge addressed by the principles of quantum control theory. This Chapter explores the mathematical and conceptual tools for designing protocols that steer quantum states and operations toward desired outcomes, with an emphasis on using quantum invariants to circumvent the slow pace of adiabatic methods. Foundational questions of controllability (*can the system reach a target?*) and reachability (*under what conditions?*) are examined alongside numerical strategies like GRAPE, illustrating how tailored control fields emerge from theoretical frameworks. Through applications in state preparation and quantum simulation, the Chapter underscores the transformative potential of control theory in overcoming inherent quantum fragility and advancing scalable technologies.

- **Chapter 4: Quantum Computing Architectures: Trapped Ions**
  Focusing on one of the most mature quantum architectures, we detail how electromagnetic fields trap ions, encode qubits in electronic states, and mediate entanglement via *spin-dependent forces*. We compare laser-based photon momentum transfer and magnetic gradient-induced coupling, highlighting their roles in high-fidelity gate operations for modern ion-trap processors.

Original Contributions (5–9)

- **Chapter 5: Quantum Control without Quantum States**
  We present a novel framework for quantum control that bypasses the need for explicit simulations of system dynamics, which typically rely on state-vector representations. Instead, our approach focuses on the evolution of operators that encode the quantum state implicitly. This shift in perspective enables exponential reductions in computational effort for certain classes of problems. Crucially, our method remains effective even in scenarios where traditional techniques, such as tensor networks, struggle to provide accurate results. By identifying polynomial-sized operator sets — collections of operators that grow only modestly with system size and remain algebraically closed under the Hamiltonian's action — we unlock efficient protocols for state preparation and analog quantum simulation.

- **Chapter 6: Quantum Control of Trapped Ion's Motion**
  Leveraging *multidimensional quantum invariants*, we develop optimized ion-shuttling protocols that achieve ground-state-to-ground-state motional state transfer during rapid, non-adiabatic transport. By exploiting the tunable degrees of freedom inherent to this framework, we engineer trajectories that directly address experimental bottlenecks. For instance, we minimize ion displacement from the trap center to suppress distortions from potential anharmonicities, or achieve tightly confined wave packets even in weak trapping potentials — a common limitation imposed by geometric constraints in experimental setups. This approach ensures robust, high-fidelity ion transport, critical for scaling up trapped-ion quantum processors.

- **Chapter 7: Generally Noise-Resilient Quantum Gates for Trapped Ions**
  We present a noise-resilient entanglement protocol that achieves *orders of magnitude* higher fidelity than conventional methods. A tailored driving strategy simultaneously excites multiple sidebands across all motional modes, enabling robust entanglement even with "hot" ions, motional heating, and detuning errors. This relaxes the need for ground-state cooling, significantly advancing scalability.

- **Chapter 8: Entangling Gates of Trapped Ions Mediated by Spectrally Crowded Modes**
  Addressing the critical bottleneck of *mode crowding* — spectral overlap of vibrational modes in long ion chains — we propose a magnetic gradient-based protocol that eliminates mode selection. By engineering a spin-dependent force coupling qubits to *all modes collectively*, we generate geometric phases proportional to total ion displacement. This enables fast, scalable entanglement gates immune to spectral crowding, bypassing limitations and approximations of traditional techniques.

- **Chapter 9: Concluding Remarks**
  We summarize the main advances of the thesis and explore potential future applications.

Chapter 2

Mathematical Framework of Quantum Mechanics

> "Our scientific work in physics consists in asking questions about nature in the language that we possess and trying to get an answer from experiment by the means at our disposal."
>
> – Werner Heisenberg, 1949 [35]

Every physical theory depends on a well-defined mathematical framework that connects abstract concepts with observable phenomena. In classical mechanics, this correspondence is relatively transparent: quantities like position, velocity, and force are represented by real numbers and vectors, in harmony with Newton's laws. In contrast, quantum mechanics requires a more abstract approach. Some of its fundamental elements — such as wave functions or quantum entanglement — do not have direct classical analogues and can seem counterintuitive. Nevertheless, just as Newton's laws and Maxwell's equations form the backbone of classical physics and electrodynamics respectively, quantum mechanics is built on a set of core principles that rigorously explain the behavior of systems at the smallest scales.

2.0.1 Quantum states

Central to quantum mechanics is the mathematical description of physical systems through the concept of a *state*, which encapsulates our knowledge of a system at any given moment. While the classical state offers a precise, deterministic description where all measurable observables (position, momentum, energy, etc.) can be determined exactly at any given time, the quantum state provides a probabilistic description.

In quantum theory, the state of a microscopic system A is represented by a vector in an abstract Hilbert space $\mathcal{H}_A$ equipped with an inner product. Using Dirac's formalism [14],

state vectors are expressed in the standard bra-ket notation. To describe the most general state $|\psi\rangle$, it is convenient to define a reference basis $\{|i_A\rangle\}$ in $\mathcal{H}_A$, satisfying the orthogonality and completeness conditions

$$\langle i_A|j_A\rangle = \delta_{ij} \ , \quad \sum_i |i_A\rangle\langle i_A| = \mathbb{I}_A \ , \tag{2.1}$$

where δ_{ij} is the usual Kroneker symbol and $\mathbb{I}_A$ the identity operator in $\mathcal{H}_A$. The subscript "A" in $\mathbb{I}_A$ or $|i_A\rangle$ will be omitted when the context makes it clear. With this basis, any state $|\psi\rangle$ in $\mathcal{H}_A$ can be expressed as a superposition of the basis vectors

$$|\psi\rangle = \sum_i \langle i_A|\psi\rangle \, |i_A\rangle = \sum_i \psi_i \, |i_A\rangle \ , \tag{2.2}$$

in terms of the *complex* coefficients $\psi_i = \langle i_A|\psi\rangle$. This is a crucial distinction between quantum and classical systems: while classical physics only requires real numbers to define states, complex numbers are indispensable in quantum theory [36].

While Eq. (2.2) is a standard result in linear algebra, it carries profound implications in quantum mechanics. In particular, it shows that a quantum system can exist in a superposition of multiple states simultaneously, giving rise to the concept of quantum coherence, which is crucial to explaining many of the non-classical predictions of quantum mechanics. Eq. (2.2) suggests that, in general, it is not possible to deterministically observe the system in a particular state $|i_A\rangle$; instead, each outcome is associated with a finite probability $|\langle i_A|\psi\rangle|^2 = |\psi_i|^2$.

To ensure the consistency of the probabilistic interpretation of quantum mechanics, the normalization condition $\langle\psi|\psi\rangle = 1$ must hold. This implies that the components of the state vector satisfy

$$\sum_i |\psi_i|^2 = 1 \ , \tag{2.3}$$

ensuring that the total probability of all possible outcomes sums to one. This principle aligns with the Copenhagen interpretation, which maintains that measurement outcomes are inherently probabilistic, with probabilities determined by the square modulus of the wavefunction [6]. The requirement of normalization naturally leads to the first postulate of quantum mechanics, which formalizes how physical systems are described:

Postulate 1: A physical system A is described by a Hilbert space $\mathcal{H}_A$, and the state of the system is represented by a ray with norm 1 in $\mathcal{H}_A$.

In some situations, however, the exact state of a system may not be fully known. For instance, in experimental settings where a quantum state is prepared in a laboratory, the system might not be in a single known state but instead be in one of a set of possible states $|\psi_i\rangle$, each with a certain probability p_i. Each state $|\psi_i\rangle$ is referred to as a *pure state*, as its

properties can be determined with certainty. In such cases, the system is described by an *ensamble of pure states* $\{p_i, |\psi_i\rangle\}$ that is typically known as a *mixed state*. To represent this ensemble, it is convenient to introduce the concept of a density operator ρ.

A density operator is a positive semi-definite ($\rho \geq 0$), Hermitian operator ($\rho = \rho^\dagger$, where the dagger † indicates the Hermitian conjugate) with trace one ($\mathrm{Tr}\,\rho = 1$). It acts on the Hilbert space $\mathcal{H}_A$ of the system and provides a compact representation of the ensemble of pure states

$$\rho = \sum_i p_i \, |\psi_i\rangle\langle\psi_i| \ , \tag{2.4}$$

with $\sum_i p_i = 1$.

Often, we encounter systems composed of multiple subsystems $\{A_i\}$ (say w of them), each with its Hilbert space $\mathcal{H}_{A_i}$. The total Hilbert space for the system is the tensor product of these individual spaces, *i.e.*, $\mathcal{H}_{A_1} \otimes \cdots \otimes \mathcal{H}_{A_w}$. Thus, any pure state that can be written in the form

$$|\psi\rangle = |\psi_1\rangle \otimes \cdots \otimes |\psi_w\rangle \, , \tag{2.5}$$

i.e. as a tensor product of the subsystem states $|\psi_j\rangle$, is called a *separable state*. In such states, measurements on one subsystem do not influence the state of the others, implying that measurement results from different subsystems are uncorrelated. Pure states that cannot be expressed in this form are called *entangled states*.

For mixed states, separability generalizes to the following convex sum

$$\rho = \sum_i p_i \rho_1^{(i)} \otimes \cdots \otimes \rho_w^{(i)}, \tag{2.6}$$

where the probabilities p_i represent classical mixtures of product states. Any mixed state that cannot be expressed in this form is considered *entangled*.

Entangled states are a defining feature of quantum mechanics and play a central role in various applications, including quantum information processing, quantum computing, quantum metrology, and quantum communication. Their unique property lies in the fact that measurements performed on one subsystem instantaneously affect the state of the remaining subsystems, even when separated by large distances — a phenomenon known as quantum non-locality [37].

2.0.2 Quantum observables

Within this formalism, measurable physical quantities — such as energy, momentum, or spin — are represented by linear operators acting on the Hilbert space $\mathcal{H}_A$ associated with the system A. Each observable is mathematically described by a Hermitian operator $\hat{M}$, which ensures that the possible outcomes of a measurement are real numbers. The

Hermiticity of these operators also guarantees that their eigenvectors form a complete orthonormal basis for the Hilbert space, meaning that any quantum state $|\psi\rangle$ can be expressed as a superposition of these eigenstates. This leads to the second fundamental postulate of quantum mechanics, which formalizes the relationship between physical observables and operators:

Postulate 2: Every physical observable M is represented by a Hermitian operator $\hat{M}$ acting on the Hilbert space $\mathcal{H}_A$. The eigenvalues of $\hat{M}$[a] correspond to the possible outcomes of a measurement, and its eigenvectors form a complete orthonormal basis for $\mathcal{H}_A$.

[a] For simplicity, the hat notation will generally be omitted unless explicitly needed to distinguish the operator from the observable.

When a measurement of an observable M is performed, the only possible outcomes are the eigenvalues m_i of the corresponding Hermitian operator. The probability of obtaining a specific outcome is determined by the Born rule. If the system is in the quantum state described by a density matrix ρ, the probability $p(m_i)$ of measuring the eigenvalue m_i is given by the trace of the projection of ρ onto the corresponding eigenspace. Formally:

Postulate 3: The probability $p(m_i)$ of obtaining the outcome m_i when measuring an observable M is given by the Born rule:

$$p(m_i) = \mathrm{Tr}[\Pi_i \rho] \ , \tag{2.7}$$

where Π_i is the total projection operator onto the eigenspace associated with m_i. If the eigenvalue m_i is k-fold degenerate, the eigenspace is spanned by a set of orthonormal eigenstates $\{\, |m_i^{(j)}\rangle \}_{j=1}^{k}$, and the total projection operator is

$$\Pi_i = \sum_{j=1}^{k} |m_i^{(j)}\rangle\langle m_i^{(j)}| \ . \tag{2.8}$$

The measurement process also affects the quantum state. Immediately after measuring an observable and obtaining a particular outcome m_i, the system collapses to the corresponding eigenspace associated with that outcome [38]. If the eigenspace is non-degenerate, the system collapses to a single eigenstate. However, if the eigenspace is degenerate, the post-measurement state becomes a mixture of eigenstates within that subspace. Mathematically, this collapse is described by applying the appropriate projection operator to the pre-measurement state, followed by normalization. For a system described by a density matrix ρ, the post-measurement state ρ' is determined by the following rule:

Postulate 4: If a measurement of an observable M yields the outcome m_i, the quantum state of the system immediately collapses to the corresponding eigenspace. The post-measurement state is given by

$$\rho' = \frac{\Pi_i \rho \Pi_i}{p(m_i)} \ , \tag{2.9}$$

where Π_i is the total projection operator onto the eigenspace associated with m_i, and $p(m_i)$ is the probability of obtaining that outcome, as defined in Postulate 3. For a system initially in a pure state $|\psi\rangle$, the post-measurement state reduces to

$$|\psi'\rangle = \frac{\Pi_i |\psi\rangle}{\|\Pi_i |\psi\rangle\|} \ . \tag{2.10}$$

If m_i is degenerate, $|\psi'\rangle$ is not uniquely determined but remains within the eigenspace spanned by the eigenstates $\left\{ |m_i^{(j)}\rangle \right\}$.

Different operators M_1 and M_2 may have distinct sets of eigenstates, indicating that the corresponding measurements are incompatible. The degree to which these observables can be simultaneously measured is quantified by their commutator

$$[M_1, M_2] = M_1 M_2 - M_2 M_1 \ . \tag{2.11}$$

Another useful operation, employed throughout this thesis, is the anticommutator

$$\{M_1, M_2\} = M_1 M_2 + M_2 M_1 \ , \tag{2.12}$$

which represents the symmetrized product of two operators.

2.0.3 Imperfect measurements

Postulates 3 and 4 describe the idealized quantum measurement process, where each outcome is associated with a projector onto an orthogonal eigenstate. However, real-world measurements are often imperfect due to noise and inefficiencies. For instance, a photon detector may occasionally fail to register an incoming photon, leading to missed detections. These imperfections necessitate a more general framework for describing measurements. To account for these imperfections, measurement outcomes are modeled probabilistically. Instead of associating each outcome with a single projector, a measurement apparatus is described by a distribution $\{q_k(m_i)\}$, where $q_k(m_i)$ represents the likelihood that the detector registers outcome m_i when the system is actually in the eigenstate $|m_k\rangle$. In this framework, the probability of observing outcome m_i for a system in state ρ is given by

$$p(m_i) = \sum_k q_k(m_i) \operatorname{Tr}[\Pi_k \rho] = \operatorname{Tr}\left[\sum_k q_k(m_i) \Pi_k \rho \right] \equiv \operatorname{Tr}[E_i \rho] \ , \tag{2.13}$$

where $\Pi_k = |m_k\rangle\langle m_k|$ are the projectors associated with the ideal measurement outcomes. This expression naturally extends to degenerate eigenspaces by replacing Π_k with the total projector onto each eigenspace.

The operators $E_i = \sum_k q_k(m_i)\Pi_k$ are known as the elements of a *Positive Operator-Valued Measure (POVM)*, which generalizes the notion of projective measurements to encompass noisy, incomplete, or otherwise generalized measurement processes that cannot be described solely by orthogonal projectors. Since the total probability of all possible outcomes must sum to one, we impose the normalization condition

$$\sum_i p(m_i) = 1 \quad \Rightarrow \quad \sum_i \mathrm{Tr}[E_i\rho] = \mathrm{Tr}\left[\sum_i E_i\rho\right] = 1 \ , \tag{2.14}$$

which must hold for any state ρ. By the cyclic property of the trace and its linearity, this implies the completeness relation

$$\sum_i E_i = \mathbb{I} \ , \tag{2.15}$$

ensuring that the measurement covers all possible outcomes. Upon obtaining the outcome m_i, the system transitions to a new state ρ'. In the presence of measurement imperfections, this post-measurement state is given by a weighted sum over the possible underlying eigenstates, *i.e.*

$$\rho' = \frac{\sum_k q_k(m_i)\Pi_k\rho\Pi_k^\dagger}{\mathrm{Tr}[E_i\rho]} \ , \tag{2.16}$$

where the denominator normalizes the state to preserve the trace. This expression captures the probabilistic nature of imperfect measurements, where the system collapses not to a single eigenstate but to a mixture of possible states. A more compact form of this update rule is obtained by introducing the so-called *Kraus operators*

$$A_{ki} = \sqrt{q_k(m_i)}\Pi_k \ , \tag{2.17}$$

in terms of which the POVM elements can be rewritten as

$$E_i = \sum_k A_{ki}^\dagger A_{ki} \ , \tag{2.18}$$

and the post-measurement state becomes

$$\rho' = \frac{\sum_k A_{ki}\rho A_{ki}^\dagger}{\mathrm{Tr}[E_i\rho]} \ . \tag{2.19}$$

This Kraus representation offers a rigorous and versatile formalism for describing general quantum measurements, particularly in scenarios where information is partially lost or measurements are intrinsically noisy. Moreover, this representation extends naturally to describe non-unitary evolution in open quantum systems. When no specific measurement

outcome is registered — or when the system interacts with an external environment without direct observation — the state transformation is given by

$$\rho' = \mathcal{E}(\rho) = \sum_k A_k \rho A_k^\dagger \ , \tag{2.20}$$

where $\mathcal{E}$ is a quantum operation defined by a set of Kraus operators $\{A_k\}$ that satisfy the completeness relation

$$\sum_k A_k^\dagger A_k = \mathbb{I} \ . \tag{2.21}$$

These conditions (Eqs. (2.20) and (2.21)) define a *quantum channel*, the most general class of physically admissible quantum evolution. Formally, such channels are Completely Positive Trace-Preserving (CPTP) maps [39], which enforce two critical properties:

- Trace preservation: The total probability is conserved, as shown by

$$\mathrm{Tr}\left(\rho'\right) = \mathrm{Tr}\left(\sum_k A_k \rho A_k^\dagger\right) = \sum_k \mathrm{Tr}\left(A_k \rho A_k^\dagger\right) = \mathrm{Tr}\left(\sum_k A_k^\dagger A_k \rho\right) = \mathrm{Tr}\left(\rho\right) \ . \tag{2.22}$$

- Complete positivity: The map remains physically valid even when the system is entangled with an auxiliary system E. For any positive semidefinite operator $\sigma \in \mathcal{H}_S \otimes H_E$ and vector $|\mu\rangle$ in the composite space, the extended map $\mathcal{E} \otimes \mathbb{I}_E$ (where $\mathbb{I}_E$ is the identity on the auxiliary system) satisfies

$$\langle\mu| \left(\mathcal{E} \otimes \mathbb{I}_E\right)(\sigma) |\mu\rangle \geq 0 \ . \tag{2.23}$$

  To verify this, expand the action of $\mathcal{E} \otimes \mathbb{I}_E$ on σ. For an arbitrary $|\mu\rangle$, we have

$$\langle\mu| \left(\mathcal{E} \otimes \mathbb{I}_E\right)(\sigma) |\mu\rangle = \sum_k \langle\mu| A_k \otimes \mathbb{I}_E \sigma A_k^\dagger \otimes \mathbb{I}_E |\mu\rangle = \sum_k \langle\mu_k| \sigma |\mu_k\rangle \ , \tag{2.24}$$

  where $|\mu_k\rangle = A_k^\dagger \otimes \mathbb{I}_E |\mu\rangle$. Using the spectral decomposition $\sigma = \lambda_m |\lambda_m\rangle\langle\lambda_m|$, with $\lambda_m \geq 0$ (since $\sigma \geq 0$), this becomes

$$\langle\mu| \left(\mathcal{E} \otimes \mathbb{I}_E\right)(\sigma) |\mu\rangle = \sum_k \langle\mu_k| \left(\sum_m \lambda_m |\lambda_m\rangle\langle\lambda_m|\right) |\mu_k\rangle = \sum_{k,m} \lambda_m |\langle\mu_k|\lambda_m\rangle|^2 \geq 0 \ , \tag{2.25}$$

  where non-negativity follows from $\lambda_m \geq 0$.

By satisfying both trace preservation and complete positivity, $\mathcal{E}$ is guaranteed to map valid quantum states (positive semidefinite, unit-trace operators) to valid states, even in the presence of entanglement with an external environment. This CPTP structure underpins quantum error correction, noise mitigation, and the study of open quantum systems, offering a unified framework for dynamics spanning controlled measurements to complex environmental interactions.

2.0.4 Quantum dynamics

Closed quantum systems

A complete description of a quantum system requires specifying how it evolves over time. In the canonical formulation of quantum mechanics, the evolution of a closed quantum system — one that does not interact with its environment (where "environment" refers to everything external to the system) — is governed by unitary dynamics. This principle encapsulates the deterministic and reversible nature of quantum evolution, ensuring that the total probability is conserved over time. Formally, this is captured by the fifth postulate:

Postulate 5: The time evolution of a closed quantum system is governed by a unitary transformation. If the system is in the state $|\psi(t_0)\rangle$ at time t_0, its state at a later time t is given by

$$|\psi(t)\rangle = U(t;t_0)\,|\psi(t_0)\rangle \ , \tag{2.26}$$

where $U(t;t_0)$ is the unitary time-evolution operator satisfying

$$U(t;t_0)U^\dagger(t;t_0) = U^\dagger(t;t_0)U(t;t_0) = \mathbb{I} \ , \tag{2.27}$$

which ensures the preservation of the norm of the state vector.

The unitarity condition guarantees that the total probability of all measurement outcomes remains equal to one, maintaining the physical consistency of the theory. The time-evolution operator $U(t;t_0)$ encapsulates how the system evolves between two time points t_0 and t. For convenience, the initial time t_0 is often omitted in the notation, so $U(t)$ typically refers to the evolution from some implicit initial time.

Imposing the composition property on $U(t;t_0)$ — that is, requiring that time evolution over successive intervals is equivalent to evolution over the combined interval — leads to the equation of motion for the time-evolution operator [40]

$$i\frac{\partial U(t;t_0)}{\partial t} = H(t)U(t;t_0) \ , \tag{2.28}$$

where $H(t)$ is the system's Hamiltonian, which acts as the generator of the dynamics and represents the system's total energy. Throughout this thesis, we adopt natural units with $\hbar = 1$, such that energy and frequency share the same units.

Substituting this result into Eq. (2.2) yields the Schrödinger equation of motion

$$i\frac{\partial\,|\psi(t)\rangle}{\partial t} = H(t)\,|\psi(t)\rangle \ . \tag{2.29}$$

This result naturally extends to mixed states with density matrix ρ. For isolated systems,

the time evolution of ρ is governed by the equation

$$i\frac{d\rho(t)}{dt} = [H(t), \rho(t)] + i\frac{\partial\rho(t)}{\partial t} \ , \tag{2.30}$$

where the additional term $\frac{\partial\rho(t)}{\partial t}$ accounts for explicit time dependence in the probabilities p_k of the mixed state $\rho = \sum_k p_k(t) \left|\psi_k\right\rangle\!\left\langle\psi_k\right|$. In most cases, however, the probabilities p_k are time-independent, and this term vanishes, simplifying Eq. (2.30) to the Liouville–von Neumann equation

$$i\frac{d\rho(t)}{dt} = [H(t), \rho(t)] \ . \tag{2.31}$$

The time-evolved density matrix is then given by

$$\rho(t) = U(t; t_0)\rho(t_0)U^\dagger(t; t_0) \ . \tag{2.32}$$

In many contexts, such as designing quantum gates for quantum algorithms, rather than the time-evoled states, the time-evolution operator $U(t; t_0)$ itself is the primary interest. To find $U(t; t_0)$, one solves Eq. (2.28). If the Hamiltonian is time-independent (*i.e.* it is a conservative system), the solution is straightforward

$$U(t; t_0) = e^{-i(t-t_0)H} \ . \tag{2.33}$$

If the Hamiltonian depends on time but commutes at different times ($[H(t_1), H(t_2)] = 0$), the solution generalizes to

$$U(t; t_0) = e^{-i\int_{t_0}^{t} d\tau H(\tau)} \ . \tag{2.34}$$

For general time-dependent Hamiltonians that do not commute at different times, finding an exact solution is challenging. One common approach involves discretizing time into N intervals

$$t_0 < t_1 < \cdots < t_{N-1} < t_N \tag{2.35}$$

with a time step $\Delta t = t_{i+1} - t_i = \frac{t-t_0}{N}$. If Δt is sufficiently small, the Hamiltonian can be approximated as constant within each interval, allowing the time-evolution operator to be approximated (according to Eq. (2.33)) in the interval from t_i to t_{i+1} as

$$U(t_{i+1}; t_i) \approx e^{-i\Delta t H(t_i)} \ . \tag{2.36}$$

Extending this approximation across all intervals yields

$$U(t; t_0) = U(t_N; t_{N-1}) \cdots U(t_2; t_1)U(t_1; t_0) = \prod_{i=N-1}^{0} U(t_{i+1}; t_i) \ , \tag{2.37}$$

where the product is ordered such that operators for later times appear on the left.

In the limit $N \to \infty$ (*i.e.* $\Delta t \to 0$), this solution converges to the exact result. For piecewise constant Hamiltonians, the intervals can be chosen to coincide with regions of constant Hamiltonian, making the approximation exact even for finite N. However, for highly oscillatory Hamiltonians, truncating the product at a finite N can lead to inaccuracies. In such cases, alternative approaches, like the *Dyson series* or *Magnus expansion* [41], may be more suitable.

To derive the Dyson series, one begins by integrating Eq. (2.28), yielding

$$i \int_{t_0}^{t} dt_1 \frac{\partial U(t_1; t_0)}{\partial t} = \int_{t_0}^{t} dt_1 H(t_1) U(t_1; t_0) \ , \tag{2.38}$$

which, using the initial condition $U(t_0; t_0) = \mathbb{I}$, leads to

$$U(t; t_0) = \mathbb{I} - i \int_{t_0}^{t} dt_1 H(t_1) U(t_1; t_0) \ . \tag{2.39}$$

This relation expresses the time-evolution operator at time t in terms of the Hamiltonian and the time-evolution operator at an earlier time t_1. By applying the same argument recursively, one obtains the Dyson series

$$\begin{aligned} U(t; t_0) = \mathbb{I} - i \int_{t_0}^{t} dt_1 H(t_1) - \int_{t_0}^{t} dt_1 \int_{t_0}^{t_1} dt_2 H(t_1) H(t_2) + \cdots \\ + (-i)^m \int_{t_0}^{t} dt_1 \int_{t_0}^{t_1} dt_2 \cdots \int_{t_0}^{t_{m-1}} dt_m H(t_1) H(t_2) \cdots H(t_m) + \cdots \ , \end{aligned} \tag{2.40}$$

which can be compactly written as

$$U(t; t_0) = \mathcal{T} e^{-i \int_{t_0}^{t} d\tau H(\tau)} \ . \tag{2.41}$$

Here, $\mathcal{T}$ is the time-ordering operator that ensures that operators with later times appear to the left of those with earlier times, *i.e.*

$$\mathcal{T} A(t_1) B(t_2) = \begin{cases} A(t_1) B(t_2), & \text{if } t_1 > t_2 \ , \\ B(t_2) A(t_1), & \text{if } t_2 > t_1 \ . \end{cases} \tag{2.42}$$

While Eq. (2.41) formally solves the Schrödinger equation, its practical application is limited due to the complexity of time-ordering and potential divergence for large time intervals or strong interactions. Truncating the Dyson series can also lead to significant non-unitary errors, compromising the physical interpretation of the approximation [42, 43].

An alternative approach to solving the time-dependent Schrödinger equation is the Magnus expansion [42], which provides an iterative solution while preserving unitarity at each order of approximation. Unlike conventional perturbative methods, the Magnus expansion often exhibits better convergence properties, making it particularly useful in quantum control and driven quantum systems. The method starts by assuming an ansatz for the time-

evolution operator in the form of an exponential map

$$U(t;t_0) = \exp(\Omega(t;t_0)) \ , \tag{2.43}$$

where $\Omega(t;t_0)$ is an effective generator, expanded as a power series

$$\Omega(t;t_0) = \sum_k \Omega_k(t;t_0) \ . \tag{2.44}$$

To derive an equation for $\Omega(t;t_0)$, we differentiate both sides of Eq. (2.43) using the identity for the derivative of the exponential map (for a detailed derivation, see Appendix A.1)

$$\frac{\partial}{\partial t}\exp(\Omega(t;t_0)) = \left(\int_0^1 d\alpha \ e^{\alpha\Omega(t;t_0)}\frac{\partial\Omega}{\partial t}e^{-\alpha\Omega(t;t_0)}\right)e^{\Omega(t;t_0)} \ . \tag{2.45}$$

Substituting this into the Schrödinger equation for $U(t;t_0)$ (Eq. (2.28)) yields the integral equation

$$\int_0^1 d\alpha \ e^{\alpha\Omega(t;t_0)}\frac{\partial\Omega}{\partial t}e^{-\alpha\Omega(t;t_0)} = -iH(t) \ . \tag{2.46}$$

Using the identity from Eq. (A.18), the left-hand side can be rewritten as

$$\int_0^1 d\alpha \exp\big(\alpha \mathrm{ad}_{\Omega(t;t_0)}\big)\left(\frac{\partial\Omega}{\partial t}\right) = -iH(t) \ , \tag{2.47}$$

where $\mathrm{ad}_A(X) = [A,X]$. Integrating the left hand-side (using Eq. (A.10) from the Appendix), we arrive at

$$\big(\mathrm{ad}_{\Omega(t;t_0)}\big)^{-1}\left(\exp\big(\mathrm{ad}_{\Omega(t;t_0)}\big) - \mathbb{I}\right)\left(\frac{\partial\Omega}{\partial t}\right) = -iH(t) \ . \tag{2.48}$$

Rearranging to isolate $\frac{\partial\Omega}{\partial t}$,

$$\frac{\partial\Omega}{\partial t} = \left(\exp\big(\mathrm{ad}_{\Omega(t;t_0)}\big) - \mathbb{I}\right)^{-1}\left(\mathrm{ad}_{\Omega(t;t_0)}\right)\Big(-iH(t)\Big) \ . \tag{2.49}$$

Using the standard expansion,

$$(e^x - 1)^{-1}x = \sum_{k=0}^{\infty}\frac{B_k x^k}{k!} \ , \tag{2.50}$$

where B_n are the Bernoulli numbers, we express the inverse operator as

$$\left(\exp\big(\mathrm{ad}_{\Omega(t;t_0)}\big) - \mathbb{I}\right)^{-1}\left(\mathrm{ad}_{\Omega(t;t_0)}\right) = \sum_{k=0}^{\infty}\frac{B_k}{k!}\mathrm{ad}^k_{\Omega(t;t_0)} \ . \tag{2.51}$$

Thus, the evolution equation for Ω takes the recursive form

$$\frac{\partial \Omega}{\partial t} = \sum_{k=0}^{\infty} \frac{B_k}{k!} \mathrm{ad}^k_{\Omega(t;t_0)}\Big(-iH(t)\Big) \ . \tag{2.52}$$

Expanding the first few terms explicitly,

$$\frac{\partial \Omega}{\partial t} = \sum_{k=0}^{\infty} \frac{B_k}{k!} \underbrace{[\Omega, [\cdots, [\Omega, -iH(t)]]]}_{k \text{ commutators}} = -iH + \frac{i}{2}[\Omega, H] - \frac{i}{12}[\Omega, [\Omega, H]] + \cdots \ . \tag{2.53}$$

With the initial condition $\Omega(0) = 0$, this equation is solved iteratively, yielding the Magnus expansion [42]

$$\begin{aligned}
\Omega(t;t_0) = &-i \int_{t_0}^{t} dt_1 H(t_1) \\
&- \frac{1}{2} \int_{t_0}^{t} dt_1 \int_{t_0}^{t_1} dt_2 [H(t_1), H(t_2)] \\
&+ \frac{i}{6} \int_{t_0}^{t} dt_1 \int_{t_0}^{t_1} dt_2 \int_{t_0}^{t_2} dt_3 \Big([H(t_1), [H(t_2), H(t_3)]] + [H(t_3), [H(t_2), H(t_1)]] \Big) \\
&+ \frac{1}{12} \int_{t_0}^{t} dt_1 \int_{t_0}^{t_1} dt_2 \int_{t_0}^{t_2} dt_3 \int_{t_0}^{t_3} dt_4 \Big([[[H(t_1), H(t_2)], H(t_3)], H(t_4)] \\
&\qquad\qquad + [H(t_1), [[H(t_2), H(t_3)], H(t_4)]] \\
&\qquad\qquad + [H(t_1), [H(t_2), [H(t_3), H(t_4)]]] \\
&\qquad\qquad + [H(t_2), [H(t_3), [H(t_4), H(t_1)]]] \Big) \\
&+ \cdots
\end{aligned} \tag{2.54}$$

Each term in this expansion involves nested time integrals and commutators of the Hamiltonian evaluated at different times. Importantly, since $H(t)$ is Hermitian and the commutator (Eq. (2.11)) is anti-Hermitian, $\Omega(t;t_0)$ remains anti-Hermitian to all orders in the expansion. This guarantees that the time-evolution operator (Eq. (2.43)) is unitary, preserving the norm of quantum states and ensuring physical consistency.

This structure-preserving property is a central strength of the Magnus expansion. However, it comes with a significant caveat: convergence is not always guaranteed. A commonly cited sufficient condition for convergence is that the time-integrated operator norm of the Hamiltonian remains below a critical threshold [42],

$$\int_{t_0}^{t} ds \|H(s)\| < \pi \ , \tag{2.55}$$

where the operator norm is defined as $\|A\| = \sup_{\||\psi\rangle\|=1} \|A|\psi\rangle\|$. When this condition is satisfied, the operator $\left(\exp\left(\mathrm{ad}_{\Omega(t;t_0)}\right) - \mathbb{I}\right)^{-1} \left(\mathrm{ad}_{\Omega(t;t_0)}\right)$ in Eq. (2.51) remains well-defined, and the series for $\Omega(t;t_0)$ converges absolutely (see Appendix A.5).

While practical and easy to apply, this bound is merely sufficient, not necessary. More generally, convergence of the Magnus expansion occurs if and only if the exact evolution operator $U(t;t_0)$ admits a single-valued, analytic logarithm near the identity in the complex plane. This implies that the eigenvalues of $U(t;t_0)$ must not encircle the origin. In terms of $\Omega(t;t_0)$ this requirement translates into a spectral condition: the eigenvalues of $\Omega(t;t_0)$ must lie within a horizontal strip of width 2π in the complex plane. For example, if the time-averaged Hamiltonian $\Phi(t) = \int_{t_0}^{t} dsH(s)$ is diagonalizable with eigenvalues λ_j, convergence is ensured provided [42]

$$\|\mathfrak{Im}(\lambda_j - \lambda_k)\| < 2\pi \quad \text{for all } j,k \ , \tag{2.56}$$

which avoids ambiguities in the logarithm introduced by branch cuts in the exponential map.

Thus, although norm bounds offer a convenient check, the true convergence criteria depend on deeper spectral and analytic properties of the evolution operator. When satisfied, these conditions allow the Magnus expansion to serve as a rigorous, unitarity-preserving framework for solving time-dependent quantum dynamics.

Open quantum systems

While the standard formulation of quantum mechanics describes isolated systems, practical implementations — such as ion traps performing quantum gates — inevitably interact with their environment. Environmental influences, including electric field noise, magnetic field fluctuations, and collisions with residual gas molecules, induce decoherence and the degradation of quantum information.

Rather than merely postulating these effects, we derive the dynamics from first principles by extending the system's description to include its environment. Building on the Kraus representation introduced above, we systematically account for system–environment interactions and characterize their impact on the system's evolution. By considering the reduced dynamics of the system under appropriate assumptions — such as weak coupling and a memoryless (Markovian) environment — we arrive at the Lindblad master equation, which provides a general framework for describing open quantum systems. For a more comprehensive treatment, see [44].

Consider a quantum system with Hilbert space $\mathcal{H}_S$ interacting with an environment with Hilbert space $\mathcal{H}_E$. The joint system, including both the system of interest and its environment, forms a closed quantum system and evolves unitarily under the Schrödinger equation, as stated in Postulate 5, *i.e.*

$$\rho_{SE}(t) = U(t;t_0)\rho_{SE}(t_0)U^{\dagger}(t;t_0) \ , \tag{2.57}$$

where $U(t;t_0)$ is the joint unitary evolution operator acting on $\mathcal{H}_S \otimes \mathcal{H}_E$ and t_0 is the initial time. Assuming the system and environment are initially uncorrelated, the initial

state of the total system takes the form

$$\rho_{SE}(t_0) = \rho_S(t_0) \otimes \rho_E(t_0) \ , \tag{2.58}$$

where $\rho_E(t_0)$ is the initial state of the environment, which can be expressed in its spectral decomposition as

$$\rho_E(t_0) = \sum_j \lambda_j \left|\lambda_j\right\rangle\!\left\langle\lambda_j\right| \ , \tag{2.59}$$

where λ_j are the eigenvalues (satisfying $\sum_j \lambda_j = 1$) and $|\lambda_j\rangle$ the corresponding orthonormal eigenvectors. The reduced state of the system at time t is obtained by tracing over the environmental degrees of freedom

$$\rho_S(t) = \mathrm{Tr}_E(\rho_{SE}(t)) \ . \tag{2.60}$$

Expanding the trace over the orthonormal basis $\{|\lambda_k\rangle\}$ of $\mathcal{H}_E$ from Eq. (2.59) gives

$$\rho_S(t) = \sum_k \left\langle\lambda_k\right| U(t;t_0)\rho_{SE}(t_0)U^\dagger(t;t_0) \left|\lambda_k\right\rangle \ . \tag{2.61}$$

Substituting the spectral decomposition of $\rho_E(t_0)$ yields

$$\begin{aligned}
\rho_S(t) &= \sum_k \left\langle\lambda_k\right| U(t;t_0)\Big(\rho_S(t_0) \otimes \rho_E(t_0)\Big)U^\dagger(t;t_0) \left|\lambda_k\right\rangle \\
&= \sum_{k,j} \left\langle\lambda_k\right| U(t;t_0)\Big(\rho_S(t_0) \otimes \lambda_j \left|\lambda_j\right\rangle\!\left\langle\lambda_j\right| \Big)U^\dagger(t;t_0) \left|\lambda_k\right\rangle \\
&= \sum_{k,j} \Big(\sqrt{\lambda_j}\left\langle\lambda_k\right| U(t;t_0) \left|\lambda_j\right\rangle \Big)\rho_S(t_0)\Big(\sqrt{\lambda_j}\left\langle\lambda_j\right| U^\dagger(t;t_0) \left|\lambda_k\right\rangle \Big) \\
&= \sum_{k,j} A_{kj}(t;t_0)\rho_S(t_0)A_{kj}^\dagger(t;t_0) \ ,
\end{aligned} \tag{2.62}$$

where we have defined the Krauss operators

$$A_{kj}(t;t_0) = \sqrt{\lambda_j}\left\langle\lambda_k\right| U(t;t_0) \left|\lambda_j\right\rangle \ . \tag{2.63}$$

This allows us to recognize the familiar Kraus representation of the system's evolution, as seen in Eq. (2.20). To confirm the physical validity of this representation, we can explicitly verify the completeness relation (Eq. (2.21)),

$$\begin{aligned}
\sum_{k,j} A_{kj}^\dagger(t;t_0)A_{kj}(t;t_0) &= \sum_{k,j} \lambda_j \left\langle\lambda_k\right| U(t;t_0) \left|\lambda_j\right\rangle \left\langle\lambda_j\right| U^\dagger(t;t_0) \left|\lambda_k\right\rangle \\
&= \sum_j \Big(\sum_k \left|\lambda_k\right\rangle\!\left\langle\lambda_k\right| \Big)\lambda_j \left\langle\lambda_j\right| U^\dagger(t;t_0)U(t;t_0) \left|\lambda_j\right\rangle \\
&= \mathbb{I}\sum_j \lambda_j = \mathbb{I} \ .
\end{aligned} \tag{2.64}$$

Finally, for notational convenience, we can relabel the indices (j, k) as α, leading to the compact and often-used form

$$\rho_S(t) = \sum_\alpha A_\alpha(t; t_0)\rho_S(t_0)A_\alpha^\dagger(t; t_0) \ . \tag{2.65}$$

Our goal now is to derive the equation of motion for the system in the limit of short time evolution, starting from t_0. We begin by Taylor-expanding $\rho_S(t)$ around t_0,

$$\rho_S(t_0 + \delta t) = \rho_S(t_0) + \dot{\rho}_S(t_0 + \delta t)\delta t + \mathcal{O}(\delta t^2) \ . \tag{2.66}$$

Using the Krauss representation in Eq. (2.62), we also have

$$\rho_S(t_0 + \delta t) = \sum_\alpha A_\alpha(t_0 + \delta t; t_0)\rho_S(t_0)A_\alpha^\dagger(t_0 + \delta t; t_0) \ . \tag{2.67}$$

In the perturbative regime of infinitesimal δt, the Kraus operators must be carefully expanded to ensure consistency with both the Taylor series and the structure of quantum stochastic calculus. Here, the evolution of $\rho_S(t)$ is interpreted as a combination of deterministic and stochastic processes, loosely analogous to classical stochastic differential equations. The deterministic component includes both coherent dynamics and non-unitary damping due to environmental interactions, while the stochastic component explicitly represents discrete quantum jumps induced by the environment.

To formalize this analogy, consider the expansion of the Kraus operators. The dominant term, labeled A_0, must approximate the identity operator as $\delta t \to 0$ to recover $\rho_S(t_0)$ in the absence of evolution. This operator is expanded as

$$A_0(t_0 + \delta t; t_0) = \mathbb{I}_S + M_0\delta t \ , \tag{2.68}$$

where M_0 encodes *deterministic* first-order corrections to the identity, including contributions from both coherent dynamics (*e.g.*, a Hamiltonian) and decoherence. The remaining Kraus operators $A_{k>0}$ account for *stochastic* effects — namely, quantum jumps arising from interactions with the environment. These are scaled as

$$A_k(t_0 + \delta t; t_0) = L_k\sqrt{\delta t} \qquad (k > 0) \ , \tag{2.69}$$

where L_k are general operators, not necessarily Hermitian. Notably, the $\sqrt{\delta t}$ scaling in Eq. (2.69) is rooted in the principles of stochastic calculus [45], specifically the Itô formalism. In classical stochastic differential equations, fluctuations are modeled by Wiener processes W_t, whose increments satisfy $dW_t \sim \sqrt{\delta t}$, with variances $\mathbb{E}[(dW_t)^2] = \delta t$. This ensures that stochastic terms contribute to the evolution at leading order in δt. Similarly, in quantum stochastic calculus [46], noise increments like the quantum annihilation operator da_t obey $da_t da_t^\dagger = \delta t$, again indicating an amplitude scaling of $\sqrt{\delta t}$. Thus, assigning this scaling to the dissipative Kraus operators $A_{k>0}$ guarantees that their contributions to the density matrix, through terms like $A_k\rho A_k^\dagger$, appear at order δt in the full Kraus map.

Substituting these expansions into the Kraus representation (Eq. (2.62)) yields

$$\rho_S(t_0+\delta t) = (\mathbb{I}_S + M_0\delta t)\,\rho_S(t_0)\left(\mathbb{I}_S + M_0^\dagger \delta t\right) + \delta t \sum_{k>0} L_k \rho_S(t_0) L_k^\dagger \ . \tag{2.70}$$

Expanding this expression to first order in δt and neglecting $\mathcal{O}(\delta t^2)$ terms (which is justified under the *weak-coupling (Born) approximation*) leads to

$$\rho_S(t_0+\delta t) = \rho_S(t_0) + \delta t\Big[M_0\rho_S(t_0) + \rho_S(t_0)M_0^\dagger\Big] + \delta t \sum_{k>0} L_k \rho_S(t_0) L_k^\dagger \ . \tag{2.71}$$

Thus, the infinitesimal change in the density matrix is

$$\rho_S(t_0+\delta t) - \rho_S(t_0) = \delta t\Big[M_0\rho_S(t_0) + \rho_S(t_0)M_0^\dagger + \sum_{k>0} L_k \rho_S(t_0) L_k^\dagger\Big] \ . \tag{2.72}$$

Dividing by δt and taking the limit $\delta t \to 0$ yields the time-local master equation

$$\dot\rho(t)|_{t_0} = \lim_{\delta t\to 0} \frac{\rho_S(t_0+\delta t) - \rho_S(t_0)}{\delta t} = M_0\rho_S(t_0) + \rho_S(t_0)M_0^\dagger + \sum_{k>0} L_k(t_0)\rho_S(t_0)L_k^\dagger \ . \tag{2.73}$$

To ensure that the evolution is trace preserving (*i.e.* that the dynamical map is CPTP), we require that the Kraus operators satisfy the completeness relation (Eq. (2.21))

$$A_0^\dagger(t_0+\delta t,t_0)A_0(t_0+\delta t,t_0) + \sum_{k>0} A_k^\dagger(t_0+\delta t,t_0)A_k(t_0+\delta t,t_0) = \mathbb{I}_S \ , \tag{2.74}$$

which implies

$$(\mathbb{I}_S + M_0^\dagger\delta t)(\mathbb{I}_S + M_0\delta t) + \delta t\sum_{k>0} L_k^\dagger L_k = \mathbb{I}_S \ . \tag{2.75}$$

Expanding and neglecting $\mathcal{O}(\delta t^2)$ terms, this relation reduces to

$$M_0^\dagger + M_0 = -\sum_{k>0} L_k^\dagger L_k \ , \tag{2.76}$$

condition that ensures the preservation of trace (and hence total probability) in the evolution of $\rho_S(t_0)$. It is then customary to decompose the operator M_0 into its Hermitian and anti-Hermitian parts, $M_0 = L_0 - iH$, with both H and L_0 Hermitian operators on $\mathcal{H}_S$. This decomposition separates the coherent and dissipative contributions to the system's dynamics. The above trace-preservation condition then implies

$$L_0 = -\frac{1}{2}\sum_{k>0} L_k^\dagger L_k \ . \tag{2.77}$$

Substituting this decomposition into the master equation yields

$$\dot{\rho}_S(t)|_{t_0} = -i[H, \rho_S(t_0)] + \sum_{k>0} \left(L_k \rho_S(t_0) L_k^\dagger - \frac{1}{2} \left\{ L_k^\dagger L_k, \rho_S(t_0) \right\} \right) . \tag{2.78}$$

At this stage, we observe that the operators L_k are not dimensionless; rather, they carry dimensions of $1/\sqrt{\text{time}}$. To make them dimensionless, we introduce a rescaling by defining $L_k \to \sqrt{\gamma_k} L_k$, where γ_k has units of $1/\text{time}$. Substituting this transformation into Eq. (2.78), we obtain

$$\dot{\rho}_S(t)|_{t_0} = -i[H, \rho_S(t_0)] + \sum_{k>0} \gamma_k \left(L_k \rho_S(t_0) L_k^\dagger - \frac{1}{2} \left\{ L_k^\dagger L_k, \rho_S(t_0) \right\} \right) . \tag{2.79}$$

This expression remains valid as a short-time expansion near $t = t_0$. To extend its validity to all times $t > t_0$, we introduce a crucial assumption: we postulate that Eq. (2.79) holds at all times. This assumption corresponds to the *Markovian limit*, which informally states that the system's evolution has no memory, meaning that it resets at each infinitesimal time step δt. This assumption is physically motivated by considering the unitary component of the evolution. Focusing on the first term in Eq. (2.79), $\dot{\rho}_S(t)|_{t_0} = -i[H, \rho_S(t_0)]$, we recognize that this equation remains valid for arbitrary t in the absence of dissipative effects, as it simply describes unitary evolution governed by the Liouville–von Neumann equation, $\dot{\rho}_S(t) = -i[H, \rho_S(t)]$. By analogy, we assume that Eq. (2.79) also holds for all times under the Markovian approximation. With this, we arrive at the *Lindblad equation*,

$$\frac{d\rho_S}{dt} = -i[H, \rho_S(t)] + \sum_{k>0} \gamma_k \left(L_k \rho_S(t) L_k^\dagger - \frac{1}{2} \left\{ L_k^\dagger L_k, \rho_S(t) \right\} \right) \equiv \mathcal{L}\left(\rho_S(t)\right) \ , \tag{2.80}$$

which describes the Markovian evolution of the system's state under the influence of its environment through the *Lindbladian* superoperator $\mathcal{L}$. The first term, involving the commutator with H, represents the unitary evolution governed by the effective system Hamiltonian, recovering the Liouville–von Neumann equation (Eq. (2.31)) when dissipation is absent. The second term, parameterized by the jump operators L_k and their corresponding rates γ_k, encodes the non-unitary effects arising from the system's interaction with the environment, such as relaxation and decoherence. This form explicitly highlights how Markovian open-system dynamics can be understood as a balance between coherent evolution and irreversible processes induced by environmental coupling.

2.1 Lie groups and Lie algebras

Symmetry principles play a foundational role in quantum mechanics, underlying the mathematical framework used to describe quantum systems. Symmetries correspond to transformations that leave certain properties of a system invariant. For instance, the symmetries of a square include rotations of $0, \pi/2, \pi$, and $3\pi/2$ radians about its center, forming a finite set known as a *discrete group*. In contrast, a unit circle exhibits continuous rotational symmetry, as any angle of rotation about its center preserves its shape. This infinite set

of transformations forms a *continuous group*.

The study of continuous symmetries is formalized using *Lie theory* [47, 48, 49]. Central to Lie theory is the concept of a *Lie group*, a group that is also a smooth manifold. A *smooth manifold*, a concept rooted in differential geometry, is a geometric space that looks locally like flat Euclidean space $\mathbb{R}^n$, where smooth (infinitely differentiable) transitions between regions are possible. This smooth structure, combined with the smooth group operations of multiplication and inversion, enables the analysis of infinitesimal transformations, giving rise to the concept of *Lie algebras*. While general Lie groups are abstract mathematical objects within group theory and representation theory, *matrix Lie groups* – a specific subclass — are particularly relevant to quantum mechanics and offer a more accessible treatment using linear algebra.

A matrix Lie group G is a closed subgroup of $GL(n, \mathbb{C})$, *i.e.* the group of $n \times n$ invertible matrices with complex entries, that possesses smooth group operations. It satisfies the following properties

- *Closure under matrix multiplication*: For any two elements $A, B \in G$, their product AB is also in G.
- *Associativity*: For any three elements $A, B, C \in G$, $A(BC) = (AB)C$.
- *Existence of identity*: There exists an identity element $\mathbb{I}$ such that for any $A \in G$, $A\mathbb{I} = \mathbb{I}A = A$.
- *Existence of inverse*: For every element A in the group, there exists an inverse element A^{-1} such that $AA^{-1} = A^{-1}A = \mathbb{I}$.
- *Closure under non-singular limits*: If a sequence of matrices $A_1, A_2, A_3, \cdots$ in G converges to a non-singular matrix A (*i.e.*, $A = \lim_{k\to\infty} A_k$), then A also belongs to G.

These properties ensure that group elements (matrices) can be continuously transformed into each other through smooth functions. The group operation (matrix multiplication) and the inverse operation (matrix inversion) are smooth functions, making the group both algebraically and geometrically well-behaved. Examples of matrix Lie groups include

- The unitary group $U(n)$ that consists of $n \times n$ unitary matrices.
- The special unitary group $SU(n)$ that consists of $n \times n$ unitary matrices with determinant 1, often used to describe symmetries in quantum mechanics.
- The special orthogonal group $SO(n)$ of all $n \times n$ orthogonal matrices with determinant 1, representing rotations in n-dimensions.

Each transformation $h(\theta)$ in a matrix Lie group G can be expressed in the exponential form

$$h(\theta) = \exp(\theta\sigma) \ , \tag{2.81}$$

where $\theta \in \mathbb{R}$ is a continuous parameter and σ is the generator of the transformation which, in an n-dimensional space, is represented as a $n \times n$ matrix.

The set of generators $\{\sigma_j\}$ that allow constructing any element $h(\theta)$ in G defines the *Lie algebra* $\mathfrak{g}$ of the (matrix) Lie group G. Since $\exp(\theta\sigma) \approx \mathbb{I} + \theta\sigma$, the Lie algebra provides a linear approximation to the group structure near the identity element and thus captures the *infinitesimal* structure of a Lie group. The Lie algebra is equipped with a binary operation, the commutator (or Lie bracket), defined in Eq. (2.11), that satisfies the following key properties

- Bilinearity: $[a\sigma_1 + b\sigma_2, \sigma_3] = a[\sigma_1, \sigma_3] + b[\sigma_2, \sigma_3]$ and $[\sigma_1, a\sigma_2 + b\sigma_3] = a[\sigma_1, \sigma_2] + b[\sigma_1, \sigma_3]$ for all $\sigma_1, \sigma_2, \sigma_3 \in \mathfrak{g}$ and $a, b \in \mathbb{C}$.
- Alternating: $[\sigma_1, \sigma_1] = 0$ for all $\sigma_1 \in \mathfrak{g}$.
- Jacobi identity: $[\sigma_1, [\sigma_2, \sigma_3]] + [\sigma_2, [\sigma_3, \sigma_1]] + [\sigma_3, [\sigma_1, \sigma_2]] = 0$ for all $\sigma_1, \sigma_2, \sigma_3 \in \mathfrak{g}$.

Unlike Lie groups, Lie algebras are closed under the commutator operation, not matrix multiplication. This means that for any two elements $\sigma_1, \sigma_2 \in \mathfrak{g}$ their products $\sigma_1\sigma_2$ or $\sigma_2\sigma_1$ might not belong to $\mathfrak{g}$ but their commutator $[\sigma_1, \sigma_2]$ belongs to $\mathfrak{g}$. This closure property can be formalized as

$$[\sigma_j, \sigma_k] = \sum_l \lambda_{jl}^k \sigma_l \ , \tag{2.82}$$

where the constants λ_{jl}^k are known as the *structure constants*.

The exponential map, $\exp : \mathfrak{g} \to G$, is a fundamental tool in Lie theory that establishes a connection between Lie algebras and Lie groups. It is defined by the following series expansion

$$\exp(\sigma) = \sum_{n=0}^{\infty} \frac{1}{n!}\sigma^n \ , \tag{2.83}$$

where $\sigma \in \mathfrak{g}$. This map is essential for generating (matrix) elements of the Lie group G from the (matrix) elements of its Lie algebra $\mathfrak{g}$.

The relationship between the multiplication rules of the Lie group and its Lie algebra is captured by the Baker-Campbell-Hausdorff (BCH) formula, which gives a series expansion for the product of two exponentiated Lie algebra elements

$$e^{\sigma_1} e^{\sigma_2} = e^{\sigma_1 + \sigma_2 + \frac{1}{2}[\sigma_1, \sigma_2] + \frac{1}{12}[\sigma_1, [\sigma_1, \sigma_2]] - \frac{1}{12}[\sigma_2, [\sigma_1, \sigma_2]] + \cdots} \ , \tag{2.84}$$

where $e^{\sigma_1}, e^{\sigma_2}$ are elements of the Lie group, and σ_1, σ_2 are elements of the corresponding Lie algebra. A particularly valuable application of the BCH formula arises in the context of unitary transformations, as it facilitates the construction of the conjugation of any algebra element σ_2, by a group element e^{σ_1}

$$e^{\sigma_1}\sigma_2 e^{-\sigma_1} = \sigma_2 + [\sigma_1, \sigma_2] + \frac{1}{2!}[\sigma_1, [\sigma_1, \sigma_2]] + \frac{1}{3!}[\sigma_1, [\sigma_1, [\sigma_1, \sigma_2]]] + \cdots \ , \tag{2.85}$$

operation that will be frequently applied throughout this thesis.

The mathematical structure of quantum mechanics is deeply intertwined with Lie theory, as quantum operators often exhibit Lie algebraic properties. For example, the ladder operators a and $a^\dagger$ involved in the quantization of a harmonic oscillator (discussed in detail in Sec. 4.1.2) satisfy the commutation relation

$$\left[a, a^\dagger\right] = 1 \ , \tag{2.86}$$

which reflects the underlying Lie algebraic structure. Similarly, the Pauli matrices

$$\sigma_x \equiv X = \begin{pmatrix} 0 & 1 \\ 1 & 0 \end{pmatrix} \ , \qquad \sigma_y \equiv Y = \begin{pmatrix} 0 & -i \\ i & 0 \end{pmatrix} \ , \qquad \sigma_z \equiv Z = \begin{pmatrix} 1 & 0 \\ 0 & -1 \end{pmatrix} \ , \tag{2.87}$$

used to describe spin-1/2 particles and other two-level quantum systems, obey the commutation relations

$$[\sigma_a, \sigma_b] = 2i\epsilon_{abc}\sigma_c \ , \tag{2.88}$$

where ϵ_{abc} is the Levi-Civita symbol, and $a, b, c \in \{x, y, z\}$. These matrices are the generators of the $\mathfrak{su}(2)$ Lie algebra, which is associated with the $SU(2)$ group of unitary 2×2 matrices with unit determinant. This group plays a pivotal role in quantum information theory.

The influence of Lie theory extends to quantum dynamics as well. The time evolution of a quantum system, governed by the Schrödinger equation (Eq. (2.29)), is described by a unitary time-evolution operator (Eq. (2.28)). This operator can be understood as the exponential map from the Lie algebra of quantum operators to the Lie group of unitary transformations.

The Magnus expansion (Eq. (2.54)) provides a concrete realization of this connection. It reveals that the exponent $\Omega(t)$ in the unitary operator $U = \exp(\Omega(t))$ is a series involving nested commutators of the system's Hamiltonian $H(t)$, structure that is directly linked to the BCH formula. Thus, by examining the time-evolution operator and its expansion, one can see the explicit manifestation of Lie algebraic and Lie group structures in the dynamics of quantum systems. This interplay between the Hamiltonian, its associated Lie algebra, and the corresponding Lie group will be a central theme explored throughout this thesis.

Chapter 3

Quantum Control Theory

> "The imagination of nature is far, far greater than the imagination of man."
>
> – Richard Feynman, 1982 [50]

Quantum control theory provides a rigorous framework for manipulating and directing the evolution of quantum systems [51, 52]. Unlike classical systems, quantum systems exhibit phenomena such as superposition and entanglement, which necessitate a fundamentally quantum-mechanical approach to their dynamics. The primary goal of quantum control is to achieve precise and deterministic control over a system's evolution, which involves not only driving the system toward specific target states but also might involve shaping the time-evolution operators that govern its dynamics. This process often requires the careful modulation of external fields — such as laser or microwave pulses — to induce targeted quantum transitions and steer the system toward the desired behavior.

Quantum control theory has found widespread applications, revolutionizing fields like quantum information processing (enabling quantum computation and communication) [53], quantum sensing (enhancing the sensitivity of quantum sensors) [54], and physical chemistry (controlling chemical reactions with unprecedented precision) [55]. Moreover, it has significantly advanced our fundamental understanding of quantum mechanics by providing experimental platforms for probing and manipulating quantum phenomena, leading to profound insights into the quantum world [25].

A typical quantum control problem involves a quantum system initially prepared in an easily accessible state (*e.g.*, a product state) and the objective of driving the system towards a specific target state or inducing desired dynamics. The evolution of the quantum system is governed by the system Hamiltonian $H(t)$, which typically comprises a drift Hamiltonian, H_0, describing the intrinsic dynamics of the system, and a control Hamiltonian,

$\sum_{k=1}^{N_h} u_k(t)\mathfrak{h}_k$, representing the interaction with N_h external control fields, *i.e.*

$$H(t) = H_0 + \sum_{k=1}^{N_h} u_k(t)\mathfrak{h}_k \ . \tag{3.1}$$

The goal is to determine a set of time-dependent control functions, $u_k(t)$, and the duration of the control process, T, that drive the system to achieve the desired objective. This objective can either involve reaching a specific target state or implementing a particular time-evolution operator. In the first case, the goal is to drive the system from an initial state $|\psi_I\rangle$ to a target state $|\psi_T\rangle$, with the system dynamics governed by the time-dependent Schrödinger equation (Eq. (2.29)), *i.e.*

$$i\frac{\partial\,|\psi(t)\rangle}{\partial t} = \Big(H_0 + \sum_{k=1}^{N_h} u_k(t)\mathfrak{h}_k\Big)\,|\psi(t)\rangle \ , \tag{3.2}$$

with the initial condition $|\psi(0)\rangle = |\psi_I\rangle$. Although this formulation can be generalized to density matrices to encompass mixed states, the focus is often on pure states due to the high fidelity with which they can be experimentally prepared. When environmental interactions become significant, master equations (Eq. (2.80)) can be employed to incorporate decoherence and other perturbative effects into the system's dynamics.

In the second case, the goal is to achieve a target gate $\mathcal{U}_T$ at $t = T$, compatible with the differential equation

$$i\frac{\partial U(t)}{\partial t} = \Big(H_0 + \sum_{k=1}^{N_h} u_k(t)\mathfrak{h}_k\Big)U(t) \ , \tag{3.3}$$

with the initial condition $U(0) = \mathbb{I}$.

3.1 Controllability and reachability

The set of states that a quantum system can reach is fundamentally determined by its initial state and the properties of the Hamiltonian governing its time evolution. The Hamiltonian defines the system's dynamics, specifying the pathways available from the initial state and, consequently, constraining the set of accessible states. Importantly, not every state in the system's Hilbert space can be reached from a given initial state; the accessible states are limited by the structure of the Hamiltonian and the nature of the control fields. In closed systems, these dynamics are described by the Schrödinger equation (Eq. (2.29)), while in open systems, they are governed by a master equation (Eq. (2.80)).

To illustrate this concept, consider a single qubit initialized in the ground state $|\psi_r(0)\rangle = |g\rangle$ and suppose that the system evolves under a Hamiltonian of the form $H(t) = f(t)\sigma_x$, where $f(t)$ is any real, time-dependent control function. The most general pure state of a qubit is given by $|\psi_g\rangle = \cos(\theta/2)\,|e\rangle + e^{i\phi}\sin(\theta/2)\,|g\rangle$, where $\theta \in [0,\pi]$ and $\phi \in [0, 2\pi)$ are arbitrary parameters. However, the evolution of the qubit under the Hamil-

tonian $H(t)$ yields a restricted subset of states, given by $|\psi_r(T)\rangle = \cos\left(\int_0^T dt f(t)\right)|e\rangle + e^{i3\pi/2}\sin\left(\int_0^T dt f(t)\right)|g\rangle$, where the relative phase between $|g\rangle$ and $|e\rangle$ is fixed at $e^{i3\pi/2}$. This fixed relative phase demonstrates that the reachable states do not span the full set of general qubit states $|\psi_g\rangle$, as arbitrary relative phases $e^{i\phi}$ cannot be achieved with a real-valued control function $f(t)$. Similarly, for the same Hamiltonian $H(t)$, the target unitary evolution $\mathcal{U}_T = \exp(-i\theta\sigma_y)$ represents an example of a non-realizable gate, starting from the trivial unitary $U(0) = \mathbb{I}$, for any $\theta \neq \{0, \pi\}$.

To formalize these concepts, the notions of *state controllability* and *operator controllability* are introduced. A quantum system is said to be state controllable if, for every pair of initial and final states $\{|\psi_I\rangle, |\psi_T\rangle\}$, there exists a set of control functions $u_k(t)$ in the system Hamiltonian $H(t)$ and a time T such that the system, initialized in state $|\phi(0)\rangle = |\psi_I\rangle$ evolves to the final state $|\phi(T)\rangle = |\psi_T\rangle$ in accordance to Eq. (3.2). Similarly, the system is said to be operator controllable if there exist control functions $u_k(t)$ that drive the unitary operator from $U(0) = \mathbb{I}$ to any desired $\mathcal{U}_T$ in $SU(N)$, the special unitary group of dimension N, in accordance to Eq. (3.3).

A unified criterion for assessing whether a quantum system is both pure state controllable and operator controllable relies on the properties of its dynamical Lie algebra. Specifically, the system satisfies both controllability conditions if and only if the corresponding dynamical Lie algebra is $\mathfrak{su}(N)$, the Lie algebra of traceless Hermitian matrices that generate the special unitary group $SU(N)$. Moreover, operator controllability implies pure state controllability, as the evolution of any quantum state can be expressed through the relation $|\psi(t)\rangle = U(t)|\psi(0)\rangle$. The Lie algebra method provides a rigorous and systematic mathematical framework for analyzing controllability in closed quantum systems.

To construct the dynamical Lie algebra $\mathfrak{h}$ associated with the system Hamiltonian in Eq. (3.1) for an N-level system ($N = 2^n$ in the case of a n-qubit system), a systematic procedure is employed. Begin by forming an initial set of operators composed of all terms in the Hamiltonian, *i.e.*, $\mathfrak{h} = \{\mathfrak{h}_1, \cdots, \mathfrak{h}_{N_h}, H_0\}$, where H_0 is the drift Hamiltonian and $\{\mathfrak{h}_k\}$ are the operators in the control Hamiltonian. If the drift Hamiltonian can be decomposed as the sum of N_c operators, $H_0 = \sum_{k=1}^{N_c} c_k \mathfrak{h}_k^{(0)}$, then the set is expanded to include these components: $\mathfrak{h} = \{\mathfrak{h}_1, \cdots, \mathfrak{h}_{N_h}, \mathfrak{h}_1^{(0)}, \cdots, \mathfrak{h}_{N_c}^{(0)}\}$. Next, compute all possible commutators between the elements in $\mathfrak{h}$, including the nested commutators $[\mathfrak{h}_j, \mathfrak{h}_k]$, $\left[\mathfrak{h}_j, \mathfrak{h}_k^{(0)}\right]$ and $\left[\mathfrak{h}_j^{(0)}, \mathfrak{h}_k^{(0)}\right]$ for all indices j and k. Each new operator generated by these commutators that is not already in $\mathfrak{h}$ is added to the set. This iterative process is repeated, expanding the set $\mathfrak{h}$ at each step, until no additional operators are generated. At this point, the construction of $\mathfrak{h}$ is complete, and the resulting set represents the dynamical Lie algebra of the system.

For an n-qubit system, the Lie algebra $\mathfrak{su}(N = 2^n)$ of the $SU(N = 2^n)$ group can be constructed from tensor products of Pauli matrices. In particular, a basis for $\mathfrak{su}(2^n)$ is given by elements of the form

$$\sigma_{j_1} \otimes \sigma_{j_2} \otimes \cdots \otimes \sigma_{j_n} \ , \tag{3.4}$$

with $\sigma_{j_k} \in \{\mathbb{I}, \sigma_x, \sigma_y, \sigma_z\}$ for each qubit k, and at least one $\sigma_{j_k} \neq \mathbb{I}$. Since each qubit can be associated with any of the four Pauli matrices (excluding the identity), the dimension of the Lie algebra is $|\mathfrak{su}(N = 2^n)| = N^2 - 1 = 4^n - 1$. While this basis involves individual tensor products, linear combinations of these elements can also generate a Lie algebra that is maximal, allowing for complete controllability of the quantum system. A necessary and sufficient condition for complete controllability is that the Lie algebra generated by the control Hamiltonians has dimension N^2 [56].

3.2 Optimal quantum control

When a quantum system satisfies the conditions for controllability, it guarantees that any quantum state or gate can, in principle, be reached using the available physical platform and control functions. However, this theoretical assurance does not translate directly into practical guidance. In most real-world scenarios, the focus is not on accessing all possible states or gates — many of which are neither useful nor relevant — but rather on achieving a well-defined objective, such as preparing a specific target state or implementing a particular quantum gate. Consequently, full controllability, while sufficient, is often unnecessary. What truly matters in many cases is whether the system's Hamiltonian, initial state, and controls are capable of realizing the desired outcome, and, crucially, whether the time-dependent control functions $u_k(t)$ required for this goal can be explicitly designed and implemented.

Optimal control theory offers a robust framework for addressing these challenges [57]. Within this approach, the quantum control problem is recast as the task of finding admissible control functions $u_k(t)$ that satisfy the system's dynamical equations while optimizing a cost functional. This functional is tailored to the specific requirements of the task, such as minimizing control time, reducing power consumption, maximizing fidelity to a target state or gate, or maximizing the robustness to noise or parameter fluctuations. By combining theoretical guarantees with practical optimization tools, this methodology provides a clear pathway to achieving precise and efficient quantum control.

In optimal quantum control, the primary objective is to determine the temporal profiles of the control functions $u_k(t)$ that drive a quantum system from its initial state $|\psi(0)\rangle$ to a final state $|\psi(T)\rangle$ while optimizing a specific performance metric. This metric quantifies the deviation between the target state $|\psi_T\rangle$ and the final state $|\psi(T)\rangle$, often using a measure of fidelity, distance, or other relevant criteria. The cost functional typically also includes a regularization term or additional constraints, such as limits on control amplitude, energy consumption, or other properties of the control fields, as well as some state-dependent running cost that could encode time-dependent control targets or to penalize population in a subspace. Thus, the overall loss functional can be written as

$$\mathcal{L}\left(|\psi_T\rangle, |\psi(T)\rangle, u_k(t)\right) = \mathcal{C}\left(|\psi_T\rangle, |\psi(T)\rangle\right) + \lambda \cdot \mathcal{R}\left(u_k(t), |\psi(t)\rangle\right) \ , \tag{3.5}$$

where $0 \leq \lambda \leq 1$ is a parameter that balances the tradeoff between optimizing the primary

objective and satisfying the additional constraints. Here, $\mathcal{C}\left(|\psi_T\rangle, |\psi(T)\rangle\right)$ quantifies the similarity between the achieved and target states, while $\mathcal{R}\left(u_k(t), |\psi(t)\rangle\right)$ is a regularization term accounting for other dynamical features to be optimized. The optimal solution corresponds to the set of control functions $u_k(t)$ that minimize

$$\min_{u_k(t)} \mathcal{L}\Big(|\psi_T\rangle, |\psi(T)\rangle, u_k(t)\Big) \ . \tag{3.6}$$

The choice of $\mathcal{C}$ depends on the specific problem. Typical choices include the gate infidelity $\mathcal{C} = 1 - |\langle\psi_T|\psi(T)\rangle|^2$, the L^2-norm $\mathcal{C} = \| |\psi_T\rangle - |\psi(T)\rangle \|^2$, or the impurity of the density matrix, $\mathcal{C} = 1 - \mathrm{Tr}\big(\rho(T)^2\big)$ when working with mixed states targeting a pure state.

The regularization term $\mathcal{R}$ is included to impose additional constraints or promote desirable properties in the control parameters, ensuring that the optimized solution remains experimentally feasible and robust. Some common regularization choices include:

- *Minimizing control amplitude*: This can be achieved using $\mathcal{R} = \int_0^T dt \sum_k |u_k(t)|^2$, which also corresponds to minimizing the total energy consumed by the control field.
- *Limiting the maximum control amplitude*: This can be enforced by the constraint $\mathcal{R} = \max_{t,k} |u_k(t)|^2 - u_{max}$, ensuring the control fields do not exceed a specified maximum value u_{max}.
- *Ensuring smooth control pulses*: To avoid sharp transitions that could introduce noise, the regularization term can take the form $\mathcal{R} = \int_0^T dt \sum_k \left(\frac{\partial^2 u_k(t)}{\partial t^2}\right)^2$, promoting smoother control profiles.
- *Promoting robustness to perturbations*: When the system is sensitive to noise or uncertainties, regularization can penalize the sensitivity of the control outputs to changes in the control fields or the Hamiltonian. This can be expressed as $\mathcal{R} = \int_0^T dt \sum_k \left(\frac{\partial \mathcal{C}}{\partial u_k(t)}\right)^2$, where $\mathcal{C}$ is the cost functional in Eq. (3.5).

If the objective of the quantum control problem is not a specific quantum state but rather a target unitary evolution $\mathcal{U}_T$, the optimization functional typically measures the deviation between $\mathcal{U}_T$ and the implemented unitary at the gate time T, $U(T)$. The total cost functional, along with its minimization, is expressed as

$$\mathcal{L}(\mathcal{U}_T, U(T), u_k(t)) = \mathcal{C}(\mathcal{U}_T, U(T)) + \lambda \cdot \mathcal{R}(u_k(t), |\psi(t)\rangle) \ ,$$

where the goal is to minimize

$$\min_{u_k(t)} \ \mathcal{L}\left(\mathcal{U}_T, U(T), u_k(t)\right) \ . \tag{3.7}$$

The functional $\mathcal{C}$ can take various forms depending on the optimization goal. One of the most commonly used performance estimates is the gate infidelity, $\mathcal{C} = 1 - \frac{1}{d^2}\left|\mathrm{Tr}\,\mathcal{U}_T^\dagger U(T)\right|^2$, where d is the Hilbert space dimension. Alternatively, the average gate infidelity $\mathcal{C} = 1 - \frac{1}{d}\sum_{i=1}^{d}\left|\langle\psi_i|\,\mathcal{U}_T^\dagger U(T)\,|\psi_i\rangle\right|^2$ can be used, with $\{|\psi_j\rangle\}$ denoting a set of orthonormal

states. Another option is the gate deviation $\mathcal{C} = \max_{\||\psi\rangle\|=1} \|(\mathcal{U}_T - U(T))\,|\psi\rangle\,\|$, over all possible states $\{|\psi\rangle\}$.

A wide range of optimization strategies exist for minimizing functionals, which can generally be categorized into two main approaches. The first category consists of standard direct search algorithms, such as the Nelder-Mead simplex method [58], Powell's conjugate direction method [59], particle swarm optimization [60], Monte Carlo optimization [61], and evolutionary algorithms like differential evolution [62]. These methods are particularly advantageous in scenarios where gradient information is unavailable, the functional landscape is noisy or non-differentiable, or the parameter space is low-dimensional and highly non-convex. The second category consists of gradient-based techniques, which leverage the functional's derivatives with respect to the control parameters to navigate the multidimensional landscape toward an optimal solution. Gradient-based approaches are especially suitable for high-dimensional, smooth optimization problems where gradients can be computed efficiently and accuracy is critical.

Within quantum optimal control, several prominent methods illustrate these two strategies. The CRAB algorithm [63] (Chopped Random Basis Optimization) represents a gradient-free approach, optimizing control fields parameterized in a truncated basis via direct search techniques. In contrast, GRAPE [26] (Gradient Ascent Pulse Engineering) and Krotov's method [64] are gradient-based. GRAPE refines control pulses by explicitly computing and ascending the gradient of the performance functional, while Krotov's method ensures monotonic convergence by iteratively updating control fields through coupled forward and backward propagation of the system's dynamics. A brief summary of these methods can be found in Appendix C.

3.3 Challenges in classical quantum control simulations

In Sec. 3.2, quantum control problems were formulated as optimization tasks where a cost function guides the tuning of control parameters to steer a quantum system toward a desired state or evolution. However, classical computational methods based on explicit state-vector representations face severe limitations when applied to large quantum systems due to the exponential growth of the Hilbert space dimension with qubit count. Specifically, an n-qubit system requires a state vector in a 2^n-dimensional complex Hilbert space. Storing this vector demands 2^n complex amplitudes, where each amplitude requires 16 bytes of memory (8 bytes for both the real and imaginary components). For a system with 50 qubits, this results in $16 \times 2^{50} \approx 16$ petabytes (PB) of memory. This exceeds the memory capacities of state-of-the-art supercomputers, which currently range between 4 and 5 PB [65, 66], thereby limiting the feasibility of direct classical simulations for large-scale quantum systems.

Representing the Hamiltonian poses an even greater challenge, requiring $2^n \times 2^n = 4^n$ entries for an n-qubit system. Storing the Hamiltonian for a 20-qubit system, thus demands about 16 terabytes (TB), while a 30-qubit system would require a staggering 16

exabytes (EB) — far surpassing the memory capacity of even the largest supercomputers. While sparse representations can mitigate this growth to some extent, their effectiveness diminishes with increasing qubit numbers, particularly for systems lacking exploitable symmetries or sparsity patterns.

These memory limitations are further compounded by the computational complexity of simulating quantum dynamics. Solving the time-dependent Schrödinger equation involves repeated matrix-vector multiplications, requiring $\mathcal{O}(4^n)$ operations per time step. Simulating a 30-qubit system involves approximately 10^{18} operations per time step, while a 40-qubit system requires an astonishing 10^{24} operations per step. Even with the fastest exascale supercomputers (capable of 10^{18} operations per second [65, 66]), simulating the dynamics of a 40-qubit system for a single time step would take hours or even days.

These computational and memory limitations necessitate alternative approaches to quantum control. One promising direction is the use of compact representations of quantum states, such as tensor network methods (see Sec. 3.4.3), which exploit the structure of entanglement in many-body systems to reduce the effective dimensionality of the problem. These methods approximate the quantum state using a compressed representation, significantly reducing the memory and computational resources required. While highly effective for one-dimensional systems with limited entanglement, their application becomes challenging for higher-dimensional systems or systems with highly entangled states. Another emerging approach involves machine learning techniques, which can learn control strategies directly from data or simulations, bypassing the need to model the full quantum state explicitly and offering scalability in complex or poorly understood systems [67]. However, these methods often require extensive training data, lack interpretability, and may struggle to generalize beyond the regimes in which they were trained.

3.4 Quantum simulation

The limitations of classical simulations underscore the growing importance of quantum simulation — the use of controllable quantum systems to emulate complex quantum phenomena that are otherwise intractable with classical methods [19]. A quantum simulator is a well-controlled quantum platform (such as trapped ions, superconducting circuits, or ultracold atoms) designed to replicate the dynamics of a more complex target model [68]. By evolving under a carefully constructed Hamiltonian H_{sys} that approximates the target Hamiltonian H_T, quantum simulators enable the study of phenomena such as quantum phase transitions, quantum magnetism, and high-T_c superconductivity.

Quantum simulation methods can be broadly categorized into three types [19]: *digital quantum simulation*, which approximates evolution via quantum circuits; *analog quantum simulation*, where the simulator naturally follows the dynamics of the target system; and *quantum-information-inspired classical algorithms*, which leverage quantum principles to enhance classical simulations.

For successful emulation, the simulator must reproduce the target system's dynamics with

high fidelity. Given an initial state $|\psi(0)\rangle$ in the simulator and $|\phi(0)\rangle$ in the target system, their respective time evolutions are

$$|\psi(t)\rangle = U_{\text{sys}}(t)\,|\psi(0)\rangle\,, \qquad |\phi(t)\rangle = \mathcal{U}_T(t)\,|\phi(0)\rangle \ . \tag{3.8}$$

Thus, faithful emulation demands a bijective mapping between the two systems

$$|\psi(0)\rangle \leftrightarrow |\phi(0)\rangle \ , \qquad |\psi(t)\rangle \leftrightarrow |\phi(t)\rangle \ , \qquad U_{sys}(t) \leftrightarrow \mathcal{U}_T(t) \ , \tag{3.9}$$

guaranteeing that the simulator's dynamics and states consistently mirror those of the target system.

This level of precision is achievable because, unlike many naturally occurring quantum systems, simulators are experimentally controllable. While the target system may be inaccessible or difficult to manipulate, the simulator allows for precise state preparation ($|\psi(0)\rangle$), controlled time evolution ($U_{sys}(t)$), and measurement of the final state ($|\psi(t)\rangle$), thereby providing insights into the target system's behavior.

While quantum simulators are powerful tools, their scope differs from that of universal quantum computers. Unlike a universal quantum computer, which implements arbitrary quantum algorithms through a programmable gate set, a quantum simulator typically focuses on reproducing the dynamics of a particular class of models, trading generality for experimental scalability and fidelity. Nevertheless, the distinction is increasingly fluid: modern platforms such as Google's Sycamore [22] and IBM's superconducting processors [69] are built as universal gate-based quantum computers, yet they are routinely used to digitally simulate many-body Hamiltonians. Conversely, analog quantum simulators — such as those based on ultracold atoms or trapped ions — excel at simulating specific models with high precision but limited flexibility.

3.4.1 Digital quantum simulation (DQS)

A target unitary evolution $\mathcal{U}_T$ is typically expressed as the exponential of a target Hamiltonian H_T, *i.e.* $\mathcal{U}_T(t) = e^{-itH_T}$. However, in general, $\mathcal{U}_T$ represents a complex many-qubit unitary transformation that cannot be directly implemented in an experimental system, as physical devices are usually limited to applying single- and two-qubit gates. In DQS, $\mathcal{U}_T(t)$ is realized by decomposing it into a sequence of these fundamental gates. Since any unitary operation can be expressed in terms of single- and two-qubit gates, DQS is theoretically universal — capable, in principle, of simulating any quantum system [70].

However, universality does not imply efficient simulation. Some unitary operations may require an exponential number of gates, making their simulation infeasible. Finding an efficient decomposition in terms of universal gates is often itself a difficult computational problem [71]. Additionally, the implemented unitary evolution is generally an approximation of the desired evolution. While increasing the number of gates can improve accuracy, it comes at the cost of higher computational resources.

Suppose the target Hamiltonian can be decomposed into a sum of local interaction terms H_k, where each $\mathfrak{h}_k$ acts on a finite number of qubits

$$H_T = \sum_k \mathfrak{h}_k \ . \tag{3.10}$$

Since these terms typically do not commute (*i.e.*, $[\mathfrak{h}_k, \mathfrak{h}_l] = 0$ for $k \neq l$), the corresponding unitary evolution cannot be exactly factorized as a product of unitaries, $\mathcal{U}_T(t) = \prod_k \exp(-it\mathfrak{h}_k)$. To circumvent this, one approximates the evolution using small time steps of duration Δt (similar to Eq. (2.37)) so that

$$\mathcal{U}_T(t) = \left(e^{-i\Delta t H_T}\right)^{t/\Delta t} \ . \tag{3.11}$$

Each short-time evolution $e^{-i\Delta t H_T}$ can then be further approximated in terms of local gates. Using the BCH identity (Eq. (2.84)), we obtain the first-order Trotter formula [53]

$$e^{-i\Delta t H_T} = \prod_k \exp(-i\Delta t \mathfrak{h}_k) + \mathcal{O}(\Delta t^2) \ . \tag{3.12}$$

This expression demonstrates that the complex unitary evolution $e^{-i\Delta t H_T}$ can be approximated by a sequence of local unitaries $\exp(-i\Delta t\mathfrak{h}_k)$, each of which can be directly implemented in the quantum simulator. The error in this approximation scales as Δt^2, meaning that as the timestep Δt decreases, the approximation becomes more accurate. In the limit of infinitely many steps, the exact evolution is recovered. Higher-order Trotter decompositions, such as the second-order formula and beyond [72], reduce the error scaling further, but at the cost of a more complex decomposition that requires additional resources.

3.4.2 Analog quantum simulation (AQS)

In analog quantum simulation (AQS), a controllable quantum system emulates another quantum system by reproducing its effective many-body dynamics or properties, such as ground states or time evolution [19]. This requires establishing a mapping between the Hamiltonian H_T of the system to-be-simulated and the Hamiltonian H_{sys} of the controllable "toy" system. A paradigmatic example is simulating the Dirac equation, which governs relativistic quantum particles [73]

$$i\frac{\partial \phi}{\partial t} = H_T \phi = (cp\sigma_x + mc^2\sigma_z)\phi \ , \tag{3.13}$$

where c is the effective speed of light, p the momentum operator, m the mass, and σ_x, σ_z Pauli matrices. Remarkably, this equation can be emulated using a single trapped ion, which is addressed by two lasers.

The setup involves selecting two electronic levels of the ion to encode a qubit, while the ion's motional degrees of freedom (oscillations in the trap) simulate the momentum dependence. The interaction between the ion and bichromatic laser fields generates a coupling between the internal qubit states and its motional modes. For example, one laser configuration

results in the Hamiltonian (see Sec. 4.1.4)

$$H_{sys,1} = i\eta\Omega_1(a^\dagger - a)\sigma_x \ , \tag{3.14}$$

where η is the Lamb-Dicke parameter (quantifying the coupling strength), Ω_1 the Rabi frequency, and $a^\dagger, a$ the creation and annihilation operators of the ions's motional modes. The momentum operator along the quantization axis (here, the z-axis) is related to the motional modes via $p = i(a^\dagger - a)/(2z_0)$, where z_0 represents the spatial spread of the ion's zero-point wavefunction. Substituting p into $H_{sys,1}$ yields

$$H_{sys,1} = 2\eta z_0\Omega_1 p\sigma_x \ . \tag{3.15}$$

A second laser, tuned to induce a Stark shift (see Sec. 4.1.3), adds a term proportional to

$$H_{sys,2} = \Omega_2\sigma_z \ . \tag{3.16}$$

Combining these contributions gives the full Hamiltonian

$$H_{sys} = 2\eta z_0\Omega_1 p\sigma_x + \Omega_2\sigma_z \ . \tag{3.17}$$

By identifying $2\eta z_0\Omega_1 = c$ and $\Omega_2 = mc^2$, the trapped-ion system directly emulates the Dirac equation. This mapping illustrates how precisely controlled, engineered quantum systems can emulate the dynamics of quantum models that are otherwise experimentally inaccessible.

In AQS, however, the goal is not always to employ systems that are fundamentally different from the target system, but rather to simulate a complex many-body Hamiltonian using a simpler, more controllable Hamiltonian. A generic time-dependent Hamiltonian can be expressed as $H(t) = \sum_k f_k(t)\mathfrak{h}_k$, where $f_k(t)$ are time-dependent control functions and $\mathfrak{h}_k$ are local terms of the controllable "toy" system. The corresponding unitary time-evolution operator, as suggested by the Magnus expansion (see Eq. (2.54)), generally involves nested commutators of $H(t)$ evaluated at different times. These commutators can generate effective dynamics that include terms not explicitly present in the original Hamiltonian $H(t)$.

By carefully designing the control functions $f_k(t)$, it is possible to suppress or eliminate undesired contributions to the time-evolution operator, leaving only the desired components [74]. This approach allows for the engineering of effective Hamiltonians that mimic the behavior of more complex systems, even if the underlying interactions in the simulator are simpler. Thus, through precise control of the time-dependent parameters, one can tailor the dynamics of the simulator to reproduce the physics of interest, enabling the study of otherwise inaccessible many-body systems.

A notable example of this approach is the Mølmer–Sørensen gate [75], which will be explored in detail in this thesis (see Sec. 4.1.4). In an n-ion chain, this gate implements a

non-local entangling operation with a target Hamiltonian of the form

$$H_T = \sigma_y^{(1)} \otimes \cdots \otimes \sigma_y^{(n)} \ , \tag{3.18}$$

despite being derived from a system Hamiltonian (as in Eq. (3.14)) that involves only local operators acting on individual subsystems (each qubit or the collective motional degrees of freedom). Through the careful design of the control fields $f_k(t)$, the local interactions are combined in a way that produces the desired effective many-body entangling term (see Sec. 4.1.4).

3.4.3 Quantum-information-inspired algorithms

Classical numerical algorithms offer a third approach to simulating quantum many-body systems. Emerging from research in quantum information theory, these methods provide powerful tools for addressing problems that would otherwise be computationally intractable. The main challenge arises because an exact representation of a many-body quantum state typically requires an exponentially large number of parameters, making direct computation infeasible for large systems. To address this, techniques such as matrix product states (MPS) and projected entangled-pair states (PEPS) have been developed (see [76, 77] for an extensive review). These methods provide efficient ways to represent and manipulate quantum states by exploiting their inherent structure and entanglement properties.

Matrix Product States (MPS)

MPS is a one-dimensional tensor network representation particularly well-suited for systems with low entanglement, such as the ground states of gapped one-dimensional Hamiltonians. In a conventional description, the wavefunction of an n-site system is written as

$$|\psi\rangle = \sum_{\{s_i\}} C_{s_1,s_2,\cdots,s_n} |s_1\rangle \otimes |s_2\rangle \otimes \cdots \otimes |s_n\rangle \ , \tag{3.19}$$

where the amplitudes $C_{s_1,s_2,\cdots,s_n}$ can be understood as the entires of a p^n-dimensional tensor C (for qubits, $p = 2$). The MPS approach factorizes this large tensor C into a product of local tensors or reduced dimension

$$C_{s_1,s_2,\cdots,s_n} = \sum_{\{\alpha_i\}} A^{s_1}_{\alpha_1} A^{s_2}_{\alpha_1\alpha_2} A^{s_3}_{\alpha_2\alpha_3} \cdots A^{s_n}_{\alpha_{n-1}} \ , \tag{3.20}$$

with A^{s_i} representing matrices associated with the local basis states at site $|s_i\rangle$ at site i and $\alpha_i \in \{1, \cdots, \mathcal{D}\}$. The bond dimension $\mathcal{D}$ of these matrices controls the amount of entanglement that can be captured by the MPS. By limiting $\mathcal{D}$, MPS provides a compressed representation of the state (of polynomial dimension $2p\mathcal{D} + (n-2)p\mathcal{D}^2 \sim np\mathcal{D}^2$), enabling efficient computation of physical quantities such as expectation values and correlation functions.

Projected Entangled-Pair States (PEPS)

PEPS generalizes the MPS framework to higher dimensions, making it suitable for simulating two-dimensional and higher-dimensional quantum systems. In PEPS, the quantum state is represented as a network of tensors, where each tensor is associated with a lattice site and connected to its neighbors via auxiliary indices. This structure allows PEPS to capture the more complex entanglement patterns that arise in higher-dimensional systems.

Both MPS and PEPS have been successfully applied to a wide range of problems, including the simulation of spin chains, fermionic systems, and quantum phase transitions. However, their efficiency is closely tied to the entanglement structure of the system. In cases where the quantum state exhibits high entanglement — such as in critical systems or during long-time dynamics — the required bond dimension can grow significantly, thereby limiting the practicality of these methods.

3.5 Quantum Invariants

While many of the numerical methods discussed in Sec. 3.4 require explicit construction of quantum states (either exactly or approximately) to design optimal control pulses for the simulator, alternative approaches circumvent this limitation by avoiding direct state representations. These methods instead leverage operator-based frameworks to implicitly encode the system's properties. A foundational example is the *stabilizer formalism* [78], which defines quantum states through algebraic constraints imposed by a set of stabilizing operators. Formally, a quantum state $|\psi\rangle$ is uniquely determined by a stabilizer group $\mathcal{S} = \langle S_1, \cdots, S_k \rangle$, where each stabilizer S_i satisfies $S_i |\psi\rangle = |\psi\rangle$. The state $|\psi\rangle$ is the simultaneous eigenvector of all S_i with eigenvalue $+1$, effectively encoding the state through the algebraic relations of the stabilizers rather than an explicit vector representation. This approach is computationally efficient because stabilizers are typically Pauli operators (tensor products of Pauli matrices X, Y, Z), which admit compact descriptions and enable efficient manipulation of their group structure.

A related strategy is found in *adiabatic quantum computation* [79]. Here, the system's state is continuously associated with the instantaneous ground state of a time-dependent Hamiltonian $H(t)$. Provided the evolution is slow enough (*i.e.*, adiabatic), the system remains in the ground state of $H(t)$ throughout the process. Thus, specifying $H(t)$ implicitly defines the state at all times, eliminating the need for an explicit state-vector description. This approach leverages the fact that Hamiltonians (often local or sparse) are typically easier to engineer and analyze than high-dimensional state vectors. However, its validity depends on maintaining adiabaticity, which requires evolution to be slow enough to prevent excitations out of the ground state.

For systems evolving rapidly or non-adiabatically, *quantum invariants* [80, 81, 82] provide a powerful generalization of operator-based state representations. These invariants are Hermitian, time-dependent operators whose expectation values remain constant over time,

even when the Hamiltonian explicitly depends on time. Formally, this is expressed as

$$\frac{d}{dt}\langle\psi(t)|\,\mathcal{I}(t)\,|\psi(t)\rangle = 0\ . \tag{3.21}$$

Rather than solving the full time-dependent Schrödinger equation to obtain the state $|\psi(t)\rangle$, one can construct an operator $\mathcal{I}(t)$ that satisfies Eq. (3.21). As demonstrated in the following sections, this provides an implicit description of the state $|\psi(t)\rangle$. Crucially, unlike adiabatic methods, which require slow evolution to keep the system in its ground state, the invariant approach holds for arbitrary timescales.

3.5.1 Equation of motion

As with any quantum operator, the explicit form of $\mathcal{I}(t)$ depends on the chosen dynamical picture (for a detailed overview of the main pictures, see Appendix B). In the Schrödinger picture, we denote it as $\mathcal{I}_S(t)$, but the subscript "S" is often omitted when the context is clear. In this picture, quantum states evolve according to the time-dependent Schrödinger equation, and the invariants themselves have explicit time dependence through their functional form. For example, if an invariant is written as $\mathcal{I}_S(t) = f(t)\sigma_x$, where σ_x is the Pauli-X operator, then the time dependence comes solely from the scalar function $f(t)$. Consequently, the time derivative of the invariant is given by $\frac{\partial\mathcal{I}_S}{\partial t} = \dot{f}(t)\sigma_x$, while σ_x remains constant, as is generally the case for operators in the Schrödinger picture.

To derive the equation of motion for the invariant, we expand Eq. (3.21)

$$\begin{aligned}
0 &= \frac{d\,\langle\psi(t)|}{dt}\mathcal{I}_S(t)\,|\psi(t)\rangle + \langle\psi(t)|\,\frac{d\mathcal{I}_S(t)}{dt}\,|\psi(t)\rangle + \langle\psi(t)|\,\mathcal{I}_S(t)\frac{d\,|\psi(t)\rangle}{dt} \\
&= i\,\langle\psi(t)|\,H(t)\mathcal{I}_S(t)\,|\psi(t)\rangle + \langle\psi(t)|\,\frac{d\mathcal{I}_S(t)}{dt}\,|\psi(t)\rangle - i\,\langle\psi(t)|\,\mathcal{I}_S(t)H(t)\,|\psi(t)\rangle \\
&= \langle\psi(t)|\left(\frac{d\mathcal{I}_S(t)}{dt} + i[H(t),\mathcal{I}_S(t)]\right)|\psi(t)\rangle\ ,
\end{aligned} \tag{3.22}$$

where we have used the Schrödinger equation (Eq. (2.29)). Since this must hold for all states $|\psi(t)\rangle$, the invariant operator must satisfy the equation of motion

$$\frac{\partial\mathcal{I}_S(t)}{\partial t} = -i[H(t),\mathcal{I}_S(t)]\ . \tag{3.23}$$

This equation resembles the Heisenberg equation of motion for a time-independent operator, but with an opposite sign (see Eq. (B.10)). However, it describes the explicit time dependence of $\mathcal{I}_S(t)$ in the Schrödinger picture, rather than the evolution of an operator in the Heisenberg picture. Indeed, a generic time-independent operator involves the transformed Hamiltonian H_H, and thus evolves in the Heisenberg picture as $\frac{\partial\mathcal{O}_H(t)}{\partial t} = i[H_H(t),\mathcal{O}_H(t)]$.

The Heisenberg version of an invariant is related to its Schrödinger counterpart by the unitary transformation in Eq. (B.4), *i.e.* $\mathcal{I}_H(t) = U^\dagger(t)\mathcal{I}_S(t)U(t)$. In this picture, the evolution of a quantum invariant follows Heisenberg's equation of motion (see Eq. (B.9) in

Appendix B),

$$\frac{\partial \mathcal{I}_H(t)}{\partial t} = i[H_H(t), \mathcal{I}_H(t)] + U^\dagger(t)\frac{\partial \mathcal{I}_S(t)}{\partial t}U(t) \ . \tag{3.24}$$

Substituting the previously derived equation (Eq. (3.23)), we find

$$\begin{aligned}\frac{\partial \mathcal{I}_H(t)}{\partial t} &= i[H_H(t), \mathcal{I}_H(t)] - iU^\dagger(t)[H(t), \mathcal{I}_S(t)]U(t) \\ &= i[H_H(t), \mathcal{I}_H(t)] - i[H_H(t), \mathcal{I}_H(t)] \\ &= 0 \ .\end{aligned} \tag{3.25}$$

Thus, in the Heisenberg picture, the invariant is completely time-independent

$$\frac{\partial \mathcal{I}_H(t)}{\partial t} = 0 \ . \tag{3.26}$$

3.5.2 Time-independence of invariant eigenvalues

A key implication of the invariant's equation of motion (Eq. (3.23)) is that the eigenvalues λ of an invariant operator $\mathcal{I}(t)$ remain constant over time — even though its eigenstates $|\lambda, \kappa; t\rangle$ may evolve, property that is deeply connected to the invariant's role as a dynamical anchor for the system.

The eigendecomposition of an invariant $\mathcal{I}(t)$ is given by [80]

$$\mathcal{I}(t)\,|\lambda, \kappa; t\rangle = \lambda\,|\lambda, \kappa; t\rangle \ , \tag{3.27a}$$

$$\langle \lambda, \kappa'; t | \lambda, \kappa'; t\rangle = \delta_{\lambda\lambda'}\delta_{kk'} \ , \tag{3.27b}$$

where λ denotes the eigenvalue, and the label κ runs over all quantum numbers besides the eigenvalues λ to uniquely characterize the time-dependent eigenstates $|\lambda, \kappa; t\rangle$. To show that λ does not change with time, we differentiate the eigenvalue equation (3.27a) with respect to time

$$\frac{\partial \mathcal{I}(t)}{\partial t}\,|\lambda, \kappa; t\rangle + \mathcal{I}(t)\frac{\partial\,|\lambda, \kappa; t\rangle}{\partial t} = \frac{\partial \lambda}{\partial t}\,|\lambda, \kappa; t\rangle + \lambda\frac{\partial\,|\lambda, \kappa; t\rangle}{\partial t} \ , \tag{3.28}$$

which, operating with $\langle \lambda', \kappa'; t|$ on the left-hand side, results in the matrix element

$$\langle \lambda', \kappa'; t| \frac{\partial \mathcal{I}(t)}{\partial t}\,|\lambda, \kappa; t\rangle = \langle \lambda', \kappa'; t| \frac{\partial \lambda}{\partial t}\,|\lambda, \kappa; t\rangle + (\lambda - \lambda')\,\langle \lambda', \kappa'; t| \frac{\partial\,|\lambda, \kappa; t\rangle}{\partial t} \ . \tag{3.29}$$

An alternative expression for the matrix element $\langle \lambda', \kappa'; t| \frac{\partial \mathcal{I}(t)}{\partial t}\ |\lambda, \kappa; t\rangle$ can be obtained by sandwiching the equation of motion for the invariant (Eq. (3.23)) between $\langle \lambda', \kappa'; t|$ and $|\lambda, \kappa; t\rangle$

$$\langle \lambda', \kappa'; t| \frac{\partial \mathcal{I}(t)}{\partial t}\,|\lambda, \kappa; t\rangle = -i(\lambda - \lambda')\,\langle \lambda', \kappa'; t|\, H(t)\,|\lambda, \kappa; t\rangle \ . \tag{3.30}$$

Comparing these two expressions and setting $\lambda = \lambda'$ directly leads to

$$\frac{\partial \lambda}{\partial t} = 0 \ , \tag{3.31}$$

which proves the time-independence of the eigenvalues λ.

3.5.3 Eigenstates of the invariant and the Schrödinger equation

The time-independence of the eigenvalues has a significant consequence: all time-dependence of the operator $\mathcal{I}(t)$ is entirely contained within its eigenstates $|\lambda, \kappa; t\rangle$. These eigenstates, according to Eq. (3.29), satisfy the following equation of motion

$$\begin{aligned}\Big(\lambda - \lambda'\Big) \langle \lambda', \kappa'; t| \frac{\partial |\lambda, \kappa; t\rangle}{\partial t} &= \langle \lambda', \kappa'; t| \frac{\partial \mathcal{I}(t)}{\partial t} |\lambda, \kappa; t\rangle \\ &= -i \langle \lambda', \kappa'; t| [H(t), \mathcal{I}(t)] |\lambda, \kappa; t\rangle \\ &= -i(\lambda - \lambda') \langle \lambda', \kappa'; t| H(t) |\lambda, \kappa; t\rangle \ ,\end{aligned} \tag{3.32}$$

where Eq. (3.23) has been applied in the second line. Consequently, for $\lambda \neq \lambda'$, we obtain

$$i \langle \lambda', \kappa'; t| \frac{\partial |\lambda, \kappa; t\rangle}{\partial t} = \langle \lambda', \kappa'; t| H(t) |\lambda, \kappa; t\rangle \ , \tag{3.33}$$

which is reminiscent of the Schrödinger equation (Eq. (2.29)), in matrix form, with the system state $|\psi(t)\rangle$. To make the connection explicit, we express the Schrödinger equation in the eigenbasis of $\mathcal{I}(t)$ as

$$i \sum_{\lambda', \kappa'} |\lambda', \kappa'; t\rangle\langle \lambda', \kappa'; t| \frac{\partial |\psi(t)\rangle}{\partial t} = \sum_{\lambda', \kappa'} |\lambda', \kappa'; t\rangle\langle \lambda', \kappa'; t| H(t) |\psi(t)\rangle \ . \tag{3.34}$$

By comparing Eq. (3.33) and Eq. (3.34), one might be tempted to conclude that $|\psi(t)\rangle = |\lambda, \kappa; t\rangle$. However, this conclusion is not yet fully justified, as Eq. (3.33) is only valid for $\lambda \neq \lambda'$, whereas Eq. (3.34) must hold for all values of λ, κ, including $\lambda = \lambda'$. Our goal is therefore to demonstrate that

$$i \langle \lambda, \kappa'; t| \frac{\partial |\lambda, \kappa; t\rangle}{\partial t} = \langle \lambda, \kappa'; t| H(t) |\lambda, \kappa; t\rangle \ , \tag{3.35}$$

also holds. To achieve this, we note that all conclusions drawn for the eigenstates $|\lambda, \kappa; t\rangle$ also apply to the states modified by an arbitrary time-dependent phase factor,

$$e^{i\theta_{\lambda,\kappa}(t)} |\lambda, \kappa; t\rangle \ . \tag{3.36}$$

This phase freedom, known as a *gauge transformation*, allows us to prove Eq. (3.35). Substituting the phase-modified eigenstates into Eq. (3.35) yields, after rearranging,

$$\langle \lambda, \kappa'; t| \left(i \frac{\partial}{\partial t} - H(t)\right) |\lambda, \kappa; t\rangle = \frac{\partial \theta_{\lambda,\kappa}(t)}{\partial t} \delta_{kk'} \ . \tag{3.37}$$

For $\kappa \neq \kappa'$, this equation simplifies to

$$\langle \lambda, \kappa'; t | \left(i\frac{\partial}{\partial t} - H(t) \right) | \lambda, \kappa; t \rangle = 0 \ , \tag{3.38}$$

which holds if $\left(i\frac{\partial}{\partial t} - H(t) \right) | \lambda, \kappa; t \rangle = p \, | \lambda, \kappa; t \rangle$ for some scalar p. Since $\langle \lambda, \kappa'; t | \lambda, \kappa; t \rangle = \delta_{\kappa\kappa'}$, this is satisfied if $| \lambda, \kappa; t \rangle$ is an eigenstate of the operator $\left(i\frac{\partial}{\partial t} - H(t) \right)$. This condition can always be imposed because $\left(i\frac{\partial}{\partial t} - H(t) \right)$ is Hermitian and thus can be diagonalized. For the case $\kappa = \kappa'$, Eq. (3.37) holds if the phase $\theta_{\lambda,\kappa}(t)$ is chosen as

$$\theta_{\lambda,\kappa}(t) = \int_0^t dt' \, \langle \lambda, \kappa; t | \left(i\frac{\partial}{\partial t'} - H(t') \right) | \lambda, \kappa; t \rangle \ . \tag{3.39}$$

It thus follows that the general solution of the Schrödinger equation can be written in terms of the eigenstates of the invariant $\mathcal{I}(t)$ as

$$| \psi(t) \rangle = \sum_{\lambda,\kappa} c_{\lambda,\kappa} e^{i\theta_{\lambda,\kappa}(t)} \, | \lambda, \kappa; t \rangle \ , \tag{3.40}$$

where $c_{\lambda,\kappa}$ are time-independent coefficients[1].

3.5.4 Quantum invariants and the harmonic oscillator

Quantum invariants were originally introduced as a framework for determining the exact quantum state $|\psi(t)\rangle$ of a system at any time t, given a known time-dependent Hamiltonian $H(t)$. By identifying an invariant $\mathcal{I}(t)$, one can directly construct solutions to the Schrödinger equation, as described in Eq. (3.40), without requiring explicit time integration. A fundamental example of this approach is the harmonic oscillator with a time-dependent frequency [80]

$$H(t) = \frac{p^2}{2m} + \frac{1}{2} m\Omega^2(t) x^2 \ . \tag{3.41}$$

To construct a dynamical invariant $\mathcal{I}(t)$, one assumes an *ansatz* of the form

$$\mathcal{I}(t) = \frac{1}{2} \left(a_1(t) x^2 + a_2(t) p^2 + a_3(t)(px + xp) \right) \ , \tag{3.42}$$

[1] Invariants with degenerate eigenspaces complicate the construction of solutions to the Schrödinger equation, as they necessitate diagonalizing the operator $\left(i\frac{\partial}{\partial t} - H(t) \right)$. While possible for some systems, this task is generally computationally demanding. Ensuring non-degenerate eigenspaces for $\mathcal{I}(t)$ avoids this challenge: in such cases, solving the Schrödinger equation reduces to diagonalizing $\mathcal{I}(t)$ alone. Moreover, in many practical applications, even this step can be bypassed — knowledge of key eigenstates (*e.g.*, the ground state) is often sufficient to determine the system's evolution.

where the time-dependent coefficients $a_i(t)$ must satisfy the condition for invariance (Eq. (3.23)), which leads to the constraint equation

$$\begin{aligned}&\dot{a}_1(t)x^2 + \dot{a}_2(t)p^2 + \dot{a}_3(t)(px + xp)\\ &= 2m\Omega^2(t)a_3(t)x^2 + \frac{-2a_3(t)}{m}p^2 + \frac{m^2\Omega^2(t)a_2(t) - a_1(t)}{m}(px + xp)\ .\end{aligned} \tag{3.43}$$

By matching coefficients, the following system of coupled differential equations for $a_i(t)$ is obtained

$$\dot{a}_1(t) = 2m\Omega^2(t)a_3(t)\ , \qquad \dot{a}_2(t) = \frac{-2a_3(t)}{m}\ , \qquad \dot{a}_3(t) = \frac{m^2\Omega^2(t)a_2(t) - a_1(t)}{m}\ . \tag{3.44}$$

Solving this system [80] yields the explicit form of the invariant

$$\mathcal{I}(t) = \frac{1}{2}\left(\frac{1}{\mu(t)^2}x^2 + (\mu(t)p - m\dot{\mu}(t)x)^2\right)\ , \tag{3.45}$$

where $\mu(t)$ is a time-dependent scaling function satisfying the auxiliary nonlinear differential equation

$$m^2\ddot{\mu}(t) + m^2\Omega^2(t)\mu(t) - \frac{1}{\mu^3(t)} = 0\ . \tag{3.46}$$

Any particular solution of Eq. (3.46) defines a valid invariant of the form given in Eq. (3.45). Once $\mu(t)$ is specified, the exact analytic form of $\mathcal{I}(t)$ follows directly. By diagonalizing $\mathcal{I}(t)$, one can obtain its eigenstates and thus construct an exact expression for the quantum state $|\psi(t)\rangle$ for any choice of the time-dependent frequency $\Omega(t)$ in the Hamiltonian $H(t)$ of Eq. (3.41).

3.5.5 Invariant-based inverse engineering

From a complementary perspective, quantum invariants can be employed not merely as a tool to determine the quantum state from a given Hamiltonian (as in the example above), but also to design a Hamiltonian that drives the system along a desired state evolution. In this inverse-engineering approach, one constructs a Hamiltonian that transitions the system from an initial state $|\psi(0)\rangle$ to a target state $|\psi_T\rangle$. To illustrate this, consider a time evolution operator of the form

$$U(t;t_0) = \sum_{\lambda,\kappa} e^{i\theta_{\lambda,\kappa}(t)}\,|\lambda,\kappa;t\rangle\langle\lambda,\kappa;t_0|\ , \tag{3.47}$$

which maps the eigenstate $|\lambda,\kappa;t_0\rangle$ of a dynamical invariant $\mathcal{I}(t)$ at $t = t_0$ to their time-evolved counterparts $|\lambda,\kappa;t\rangle$ at time t. Since $U(t;t_0)$ satisfies the evolution equation in Eq. (2.28), the Hamiltonian generating the desired dynamics is given by $H(t) = i\frac{\partial U(t)}{\partial t}U^\dagger(t)$. This equation encapsulates the inverse-engineering paradigm: instead of solving for $U(t;t_0)$ from a given $H(t)$, we *design* $H(t)$ directly from a predefined $U(t;t_0)$ that encodes the desired state evolution.

A particularly useful scenario for invariant-based inverse engineering occurs when the system is initially prepared in a single eigenstate $|\lambda^*, \kappa^*; 0\rangle$ of the invariant $\mathcal{I}(t)$, *i.e.*, $|\psi(0)\rangle = |\lambda^*, \kappa^*; 0\rangle$. In this case, the expansion in Eq. (3.40) reduces to a single term with $c_{\lambda,\kappa} = 0, \forall\{\lambda, \kappa\} \neq \{\lambda^*, \kappa^*\}$. In this scenario, it follows from Eq. (3.40) that the quantum state will remain confined to this single eigenstate of the invariant,

$$|\psi(t)\rangle = e^{i\theta_{\lambda^*,\kappa^*}(t)} |\lambda^*, \kappa^*; t\rangle \ , \tag{3.48}$$

at all times. The evolution of the system is thus governed solely by an accumulated phase factor $e^{i\theta_{\lambda^*,\kappa^*}(t)}$, which does not affect the physical state of the system, and the inherent time evolution of the eigenstate $|\lambda^*, \kappa^*; t\rangle$.

This observation underscores the fundamental utility of dynamical invariants in quantum control. Once an invariant $\mathcal{I}(t)$ is constructed and its eigenstates are determined — whether analytically or numerically — one can predict the system's evolution without solving the Schrödinger equation explicitly. In quantum control protocols, if the desired target state is associated with a specific eigenstate of $\mathcal{I}(t)$, then preparing the system in that eigenstate at $t = 0$ guarantees that it will follow the intended trajectory. Specifically, if the target state $|\psi_T\rangle$ is identified as the (non-degenerate) eigenstate $|\lambda^*, \kappa^*; t\rangle$ at a specific time $t = T$, *i.e.* $|\psi_T\rangle = |\lambda^*, \kappa^*; T\rangle$, then it follows that the Hamiltonian $H(t)$ can be designed to drive the system to $|\psi_T\rangle$ at $t = T$.

A multidimensional Gaussian quantum invariant

The inverse-engineering framework based on dynamical invariants provides a powerful approach to designing control protocols in quantum systems. However, its direct applicability has traditionally been limited to systems where an invariant can be explicitly constructed. This limitation motivates the reformulation introduced in Chapter 5, which extends the framework to systems where such invariants are not readily available.

In the preceding section, we examined one such analytically solvable invariant: the well-established case of a one-dimensional harmonic oscillator, where the invariant takes the form in Eq. (3.45). This construction has played a crucial role in a range of control protocols, including fast adiabatic-like transport and quantum state expansions and compressions [83, 84]. These methods have been experimentally implemented in trapped-ion platforms, where they enable precise and rapid control over motional states while mitigating motional heating. Nevertheless, their restriction to one-dimensional systems inherently limits their applicability in practical quantum technologies, which require control in multiple spatial dimensions to accommodate scalability and increased system complexity.

Recent theoretical advancements have addressed this limitation by generalizing the invariant framework to arbitrary spatial dimensions for single-particle systems [85]. This extension opens new possibilities for controlling trapped ions in fully three-dimensional configurations, a topic that will be explored further in Chapter 6.

To establish such an invariant, it is convenient to reformulate the harmonic oscillator problem in the language of multidimensional phase-space variables. In this approach, the position and momentum operators, $\vec{r}$ and $\vec{p}$, are combined into a single compact operator

$$\vec{X} = (r_1, \cdots, r_d, p_1, \cdots, p_d) \ , \tag{3.49}$$

where d is the number of spatial dimensions. As a generalization of the commutation relation $[x_j, p_k] = i\delta_{jk}$, the components of $\vec{X}$ satisfy the commutation relation

$$[X_j, X_k] = i\mathbb{S}_{jk} \ , \tag{3.50}$$

with the elements $\mathbb{S}_{jk}$ belonging to the symplectic matrix

$$\mathbb{S} = \begin{pmatrix} \mathbb{O}_{d\times d} & \mathbb{I}_{d\times d} \\ -\mathbb{I}_{d\times d} & \mathbb{O}_{d\times d} \end{pmatrix} \ , \tag{3.51}$$

which satisfies $\mathbb{S}^T = -\mathbb{S}$. In this compact notation, the Hamiltonian of a multidimensional displaced harmonic oscillator can be expressed as

$$H(t) = \frac{1}{2}\vec{X}^T \boldsymbol{K}(t)\vec{X} + \vec{X}^T \cdot \vec{V}(t) \ , \tag{3.52}$$

in terms of the $2d \times 2d$-dimensional symmetric matrix given by

$$\boldsymbol{K}(t) = \begin{pmatrix} m\boldsymbol{M}(t) & \mathbb{O}_{d\times d} \\ \mathbb{O}_{d\times d} & \frac{1}{m}\mathbb{I}_{d\times d} \end{pmatrix} \ , \tag{3.53}$$

with the positive-definite matrix $\boldsymbol{M}$ encoding the oscillator's curvature, and the $2d$-dimensional vector

$$\vec{V}^T(t) = (-\vec{F}(t), \vec{0}) \ , \tag{3.54}$$

where $\vec{F}(t)$ corresponds to the restoring force that arises when the system is displaced from the oscillator's center $\vec{C}$. Indeed, the role of $\vec{F}$ becomes explicit upon rewriting $H(t)$ in a displaced coordinate system. By completing the square, Eq. (3.52) transforms to

$$H(t) = \frac{1}{2}(\vec{X} - \vec{D})^T \boldsymbol{K}(t)(\vec{X} - \vec{D}) \ , \tag{3.55}$$

where $\vec{D} = (\vec{C}, \vec{0}_d)$ shifts the spatial coordinates of $\vec{X}$ to the oscillator's center $\vec{C}$, which is related to $\vec{F}$ via

$$\vec{C} = \frac{1}{m}\boldsymbol{M}^{-1}\vec{F} \ . \tag{3.56}$$

To inverse-engineer control protocols, we aim to find an operator $\mathcal{I}(t)$ that satisfies Eq. (3.23) with the Hamiltonian $H(t)$ in Eq. (3.52). Following Ref. [85], we adopt a quadratic ansatz for this operator

$$\mathcal{I}(t) = \frac{1}{2}\Big(\vec{X} - \vec{W}(t)\Big)^T \mathbf{\Gamma}(t)\Big(\vec{X} - \vec{W}(t)\Big) \ , \tag{3.57}$$

where $\vec{W}(t)$ is a yet-to-be-determined $2d$-dimensional vector, and $\mathbf{\Gamma}(t)$ is a to-be-determined $2d \times 2d$ real antisymmetric matrix. Substituting this ansatz into the equation of motion for the invariant (Eq. (3.23)) yields the coupled equations

$$\dot{\mathbf{\Gamma}}(t) = \boldsymbol{K}\mathbb{S}\mathbf{\Gamma}(t) - \mathbf{\Gamma}(t)\mathbb{S}\boldsymbol{K} \ , \tag{3.58a}$$

$$\dot{\vec{W}}(t) = \mathbb{S}\boldsymbol{K}\vec{W}(t) + \mathbb{S}\vec{V}(t) \ . \tag{3.58b}$$

Solving Eq. (3.58a) provides an explicit expression for the matrix $\mathbf{\Gamma}(t)$ [85]

$$\mathbf{\Gamma}(t) = \begin{pmatrix} m\left(\dot{\boldsymbol{R}}^2 + \mathrm{Re}(\Big[\dot{\boldsymbol{R}}, \boldsymbol{R}\Big]_{\boldsymbol{A}} - \boldsymbol{R}\boldsymbol{A}^2\boldsymbol{R})\right) & \frac{1}{2}\Big(\boldsymbol{J} - \Big\{\boldsymbol{R}, \dot{\boldsymbol{R}}\Big\}\Big) \\ \frac{-1}{2}\Big(\boldsymbol{J} + \Big\{\boldsymbol{R}, \dot{\boldsymbol{R}}\Big\}\Big) & \frac{1}{m}\boldsymbol{R}^2 \end{pmatrix} \ , \tag{3.59}$$

where $[A, B]_C = ACB - BCA$ and $\{A, B\} = AB + BA$. The auxiliary matrices $\boldsymbol{A}$ and $\boldsymbol{J}$ are determined via

$$\boldsymbol{A} = i\boldsymbol{R}^{-2} + \frac{1}{2}\Big[\boldsymbol{R}^{-1}, \dot{\boldsymbol{R}}\Big] + \frac{1}{2}\boldsymbol{R}^{-1}\boldsymbol{J}\boldsymbol{R}^{-1} \ , \tag{3.60a}$$

$$\Big\{\boldsymbol{J}, \boldsymbol{R}^{-2}\Big\} = \Big[\dot{\boldsymbol{R}}, \boldsymbol{R}^{-1}\Big] + \Big[\boldsymbol{R}, \boldsymbol{R}^{-2}\Big]_{\dot{\boldsymbol{R}}} \ , \tag{3.60b}$$

in terms of the real, positive semidefinite $d \times d$ matrix $\boldsymbol{R}(t)$. Since $\boldsymbol{R}(t)$ ultimately determines $\mathbf{\Gamma}(t)$, the quadratic invariant in Eq. (3.57) is fully characterized by the choices of $\boldsymbol{R}(t)$ and $\vec{W}(t)$.

Due to the defining conditions of the invariant $\mathcal{I}(t)$ (Eq. (3.23)), the operators in $\mathcal{I}(t)$ are linked to the operators in the Hamiltonian $H(t)$ in Eq. (3.52). This interplay is what enables the inverse-engineering of a valid Hamiltonian $H(t)$ for control problem solutions. Notably, $\boldsymbol{R}(t)$ is related to the quadratic component of the Hamiltonian $\boldsymbol{M}(t)$ — which in turn determines $\boldsymbol{K}(t)$ in Eq. (3.52) — in a highly nonlinear manner [85]

$$\Big\{\boldsymbol{R}^2, \boldsymbol{M}\Big\} = 2\Big[\dot{\boldsymbol{R}}, \boldsymbol{R}\Big]_{\boldsymbol{A}} - \Big\{\ddot{\boldsymbol{R}}, \boldsymbol{R}\Big\} - 2\boldsymbol{R}\boldsymbol{A}^2\boldsymbol{R} \ . \tag{3.61}$$

In practice, to isolate $\boldsymbol{M}$, we apply the vectorization (see Eq. (5.86)) to both sides of Eq. (3.61), yielding the linear equation

$$|\boldsymbol{M}\rangle\rangle = \Big[\big(\boldsymbol{R}^2\big)^T \otimes \mathbb{I} + \mathbb{I} \otimes \boldsymbol{R}^2\Big]^{-1} |\boldsymbol{Y}\rangle\rangle \ , \tag{3.62}$$

where $|\boldsymbol{Y}\rangle\rangle$ is the vectorized form of $\boldsymbol{Y} = 2\Big[\dot{\boldsymbol{R}}, \boldsymbol{R}\Big]_{\boldsymbol{A}} - \Big\{\ddot{\boldsymbol{R}}, \boldsymbol{R}\Big\} - 2\boldsymbol{R}\boldsymbol{A}^2\boldsymbol{R}$. Thus, from the vectorized form $|\boldsymbol{M}\rangle\rangle$, we can then reconstruct the matrix $\boldsymbol{M}(t)$.

On the other hand, $\vec{W}(t)$ is related to the vector $\vec{F}(t)$ in the Hamiltonian — which determines $\vec{V}(t)$ in Eq. (3.52) — in the following manner

$$\vec{F}(t) = m\boldsymbol{M}(t)\vec{W}_x(t) + \dot{\vec{W}}_p \ , \tag{3.63}$$

where we have defined $\vec{W}(t) = (\vec{W}_x(t), \vec{W}_p(t))$, with the d-dimensional vectors $\vec{W}_x(t)$ and $\vec{W}_p(t)$.

Thus, for any choice of $\boldsymbol{R}(t)$ and $\vec{W}(t)$ in the invariant $\mathcal{I}(t)$, the Hamiltonian $H(t)$ is uniquely determined through Eqs. (3.62) and (3.63). The Hamiltonian obtained in this fashion has the key property that, as discussed in Sec. 3.5.5, if the quantum system is initially prepared in a *unique* eigenstate of the invariant (such as the ground-state), it will remain in that eigenstate throughout the dynamics — a feature that can be exploited to design state transfer protocols on diabatic timescales, as discussed in Chapter 6.

Chapter 4

Quantum Computing Architectures: Trapped Ions

> "Nature isn't classical, dammit, and if you want to make a simulation of nature, you'd better make it quantum mechanical, and by golly it's a wonderful problem, because it doesn't look so easy."
>
> – Richard Feynman, 1982 [86]

The transition from classical to quantum computing represents more than just an engineering challenge — it redefines how information can be processed at a fundamental level. Classical computation, rooted in deterministic logic and binary states, has driven technological progress for decades. Yet, as we probe the limits of classical systems — from cryptographic security [87] to simulating quantum many-body dynamics [68] — it becomes increasingly evident that these frameworks are inadequate to capture the full complexity of natural phenomena. Quantum computing, by contrast, leverages the intrinsic properties of quantum mechanics, such as superposition, entanglement, and interference, to process information in ways that classical systems cannot replicate. This paradigm shift invites a critical question: *How can we systematically exploit quantum mechanics to solve problems that are otherwise computationally intractable?*

The theoretical promise of quantum computing is well-established. Shor's algorithm [18], revolutionized the field by demonstrating that quantum systems can factor large integers exponentially faster than any known classical algorithm, challenging the security of widely used cryptographic protocols. Grover's search algorithm [88] provides a quadratic speedup for unstructured search problems, while quantum simulation techniques [19] offer unparalleled capabilities to model complex physical phenomena, including molecular dynamics, topological phases of matter, and high-energy physics. These breakthroughs suggest

far-reaching applications in fields such as secure communication, materials science, and drug discovery. Yet, realizing these possibilities requires overcoming significant practical challenges, particularly the translation of abstract quantum circuit models into physically realizable systems.

Among the various platforms under development — superconducting circuits [89], photonic networks [90], topological qubits [91], and Rydberg atom arrays [92], to name a few — trapped-ion systems [93, 94] have emerged as a leading contender. Their exceptional coherence times [95], precise qubit control [96], and high-fidelity entangling operations [32] make them an ideal medium for exploring the fundamental limits of quantum information processing [97].

Unlike superconducting circuits, which achieve rapid gate operations on nanosecond timescales at the cost of coherence times typically ranging from hundreds of microseconds to a few milliseconds [98], or photonic networks, which excel at long-distance quantum communication but struggle with implementing deterministic two-qubit interactions [99], trapped ions uniquely combine multi-second coherence [100] with high-fidelity entangling gates. In contrast, Rydberg atoms exploit strong interactions between highly excited states to enable fast, parallelized gates across large neutral-atom arrays [92], offering a promising path to massive scalability, albeit at the cost of increased technical challenges in laser stabilization, atom trapping, and maintaining Rydberg-state coherence. Similarly, while topological qubits promise intrinsic fault tolerance through non-Abelian anyons [91], their experimental realization remains at a nascent stage compared to the mature trapped-ion platforms.

This thesis is primarily concerned with advancing methodologies for trapped-ion systems. However, the techniques developed — such as error-resilient gate designs or ion-shuttling protocols — are intended to be adaptable across different quantum architectures. For instance, gate engineering strategies that mitigate sensitivity to control errors could benefit superconducting qubits [69], while modular ion-shuttling schemes may inspire scalable routing architectures for photonic or Rydberg-based networks. By addressing challenges common to multiple architectures, the insights presented here contribute broadly to the advancement of quantum engineering.

4.1 Trapped ion quantum computing

Trapped-ion quantum computing exploits individual ions confined and manipulated using electromagnetic fields [96]. These ions act as qubits, with their internal electronic states representing computational basis states. Different conventions exist for labeling these states, with $|0\rangle$ and $|1\rangle$ being the most widely adopted in the quantum computing community, while $|g\rangle$ and $|e\rangle$ are more commonly used in the quantum optics community. In this thesis, we will use both notations as needed for clarity, ensuring that the meaning is unambiguous in each case. Trapped-ion systems satisfy several key criteria required for quantum computation, known as the DiVincenzo criteria [101]:

- **Well-defined qubits:** Trapped ions provide naturally isolated and highly stable quantum states, making them resilient to environmental noise. Depending on the energy splitting between $|0\rangle$ and $|1\rangle$, ion qubits fall into four main categories (see Fig. 4.1):

  - *Hyperfine qubits:* These qubits rely on energy splittings between hyperfine levels of the electronic ground state, typically in the gigahertz range. Their key advantage is exceptionally long coherence times, often exceeding hundreds of seconds in magnetically insensitive clock states [100], far surpassing the millisecond coherence typical of superconducting transmon qubits [102] and the 1–10 ms lifetimes of Rydberg atoms [92]. Hyperfine qubits can be manipulated using microwave or Raman laser transitions [103].

  - *Zeeman qubits:* These are formed from magnetic sublevels within a single electronic state, with energy splittings in the tens of megahertz, depending on the applied magnetic field. While Zeeman qubits are simpler to implement than hyperfine qubits, they are more susceptible to magnetic field fluctuations, necessitating active stabilization techniques [94].

  - *Fine-structure qubits:* These qubits utilize energy levels from the fine structure splitting in the electronic excited states, which typically lie in the tens of terahertz range. They are less commonly used for computation due to their shorter coherence times but can enable faster gate operations [93], mirroring the speed-versus-coherence trade-offs seen in semiconductor spin qubits [104] and Rydberg atom systems [92].

  - *Optical qubits:* Defined using electronic transitions between ground and excited states with splittings in the hundreds of terahertz, optical qubits are manipulated using narrow-linewidth lasers. While they benefit from fast gate operations and well-defined energy levels, they require stringent laser phase stability and ultra-low-noise environments to maintain coherence [94], challenges shared with photonic qubit platforms [99] and Rydberg atom arrays [92].

- **State initialization:** High-fidelity qubit initialization is achieved via optical pumping, a process that selectively excites population from undesired states and relies on spontaneous emission to populate the target state. By tuning laser polarization and frequency, specific transitions are addressed, ensuring near-unity initialization fidelity. For hyperfine and Zeeman qubits, fidelities exceeding 99.9% have been demonstrated [105, 106], surpassing the 99% thresholds typical of superconducting qubits [102].

- **Long coherence times:** Trapped-ion qubits exhibit exceptional coherence times due to their isolation from environmental noise. Hyperfine qubits, particularly in magnetically insensitive clock states, achieve coherence times exceeding 600 s [100], orders of magnitude longer than the 0.1–1 ms coherence times of superconducting

or semiconductor qubits [98, 104] and the 1–10 ms lifetimes of Rydberg states [92]. Optical qubits, limited by spontaneous emission, typically achieve coherence times around 0.2 s [107]. These extended coherence times enable the execution of complex quantum algorithms.

- **Universal gate operations:** Quantum gates are implemented using laser- or microwave-driven interactions. Single-qubit gates, performed on microsecond timescales, involve resonant transitions driven by focused lasers or global microwave fields. Two-qubit gates, such as the Mølmer–Sørensen [75] and Cirac–Zoller [31] gates, rely on ion–ion interactions mediated by shared motional modes. With gate times ranging from 10 to 100 μs, these operations are completed well within qubit coherence limits, though they are slower than the nanosecond-scale gates of superconducting circuits [98].

- **High-fidelity measurements:** State readout is performed via fluorescence detection, where a resonant laser drives a cycling transition in one qubit state, causing it to fluoresce while the other remains dark. This binary discrimination achieves fidelities exceeding 99.9% [105], comparable to the best superconducting qubit readout fidelities [102], with measurement times of a few milliseconds.

While trapped-ion systems demonstrate excellent coherence, control, and readout, scaling up to hundreds or thousands of qubits presents substantial challenges. These include increasing physical resources, mitigating crosstalk, and maintaining gate fidelity across large systems. Recent advances have focused on modularity, integration, and error correction to address these obstacles:

- **Modular architectures with photonic interconnects:** Instead of scaling a single monolithic trap, photonic links allow individual ion-trap modules to be networked together [93]. Each module operates a medium-sized quantum processor, and entanglement between modules is generated via probabilistic photon-mediated gates.

- **Multi-zone traps and QCCD architecture:** The Quantum Charge-Coupled Device (QCCD) paradigm enables ion transport between dedicated zones for memory, logic, and readout [108]. This dynamic reconfiguration supports parallel operations and minimizes local heating or laser crosstalk.

- **Integrated optics and microfabrication:** Advances in microfabricated ion traps with embedded waveguides and optics [109] allow for compact, scalable delivery of laser control and detection, critical for high-qubit-count systems.

- **Fault-tolerant operations and error correction:** Trapped-ion systems are well-suited for implementing surface code error correction [110], thanks to long coherence times and high gate fidelities. Combined with robust ion-shuttling protocols and error-resilient gate designs, this makes fault-tolerant computation within reach.

4.1.1 Dynamics of single trapped ions

Trapped-ion quantum processors rely on the careful engineering of electromagnetic fields to confine individual ions. However, achieving stable confinement in all three spatial dimensions is not possible using static electric fields alone. This limitation arises from a fundamental principle of electrostatics. According to Gauss's law, in regions devoid of free charges, the divergence of the electric field must vanish [111]

$$\vec{\nabla} \cdot \vec{E}(\vec{r}, t) = 0 \ . \tag{4.1}$$

Given that the electric field is related to the electrostatic potential by $V(\vec{r}, t)$ by $\vec{E}(\vec{r}, t) = -\vec{\nabla} V(\vec{r}, t)$, Gauss's law directly implies Laplace's equation,

$$\vec{\nabla}^2 V(\vec{r}, t) = 0 \ . \tag{4.2}$$

Laplace's equation imposes a significant constraint on the potential $V(\vec{r}, t)$: the curvature of the potential cannot be positive (*i.e.*, confining) in all three spatial dimensions simultaneously. For example, if the potential is confining in two dimensions, it must necessarily be anti-confining in the third.

To address this limitation, various ion trap geometries have been developed, combining electric and magnetic fields. The *Penning trap* [112, 113, 96], for example, uses static magnetic and electric fields to confine charged particles. The quadrupole electric field provides axial confinement, while the strong magnetic field confines particles radially. Penning traps can create large, two-dimensional ion crystals that rotate at a constant angular velocity when the axial frequency exceeds the radial frequencies. This rotation enhances the trap's resistance to stray electric fields, making it suitable for applications such as mass spectrometry, spectroscopy, and fundamental physics. However, the rotation poses challenges for quantum computing, which requires a stationary array of ions.

Paul traps [114, 115, 96] utilize a combination of static (DC) and oscillating radiofrequency (RF) fields to provide three-dimensional confinement for ions. RF voltages are applied to selected trap electrodes, creating a time-dependent potential. Although the instantaneous potential may contain anti-confining regions, the rapid oscillations of the RF field cause these regions to average out over time, resulting in an effective potential that ensures net confinement. This dynamic stabilization arises from the fact that ions cannot respond instantaneously to the high-frequency oscillations, instead experiencing a smooth, time-averaged potential.

The total time-dependent potential in such traps is typically expressed as

$$V(\vec{r}, t) = V^{(DC)}(\vec{r}) + V^{(RF)}(\vec{r}) \cos(\omega_{rf} t) \ , \tag{4.3}$$

where $\vec{r}^T = (x, y, z)$ represents the ion's position, $V^{(DC)}(\vec{r})$ and $V^{(RF)}(\vec{r})$ are the static and RF components of the potential, respectively, and ω_{rf} is the RF frequency.

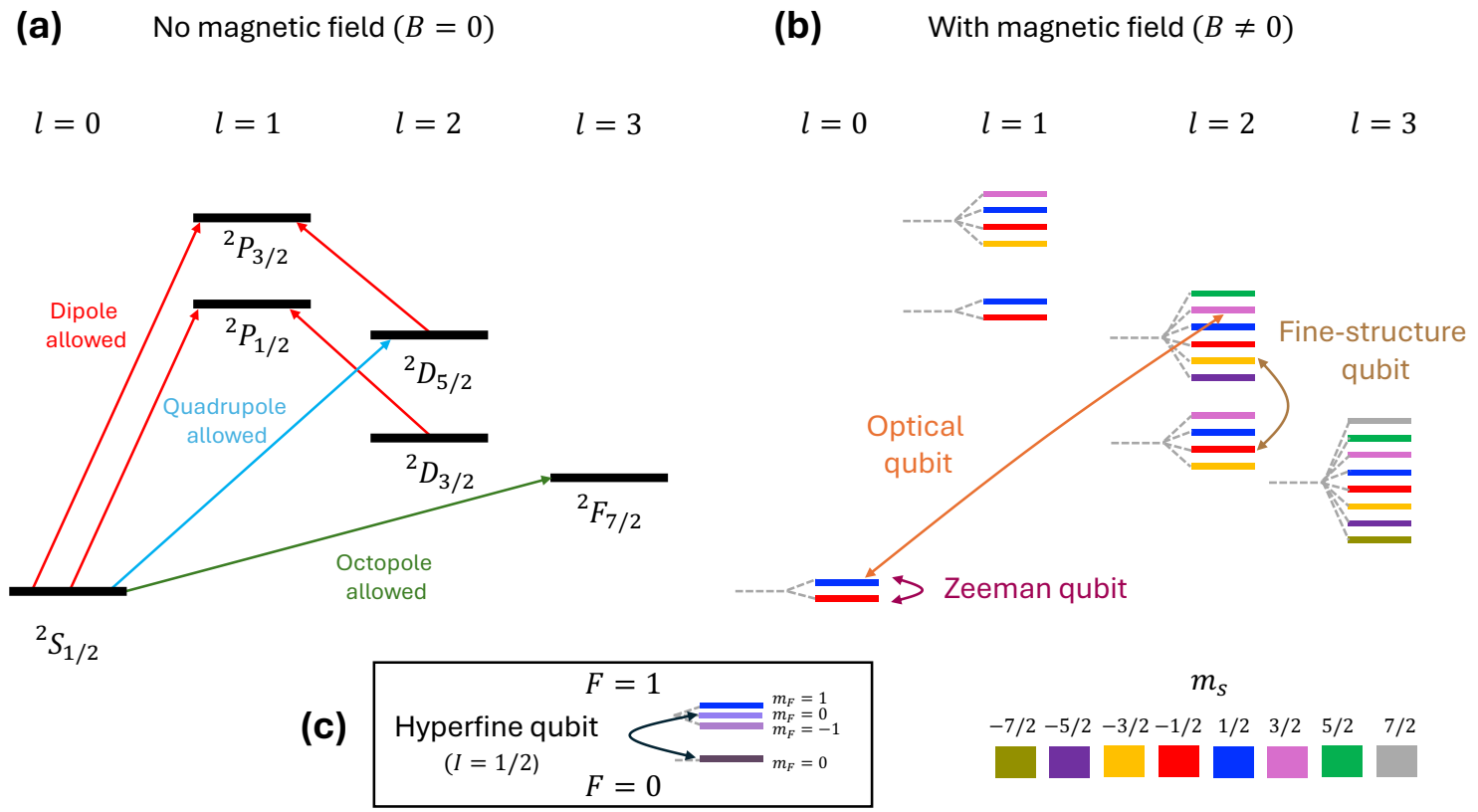

Figure 4.1: Level structure and qubit encodings in monovalent ions (energy splittings not to scale), inspired by [96]. Panel (a) shows the basic electronic structure of ions, with levels labeled using spectroscopic notation (s, p, d, and f corresponding to orbital angular momentum quantum numbers $l = 0, 1, 2, 3$). Colored lines represent transitions allowed by dipole, quadrupole, or octupole selection rules. In panel (b), the application of a magnetic field causes energy level splitting due to the Zeeman effect, with the number of sublevels determined by the total angular momentum j. For example, the ground-state s-levels ($^2S_{1/2}$) split into two Zeeman sublevels, which can be used for Zeeman qubits. Fine-structure qubits are encoded within levels differing by the spin-orbit interaction (*e.g.*, within the D manifold); optical qubits are typically defined between s and d levels. Panel (c) focuses on the $^2S_{1/2}$ manifold, where nuclear spin further splits the Zeeman sublevels into hyperfine levels. This hyperfine splitting occurs in all levels with nuclear spin, though only the $^2S_{1/2}$ hyperfine structure is shown. Levels are labeled using the spectroscopic notation $^{2s+1}L_j$, where s is the total spin quantum number, L is the orbital angular momentum quantum number, and j is the total angular momentum quantum number.

Near the trap center, the potentials $V^{(DC)}(\vec{r})$ and $V^{(RF)}(\vec{r})$ are engineered to exhibit a quadrupole spatial structure, allowing for approximate representation as

$$V(\vec{r},t) = \frac{1}{2}V_{DC}\frac{\vec{r}^T\mathbf{M}\vec{r}}{r_0^2} + \frac{1}{2}V_{RF}\cos(\omega_{rf}t)\frac{\vec{r}^T\mathbf{N}\vec{r}}{r_0^2} \ , \tag{4.4}$$

where V_{DC} and V_{RF} are the peak amplitudes of the static and dynamic (RF) fields, respectively, $\mathbf{M}$ and $\mathbf{N}$ are dimensionless, symmetric matrices defining the potential's geometry, and r_0 is the effective trap radius (typically $r_0 \sim 10^{-5}$ m for planar traps), representing the characteristic distance from the trap axis to the electrodes. In the simplest case, where the matrices $\mathbf{M}$ and $\mathbf{N}$ are diagonal, Eq. (4.4) simplifies to the familiar form of a harmonic potential

$$V(x,y,z,t) = \frac{V_{DC}}{2}\sum_i M_{ii}\left(\frac{r_i}{r_0}\right)^2 + \frac{V_{RF}}{2}\cos(\omega_{rf}t)\sum_i N_{ii}\left(\frac{r_i}{r_0}\right)^2 \ , \tag{4.5}$$

where r_i corresponds to the spatial coordinates (x,y,z), and A_{ij} denotes the element in the i-th row and j-th column of matrix $\mathbf{A}$. This simplified form is a reasonable approximation for static scenarios or when ions move along a single dimension. However, in general cases, off-diagonal terms in the matrices $\mathbf{M}$ and $\mathbf{N}$ can couple different spatial dimensions, resulting in a more complex potential landscape.

The coefficients in $\mathbf{M}$ and $\mathbf{N}$ can be tuned by adjusting the voltages applied to the electrodes, but these coefficients must always satisfy the condition imposed by Laplace's equation (Eq. (4.2)), which ensures that the potential remains consistent with the electrostatic boundary conditions

$$\mathrm{Tr}(\mathbf{M}) = \sum_i M_{ii} = 0 \ , \qquad \mathrm{Tr}(\mathbf{N}) = \sum_i N_{ii} = 0 \ . \tag{4.6}$$

These conditions ensure that the potential corresponds to a saddle point in the potential landscape, with some directions being confining and others anti-confining. A common choice for the coefficients in linear (Paul) traps [116] that satisfies Eq. (4.6) is

$$M_{33} = -(M_{11}+M_{22}) > 0 \ , \qquad N_{11} = -N_{22} \ , \qquad N_{33} = 0 \ . \tag{4.7}$$

This configuration results in static confinement along the z-direction and dynamic confinement along the x and y directions (note that the choice of these axes is arbitrary). In this scenario, the z-axis is referred to as the *axial* direction, while the x and y axes are considered *radial* directions.

The classical motion of an ion with charge $Z|e|$ and mass m can be determined from Newton's second law

$$m\ddot{\vec{r}} = -Z|e|\vec{\boldsymbol{\nabla}}V(\vec{r},t) \ , \tag{4.8}$$

where $e \approx 1.602 \cdot 10^{-19}$ C is the elementary charge, Z is the atomic number, and the

dot denotes the temporal derivative (*i.e.*, $\dot{a} = \frac{da}{dt}$). By introducing the dimensionless time parameter $\tau = \frac{\omega_{rf} t}{2}$, scaled by the RF drive frequency, the equation of motion can be transformed into the following system of coupled Mathieu-like equations [117, 118], written in matrix form

$$\frac{d^2\vec{r}}{d\tau^2} + \Big(\mathbf{P} + 2\cos(2\tau)\mathbf{Q}\Big)\vec{r} = 0 \ , \tag{4.9}$$

with the symmetric matrices $\mathbf{P}$ and $\mathbf{Q}$ with dimensionless elements

$$P_{ij} = \frac{4Z|e|V_{DC}M_{ij}}{m\omega_{rf}^2 r_0^2} \ , \qquad Q_{ij} = \frac{2Z|e|V_{RF}N_{ij}}{m\omega_{rf}^2 r_0^2} \ . \tag{4.10}$$

This system of equations is well-documented in the literature [115]. Solving them typically involves perturbative techniques, with particular attention to identifying stability regions in parameter space where the solutions remain bounded. For a more detailed discussion of solution methods and stability criteria, refer to Appendix D. In the simplest scenario where the potential is aligned with the coordinate axes (*i.e.* $\mathbf{P}$ and $\mathbf{Q}$ are diagonal matrices), the system of equations in Eq. (4.9) decouples. This decoupling enables simple analytical solutions for the ion's motion along each spatial dimension. In this scenario, the ion exhibits oscillatory motion along each axis, as described by specific solutions to Eq. (D.9) in Appendix D. Under the constraints given in Eq. (4.7), and in the limit of a high-frequency oscillatory RF field (*i.e.*, $P_{ij}, Q_{ij} \ll 1$), these solutions take the approximate forms

$$x(t) \approx x_0 \cos(\nu_x t)\left(1 - \frac{Q_{11}}{2}\cos(\omega_{rf} t)\right) \ , \tag{4.11a}$$

$$y(t) \approx y_0 \cos(\nu_y t)\left(1 - \frac{Q_{22}}{2}\cos(\omega_{rf} t)\right) \ , \tag{4.11b}$$

$$z(t) = z_0 \cos(\nu_z t) \ , \tag{4.11c}$$

where the constants x_0, y_0, z_0 are determined by the initial conditions. The effective oscillation frequencies along the x-, y- and z-axis, derived as specific solutions to Eq. (D.12) in Appendix D, are

$$\nu_x \approx \frac{\omega_{rf}}{2}\sqrt{P_{11} + \frac{Q_{11}^2}{2}} \ , \qquad \nu_y \approx \frac{\omega_{rf}}{2}\sqrt{P_{22} + \frac{Q_{22}^2}{2}} \ , \qquad \nu_z \approx \frac{\omega_{rf}}{2}\sqrt{P_{33}} \ , \tag{4.12}$$

which, for the standard choices for Paul traps (Eq. (4.7)), take the form

$$\nu_x \approx \frac{\omega_{rf}}{2}\sqrt{\frac{4Z|e|V_{DC}M_{11}}{m\omega_{\mathrm{rf}}^2 r_0^2} + \frac{2Z^2|e|^2V_{RF}^2N_{11}^2}{m^2\omega_{rf}^4 r_0^4}} \ , \tag{4.13a}$$

$$\nu_y \approx \frac{\omega_{rf}}{2}\sqrt{\frac{4Z|e|V_{DC}M_{22}}{m\omega_{\mathrm{rf}}^2 r_0^2} + \frac{2Z^2|e|^2V_{RF}^2N_{11}^2}{m^2\omega_{rf}^4 r_0^4}} \ , \tag{4.13b}$$

$$\nu_z \approx \frac{\omega_{rf}}{2}\sqrt{\frac{-4Z|e|V_{DC}(M_{11}+M_{22})}{m\omega_{rf}^2 r_0^2}} \ . \tag{4.13c}$$

Notably, while the frequencies in the *radial* directions (x and y) depend on both the DC

and RF field contributions, confinement along the *axial* direction (z-axis) arises solely from the static DC component of the field.

Eq. (4.11) reveals a characteristic feature of the motion. In the radial directions (x and y), the ion undergoes a combination of two distinct oscillations: a slow secular oscillation at frequency ν_u, and a faster, smaller-amplitude oscillation at the drive frequency ω_{rf}, referred to as *micromotion*. When the condition $\nu_u \ll \omega_{rf}$ is satisfied, the micromotion's influence becomes negligible, allowing the radial motion to be effectively approximated as simple harmonic oscillation at the *secular frequency* ν_u. In the axial direction (z), the motion corresponds to a simple harmonic oscillation of frequency ν_z.

This analytical description of motion, as given by Eq. (4.11), holds when the trap axes perfectly align with the coordinate axes, establishing a clear correspondence between radial and axial directions. However, in general scenarios where the potential exhibits significant coupling between axes, this simple picture breaks down. The radial and axial directions appear in rotated frames, making analytical approximations more challenging and often necessitating numerical methods to estimate the equations of motion.

Pseudopotential

While solutions based on Mathieu's equation (Eq. (4.9)) provide an accurate description of the classical motion of the ion, a semiclassical or quantum treatment of the dynamics often benefits from a more tractable approximation of the potential experienced by the trapped ion. Such an approximation is advantageous because it avoids the complexities associated with non-positive semidefinite matrices in the exact potential, while still capturing the net, confining effects of the field in all directions. To achieve this, instead of relying on the precise form of the electric potential, one can derive an approximate time-averaged potential. This simplified potential, known as *pseudopotential* [119, 120], captures the average confining nature of the field and allows for a more straightforward determination of the ion's dynamics.

Although the exact form of Eq. (4.11) may not hold for potential landscapes that couple different axes, it still provides valuable insights into the ion's dynamics. Specifically, it reveals that the motion can be decomposed into two components: a slow, high-amplitude oscillation $\vec{r_S}(t)$ and a fast, small-amplitude oscillation $\vec{r}_F(t)$. In general, thus, the total motion can be expressed as [121]

$$\vec{r}(t) = \vec{r}_S(t) + \vec{r}_F(t) \ . \tag{4.14}$$

Since the amplitude of the fast component $\vec{r}_F(t)$ is much smaller than that of the slower component $\vec{r}_S(t)$, the ion's motion remains approximately centered around $\vec{r}_S(t)$. This allows for a Taylor expansion to approximate the dynamics. Starting from the equation of

motion $m\ddot{\vec{r}} = -Z|e|\vec{\nabla}V(\vec{r},t)$, it follows that

$$\ddot{\vec{r}}_S(t) + \ddot{\vec{r}}_F(t) = -\frac{Z|e|}{m}\left(\vec{\nabla}V(\vec{r},t)\Big|_{\vec{r}=\vec{r_S}} + \mathbf{J}\Big|_{\vec{r}=\vec{r}_S}\vec{r}_F(t) + \cdots\right), \tag{4.15}$$

where the Jacobian matrix is $\mathbf{J}_{ij} = \frac{\partial^2 V(\vec{r},t)}{\partial r_i \partial r_j}$, and we applied Eq. (4.14). Assuming $\|\vec{r}_F(t)\|$ is sufficiently small, the term $\mathbf{J}\Big|_{\vec{r}=\vec{r}_S}\vec{r}_F(t)$ can be neglected.

On the faster timescale of $\vec{r}_F(t)$, $\vec{r}_S(t)$ can be treated as approximately constant, and changes in $\vec{r}_F(t)$ are dominated by the rapidly oscillating field component $V^{(RF)}(\vec{r})\cos(\omega_{rf}t)$. Thus,

$$\ddot{\vec{r}}_F(t) \approx -\frac{Z|e|}{m}\vec{\nabla}V^{(RF)}(\vec{r})\Big|_{\vec{r}=\vec{r}_S}\cos(\omega_{rf}t)\ . \tag{4.16}$$

Integrating this expression yields

$$\vec{r}_F(t) \approx \frac{Z|e|}{m\omega_{rf}^2}\vec{\nabla}V^{(RF)}(\vec{r})\Big|_{\vec{r}=\vec{r}_S}\cos(\omega_{rf}t)\ . \tag{4.17}$$

Substituting this result into the equation of motion Eq. (4.15) gives

$$\begin{aligned}\ddot{\vec{r}}_S(t) = -\frac{Z|e|}{m}\Bigg(&\vec{\nabla}V^{(DC)}(\vec{r})\Big|_{\vec{r}=\vec{r_S}} \\ &+ \mathbf{J}^{(DC)}\Big|_{\vec{r}=\vec{r_S}}\frac{Z|e|}{m\omega_{rf}^2}\vec{\nabla}V^{(DC)}(\vec{r})\Big|_{\vec{r}=\vec{r}_S}\cos(\omega_{rf}t) \\ &+ \mathbf{J}^{(RF)}\Big|_{\vec{r}=\vec{r_S}}\frac{Z|e|}{m\omega_{rf}^2}\vec{\nabla}V^{(RF)}(\vec{r})\Big|_{\vec{r}=\vec{r}_S}\cos^2(\omega_{rf}t) + \cdots\Bigg),\end{aligned} \tag{4.18}$$

where $\mathbf{J}\Big|_{\vec{r}=\vec{r}_S} = \mathbf{J}^{(DC)}\Big|_{\vec{r}=\vec{r}_S} + \mathbf{J}^{(RF)}\Big|_{\vec{r}=\vec{r}_S}\cos(\omega_{rf}t)$, with $\mathbf{J}_{ij}^{(DC/RF)} = \frac{\partial^2 V^{(DC/RF)}(\vec{r},t)}{\partial r_i \partial r_j}$.

In the regime where ω_{rf} is much larger than the characteristic timescales of $\vec{r}_S(t)$, the dynamics averaged over an RF period $T = 2\pi/\omega_{rf}$ are given by

$$\begin{aligned}\langle\ddot{\vec{r}}_S(t)\rangle &= -\frac{Z|e|}{m}\left(\vec{\nabla}V^{(DC)}(\vec{r})\Big|_{\vec{r}=\vec{r}_S} + \mathbf{J}^{(RF)}\Big|_{\vec{r}=\vec{r}_S}\frac{Z|e|}{2m\omega_{rf}^2}\vec{\nabla}V^{(RF)}(\vec{r})\Big|_{\vec{r}=\vec{r}_S} + \cdots\right) \\ &= -\frac{1}{m}\vec{\nabla}\left(Z|e|V^{(DC)}(\vec{r}) + \frac{Z^2|e|^2}{4m\omega_{rf}^2}\left(\vec{\nabla}V^{(RF)}(\vec{r})\right)^2\right)\Bigg|_{\vec{r}=\vec{r}_S},\end{aligned} \tag{4.19}$$

where $\langle\cdot\rangle = \frac{1}{T}\int_0^T \cdot\, dt$, $\langle\cos(\omega_{rf}t)\rangle = 0$, $\langle\cos^2(\omega_{rf}t)\rangle = 1/2$ and we used the relation

$$\frac{\partial}{\partial r_k}(\vec{\nabla}V)^2 = \frac{\partial}{\partial r_k}\left[\sum_i\left(\frac{\partial V}{\partial r_i}\right)^2\right] = 2\sum_i\frac{\partial^2 V}{\partial r_k \partial r_i}\frac{\partial V}{\partial r_i} = 2\left(\mathbf{J}\cdot\vec{\nabla}V\right)_k\ . \tag{4.20}$$

This result shows that the slow oscillatory motion $\vec{r}_S(t)$ is governed by an effective force

derived from a *pseudopotential* with time-averaged energy

$$U_{pseudo}(\vec{r}) = Z|e|V^{(DC)}(\vec{r}) + \frac{Z^2|e|^2}{4m\omega_{rf}^2}\left(\vec{\nabla}V^{(RF)}(\vec{r})\right)^2 . \tag{4.21}$$

For practical trapping, the potentials $V^{(DC)}(\vec{r})$ and $V^{(RF)}(\vec{r})$ are designed to approximate harmonic confinement in a small region around the ion (see Eq. (4.4)). Under the assumptions that the spatial dimensions are decoupled and that the electrode symmetry constraints from Eq. (4.7) hold, the pseudopotential can be written as

$$U_{pseudo}(\vec{r}) = \frac{Z|e|}{2}\left[\left(\frac{Z|e|N_{11}^2V_{RF}^2}{2m\omega_{rf}^2r_0^2} - |M_{11}|V_{DC}\right)(x^2+y^2) + |M_{33}|V_{DC}z^2\right] . \tag{4.22}$$

Here, we have assumed additional radial symmetry ($M_{11} = M_{22}$) and applied the electrode polarity conditions $M_{11} = -|M_{11}|$ and $M_{33} = |M_{33}|$ from Eq. (4.7). Crucially, this formulation demonstrates that effective three-dimensional confinement is achievable — as long as the radial RF confinement is strong enough to overcome the deconfining effect of the DC potential in the radial directions. Specifically, the condition

$$\frac{Z|e|}{2m\omega_{rf}^2}N_{11}^2V_{RF}^2 > |M_{11}|V_{DC} \tag{4.23}$$

ensures a net restoring force in the (x, y) plane. When this condition holds, the system exhibits effective time-averaged confinement in all three spatial dimensions.

In more general scenarios where residual coupling between spatial axes is present, the pseudopotential $U_{pseudo}(\vec{r})$ can be locally approximated by a second-order Taylor expansion around its minimum, the trap center $\vec{C}$,

$$U_{pseudo}(\vec{r}) \approx U_{pseudo}(\vec{C}) + \frac{1}{2}\left(\vec{r}-\vec{C}\right)^T \mathbf{H}^{(U)}\Big|_{\vec{r}=\vec{C}}\left(\vec{r}-\vec{C}\right) , \tag{4.24}$$

where $\mathbf{H}_{ij}^{(U)} = \frac{\partial^2 U_{pseudo}(\vec{r})}{\partial r_i \partial r_j}$ represents the Hessian matrix of the second derivatives of the pseudopotential. Importantly, the positive semidefiniteness of $\mathbf{H}^{(U)}$ ensures that the pseudopotential exhibits a local minimum at $\vec{C}$, reflecting the confining nature of the effective potential in all directions. The eigenvectors and eigenvalues of $\mathbf{H}^{(U)}$ reveal the trap's principal axes and the corresponding trapping frequencies, respectively. This harmonic approximation holds when the ion's motion is confined near $\vec{C}$, rendering higher-order anharmonic terms negligible — a condition met through cryogenic cooling or laser cooling techniques.

The resulting quantum Hamiltonian that governs the dynamics of a single trapped ion can thus be expressed as

$$H = \frac{\vec{p}^2}{2m} + \frac{1}{2}\left(\vec{r}-\vec{C}\right)^T \mathbf{H}^{(U)}\Big|_{\vec{r}=\vec{C}}\left(\vec{r}-\vec{C}\right) , \tag{4.25}$$

where $\vec{p} = (p_x, p_y, p_z)^T$ represents the momentum operator, and m is the ion's mass. In

this expression, the term $U_{pseudo}(\vec{C})$, which depends only on the position of the trap center, is omitted because it contributes merely an overall phase to the quantum state and does not affect the ion's dynamics.

Given the resemblance of this Hamiltonian to that of a harmonic oscillator, it is convenient to rewrite it in the form

$$H = \frac{\vec{p}^2}{2m} + \frac{1}{2}m\left(\vec{r} - \vec{C}\right)^T \mathbf{M}\left(\vec{r} - \vec{C}\right) \ , \tag{4.26}$$

where the matrix $\mathbf{M}$ encapsulates the effective harmonic trapping frequencies and is defined as

$$\mathbf{M} = \frac{1}{m}\mathbf{H}^{(U)}\Big|_{\vec{r}=\vec{C}} \ . \tag{4.27}$$

This reformulation highlights the harmonic nature of the trapping potential, enabling straightforward connections to the standard quantum harmonic oscillator framework. Since $\mathbf{M}$ is symmetric, the Hamiltonian can alternatively be written in a form that will prove useful in Chapter 6,

$$H = \frac{\vec{p}^2}{2m} + \frac{1}{2}m\vec{r}^T\mathbf{M}\vec{r} - \vec{F}^T\vec{r} \ , \tag{4.28}$$

where the static offset $\frac{1}{2}m\vec{C}^T\mathbf{M}\vec{C}$ has been omitted, and the vector $\vec{F}$, defined as

$$\vec{F} = \mathbf{H}^{(U)}\Big|_{\vec{r}=\vec{C}}\vec{C} \ , \tag{4.29}$$

represents an effective force that drives the ion towards the center of the potential.

4.1.2 Dynamics of multiple trapped ions

Trapping a single ion is, in itself, a remarkable achievement, requiring precise engineering of the trapping potential with the necessary characteristics to confine the ion effectively as explained in the previous section. This process is further complicated by the need to mitigate perturbative influences from the surrounding environment, such as stray electric fields, thermal noise, and vibrations, all of which can disrupt the stability of the ion's position. Reaching this level of control reflects the advanced capabilities of modern experimental techniques and technologies.

However, building a functional quantum computer — one capable of leveraging a significant number of qubits to solve complex problems — goes far beyond trapping just one ion. It demands the ability to confine and control multiple ions simultaneously within the same trap while ensuring they remain isolated from external disturbances yet strongly coupled to one another for effective quantum operations.

For a system of N ions, the trapping potential is similar to the single-ion case, but the

system Hamiltonian must account for the Coulomb repulsion between ions,

$$H = \sum_{j=1}^{N} \frac{\vec{p}_j^2}{2m_j} + \sum_{j=1}^{N} \frac{1}{2} m_j (\vec{r}_j - \vec{C})^T \mathbf{M}_j (\vec{r}_j - \vec{C}) + \frac{1}{4\pi\epsilon_0} \sum_{i<j=1}^{N} \frac{Z^2|e|^2}{|\vec{r}_i - \vec{r}_j|} \ , \tag{4.30}$$

where $\vec{r}_i$ and $\vec{r}_j$ denote the positions of the i-th and j-th ions, respectively, and ϵ_0 is the permittivity of free space. Here, all ions are assumed to carry the same charge, Z (*i.e.*, $Z_i = Z, \forall i$). The Coulomb interaction depends on the relative distance between ion pairs, introducing a position-dependent coupling mechanism that is essential for the generation of entangling gates — key components for implementing quantum logic operations.

In static scenarios, where ions are confined to fixed locations, the potential's center is stationary, and the matrices of curvatures $\mathbf{M}_j$ remains constant. However, when dealing with time-varying potentials, such as those required to move ions, both the potential's center and curvatures evolve dynamically to achieve effective ion displacement (see Chapter 6).

When the primary objective is not ion shuttling but rather implementing quantum operations, it is typically sufficient to consider only one spatial dimension for gate operations. This direction is conventionally chosen as the axial direction along the trap axis, simplifying individual ion addressing by eliminating the need for complex stroboscopic techniques. This simplification is justified by the significantly stronger confinement along the radial directions, which effectively suppresses motion in those directions and confines the ions to a near-one-dimensional chain along the axial direction. Under these conditions, the approximate potential can be expressed as

$$V = \sum_{j} \frac{1}{2} m_j \nu_z^2 \Delta z_j^2 + \frac{1}{4\pi\epsilon_0} \sum_{i<j} \frac{Z^2|e|^2}{|\Delta z_i - \Delta z_j|} \ , \tag{4.31}$$

where $\Delta z_j = z_j - C_z$ represents the displacement of the j-th ion relative to the center of the potential. For sufficiently cold ions (*i.e.*, ions with low kinetic energy), their motion consists of small oscillations around equilibrium positions, determined by the minima of the potential. These equilibrium positions are obtained by setting the gradient of the potential with respect to the ions' positions to zero. This results in a set of coupled differential equations, which can be solved analytically for two and three ions but generally require numerical methods for larger ion chains. This work considers chains of identical ions for simplicity, where all ions have equal mass (*i.e.*, $m_i = m$ for all i). By introducing the scaled variables

$$\Delta z_k = \lambda \mathfrak{z}_k \ , \quad \text{with } \lambda = \left(\frac{Z^2|e|^2}{4\pi\epsilon_0 m \nu_z^2} \right)^{1/3} \ , \tag{4.32}$$

the equations simplify to

$$\frac{1}{\lambda^2 m \nu_z^2} \frac{\partial V}{\partial \mathfrak{z}_k} = \left[\mathfrak{z}_k - \Big(\sum_{j=1}^{k-1} \frac{1}{(\mathfrak{z}_k - \mathfrak{z}_j)^2} - \sum_{j=k+1}^{N} \frac{1}{(\mathfrak{z}_k - \mathfrak{z}_j)^2} \Big) \right] = 0 \ . \tag{4.33}$$

The values $\{\mathfrak{z}_k\}$ that satisfy Eq. (4.33) are denoted by $\{\mathfrak{z}_k^{(eq)}\}$ (or $\{\Delta z_k^{(eq)}\}$ in the original variables). For two and three ions, the equilibrium positions $\{\mathfrak{z}_k^{(eq)}\}$ are given by

$$\mathfrak{z}_1^{(eq)} = -2^{-2/3} \ , \qquad \mathfrak{z}_2^{(eq)} = 2^{-2/3} \ , \tag{4.34}$$

and

$$\mathfrak{z}_1^{(eq)} = -5^{1/3}2^{-2/3} \ , \qquad \mathfrak{z}_2^{(eq)} = 0 \ , \qquad \mathfrak{z}_3^{(eq)} = 5^{1/3}2^{-2/3} \ , \tag{4.35}$$

respectively (see Fig. 4.2). For larger ion chains, the equilibrium positions can be determined numerically. Eq. (4.33) determines the equilibrium positions of the ions relative to the center of the potential ($\vec{C}$), defined as the point where the potential energy, in the absence of Coulomb interactions, is minimized. The kinetic energy of the ions induces oscillations around these equilibrium positions. This behavior can be understood by expanding the potential in a Taylor series around the equilibrium positions,$\{\mathfrak{z}_k^{(eq)}\}$

$$V \approx \frac{1}{2}\sum_{jk} \frac{\partial^2 V}{\partial \mathfrak{z}_j \partial \mathfrak{z}_k}\Big|_{\{\mathfrak{z}_j^{(eq)}\}} \delta z_j \delta z_k \ , \tag{4.36}$$

where $\sum_j V|_{\mathfrak{z}_j=\mathfrak{z}_j^{(eq)}}$ is omitted as it represents a constant energy offset and does not affect the dynamics of the system, and $\delta z_j = \mathfrak{z}_j - \mathfrak{z}_j^{(eq)}$ represents the displacement of ion j from its respective equilibrium position. The linear term in the Taylor expansion vanishes at the equilibrium points, as the gradient of the potential is zero at these points by definition. To further analyze the system's dynamics, we define the matrix $\mathbf{J}$ with entries

$$\begin{aligned}
\mathbf{J}_{jk} &= \frac{1}{\lambda^2 m \nu_z^2} \frac{\partial^2 V}{\partial \mathfrak{z}_j \partial \mathfrak{z}_k}\Big|_{\{\mathfrak{z}_j^{(eq)}\}} \\
&= \left[\delta_{jk} + 2\left(\sum_{m=1}^{k-1} \frac{\delta_{jk}-\delta_{jm}}{(\mathfrak{z}_k^{(eq)} - \mathfrak{z}_m^{(eq)})^3} - \sum_{m=k+1}^{N} \frac{\delta_{jk}-\delta_{jm}}{(\mathfrak{z}_k^{(eq)} - \mathfrak{z}_m^{(eq)})^3}\right)\right] \\
&= \left[\delta_{jk}\left(1 + \sum_{m\neq k,\ m=1}^{N} \frac{2}{\left|\mathfrak{z}_k^{(eq)} - \mathfrak{z}_m^{(eq)}\right|^3}\right) - \frac{2(1-\delta_{jk})}{\left|\mathfrak{z}_k^{(eq)} - \mathfrak{z}_j^{(eq)}\right|^3}\right] .
\end{aligned} \tag{4.37}$$

The matrix $\mathbf{J}$, being real and symmetric, is diagonalizable. Thus, there exists a set of eigenvectors, $\vec{\chi}_k$, and corresponding eigenvalues, κ_k, satisfying

$$\mathbf{J} = \sum_k \kappa_k \vec{\chi}_k \cdot \vec{\chi}_k^T \ , \tag{4.38}$$

where $\vec{\chi}_k^T = (\chi_{1k}, \cdots, \chi_{Nk})$. These eigenvectors represent the normal modes of the system, describing collective oscillations of the ion chain. By transforming to this normal mode

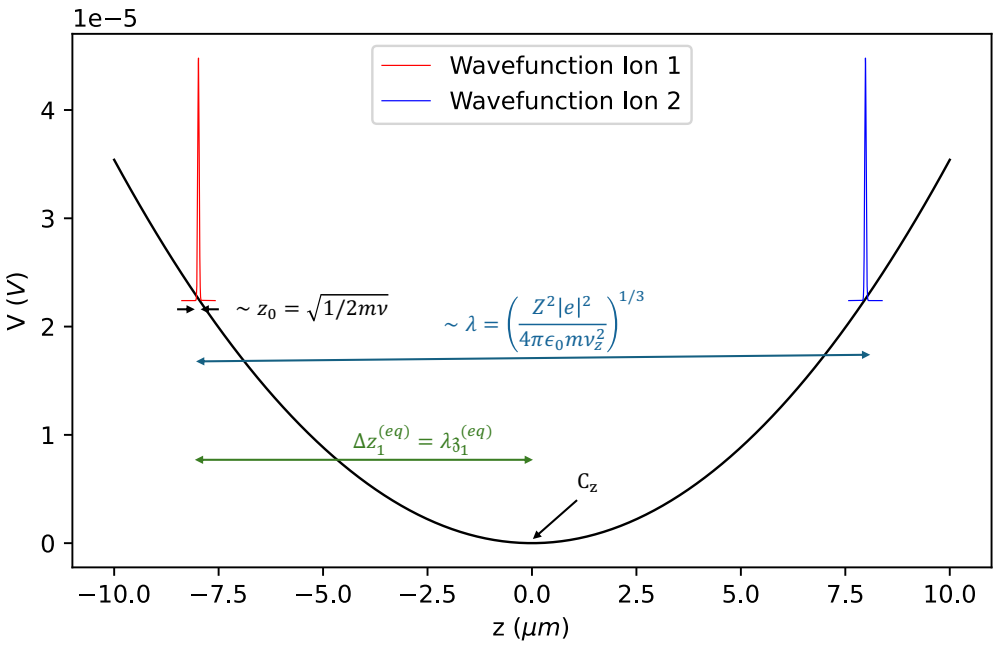

Figure 4.2: Schematic illustration of a harmonic trapping potential V along the z-axis (black curve). Two ions are depicted by their quantum wavefunctions — red and blue, respectively — located at their equilibrium positions, separated by a distance $\Delta z_j^{(eq)}$ from the trap center C_z. The spatial spread of each ion's wavefunction is on the order of z_0, while the typical separation between the ions is characterized by the length scale λ.

basis, the potential energy can be expressed as

$$\begin{aligned} V &\approx \frac{1}{2}\lambda^2 m\nu_z^2 \vec{\delta z}^T \boldsymbol{J} \vec{\delta z} \\ &= \frac{1}{2}\sum_{k=1}^{M} m\left(\sqrt{\kappa_k}\nu_z\right)^2 \left(\lambda\vec{\delta z}^T \cdot \vec{\chi}_k\right)\cdot\left(\lambda\vec{\chi}_k^T \cdot \vec{\delta z}\right) \\ &= \frac{1}{2}\sum_{k=1}^{M} m\left(\sqrt{\kappa_k}\nu_z\right)^2 \left(\vec{\chi}_k^T \cdot \vec{\xi}\right)^2 , \end{aligned} \tag{4.39}$$

where $\vec{\xi}^T = (\xi_1, \cdots, \xi_N) = \lambda\vec{\delta z}^T = \lambda(\mathfrak{z}_1 - \mathfrak{z}_1^{(eq)}, \cdots, \mathfrak{z}_N - \mathfrak{z}_N^{(eq)}) = (\Delta z_1 - \Delta z_1^{(eq)}, \cdots, \Delta z_N - \Delta z_N^{(eq)})$ denotes the vector of displacements from the equilibrium positions of the ions, and the summation runs over M normal modes — which in the case of a one-dimensional motional system corresponds to $M = N$, though we retain M for generality. This expression reveals that the potential can be decomposed into a sum of independent harmonic oscillator potentials, each corresponding to a normal mode with frequency $\nu_k \equiv \sqrt{\kappa_k}\nu_z$. The transformation to normal mode coordinates is given by

$$\begin{pmatrix} Q_1 \\ \vdots \\ Q_M \end{pmatrix} = \begin{pmatrix} \chi_{11} & \cdots & \chi_{N1} \\ \vdots & \ddots & \vdots \\ \chi_{1M} & \cdots & \chi_{NM} \end{pmatrix} \begin{pmatrix} \xi_1 \\ \vdots \\ \xi_N \end{pmatrix} . \tag{4.40}$$

This shows that each normal mode coordinate Q_k is a linear combination of the displace-

ments of all ions in the chain, with the coefficients χ_{jk} quantifying the contribution of the displacement of the j-th ion to the k-th normal mode, *i.e.* $Q_k = \sum_{j=1}^{N} \chi_{jk}\xi_j$. By applying the same transformation to the momenta, *i.e.* $P_k = \sum_{j=1}^{N} \chi_{jk}p_{j,z}$, where $p_{j,z}$ is the z-component of the momentum operator $\vec{p}_j$ of ion j, the system Hamiltonian simplifies to

$$H = \sum_{k=1}^{M} \frac{P_k^2}{2m} + \frac{1}{2}m\sum_{k=1}^{M} \nu_k^2 Q_k^2 \ , \tag{4.41}$$

where the sum now runs over the motional modes, rather than individual ions. This demonstrates that the system can be effectively described as a collection of independent harmonic oscillators, each corresponding to a distinct normal mode of the ion chain.

Since the transformation matrix in Eq. (4.40) consists of the eigenvectors of the matrix $\boldsymbol{J}$, it is invertible. This invertibility allows us to express the displacement ξ_j of each ion in terms of the normal mode coordinates Q_k as

$$\xi_j = \sum_{k=1}^{M} \chi_{jk} Q_k \ . \tag{4.42}$$

This relationship reformulates the motion of individual ions in terms of the collective dynamics of independent harmonic oscillators (normal modes).

The normal mode coordinates can then be quantized in the standard manner of the harmonic oscillator by defining the position and momentum operators for each mode as

$$Q_k = z_{k,0}\left(a_k + a_k^\dagger\right) \ , \tag{4.43a}$$

$$P_k = \frac{i}{2z_{k,0}}\left(a_k - a_k^\dagger\right) \ , \tag{4.43b}$$

where $a_k^\dagger$ and a_k are the creation and annihilation operators, respectively, that satisfy the commutation relation $\left[a_j, a_k^\dagger\right] = \delta_{jk}$ and $z_{k,0} = \sqrt{\frac{1}{2m\nu_k}}$ is the zero-point motion amplitude for mode k. This results in the Hamiltonian taking the form

$$H = \sum_{k=1}^{M} \nu_k a_k^\dagger a_k \ , \tag{4.44}$$

up to the constant factor $\sum_k \nu_k/2$. This Hamiltonian describes a system of uncoupled quantum harmonic oscillators, where each mode k vibrates at a characteristic frequency ν_k. This is evident from the diagonal structure of the Hamiltonian in the normal mode basis, and implies that the dynamics of one mode do not influence the others. However, the situation is quite different in the original basis of ion displacements. Since each normal mode is a linear combination of the individual ion displacements, the motion of each oscillator influences a subset of ions — specifically those with a non-zero coupling element $\chi_{jk} \neq 0$. This interdependence is crucial because it enables the collective motion of the ions to mediate interactions between them — a fundamental mechanism underpinning the

implementation of most quantum gates.

Although Eq. (4.44) provides an excellent approximation for the Hamiltonian in most scenarios, it is essential to consider the conditions under which this model holds. While examining these conditions is beyond the scope of this thesis, it is important to note that deviations from the assumptions can require a more detailed treatment. For example, higher-order terms in the Taylor expansion of the potential around the equilibrium positions, such as cubic or quartic terms, may introduce perturbative corrections to the mode frequencies and alter the corresponding eigenvectors [122]. Similarly, in ion chains consisting of non-homogeneous species, variations in mass can significantly affect the dynamics [122]. Moreover, if the trap axes are not perfectly aligned, coupling between the axial and radial modes (in the x- and/or y-directions) could become significant, necessitating an expansion of the Hamiltonian to include additional vibrational modes. In such cases, a more refined model would be needed to accurately describe the system's dynamics and ensure the precision of gate operations.

4.1.3 Light-matter interaction

The interaction between an atom (or a molecule) and a classical electromagnetic field constitutes a fundamental basis for realizing quantum gates. In the semi-classical framework adopted in this thesis, the atom is modeled as a quantum system, while the electromagnetic field is treated classically.

In the standard treatment, the atomic model assumes a stationary nucleus, with dynamics confined to the outer electrons. The electromagnetic field is described by a vector potential $\vec{A}(\vec{r},t)$, and a scalar potential, $U(\vec{r},t)$ [111], which include the internal fields generated by the nucleus as well as externally applied fields, such as trapping or control fields used for implementing quantum gates. The system's dynamics are governed by the Hamiltonian [123, 111]

$$H = \frac{\left(\vec{p} - Z|e|\vec{A}(\vec{r},t)\right)^2}{2m} + Z|e|U(\vec{r},t) \ , \tag{4.45}$$

where the momentum operator $\vec{p}$ is shifted by the vector potential $\vec{A}(\vec{r},t)$, with a coupling strength proportional to the atomic charge $Z|e|$.

The electromagnetic potentials $\vec{A}(\vec{r},t)$ and $U(\vec{r},t)$ are not uniquely defined due to *gauge freedom*: transformations of the form

$$\vec{A} \to \vec{A} + \vec{\boldsymbol{\nabla}} F \ , \quad U \to U - \frac{\partial F}{\partial t} \ ,$$

preserve the physical fields ($\vec{E}$ and $\vec{B}$) for any scalar function F [124, 123] (see Appendix E). To resolve this ambiguity, the *Coulomb gauge* is adopted, defined by the condition

$$\vec{\boldsymbol{\nabla}} \cdot \vec{A}(\vec{r},t) = 0 \quad \text{(see Appendix E)}.$$

In this gauge, the vector potential $\vec{A}(\vec{r},t)$ simplifies to a transverse plane wave (see Appendix E), enabling analytical tractability.

Expanding the interaction Hamiltonian H from Eq. (4.45), we obtain

$$H = \underbrace{\frac{\vec{p}^2}{2m} + Z|e|U(\vec{r},t)}_{H_{\text{bare}}} \underbrace{-Z|e|\frac{\vec{p}\cdot\vec{A}(\vec{r},t) + \vec{A}(\vec{r},t)\cdot\vec{p}}{2m}}_{H_{\text{light-matter}}} \underbrace{+Z^2|e|^2\frac{\vec{A}^2(\vec{r},t)}{2m}}_{H_{A^2}} , \tag{4.46}$$

where H_{bare} represents the unperturbed Hamiltonian containing kinetic and electrostatic potential energy. The second term ($H_{\text{light-matter}}$) describes the linear coupling between the electromagnetic field and the particle's momentum, while the third term (H_{A^2}), proportional to $\vec{A}^2$, is negligible for typical field strengths but becomes significant in extreme regimes (*e.g.*, ultra-intense lasers), where it induces nonperturbative distortions of the molecular binding potential.

Given the quantization of momentum, $\vec{p} = -i\vec{\boldsymbol{\nabla}}$, and the Coulomb gauge condition, it can be shown that the momentum operator $\vec{p}$ and the vector potential $\vec{A}(\vec{r},t)$ commute. This can be demonstrated by applying the commutator to an arbitrary function ψ,

$$\begin{aligned}
\Big[\vec{p},\vec{A}\Big]\psi &= \Big(\vec{p}\cdot\vec{A} - \vec{A}\cdot\vec{p}\Big)\psi \\
&= \vec{p}\cdot(\vec{A}\psi) - \vec{A}\cdot(\vec{p}\psi) \\
&= -i\vec{\boldsymbol{\nabla}}\cdot(\vec{A}\psi) + i\vec{A}\cdot(\vec{\boldsymbol{\nabla}}\psi) \\
&= -i\vec{\boldsymbol{\nabla}}\cdot(\vec{A}\psi) + i\vec{\boldsymbol{\nabla}}\cdot(\vec{A}\psi) - i(\vec{\boldsymbol{\nabla}}\cdot\vec{A})\psi \\
&= -i(\vec{\boldsymbol{\nabla}}\cdot\vec{A})\psi = 0 ,
\end{aligned} \tag{4.47}$$

where we used the identity

$$\vec{\boldsymbol{\nabla}}\cdot(\vec{A}\psi) = \vec{A}\cdot(\vec{\boldsymbol{\nabla}}\psi) + (\vec{\boldsymbol{\nabla}}\cdot\vec{A})\psi . \tag{4.48}$$

This result simplifies the light-matter interaction Hamiltonian to

$$H_{\text{light-matter}} = -\frac{Z|e|}{m}\vec{A}(\vec{r},t)\cdot\vec{p} . \tag{4.49}$$

To refine this expression further, the plane wave form of the vector potential $\vec{A}(\vec{r},t)$ (Eq. (E.9)) is substituted into the interaction Hamiltonian, yielding

$$H_{\text{light-matter}} = -\frac{Z|e|}{m}\Big(A_0\vec{\epsilon}^{\,T}\cdot\vec{p}\exp\Big(i(\vec{k}^T\cdot\vec{r}-\omega t)\Big) + A_0^*\vec{\epsilon}^{\,T}\cdot\vec{p}\exp\Big(-i(\vec{k}^T\cdot\vec{r}-\omega t)\Big)\Big) , \tag{4.50}$$

where $\vec{\epsilon}_0$ is the polarization vector, ω is the field frequency, and $\vec{k}$ is the wave vector. Letting $\vec{r}_0$ be the center of mass of the atom (*i.e.* the classical position of the atom), the

spatial component of the exponential can be expanded as

$$\exp\left(i\vec{k}^T \cdot \vec{r}\right) = \exp\left(i\vec{k}^T \cdot \vec{r}_0\right)\left[1 + i(\vec{k}^T \cdot (\vec{r} - \vec{r}_0)) + \cdots\right] , \tag{4.51}$$

which explicitly separates the dependence on the center of mass $\vec{r}_0$ and the relative displacement $\vec{r} - \vec{r}_0$.

Electric dipole Hamiltonian

In typical atom-light interactions, the wavelength λ of the electromagnetic field far exceeds the atomic dimensions [125, 126]. For instance, hydrogen atom transitions correspond to wavelengths of at least 100 nm, compared to the atomic size on the order of the Bohr radius $a_0 = 0.053$ nm. Under these conditions, the inequality $\left|\vec{k}\right| \cdot |\vec{r} - \vec{r}_0| \ll 1$ holds true. This allows us to approximate the exponential term as $\exp\left(i(\vec{k}^T \cdot \vec{r} - \omega t)\right) \approx \exp\left(i(\vec{k}^T \cdot \vec{r}_0 - \omega t)\right)$. This approximation essentially reflects that when the field's wavelength is very large, its effect on the atom is practically independent of the electron's instantaneous position and depends primarily on the classical position of its center of mass. This approximation is known as *long-wavelength approximation*. Consequently, the interaction Hamiltonian takes the form

$$H_{\text{light-matter}} \simeq \frac{-2Z|e|}{m}|A_0|\cos\left(\vec{k}^T \cdot \vec{r}_0 - \omega t + \phi\right)\left(\vec{\epsilon}^T \cdot \vec{p}\right) \equiv H_{\text{elec-dipole}} , \tag{4.52}$$

where $A_0 = |A_0|e^{i\phi}$. Substituting $\vec{E}$ (from Eq. (E.11a)) leads to

$$H_{\text{elec-dipole}} = \frac{-Z|e|}{m\omega}\vec{E}^T(\vec{r}_0, t) \cdot \vec{p} , \tag{4.53}$$

where the electric field $\vec{E}$ now depends on time and the position of the atom's center of mass ($\vec{r}_0$). Eq. (4.53) represents the *electric dipole Hamiltonian*.

Another formulation of the interaction Hamiltonian in Eq. (4.53), which will be used throughout this thesis, is expressed in terms of the energy eigenstates $\{|s\rangle\}$ of the bare Hamiltonian H_{bare}. To obtain this expression, we use the commutation relation

$$[r_j, H_{\text{bare}}] = \frac{1}{2m}\left[\vec{r}_j, \vec{p}^2\right] = \frac{ip_j}{m} , \tag{4.54}$$

which links the matrix elements of the momentum and position operators. This leads to

$$\frac{1}{m}\langle s|\, p_j \,|l\rangle = -i\,\langle s|\,[r_j, H_{\text{bare}}]\,|l\rangle = i\left(E_0^{(s)} - E_0^{(l)}\right)\langle s|\, r_j \,|l\rangle = i\omega_{sl}\,\langle s|\, r_j \,|l\rangle , \tag{4.55}$$

with $H_{\text{bare}}\,|s\rangle = E_0^{(s)}\,|s\rangle$ and $\omega_{sl} = E_0^{(s)} - E_0^{(l)}$. Substituting the matrix elements in Eq. (4.53),

$$\langle s|\, H_{\text{elec-dipole}} \,|l\rangle = \frac{-iZ|e|\omega_{sl}}{\omega}\,\langle s|\, \vec{r}^T \cdot \vec{E}(\vec{r}_0, t)\,|l\rangle , \tag{4.56}$$

which simplifies to

$$\langle s|\, H_{\text{elec-dipole}}\, |l\rangle = \frac{-i\omega_{sl}}{\omega}\, \langle s|\, \vec{D}^T \cdot \vec{E}(\vec{r}_0, t)\, |l\rangle \ , \tag{4.57}$$

where the *transition dipole moment operator* [6, 127] is defined as

$$\vec{D} = Z|e|\vec{r}\ . \tag{4.58}$$

Eq. (4.57) provides a key insight: the transition amplitude between any two given energy eigenstates $|k\rangle$ and $|s\rangle$ is proportional to the scalar product of the transition dipole moment $\vec{D}$ and the polarization vector of the electric field $\vec{\epsilon}$. This effect, known as the *linear Stark effect*, highlights that the efficiency of radiation absorption depends on the electric field's ability to induce a redistribution of charge within the system. This redistribution enhances the overlap between the initial and final states, facilitating transitions between energy levels [128].

Magnetic Dipole and Electric Quadrupole Transitions

The electric dipole Hamiltonian $H_{\text{elec-dipole}}$ is the dominant contribution to the light-matter interaction Hamiltonian $H_{\text{light-matter}}$ under typical conditions, particularly when the wavelength of the radiation field is significantly larger than the atomic length scales. However, this approximation breaks down in scenarios where the wavelength is comparable to these scales, or when the effective coupling elements $\langle s|\, \vec{D}^T \cdot \vec{E}(\vec{r}_0, t)\, |k\rangle$ in the interaction Hamiltonian Eq. (4.57) vanish due to selection rules or symmetry constraints. In such cases, other interaction terms become relevant. Among these, the leading contributions are the *electric quadrupole* and *magnetic dipole* interactions, both arising from the first-order term in the Taylor expansion of the electromagnetic field (Eq. (4.51)), which is linear in the position operator. Specifically, the interaction Hamiltonian associated with this order can be expressed as

$$H_{\text{light-matter}} \simeq -\frac{Z|e|}{m}\Big(iA_0(\vec{\epsilon}^T \cdot \vec{p})(\vec{k}^T \cdot \vec{r})e^{-i\omega t} - iA_0^*(\vec{\epsilon}^T \cdot \vec{p})(\vec{k}^T \cdot \vec{r})e^{i\omega t}\Big)\ . \tag{4.59}$$

Expanding $(\vec{\epsilon}^T \cdot \vec{p})(\vec{k}^T \cdot \vec{r})$, yields

$$(\vec{\epsilon}^T \cdot \vec{p})(\vec{k}^T \cdot \vec{r}) = \vec{\epsilon}^T\Big(\vec{p}\vec{r}^T\Big)\vec{k} = \frac{1}{2}\vec{\epsilon}^T\Big(\vec{p}\vec{r}^T + \vec{r}\vec{p}^T\Big)\vec{k} + \frac{1}{2}\vec{\epsilon}^T\Big(\vec{p}\vec{r}^T - \vec{r}\vec{p}^T\Big)\vec{k}\ , \tag{4.60}$$

where symmetric and antisymmetric terms are added and subtracted in the final equality. These terms lead to two distinct interaction mechanisms. Specifically, the interaction Hamiltonian can be expressed as $H_{\text{light-matter}} \simeq H_{\text{elec-quad}} + H_{\text{mag-dipole}}$, with

$$H_{\text{elec-quad}} = -i\frac{Z|e|}{2m}\vec{\epsilon}^T\Big(\vec{p}\vec{r}^T + \vec{r}\vec{p}^T\Big)\vec{k}\Big(A_0e^{-i\omega t} - A_0^*e^{i\omega t}\Big)\ , \tag{4.61}$$

$$H_{\text{mag-dipole}} = -i\frac{Z|e|}{2m}\vec{\epsilon}^T\Big(\vec{p}\vec{r}^T - \vec{r}\vec{p}^T\Big)\vec{k}\Big(A_0e^{-i\omega t} - A_0^*e^{i\omega t}\Big)\ , \tag{4.62}$$

where $H_{\text{elec-quad}}$ corresponds to the *electric quadrupole Hamiltonian* and $H_{\text{mag-dipole}}$ to the *magnetic dipole Hamiltonian*. To understand the terminology, we evaluate these expressions further. For $H_{\text{elec-quad}}$, we focus on the symmetrized operator $\vec{p}\vec{r}^T + \vec{r}\vec{p}^T$. Since this represents an outer product, it contains terms of the form $p_i r_j$ (with $i, j \in \{x, y, z\}$). Using Eq. (4.54), we find

$$\langle s| \, p_i r_j \, |k\rangle = -im \, \langle s| \, [r_i, H_{\text{bare}}] r_j \, |k\rangle \ , \tag{4.63}$$

$$\langle s| \, r_i p_j \, |k\rangle = -im \, \langle s| \, r_i [r_j, H_{\text{bare}}] \, |k\rangle \ , \tag{4.64}$$

leading to

$$-im \, \langle s| \, [r_i, H_{\text{bare}}] r_j + r_i [r_j, H_{\text{bare}}] \, |k\rangle = -im \, \langle s| \, [r_i r_j, H_{\text{bare}}] \, |k\rangle \ . \tag{4.65}$$

Thus,

$$\begin{aligned} H_{\text{elec-quad}} &= -\frac{Z|e|}{2} \vec{\epsilon}^T \cdot \left[\vec{r}\vec{r}^T, H_{\text{bare}}\right] \cdot \vec{k} \Big(A_0 e^{-i\omega t} - A_0^* e^{i\omega t} \Big) \\ &= i \frac{Z|e|}{4\omega} \vec{\epsilon}^T \cdot \left[\vec{r}\vec{r}^T, H_{\text{bare}}\right] \cdot \vec{k} \Big(E_0 e^{-i\omega t} + E_0^* e^{i\omega t} \Big) \\ &= i \frac{Z|e|}{2\omega} \vec{\epsilon}^T \cdot \left[\vec{r}\vec{r}^T, H_{\text{bare}}\right] \cdot \vec{k} |E_0| \cos(\omega t - \phi) \ . \end{aligned} \tag{4.66}$$

Defining the *quadrupole operator* $\mathbf{Q} = Z|e|\vec{r}\vec{r}^T$, we arrive at

$$H_{\text{elec-quad}} = \frac{i}{2\omega} \vec{E}^T(0,t) \cdot [\mathbf{Q}, H_{\text{bare}}] \cdot \vec{k} \ , \tag{4.67}$$

and, in matrix form,

$$\langle s| \, H_{\text{elec-quad}} \, |l\rangle = \frac{i\omega_{sl}}{2\omega} \, \langle s| \, \vec{E}^T(0,t) \mathbf{Q} \vec{k} \, |l\rangle \ . \tag{4.68}$$

For $H_{\text{mag-dipole}}$, the antisymmetric term simplifies as follows

$$\begin{aligned} \vec{\epsilon}^T \Big(\vec{p}\vec{r}^T - \vec{r}\vec{p}^T \Big) \vec{k} &= \sum_{i<j} \Big(k_i \epsilon_j - k_j \epsilon_i \Big) \Big(r_i p_j - r_j p_i \Big) \\ &= \Big(k_x \epsilon_y - k_y \epsilon_x \Big) L_z + \Big(k_z \epsilon_x - k_x \epsilon_z \Big) L_y + \Big(k_y \epsilon_z - k_z \epsilon_y \Big) L_x \\ &= \Big(\vec{k} \times \vec{\epsilon} \Big)^T \cdot \vec{L} \ , \end{aligned} \tag{4.69}$$

where $\vec{L} = \vec{r} \times \vec{p}$ is the *angular momentum*. Substituting this into $H_{\text{mag-dipole}}$, we find

$$\begin{aligned} H_{\text{mag-dipole}} &= -i \frac{Z|e|}{2m} \Big(\vec{k} \times \vec{\epsilon} \Big)^T \cdot \vec{L} \Big(A_0 e^{-i\omega t} - A_0^* e^{i\omega t} \Big) \\ &= -\frac{Z|e|}{4m} \vec{b}^T \Big(B_0 e^{-i\omega t} + B_0^* e^{i\omega t} \Big) \cdot \vec{L} \\ &= -\frac{Z|e|}{2m} \vec{B}^T(0,t) \cdot \vec{L} \ , \end{aligned} \tag{4.70}$$

where $\vec{B}(\vec{r}_0, t)$ represents the magnetic field, with polarization direction given by $\vec{b} = \vec{k} \times \vec{\epsilon}/\|\vec{k}\|$ and field amplitude $B_0 = 2i\|\vec{k}\|A_0$. With the *magnetic dipole moment* $\vec{\mu}_L = \frac{Z|e|}{2m}\vec{L}$, we finally obtain

$$H_{\text{mag-dipole}} = -\vec{\mu}_L^T \cdot \vec{B}(0, t) \ . \tag{4.71}$$

This expression indicates that the interaction energy depends on the projection — or overlap — of the magnetic field $\vec{B}(0, t)$ onto the dipole moment $\vec{\mu}_L$. In essence, the stronger the alignment between these two vectors, the larger (in magnitude) the interaction energy becomes.

Thus far, our semiclassical derivation has focused on the coupling of the magnetic field with the electron's orbital angular momentum $\vec{L}$. However, a complete quantum mechanical treatment must also include the coupling of the magnetic field to the electron's *intrinsic spin angular momentum* $\vec{S}$. Unlike orbital angular momentum, which arises from the electron's spatial motion, spin is an inherent property of the electron. Correspondingly, the spin magnetic dipole moment is given by [6]

$$\vec{\mu}_S = -\gamma_s \vec{S} \ , \tag{4.72}$$

where $g_s \approx 2$ is the Landé factor for intrinsic spin and $\gamma_s = g_s \mu_B$ is the gyromagnetic ratio, with $\mu_B = Z|e|/2m$ being the Bohr magneton. As demonstrated in the early Stern-Gerlach experiments [6], when a magnetic dipole is placed in a magnetic field $\vec{B}$, it experiences a torque that tends to align it parallel to the field. This interaction is modeled by the Hamiltonian

$$H_S = -\vec{\mu}_S^T \cdot \vec{B}(\vec{r}, t) \ . \tag{4.73}$$

Therefore, the complete magnetic dipole interaction Hamiltonian, which includes both orbital and spin contributions, is

$$H_{\text{mag-dipole}} = -\left(\vec{\mu}_L^T \cdot \vec{B}(0, t) + \vec{\mu}_S^T \cdot \vec{B}(\vec{r}, t)\right) \ , \tag{4.74}$$

where it is crucial to note that the magnetic field $\vec{B}$ is evaluated at the origin $\vec{r} = 0$ for the orbital contribution and at the electron's position $\vec{r}$, which can be approximated as the position of the atom $\vec{r} \approx \vec{r}_0$, for the spin contribution.

4.1.4 Quantum gates with trapped ions

Once an ion is stably confined within the electromagnetic trap, it can serve as a physical qubit. The qubit is encoded in two well-defined electronic states, $|g\rangle$ and $|e\rangle$, which satisfy the DiVincenzo criteria (see Section 4.1). The static Hamiltonian describing these electronic states can thus be expressed as

$$H_0 = \frac{\omega_{eg}}{2}\left(|e\rangle\langle e| - |g\rangle\langle g|\right) = \frac{\omega_{eg}}{2}\sigma_z \ , \tag{4.75}$$

where the energy reference is chosen at half the energy difference between the $|g\rangle$ and $|e\rangle$ states, and where the states are labeled according to the standard convention used in quantum optics, *i.e.*

$$|e\rangle \equiv |0\rangle \equiv \begin{pmatrix} 1 \\ 0 \end{pmatrix} \ , \qquad |g\rangle \equiv |1\rangle \equiv \begin{pmatrix} 0 \\ 1 \end{pmatrix} \ , \tag{4.76}$$

which results in the relations $\sigma_z |e\rangle = +|e\rangle$ and $\sigma_z |g\rangle = -|g\rangle$. The alternative notation $|0\rangle$ and $|1\rangle$ in Eq. (4.76) will be used interchangeably with $|e\rangle$ and $|g\rangle$, respectively. Similarly, we will occasionally refer to $|g\rangle$ as the *ground state* (or GS), and $|e\rangle$ as the *excited state* (ES).

Notably, the term ω_{eg} in in the Hamiltonian (Eq. (4.75)) represents the energy difference between the ground and excited states in the bare ion (without any external electromagnetic field). As will become clear in the next section, when an electromagnetic field is introduced, the energy levels can shift due to the *Zeeman effect*. This phenomena arises from the interaction between the ion's spin magnetic moment ($\vec{\mu}_S$) and the external magnetic field ($\vec{B}$), as described by the Hamiltonian in Eq. (4.73). Since the two qubit states are typically characterized by distinct spin quantum numbers (m_S), the Zeeman effect introduces an energy shift. In the simplest case of a spatially uniform and time-independent magnetic field along the z-axis, the Zeeman effect results in a static Hamiltonian H_Z

$$H_Z = \frac{\gamma_s}{2} B_z \sigma_z \ , \tag{4.77}$$

which contributes to the bare Hamiltonian H_0, modifying the resonance frequency to $\omega_{eg} + \gamma_s B_z$.

Crucially, the Zeeman effect plays a vital role in defining qubit states within the Zeeman states of an atom (see Fig. 4.1(b)). In the absence of a magnetic field, these states are degenerate ($\omega_{eg} = 0$). However, the interaction with the magnetic field lifts this degeneracy, introducing an energy splitting that effectively distinguishes the two states. In this specific case, the energy difference between the qubit states is solely determined by the Zeeman shift $\gamma_s B_z$[1].

[1] In some cases, this description represents a simplification, as the protons in the nucleus themselves possess a magnetic dipole moment, giving rise to a nonzero nuclear spin, denoted as $\vec{S}_p$. The magnetic dipole moment of the proton, $\vec{\mu}_p$, is significantly smaller than that of the electron due to the proton's comparatively larger mass, appearing in the denominator of the expression $\vec{\mu}_p = \frac{g_p Z|e|}{2m_p} \vec{S}_p$ (where $g_p \approx 5.59$ is the proton's g-factor). According to classical mechanics, the proton's magnetic dipole moment generates a magnetic field $\vec{B}_p$ at the position of the electron, which interacts with the electron's spin $\vec{S}$. This interaction, known as *spin-spin coupling*, introduces an additional correction to the energy levels, commonly referred to as *hyperfine splitting* (see Fig. 4.1(b)). The magnitude of this splitting is proportional to the scalar product $\vec{S} \cdot \vec{S}_p$, reflecting the coupling between the electron's spin and the nuclear spin [6].

Single qubit gates

Single-qubit rotations are described by a unitary operator of the form

$$U = e^{i\alpha} \exp\left(-i\theta \vec{n}^T \cdot \vec{\sigma}/2\right) = e^{i\alpha}\Big(\cos(\theta/2)\mathbb{I} - i\sin(\theta/2)\vec{n}^T \cdot \vec{\sigma}\Big) \ , \tag{4.78}$$

where $\vec{n}^T = (n_x, n_y, n_z)$ is a unit vector specifying the rotation axis on the Bloch sphere, θ is the rotation angle, α is a global phase factor, and $\vec{\sigma}^T = (\sigma_x, \sigma_y, \sigma_z)$ represents the vector of Pauli matrices. A fundamental property of unitary matrices, known as the Euler decomposition [53], is that they can always be decomposed into a product of three unitary rotations

$$U = e^{i\alpha} e^{-i\beta\sigma_n/2} e^{-i\gamma\sigma_m/2} e^{-i\delta\sigma_n/2} \ , \tag{4.79}$$

where σ_m and σ_n are distinct Pauli matrices (where m and n can be any non-parallel unit vector combination of x, y and z) and $\exp(-i\chi\sigma_k/2)$ represents a rotation about the k-axis by an angle χ. This decomposition implies that any arbitrary single-qubit rotation described U can be effectively implemented provided that individual rotations around any two distinct axes (*e.g.*, σ_y and σ_z) can be performed for arbitrary angles β, γ and δ.

In trapped-ion systems, single-qubit gates are typically implemented by applying laser pulses that induce transitions between the qubit states. These rotations are based on coherent interactions between the ion's internal electronic states and the applied electromagnetic field, typically governed by either the electric dipole Hamiltonian Eq. (4.57), the electric quadrupole Hamiltonian Eq. (4.67), the magnetic dipole interaction Hamiltonian Eq. (4.74), or, in some cases, higher-order multipole terms. While electric dipole interactions are generally dominant, some atomic species exhibit forbidden electric dipole transitions, requiring magnetic dipole or electric quadrupole interactions.

The specific coupling mechanism depends on the chosen qubit states. For instance, dipole couplings are allowed for transitions between $\left|^2S_{1/2}\right\rangle$ and $\left|^2P_{1/2}\right\rangle$ while quadrupole couplings are required for transitions between $\left|^2S_{1/2}\right\rangle$ and $\left|^2D_{5/2}\right\rangle$. In certain cases, even higher-order couplings, such as octupole couplings, may be required for specific state transitions (see Fig. 4.1(a)). These transitions are governed by selection rules based on the quantum numbers m_s, l, and j associated with the angular momentum, which dictate the allowed interactions and determine the appropriate coupling mechanisms [123].

When the ion is approximated as a two-level system, the interaction Hamiltonian for any coupling mechanism can be written in the basis $\{|g\rangle, |e\rangle\}$ as

$$H_{\text{light-matter}}(t) \simeq \Omega_{eg}(\vec{r}_0, t)\,|e\rangle\langle g| + \Omega^*_{eg}(\vec{r}_0, t)\,|g\rangle\langle e| + \Omega_{gg}(\vec{r}_0, t)\,|g\rangle\langle g| + \Omega_{ee}(\vec{r}_0, t)\,|e\rangle\langle e| \ , \tag{4.80}$$

where Ω_{ab} represents the *Rabi frequency*, quantifying the strength of the interaction between the levels $|a\rangle$ and $|b\rangle$. This form of the Hamiltonian is general and encompasses any coupling mechanism with the electromagnetic radiation, including electric and mag-

netic dipole interactions, as well as higher-order processes such as quadrupole or octupole couplings. While the analysis here focuses on magnetic and electric dipole interactions, the same structure applies to higher-order mechanisms, with the Rabi frequencies Ω_{ab} appropriately redefined to account for the nature of the specific interaction.

For the electric dipole interaction, the Rabi frequency is expressed as

$$\Omega_{ab}(\vec{r}_0, t) = \frac{-i\omega_{ab}}{\omega} \langle a| \vec{D}^T \cdot \vec{E}(\vec{r}_0, t) |b\rangle \ , \tag{4.81}$$

where ω_{ab} is the transition frequency between states $|a\rangle$ and $|b\rangle$, and ω is the laser frequency. Importantly, dipole coupling vanishes when $|a\rangle$ and $|b\rangle$ are the same state (*i.e.* $\Omega_{aa} = 0$).

For the magnetic dipole interaction, the Rabi frequency is given by

$$\Omega_{ab}(\vec{r}_0, t) = -\langle a| \left(\vec{\mu}_L^T \cdot \vec{B}(0, t) + \vec{\mu}_S^T \cdot \vec{B}(\vec{r}_0, t) \right) |b\rangle \ , \tag{4.82}$$

where $\vec{\mu}_L$ and $\vec{\mu}_S$ denote the orbital and spin magnetic moments, respectively, and $\vec{B}$ is the magnetic field. Unlike the electric dipole interaction, magnetic dipole interactions can include non-zero diagonal terms $\Omega_{aa}(\vec{r}_0, t) |a\rangle\langle a|$ in the Hamiltonian. These terms describe energy shifts in the level $|a\rangle$ due to interactions with the magnetic field. In particular, when the magnetic field $\vec{B}$ is both time-independent and spatially uniform, the term $\langle a| \vec{\mu}_S^T \cdot \vec{B} |a\rangle$ in Eq. (4.82) gives rise to the static Zeeman splitting described in Eq. (4.77). More generally, a magnetic field that varies in space or time can induce position-dependent energy shifts, which are pivotal for the implementation of quantum gates.

With the *raising* and *lowering* operatos $\sigma_+ = |e\rangle\langle g|$ and $\sigma_- = |g\rangle\langle e|$, and their relations with the Pauli operators

$$\sigma_\pm = \frac{1}{2} (\sigma_x \pm i\sigma_y) \ , \tag{4.83}$$

the total Hamiltonian of the system can be written as

$$H(t) = H_0 + H_{\text{light-matter}}(t) = \frac{\omega_{eg}}{2}\sigma_z + \Omega_{eg}(t)\sigma_+ + \Omega_{eg}^*(t)\sigma_- + \Omega_{gg}(t) |g\rangle\langle g| + \Omega_{ee}(t) |e\rangle\langle e| \ , \tag{4.84}$$

where we set the position of the centre of mass at the origin ($\vec{r}_0 = \vec{0}$) for simplicity, and H_0 is defined in Eq. (4.75). In the interaction picture with respect to the bare non-interacting Hamiltonian H_0, the system Hamiltonian transforms as

$$\begin{aligned} H'(t) = U_0^\dagger(t) H_{\text{light-matter}}(t) U_0(t) = \Omega_{eg}(t) e^{i\omega_{eg}t}\sigma_+ + \Omega_{eg}^*(t) e^{-i\omega_{eg}t}\sigma_- \\ + \Omega_{gg}(t) |g\rangle\langle g| + \Omega_{ee}(t) |e\rangle\langle e| \ . \end{aligned} \tag{4.85}$$

where $U_0(t) = \exp(-itH_0)$ and the following transformations are used

$$\exp(itH_0)\sigma_+ \exp(-itH_0) = \sigma_+ + \frac{i\omega_{eg}t}{2}[\sigma_z, \sigma_+] + \cdots = \sigma_+ \left(1 + i\omega_{10}t + \cdots\right) = \sigma_+ e^{i\omega_{eg}t} \ ,$$
$$\exp(itH_0)\sigma_- \exp(-itH_0) = \sigma_- + \frac{i\omega_{eg}t}{2}[\sigma_z, \sigma_-] + \cdots = \sigma_- \left(1 - i\omega_{10}t + \cdots\right) = \sigma_- e^{-i\omega_{eg}t} \ . \tag{4.86}$$

Including the explicit time dependence in the Rabi frequency, the Hamiltonian can be written as

$$H'(t) = \frac{\Omega_{eg}}{2}\left(e^{i(\omega_{eg}+\omega)t}e^{-i\phi} + e^{-i(\omega-\omega_{eg})t}e^{i\phi}\right)\sigma_+ + \frac{\Omega_{eg}^*}{2}\left(e^{-i(\omega_{eg}+\omega)t}e^{i\phi} + e^{i(\omega-\omega_{eg})t}e^{-i\phi}\right)\sigma_-$$
$$+ \frac{\Omega_{gg}}{2}\left(e^{i\omega t}e^{-i\phi} + e^{-i\omega t}e^{i\phi}\right)|g\rangle\langle g| + \frac{\Omega_{ee}}{2}\left(e^{i\omega t}e^{-i\phi} + e^{-i\omega t}e^{i\phi}\right)|e\rangle\langle e| \ . \tag{4.87}$$

When ω is close to the qubit's resonant frequency ω_{eg} , the interaction Hamiltonian contains two terms that slowly rotate at the frequency $\delta = \omega - \omega_{eg}$, known as the *detuning*, and six terms that rotate at a much higher frequency $\omega + \omega_{eg}$ and ω. These fast-rotating terms contribute to the dynamics at a rate proportional to $(\omega + \omega_{eg})^{-1}$ and ω^{-1}, which become negligibly small. The *rotating wave approximation* (RWA) involves neglecting these rapidly oscillating terms, providing an accurate approximation as long as $\Omega_{eg} \ll \omega_{eg}$. Under the RWA, the Hamiltonian simplifies to

$$H'(t) \approx \frac{\Omega_{eg}}{2}e^{i\phi}e^{-i\delta t}\sigma_+ + \frac{\Omega_{eg}^*}{2}e^{-i\phi}e^{i\delta t}\sigma_- \ . \tag{4.88}$$

When the driving field is tuned to match the resonance frequency of the qubit (*i.e.*, $\delta = 0$), the Hamiltonian becomes time-independent

$$H' = |\Omega_{eg}|\Big(\cos(\phi+\varphi)\sigma_x - \sin(\phi+\varphi)\sigma_y\Big) \ , \tag{4.89}$$

with $\Omega_{eg} = |\Omega_{eg}|e^{i\varphi}$, and leads to the unitary time evolution operator

$$U(T) = \exp\Big(-i|\Omega_{eg}|\Big(\cos(\phi+\varphi)T\sigma_x - \sin(\phi+\varphi)T\sigma_y\Big)\Big) \ . \tag{4.90}$$

By carefully adjusting the phases ϕ and φ along with the evolution time T, one can generate any desired single-qubit rotation about an arbitrary axis within the x-y plane. Consequently, by combining three such rotations with appropriately chosen phases and durations, one can implement the most general single-qubit gate U, as described in Eq. (4.79).

Spin-motion coupling

Coupling qubits to an external electromagnetic field enables the execution of arbitrary single-qubit gates. However, scaling to multiqubit gates — operations that entangle or conditionally evolve the states of two or more qubits — introduces a fundamental challenge. While the electromagnetic field mediates interactions between individual qubits and their environment, it does not inherently create direct interactions between qubits themselves. Without such qubit-qubit coupling, the field acts independently on each qubit, leaving their

states uncorrelated. Thus, generating entanglement or conditional logic requires additional mechanisms, such as shared motional modes (*e.g.*, phonons in trapped ions) or auxiliary quantum systems (*e.g.*, microwave resonators in superconducting circuits).

In trapped-ion systems, the Coulomb repulsion between ions provides a natural collective coupling mechanism [96]. This electrostatic interaction allows distant ions to influence one another's motion, enabling entanglement through shared vibrational modes.

Consider a linear chain of N ions confined within an electrostatic trap. The Hamiltonian describing this system can be written as the sum of two components: the electronic Hamiltonian, given by Eq. (4.75), and the motional Hamiltonian, expressed in Eq. (4.44),

$$H_0 = \sum_{j=1}^{N} \frac{\omega_{eg}^{(j)}}{2} \sigma_z^{(j)} + \sum_{k=1}^{M} \nu_k a_k^\dagger a_k \ , \tag{4.91}$$

where M represents the number of collective motional modes of the ion chain (typically equal to the number of ions when considering motion along a single spatial dimension). The first term describes the internal energy levels of the ions, with qubit frequency $\omega_{eg}^{(j)}$ for the j-th ion (potentially including the contribution due to the Zeeman effect), while the second term accounts for their collective motion, with mode k characterized by a frequency ν_k. Next, consider an electromagnetic plane wave of frequency ω propagating along the z-direction, such that $\vec{k} = k\vec{e}_z$. The interaction Hamiltonian describing the coupling between the wave and a system of N ions can be expressed as a generalization of Eq. (4.80)

$$\begin{aligned} H_{\text{light-matter}}(t) = \sum_{j=1}^{N} \Bigg(& \Omega_{eg}^{(j)}(z_j, t)\sigma_+^{(j)} + \Omega_{eg}^{*(j)}(z_j, t)\sigma_-^{(j)} \\ & + \Omega_{gg}^{(j)}(z_j, t) \left|g^{(j)}\right\rangle\!\left\langle g^{(j)}\right| + \Omega_{ee}^{(j)}(z_j, t) \left|e^{(j)}\right\rangle\!\left\langle e^{(j)}\right| \Bigg) \ , \end{aligned} \tag{4.92}$$

where $\left|g^{(j)}\right\rangle$ and $\left|e^{(j)}\right\rangle$ represent the ground and excited states of ion j, respectively. The time-dependent coupling strengths $\Omega_{ab}^{(j)}(z_j, t)$ exhibits both spatial and temporal dependence due to the oscillatory nature of the electric field. Explicitly, they take the form

$$\Omega_{ab}^{(j)}(z_j, t) = \Omega_{ab}^{(j)} \cos(kz_j - \omega t + \phi) \ , \tag{4.93}$$

where $\Omega_{ab}^{(j)}$ depends on the specific coupling mechanism (electric dipole, magnetic dipole, etc.). The spatial dependence arises from the ion's position z_j along the z-axis, while the temporal dependence follows from the wave's oscillations.

Since each ion's position can be decomposed as $z_j = z_j^{(eq)} + \xi_j$, where $z_j^{(eq)}$ is the equilibrium position and ξ_j represents its displacement, the coupling strength varies with both equilibrium positions and motional fluctuations. To systematically account for these fluctuations, we express the displacement ξ_j in terms of the system's normal modes, combining Eq. (4.42) and Eq. (4.43a). Each of the M vibrational modes is characterized by a frequency ν_k and associated creation ($a_k^\dagger$) and annihilation (a_k) operators, leading to the

expansion

$$\xi_j = \sum_{l=1}^{M} \chi_{jl} z_{l,0} (a_l + a_l^\dagger) \ , \tag{4.94}$$

where $z_{l,0} = \sqrt{1/2m\nu_l}$ is the zero-point displacement, which defines the characteristic length scale of the harmonic oscillation for the l-th motional mode, and χ_{jl} are the mode participation coefficients that describe the extent to which ion j participates in the l-th normal mode. Substituting in Eq. (4.92),

$$\begin{aligned} H_{\text{light-matter}}(t) = \sum_{j=1}^{N} \Bigg(& \frac{\Omega_{eg}^{(j)}}{2} \sigma_+^{(j)} + \frac{\Omega_{gg}^{(j)}}{2} \left| g^{(j)} \right\rangle \left\langle g^{(j)} \right| + \frac{\Omega_{ee}^{(j)}}{2} \left| e^{(j)} \right\rangle \left\langle e^{(j)} \right| \Bigg) \\ \cdot & \left(e^{-i(\omega t - \phi_j)} \prod_{l=1}^{M} \exp\Big(i\eta_{jl} (a_l + a_l^\dagger) \Big) + \text{h.c.} \right) + \text{h.c.} \ , \end{aligned} \tag{4.95}$$

where h.c. denotes the Hermitian conjugate and $\phi_j = \phi + k z_j^{(eq)}$. Here, we introduced the *Lamb-Dicke parameters*

$$\eta_{jl} = k \chi_{jl} z_{l,0} \ , \tag{4.96}$$

which characterize the coupling strength between each ion-state transition and each motional-mode transition. These parameters are directly proportional to the ion's displacement relative to the wavelength of the driving field. In typical trapped-ion experiments, η_{jl} is significantly smaller than 1, typically ranging from 1/100 to 1/10, depending on factors such as the ion species, trap frequency, and the driving field's wavelength. This smallness of η_{jl} facilitates the development of a simplified interaction model, as we will demonstrate in the following section, but also inherently limits the speed of gate operations by reducing the effective coupling strength between spin and motion.

The full system, including the ions and the electromagnetic fields, is governed by the total Hamiltonian $H = H_0 + H_{\text{light-matter}}$, where H_0 represents the bare, non-interacting part (Eq. (4.91)) and $H_{\text{light-matter}}$ describes the coupling to the electromagnetic field (Eq. (4.143)). The dependence on the bare, non-interacting component H_0 can be removed by transforming to the interaction picture with respect to this Hamiltonian, yielding

$$H'_{\text{light-matter}} = H_{\text{light-matter, coupling}} + H_{\text{light-matter, Zeeman}} \ ,$$

with

$$\begin{aligned} H_{\text{light-matter, coupling}} = \sum_{j=1}^{N} \frac{\Omega_{eg}^{(j)}}{2} \Bigg(& e^{-i((\omega - \omega_{eg}^{(j)})t - \phi_j)} \prod_{l=1}^{M} \exp\Big(i\eta_{jl} (a_l e^{-i\nu_l t} + a_l^\dagger e^{i\nu_l t}) \Big) \\ & + e^{i((\omega + \omega_{eg}^{(j)})t - \phi_j)} \prod_{l=1}^{M} \exp\Big(-i\eta_{jl} (a_l e^{-i\nu_l t} + a_l^\dagger e^{i\nu_l t}) \Big) \Bigg) \sigma_+^{(j)} + \text{h.c.} \ , \end{aligned} \tag{4.97}$$

and

$$H_{\text{light-matter, Zeeman}} = \sum_{j=1}^{N} \sum_{m\in\{g,e\}} \frac{\Omega_{mm}^{(j)}}{2} \Bigg(e^{-i(\omega t-\phi_j)} \prod_{l=1}^{M} \exp\Big(i\eta_{jl}(a_l e^{-i\nu_l t} + a_l^\dagger e^{i\nu_l t})\Big) + e^{i(\omega t-\phi_j)} \prod_{l=1}^{M} \exp\Big(-i\eta_{jl}(a_l e^{-i\nu_l t} + a_l^\dagger e^{i\nu_l t})\Big)\Bigg) \Big|m^{(j)}\Big\rangle\Big\langle m^{(j)}\Big| + \text{h.c.}\,. \tag{4.98}$$

When the driving field frequency ω is close to the qubit resonance frequencies $\omega_{eg}^{(j)}$ of the qubits (and that these frequencies are similar), one can apply the RWA. This allows us to neglect terms oscillating at $\omega+\omega_{eg}^{(j)}$ and ω and retain only those terms with small detuning $\delta_j = \omega - \omega_{eg}^{(j)}$, resulting in

$$H'_{\text{light-matter}} = \sum_{j=1}^{N} \frac{\Omega_{eg}^{(j)}}{2} e^{-i(\delta_j t-\phi_j)} \prod_{l=1}^{M} \exp\Big(i\eta_{jl}(a_l e^{-i\nu_l t} + a_l^\dagger e^{i\nu_l t})\Big)\sigma_+^{(j)} \quad + \text{ h.c.}\,. \tag{4.99}$$

To simplify this expression, standard approaches work on a regime where the Lamb-Dicke parameters satisfy $\eta_{jl} \ll 1$, commonly referred to as the *Lamb-Dicke regime*. In this regime, the ion's displacement due to motion is much smaller than the wavelength of the driving field. As a result, the exponential terms in Eq. (4.99) can be approximated by their linear expansion, yielding

$$H'_{\text{light-matter}} = \sum_{j=1}^{N} \frac{\Omega_{eg}^{(j)}}{2} e^{-i(\delta_j t-\phi_j)} \prod_{l=1}^{M} \Big(\mathbb{I} + i\eta_{jl}(a_l e^{-i\nu_l t} + a_l^\dagger e^{i\nu_l t})\Big)\sigma_+^{(j)} \quad + \text{ h.c.}\,. \tag{4.100}$$

To further simplify Eq. (4.100), it is common to assume a regime where the driving fields are tuned in close resonance with the vibrational frequency of a single motional mode — and no others. In many practical scenarios, this mode is chosen to be the center-of-mass (COM) mode, as it corresponds to the motional mode with the highest spin-motion coupling η_{jC}, owing to its lowest frequency ν_C, which allows for faster gate operations. This approximation is based on an additional RWA, which requires the driving fields to satisfy $\eta_{jC}\Omega_{eg}^{(j)} \ll |\nu_C - \nu_l|$ for all $l \neq C$. In other words, the detuning frequencies $\delta_j \pm \nu_l$ of modes other than the selected one must be clearly off-resonant, and thus the associated terms oscillate rapidly, ensuring that their contributions average out over time.

Under this approximation, the interaction Hamiltonian simplifies to

$$
\begin{aligned}
H'_{\text{light-matter}}(t) = &\sum_{j=1}^{N} \frac{\left|\Omega_{eg}^{(j)}\right|}{2}\left(e^{-i(\delta_j t-\tilde{\phi}_j)}\sigma_+^{(j)} + e^{i(\delta_j t-\tilde{\phi}_j)}\sigma_-^{(j)}\right) \\
&+ i\sum_{j=1}^{N} \eta_{jC}\frac{\left|\Omega_{eg}^{(j)}\right|}{2}\left(a_C e^{-i((\nu_C+\delta_j)t-\tilde{\phi}_j)}\sigma_+^{(j)} - a_C^\dagger e^{i((\nu_C+\delta_j)t-\tilde{\phi}_j)}\sigma_-^{(j)}\right) \\
&+ i\sum_{j=1}^{N} \eta_{jC}\frac{\left|\Omega_{eg}^{(j)}\right|}{2}\left(a_C^\dagger e^{i((\nu_C-\delta_j)t+\tilde{\phi}_j)}\sigma_+^{(j)} - a_C e^{-i((\nu_C-\delta_j)t+\tilde{\phi}_j)}\sigma_-^{(j)}\right), \quad (4.101)
\end{aligned}
$$

where the phase in $\Omega_{eg}^{(j)} = \left|\Omega_{eg}^{(j)}\right| e^{i\varepsilon_j}$ has been absorbed into $\tilde{\phi}_j$, and creation and annihilation operators $a_C^\dagger$, a_C only refer to the chosen motional mode. In this form, the Hamiltonian $H'_{\text{light-matter}}$ describes three types of processes, each of which can be enhanced by setting the driving frequency ω to be in close resonance with specific transition frequencies. In particular,

- *Carrier transitions*: Setting the frequency of the driving field to $\omega = \omega_{eg}^{(j)} + \Delta_j$ results in a near-resonant Hamiltonian given by

$$
H'_{\text{carr}}(t) = \sum_{j=1}^{N} \frac{\left|\Omega_{eg}^{(j)}\right|}{2}\left(e^{-i(\Delta_j t-\tilde{\phi}_j)}\sigma_+^{(j)} + e^{i(\Delta_j t-\tilde{\phi}_j)}\sigma_-^{(j)}\right). \quad (4.102)
$$

- *Red sideband transitions*: Setting the frequency of the driving field to $\omega = \omega_{eg}^{(j)} - \nu_C + \Delta_j$ results in a near-resonant Hamiltonian given by

$$
H'_{\text{rs}}(t) = i\sum_{j=1}^{N} \eta_{jC}\frac{\left|\Omega_{eg}^{(j)}\right|}{2}\left(a_C e^{-i(\Delta_j t-\tilde{\phi}_j)}\sigma_+^{(j)} - a_C^\dagger e^{i(\Delta_j t-\tilde{\phi}_j)}\sigma_-^{(j)}\right). \quad (4.103)
$$

- *Blue sideband transitions*: Setting the frequency of the driving field to $\omega = \omega_{eg}^{(j)} + \nu_C + \Delta_j$ results in a near-resonant Hamiltonian given by

$$
H'_{\text{bs}}(t) = i\sum_{j=1}^{N} \eta_{jC}\frac{\left|\Omega_{eg}^{(j)}\right|}{2}\left(a_C^\dagger e^{-i(\Delta_j t-\tilde{\phi}_j)}\sigma_+^{(j)} - a_C e^{i(\Delta_j t-\tilde{\phi}_j)}\sigma_-^{(j)}\right). \quad (4.104)
$$

In all three cases, depicted in Fig. 4.3 for a single motional mode, Δ_j represents a small detuning from the characteristic transition frequency between the ground state $\left|g^{(j)}\right\rangle$ and excited state $\left|e^{(j)}\right\rangle$ of ion j. Carrier transitions, shown by the green arrow in Fig. 4.3, occur when the driving fields are slightly detuned from the qubit frequencies $\omega_{eg}^{(j)}$, affecting only the internal states of the ions without causing any motional transitions (Eq. (4.102)). In contrast, the red and blue sideband transitions (represented by the red and blue arrows in Fig. 4.3) couple the internal states of the ions to the motional mode. A red sideband

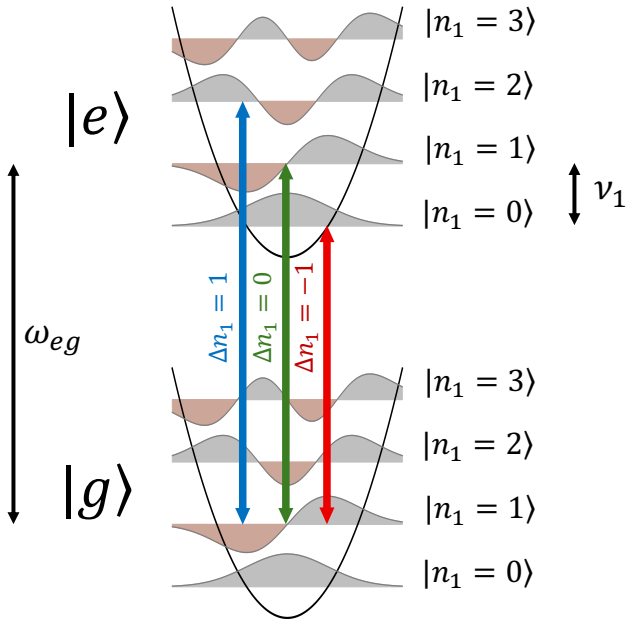

Figure 4.3: Schematic representation of sideband transitions for an ion, considering a single motional mode. Here, $|g\rangle$ and $|e\rangle$ represent the qubit's electronic states (with resonance frequency ω_{eg}), while $|n_1 = m\rangle$ denotes the Fock states of the motional mode 1 with occupation number m. Carrier transitions, indicated by the green arrow, do not change the phonon number ($\Delta n_1 = 0$), whereas red and blue correspond to the subtraction or addition of a motional phonon when starting in the state $|g\rangle$, leading to $\Delta n_1 = -1$ and $\Delta n_1 = 1$, respectively. A similar schematic can be extended to a multimode system, where each mode is treated as an independent harmonic oscillator.

transition corresponds to the removal of a phonon from the motional mode while simultaneously exciting the ion's internal state. Conversely, a blue sideband transition results in the excitation of the internal state and the addition of a phonon to the motional mode. Each of these transitions is accompanied by its Hermitian conjugate, which involves the reverse processes: de-excitation of the ion's internal state and either the loss or gain of phonons.

Entangling gates

The first proposals for generating two-qubit gates in trapped ion systems leveraged the idea of employing a shared motional mode to achieve spin-motion coupling, which can then be transformed, using the appropriate control scheme, into an effective interaction that entangles their internal electronic states.

Cirac-Zoller gate

The *Cirac–Zoller* (CZ) gate [31] was the first proposed method for entangling trapped ions. It operates via sequential red sideband transitions, governed by the interaction Hamiltonian in Eq. (4.103). A key feature of the scheme is the use of a single ground state and two excited states for each ion, which can be individually addressed using polarization-selective transitions. As a result, the standard ladder operators $\sigma_{\pm}^{(j)}$ are replaced by $\sigma_{\pm}^{(j,k)}$, with $k \in \{1, 2\}$ indexing the two excited states $\left|e^{(j,k)}\right\rangle$ of ion j.

In the standard configuration, one sets $\Delta_j = 0$ and $\tilde{\phi}_j = 3\pi/2$, and an appropriate polarization of the driving field. This enables a resonant red-sideband transition that selectively couples a specific ion j to one of its excited states k. Under these conditions, the interaction simplifies to a time-independent red-sideband Hamiltonian

$$H_{CZ}(t) = \eta_{jC}\frac{|\Omega_{eg}^{(j,k)}|}{2}\left(a_C\sigma_+^{(j,k)} + a_C^\dagger\sigma_-^{(j,k)}\right) . \tag{4.105}$$

Time evolution under this Hamiltonian for a duration $t = m\pi/(\eta_{jC}|\Omega_{eg}^{(j,k)}|)$, then yields the unitary operator

$$U_{CZ}(t) = \exp\Big(-i\frac{m\pi}{2}\left(a_C\sigma_+^{(j,k)} + a_C^\dagger\sigma_-^{(j,k)}\right)\Big) .$$

The operator inside the exponential,

$$A \equiv a_C\sigma_+^{(j,k)} + a_C^\dagger\sigma_-^{(j,k)} , \tag{4.106}$$

preserves the total excitation number $N_{ex} = a_C^\dagger a_C + \sigma_+^{(j,k)}\sigma_-^{(j,k)}$, since $[A, N_{ex}] = 0$. This conservation law restricts transitions to states sharing the same N_{ex}, coupling

$$\left|g^{(j)}, n+1\right\rangle \leftrightarrow \left|e^{(j,k)}, n\right\rangle . \tag{4.107}$$

As a result, the Hilbert space decomposes into a direct sum of invariant two-dimensional subspaces spanned by $\{\left|g^{(j)}, n+1\right\rangle, \left|e^{(j,k)}, n\right\rangle\}$, for $n \geq 0$, and a one-dimensional subspace $\mathcal{S}_0 = \text{span}\{\left|g^{(j)}, 0\right\rangle\}$, which is invariant and decoupled from the dynamics. Within each two-dimensional subspace, the operator A takes the matrix representation

$$A_n = \begin{pmatrix} 0 & \sqrt{n+1} \\ \sqrt{n+1} & 0 \end{pmatrix} = \sqrt{n+1}\sigma_x , \tag{4.108}$$

in the basis $\{\left|g^{(j)}, n+1\right\rangle, \left|e^{(j,k)}, n\right\rangle\}$. Therefore, the exponential operator reduces in each subspace to a spin rotation

$$U_n = \exp\left(-i\frac{m\pi}{2}A_n\right) = \cos\left(\frac{m\pi}{2}\sqrt{n+1}\right)\mathbb{I} - i\sin\left(\frac{m\pi}{2}\sqrt{n+1}\right)\sigma_x . \tag{4.109}$$

Combining all subspaces, the full evolution operator takes the form

$$U_{CZ}(t) = \mathbb{I}_{\mathcal{S}_0} \oplus \bigoplus_{n=0}^{\infty} U_n , \tag{4.110}$$

where $\mathbb{I}_{\mathcal{S}_0}$ is the identity on the decoupled subspace $\mathcal{S}_0$, and U_n acts nontrivially only within the two-dimensional subspace associated with the excitation manifold labeled by n.

In particular, for the lowest-lying excitation manifolds, the unitary acts as

$$U_{CZ}(t)\left|g^{(j)},1\right\rangle = \cos\left(\frac{m\pi}{2}\right)\left|g^{(j)},1\right\rangle - i\sin\left(\frac{m\pi}{2}\right)\left|e^{(j,k)},0\right\rangle \ , \tag{4.111a}$$

$$U_{CZ}(t)\left|e^{(j,k)},0\right\rangle = \cos\left(\frac{m\pi}{2}\right)\left|e^{(j,k)},0\right\rangle - i\sin\left(\frac{m\pi}{2}\right)\left|g^{(j)},1\right\rangle \ . \tag{4.111b}$$

Hence, if the motional mode is initialized in the ground state $|0\rangle$, Eqs. (4.111) fully capture the system's dynamics. This forms the basis of the three-stage protocol:

- *First stage*: A red-sideband π-pulse (*i.e.*, $m = 1$) is applied to ion $j = 1$, coupling its ground state to the excited state $k = 1$. This realizes the transformation

$$\left|g^{(1)},1\right\rangle \to -i\left|e^{(1,1)},0\right\rangle \ , \tag{4.112a}$$

$$\left|e^{(1,1)},0\right\rangle \to -i\left|g^{(1)},1\right\rangle \ , \tag{4.112b}$$

  imprinting a phase of $e^{i3\pi/2}$ while leaving other computational states unaffected.

- *Second stage*: A red-sideband 2π-pulse (*i.e.*, $m = 2$) is applied to ion $j = 2$, targeting its ground state and the second excited state $k = 2$. This induces the transformation

$$\left|g^{(2)},1\right\rangle \to -\left|g^{(2)},1\right\rangle \ , \tag{4.113a}$$

$$\left|e^{(2,2)},0\right\rangle \to -\left|e^{(2,2)},0\right\rangle \ . \tag{4.113b}$$

- *Third stage*: The initial red-sideband π-pulse is re-applied to ion $j = 1$, disentangling the motion and returning the system to the motional ground state.

Crucially, this sequence realizes a conditional gate involving the states $\left|g^{(j)}\right\rangle$ and $\left|e^{(j,1)}\right\rangle$, while the state $\left|e^{(j,2)}\right\rangle$ serves solely as an intermediate auxiliary state, with no net population transfer. When initialized in the motional ground state $|0\rangle$, the composite unitary enacts the following transformations

$$\begin{aligned}
\left|g^{(1)},g^{(2)},0\right\rangle &\to \left|g^{(1)},g^{(2)},0\right\rangle \to \left|g^{(1)},g^{(2)},0\right\rangle \to \left|g^{(1)},g^{(2)},0\right\rangle \ , \\
\left|g^{(1)},e^{(2,1)},0\right\rangle &\to \left|g^{(1)},e^{(2,1)},0\right\rangle \to \left|g^{(1)},e^{(2,1)},0\right\rangle \to \left|g^{(1)},e^{(2,1)},0\right\rangle \ , \\
\left|e^{(1,1)},g^{(2)},0\right\rangle &\to -i\left|g^{(1)},g^{(2)},1\right\rangle \to i\left|g^{(1)},g^{(2)},1\right\rangle \to \left|e^{(1,1)},g^{(2)},0\right\rangle \ , \\
\left|e^{(1,1)},e^{(2,1)},0\right\rangle &\to -i\left|g^{(1)},e^{(2,1)},1\right\rangle \to -i\left|g^{(1)},e^{(2,1)},1\right\rangle \to -\left|e^{(1,1)},e^{(2,1)},0\right\rangle \ ,
\end{aligned} \tag{4.114}$$

which corresponds to the action of a controlled-Z gate, where the state $\left|e^{(1,1)},e^{(2,1)},0\right\rangle$ acquires a -1 phase, while all other computational states remain invariant.

The fidelity of the CZ gate is highly sensitive to two experimental prerequisites: (1) near-perfect ground-state cooling of the shared motional mode ($\bar{n} \approx 0$) and (2) spatially resolved addressing of individual ions, as encoded in the position-dependent Rabi frequencies $\Omega_{eg}^{(jk)}$

of Eq. (4.103). Residual thermal phonons ($\bar{n} > 0$) populate off-resonant motional sidebands, corrupting the spin-motion coupling dynamics, while addressing errors—arising from laser intensity fluctuations or spatial beam inhomogeneity — introduce coherent phase miscalibrations and incoherent leakage via inter-ion crosstalk. These limitations underscore the necessity for protocols resilient to thermal and addressing imperfections.

Mølmer-Sørensen gate

The *Mølmer-Sørensen* (MS) gate [75] circumvents key CZ gate limitations by exploiting spin-motion coupling via bichromatic laser fields. Instead of sequential state transfers, the MS protocol drives simultaneous red and blue sideband transitions (Eqs. (4.103) and (4.104)) using two-frequency lasers, generating a spin-dependent optical dipole force. This force mediates effective spin-spin interactions through the ions' shared motional mode. The MS gate offers two key advantages over the CZ gate. First, its reliance on global laser illumination eliminates the need for individual ion addressing, enabling parallel entangling operations across entire ion chains. Second, the protocol exhibits thermal resilience: it remains functional under finite thermal phonon populations ($\bar{n} > 0$), as long as the system remains within the Lamb-Dicke regime. This tolerance arises from the gate's design, which employs closed motional phase-space trajectories to ensure disentanglement of spin and motion at the cycle's conclusion. To understand its mechanism, consider two electromagnetic fields propagating along the z-axis, characterized by driving frequencies $\omega_A = \omega_{eg}^{(j)} - \nu_C + \Delta_{Aj}$ and $\omega_B = \omega_{eg}^{(j)} + \nu_C + \Delta_{Bj}$, as well as phases $\tilde{\phi}_j^{(A)}$ and $\tilde{\phi}_j^{(B)}$ associated with each ion j. The frequency ω_A is tuned to drive the red sideband transitions, while ω_B drives the blue sideband transitions. The detunings are chosen to satisfy $\Delta_j^{(A)} = -\Delta_j^{(B)} \equiv \Delta_j$, and the Rabi frequencies of both fields are set equal for each ion, Ω_j. The resulting interaction Hamiltonian can be expressed as

$$H_{MS}(t) = \sum_{j=1}^{N} \eta_{jC} \frac{|\Omega_j|}{2} S_j(\tilde{\phi}_j^{(A)}, \tilde{\phi}_j^{(B)}) \Big(a_C e^{-i\Delta_j t} e^{i\frac{\tilde{\phi}_j^{(A)} - \tilde{\phi}_j^{(B)}}{2}} + a_C^\dagger e^{i\Delta_j t} e^{-i\frac{\tilde{\phi}_j^{(A)} - \tilde{\phi}_j^{(B)}}{2}} \Big) , \tag{4.115}$$

where the subscript eg in the Rabi frequency has been omitted for simplicity, as it is implicit, and the spin operator for ion j, S_j, depends on the choice of phases $\tilde{\phi}_j^{(A)}, \tilde{\phi}_j^{(B)}$ and is defined as

$$S_j(\tilde{\phi}_j^{(A)}, \tilde{\phi}_j^{(B)}) = i e^{i\frac{\tilde{\phi}_j^{(A)} + \tilde{\phi}_j^{(B)}}{2}} \sigma_+^{(j)} - i e^{-i\frac{\tilde{\phi}_j^{(A)} + \tilde{\phi}_j^{(B)}}{2}} \sigma_-^{(j)} . \tag{4.116}$$

Crucially, the phases $\tilde{\phi}_j^{(A)}, \tilde{\phi}_j^{(B)}$ in $S_j(\tilde{\phi}_j^{(A)}, \tilde{\phi}_j^{(B)})$ can be adjusted to select any qubit operator within the x-y plane of the Bloch sphere. For instance, choosing $\tilde{\phi}_j^{(A)} = \tilde{\phi}_j^{(B)} = \pi$ results in the convenient operator $S_j(\pi, \pi) = \sigma_y^{(j)}$, which is often used for practical implementations, with the Hamiltonian simplifying to

$$H_{MS}(t) = \sum_{j=1}^{N} \eta_{jC} \frac{|\Omega_j|}{2} \sigma_y^{(j)} \Big(a_C e^{-i\Delta_j t} + a_C^\dagger e^{i\Delta_j t} \Big) . \tag{4.117}$$

A key feature of the Hamiltonian $H_{MS}(t)$ in Eq. (4.115) is the separation of spin and motional operators into distinct, factorizable components. This structure enables precise control over the spin-motion coupling via the temporal evolution of the driving field. During the dynamics, the interaction entangles the electronic states of the ions with the shared motional states. However, by carefully tuning the parameters of the driving field, the dynamics can be designed such that the spin and motional degrees of freedom become disentangled at the end of the interaction, leaving the motional mode in its original state while inducing entanglement solely between the electronic states.

This behavior becomes apparent when constructing the time-evolution operator $U(t)$. Due to the commutativity properties of the operators in Eq. (4.115), the Magnus expansion provides an exact analytical expression for $U(t)$, requiring only the first two terms of the expansion. Explicitly, $U(t) = \exp(K_1(t) + K_2(t))$, where $K_1(t)$ and $K_2(t)$ correspond to the first and second terms in Eq. (2.54). Furthermore, since $[K_1(t), K_1(t)] = 0$, $U_{MS}(t)$ can be expressed in closed form as

$$U_{MS}(t) = \exp\left(\sum_j S_j \otimes \left(\alpha_j(t) a_C^\dagger - \alpha_j^*(t) a_C\right)\right) \exp\left(-i \sum_{jk} \Xi_{jk}(t) S_j S_k \otimes \mathbb{I}\right) , \quad (4.118)$$

where the time-dependent coefficients are given by

$$\alpha_j(t) = \frac{\eta_{jC}|\Omega_j|}{2\Delta_j} \left(e^{i\Delta_j t} - 1\right) e^{-i\frac{\tilde{\phi}_j^{(A)} - \tilde{\phi}_j^{(B)}}{2}} , \quad (4.119)$$

$$\Xi_{jk}(t) = \frac{\eta_{jC}\eta_{kC}|\Omega_j||\Omega_k|}{4\Delta_k} \left(\frac{\sin(\Delta_j t + \xi_{jk}) - \sin(\xi_{jk})}{\Delta_j} - \frac{\sin((\Delta_k - \Delta_j)t + \xi_{jk}) - \sin(\xi_{jk})}{\Delta_k - \Delta_j}\right) , \quad (4.120)$$

and $\xi_{jk} = (\tilde{\phi}_j^{(A)} - \tilde{\phi}_k^{(A)} - \tilde{\phi}_j^{(B)} + \tilde{\phi}_k^{(B)})/2$. Notably, the tensor product in Eq. (4.118) explicitly distinguishes between the spin and motional components, but it should be understood between any operators acting on subsystems with a different Hilbert space.

The structure of $U_{MS}(t)$ provides insight into the underlying dynamics. The first exponential encodes spin-dependent displacements in the motional phase space, governed by the time-dependent functions $\alpha_j(t)$. These displacements evolve along circular arcs in the complex plane, with each trajectory given by

$$\alpha_j(t) = R_j e^{-i\phi_j} \left(e^{i\theta_j(t)} - 1\right) , \quad (4.121)$$

where $R_j = \eta_{jC}|\Omega_j|/2\Delta_j$ sets the radius of the trajectory, $\theta_j(t) = \Delta_j t$ is the accumulated phase, and ϕ_j determines the direction of rotation in the complex plane.

At $t = 0$, all displacements vanish ($\alpha_j(0) = 0$), and the system starts at the origin of phase space. As time progresses, the displacement traces a circular arc centered at $C_j = \pm\alpha_j(\pi/\Delta_j)/2$, sweeping out a loop. After a full rotation (*i.e.*, when $\theta_j(t) = 2\pi q$, or equivalently $t = 2\pi q/\Delta_j$ for integer q) the trajectory returns to the origin. These specific

times mark points where the spin and motion naturally disentangle, as the motional state closes its loop and the corresponding displacement vanishes.

The second exponential in $U_{MS}(t)$ captures the spin–spin entanglement accumulated during this evolution. It arises from the time-dependent coefficients $\Xi_{jk}(t)$, which reflect the area swept out by the relative motion of the displaced trajectories. In the case of a single motional mode ($j = k$), the phase simplifies to

$$\Xi_{jj}(t) = -R_j^2 \left(t - \frac{\sin(\theta_j(t))}{\Delta_j} \right) = \frac{-1}{2} \int_0^t ds |\alpha_j(s)|^2 \ , \tag{4.122}$$

indicating that mode j acquires a *geometric* phase proportional to the area enclosed by the trajectory in phase space. Crucially, this phase depends only on extent of the trajectory in phase space and remains independent of both the traversal rate and the specific path shape. Moreover, since the term $\Xi_{jj}(t)$ appears twice in the spin–spin interaction (Eq. (4.118)), the total contribution effectively corresponds to the full enclosed area.

When multiple motional modes contribute, the structure of the accumulated phase becomes richer. The cross-mode terms $\Xi_{jk}(t)$ for $j \neq k$ arise from the relative geometry between the spin-dependent displacements. These can be interpreted as the oriented area swept in the mixed plane defined by the pair $(x_j(t), y_k(t))$, where $x_j(t) = \mathfrak{Re}[\alpha_j(t)]$ and $y_k(t) = \mathfrak{Im}[\alpha_j(t)]$. Explicitly, the cross-phase (Eq. (4.120)) can be written as

$$\Xi_{jk}(t) = \frac{1}{2} \int_{t_0}^t (x_j(s)\dot{y}_k(s) - \dot{x}_j(s)y_k(s))\, ds = \frac{1}{2} \oint_{\mathcal{C}_{jk}} (x_j \ dy_k - y_k \ dx_j) \ ,$$

where $\mathcal{C}_{jk}$ is the closed contour formed by the trajectories in this mixed phase space. This contour integral gives the signed symplectic area enclosed by the pair of displacements. Although the integrand is antisymmetric under $j \leftrightarrow k$, the orientation of the integration contour also reverses, leading to a cancellation of signs and ensuring that $\Xi_{jk}(t) = \Xi_{kj}(t)$, consistent with the symmetric nature of the spin–spin coupling in Eq. (4.118). Unlike the single-mode case, where the phase depends only on the area traced by a single trajectory, the cross-terms involve relative geometry between displacements, reflecting the interference and correlation between motional modes. Nevertheless, these phases remain geometric in character, as they depend solely on the shape and orientation of the trajectories in phase space, and not on their rate of traversal.

Thus, the explicit form of $U_{MS}(t)$ enables precise control over the gate's operation by imposing conditions on the driving field parameters (*i.e.*, Rabi frequencies, phases and detunings) and gate duration. To illustrate this, consider the standard configuration where the laser phases are set to $\tilde{\phi}_j^{(A)} = \tilde{\phi}_j^{(B)} = \pi$. In this case, the spin operators reduce to $S_j(\pi, \pi) = \sigma_y^{(j)}$, resulting in a collective $Y - Y$ coupling across all ion pairs.

Assume further that the center-of-mass mode serves as the bus, the detunings are uniform across the chain ($\Delta_j = \Delta$) — as is typical for a single-species ion chain — the Rabi frequencies are uniform ($\Omega_j = \Omega$), and the phases coincide ($\tilde{\phi}_j^{(A)} = \tilde{\phi}_j^{(B)}$ for all j). Under these

conditions, choosing a gate time $T = 2\pi/\Delta$ ensures complete spin-motion disentanglement at the end of the evolution, resulting in a purely spin-dependent transformation

$$U_{MS}\left(\frac{2\pi}{\Delta}\right) = \exp\left(-i\Psi \sum_{jk} S_j S_k\right) \otimes \mathbb{I}\ , \tag{4.123}$$

where the accumulated phase is $\Psi = \frac{-\pi\eta_C^2|\Omega|^2}{2\Delta^2}$. In the specific case where the detuning is set to $\Delta = 2\eta_C\Omega$, the geometric phase simplifies to $\Psi = -\pi/8$, which leads to the unitary gate $U_{MS} = \exp\left(i\frac{\pi}{4}\sum_{j<k} S_j S_k\right)$ that creates Bell states from initially unentangled ions.

This analysis demonstrates the generation of entanglement in trapped ions through a dynamical process mediated by electromagnetic radiation. The process relies on phonon-mediated interactions to couple the ions' electronic states with their shared motional mode. Specifically, the interaction induces state-dependent motion, which accumulates a conditional geometric phase, ultimately creating entanglement in the ions' electronic degrees of freedom. In both the CZ and MS protocols, the coupling is achieved through the photon momentum $\|\vec{p}\| = E/c = \omega/c = \|\vec{k}\|$ of the oscillating electromagnetic field, which must be sufficiently large to implement the quantum gate within the coherence times of the ions. However, the energy splittings between the electronic ground states of trapped ions typically fall in the microwave and radio frequency range, where the photon momentum produces a negligible coupling strength between the spin and motional states. As a result, microwave radiation alone is not sufficient for effective coupling.

To overcome this limitation, conventional implementations of the MS scheme involve a third state with a much larger energy difference, which serves as an intermediate state between the two qubit states. Transitions from the qubit states to this third state necessitate higher frequencies, allowing the use of laser pulses with stronger photon momenta, thereby enabling efficient coupling.

Magnetic field gradient

An alternative approach to spin-motion coupling in trapped-ion systems avoids the challenges associated with photon-momentum gates by utilizing a *static magnetic field gradient*. This method exploits the linear Zeeman effect (see Eqs. (4.73) and (4.77)) [129]. Essentially, instead of relying on the photon momentum term $kz_j\sigma_+$, this scheme employs a magnetic field gradient $\frac{\partial B(z)}{\partial z}$ to generate an interaction of the form $\frac{\partial B(z)}{\partial z} z_j\sigma_z$. This mechanism achieves spin-motion coupling in a manner analogous to photon-momentum gates but replaces the optical interaction with a magnetic one, offering a distinct set of advantages and trade-offs.

To implement this approach, a position-dependent magnetic field $B(z)$ is applied. Near the origin at $z = 0$, the magnetic field at the axial position z_j of ion j can be approximated

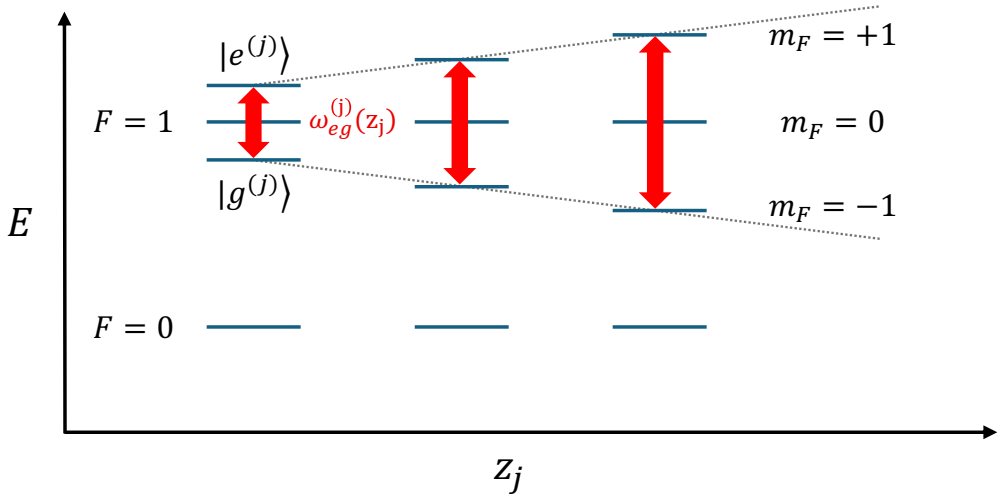

Figure 4.4: Energy diagram of an ion in a magnetic field of the form given in Eq. (4.124), which varies linearly with position z_j. Here, $\omega_{eg}^{(j)}$ denotes the resonance frequency between the qubit levels $\left|g^{(j)}\right\rangle = \left|^2S_{1/2}^{(j)}, F = 1, m_F = -1\right\rangle$ and $\left|e^{(j)}\right\rangle = \left|^2S_{1/2}^{(j)}, F = 1, m_F = 1\right\rangle$, which are encoded in magnetically sensitive states with magnetic quantum number $m_F = \pm 1$ and experience a Zeeman shift.

by a first-order Taylor expansion

$$B(z_j) = B(z = 0) + \partial_z B\Big|_{z=0} z_j \ . \tag{4.124}$$

Unlike photon-momentum mediated gates — which drive transitions between qubit states via the $\sigma_\pm$ operators — the position-dependent magnetic field modifies the resonance frequency $\omega_{eg}^{(j)}(z_j)$ between the electronic states $\left|g^{(j)}\right\rangle$ and $\left|e^{(j)}\right\rangle$ through the σ_z operators. In particular, using the Zeeman splitting relation (Eq. (4.77)), one obtains

$$\omega_{eg}^{(j)}(z_j) = \omega_{eg}^{(j)} + \frac{\gamma_s}{2} B(z = 0)\sigma_z^{(j)} + \frac{\gamma_s}{2}\partial_z B\Big|_{z=0} z_j \sigma_z^{(j)} \ , \tag{4.125}$$

where $\omega_{eg}^{(j)}$ on the right-hand side is the bare resonance frequency (without a magnetic field). The term $\frac{\gamma_s}{2}\partial_z B\Big|_{z=0} z_j\sigma_z^{(j)}$ introduces a spin- and position-dependent shift to the resonance frequency, as illustrated in Fig. 4.4. This gradient-induced frequency shift generates a spin-dependent dipole force along the axial z-direction. For ion j, the force F derived from the Zeeman Hamiltonian $H_Z(z_j)$ is

$$F = -\frac{\partial H_Z(z_j)}{\partial z_j} = -\frac{\gamma_s}{2}\partial_z B\Big|_{z=0} \sigma_z^{(j)} \ . \tag{4.126}$$

Since the force depends on the spin state, ions in $\left|e^{(j)}\right\rangle$ and $\left|g^{(j)}\right\rangle$ experience equal and opposite forces (see Fig. 4.5(a)). This force displaces the equilibrium position of the harmonic oscillator in a direction determined by the ion's electronic state. To analyze this displacement, consider the total potential $V(z_j)$ governing the ion's motion, which com-

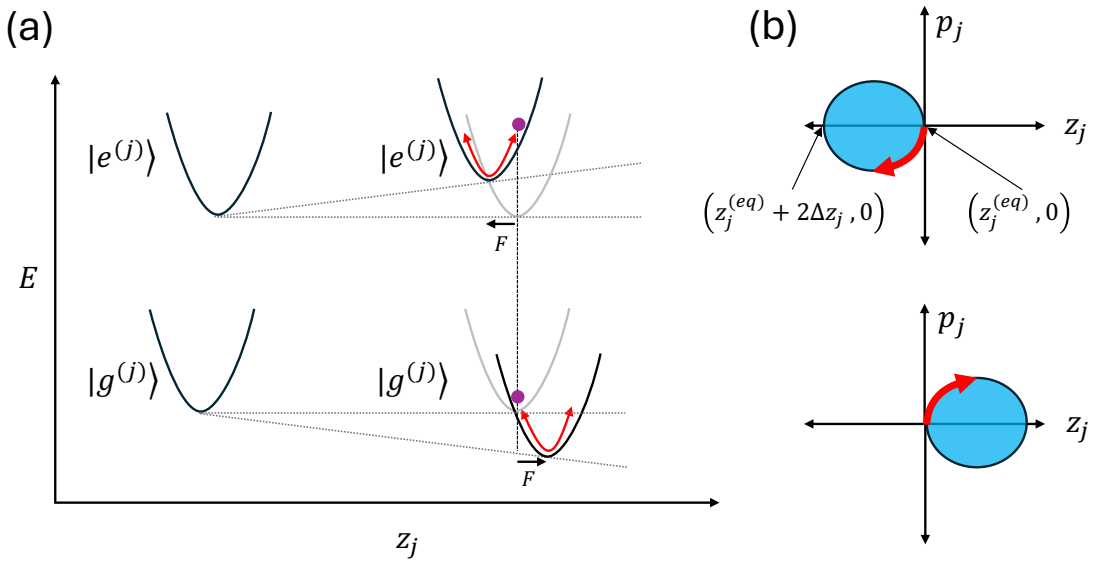

Figure 4.5: Panel (a) illustrates the combined effects of the harmonic axial trapping potential and the Zeeman energy shifts. For an ion in state $\left|e^{(j)}\right\rangle$, the Zeeman energy increases linearly with the z-coordinate, while for an ion in state $\left|g^{(j)}\right\rangle$ it decreases linearly. This magnetic field gradient produces an effective force F that shifts the ion's equilibrium position $z_j^{(eq)}$; the magnitude and direction of this shift depend on the ion's electronic state. As a result, the ion is set into an oscillatory motion (indicated by the red arrows). In Panel (b), this motion is depicted as a phase-space trajectory that reaches a maximum deviation of $2\Delta z_j$ from $z_j^{(eq)}$, with the specific orientation of the trajectory determined by the electronic state.

bines harmonic confinement from the trap and the linear Zeeman potential

$$V(z_j) = V_0 + \frac{1}{2}m\nu_z^2\left(z_j - z_j^{(eq)}\right)^2 - Fz_j\ , \tag{4.127}$$

where V_0 is a constant offset and $z_j^{(eq)}$ is the equilibrium position of ion j in the absence of the magnetic force. Minimizing $V(z_j)$ (*i.e.*, solving $\frac{\partial V}{\partial z_j} = 0$) yields the shifted equilibrium position

$$z_j^{(eq)'} = z_j^{(eq)} + \frac{F}{m\nu_z^2}\ , \tag{4.128}$$

with the *direction* of the shift $\Delta z_j = z_j^{(eq)'} - z_j^{(eq)} = \frac{F}{m\nu_z^2}$ determined by the spin state via $\sigma_z^{(j)}$ (see Fig. 4.5(a)). This shift displaces the ion from its original equilibrium, driving an oscillatory motion analogous to that of a harmonic oscillator under an external force. The dynamics of this motion are governed by Heisenberg's equations of motion (Eq. (B.10)) with $H_{\text{bare}} = p_j^2/2m + V(z_j)$, yielding

$$\dot{z}_j = i[H_{\text{bare}}, z_j] = \frac{p_j(t)}{m}\ , \tag{4.129a}$$

$$\dot{p}_j = i[H_{\text{bare}}, p_j] = -m\nu_z^2\left(z_j(t) - z_j^{(eq)}\right) - \frac{\gamma_s}{2}\partial_z B\Big|_{z=0}\sigma_z^{(j)}\ . \tag{4.129b}$$

For an ion initially at its unperturbed equilibrium ($z_j(0) = z_j^{(eq)}$, $p_j(0) = 0$), the solution for its displacement and momentum are given by

$$\xi_j(t) = z_j(t) - z_j^{(eq)} = -\Delta z_j \left(\cos(\nu_z t) - 1\right) \ , \tag{4.130a}$$

$$p_j(t) = m\nu_z \Delta z_j \sin(\nu_z t) \ , \tag{4.130b}$$

where the time-dependent displacement $\xi_j(t)$ from the equilibrium position $z_j^{(eq)}$ describes a trajectory in phase space that is elliptical in shape, with the orientation determined by the ion's spin state (see Fig. 4.5(b)).

Overall thus, the magnetic field gradient effectively "kicks" the ion, initiating a motional oscillation while simultaneously modifying the energy splitting between its electronic states. Crucially, the resulting phase-space trajectories differ for each spin state, leading to a conditional geometric phase — an effect analogous to that in photon-momentum-mediated gates. While this phase remains unobservable in a single isolated ion, it becomes a critical resource in multi-ion systems, where differential phase accumulation between ions enables spin-spin entanglement.

In an ion chain, this mechanism couples not to individual ion motion but to collective vibrational modes, which arise due to Coulomb interactions. To describe this, we express the position of each ion as $z_j = z_j^{(eq)} + \xi_j$, where $z_j^{(eq)}$ is the equilibrium position and ξ_j is the displacement from equilibrium. The total Hamiltonian in the laboratory frame is then

$$H_{MF} = \sum_{j=1}^{N} \frac{\tilde{\omega}_{eg}^{(j)}}{2} \sigma_z^{(j)} + \sum_{k=1}^{M} \nu_k a_k^\dagger a_k + \frac{\gamma_s}{2} \partial_z B\Big|_{z=0} \sum_{j=1}^{N} \xi_j \sigma_z^{(j)} \ . \tag{4.131}$$

where we introduced the modified resonance frequency

$$\tilde{\omega}_{eg}^{(j)} = \omega_{eg}^{(j)} + \gamma_s \left(B(z=0) + z_j^{(eq)} \partial_z B\Big|_{z=0} \right) \ , \tag{4.132}$$

that incorporates the Zeeman shift due to the magnetic field offset $B(z = 0)$ and increases linearly with the static equilibrium positions $z_j^{(eq)}$ of the ions (see Fig. 4.4).

To simplify the analysis, we express the displacements ξ_j in terms of normal modes, which diagonalize the ion chain's vibrational motion (see Eq. (4.94)). Substituting this into the Hamiltonian, we obtain

$$H_{MF} = \sum_{j=1}^{N} \frac{\tilde{\omega}_{eg}^{(j)}}{2} \sigma_z^{(j)} + \sum_{k=1}^{M} \nu_k a_k^\dagger a_k + \sum_{j,l} \nu_l \eta_{jl} (a_l + a_l^\dagger) \sigma_z^{(j)} \ , \tag{4.133}$$

This expression makes explicit the spin-motion coupling, which is characterized by an effective *Lamb-Dicke parameter*

$$\eta_{jl} = \frac{\gamma_s \chi_{jl} z_{l,0}}{2\nu_l} \partial_z B\Big|_{z=0} \ , \tag{4.134}$$

where χ_{jl} describes the mode participation of the ions, $z_{l,0}$ represents zero-point motion

amplitude of mode l, and ν_l its frequency.

Unlike laser-based schemes, where the effective coupling η_{jl} is primarily determined by the photon momentum $\|\vec{k}\|$, in the case of magnetic field gradients, the coupling strength depends on the gradient's magnitude and inversely on the trapping frequency ν. Strong spin-motion coupling with long-wavelength radiation can be achieved by either reducing ν, which is undesirable as it increases motional heating that complicates gate implementation [103], or by increasing the magnetic field gradient. While the latter approach is more viable, achieving gradient strengths that result in coupling η_{jl} comparable to laser-based schemes remains a practical challenge [94, 130].

Since the critical ingredient for entangling gate implementation is the existence of a spin-motion coupling term in the Hamiltonian, H_{MF} provides a pathway for realizing entangling gates, such as the MS scheme. However, deriving an expression analogous to that of laser-based gates from Eq. (4.133) requires additional steps.

In the absence of the spin-motion coupling term $(a_l+a_l^\dagger)\sigma_z^{(j)}$ in Eq. (4.133), the Hamiltonian H_{MS} reduces to a simpler form, consisting of independent qubits with energy splittings $\tilde{\omega}_{eg}^{(j)}$, and uncoupled harmonic oscillators with energy splittings ν_l. In this case, the motional states correspond to the Fock states $|n_l\rangle$ of a standard harmonic oscillator, which serve as the eigenstates of the motional component of the Hamiltonian. However, the inclusion of the spin-motion coupling term fundamentally alters this picture. The motional and spin degrees of freedom become inherently entangled, making it impossible to treat them as independent. As a result, the eigenbasis of the full Hamiltonian can no longer be expressed as a direct product of separate spin and motional states. Instead, it becomes necessary to adopt a transformed basis that decouples these degrees of freedom. To address this, we employ a transformation known as the polaron transformation, defined by the unitary operator [129]

$$U_P = \exp\left(\sum_{j,l}\left(a_l^\dagger - a_l\right)\eta_{jl}\sigma_z^{(j)}\right) . \tag{4.135}$$

This unitary operator U_P corresponds to a displacement operator for each motional mode l, $D_l\left(\sum_j \eta_{jl}\sigma_z^{(j)}\right)$, which shifts the motional states in phase space by an amount $\sum_{j,l}\eta_{jl}\sigma_z^{(j)}$ along the position axis while leaving the momentum unaffected.

In the frame defined by U_P, the Hamiltonian becomes diagonal

$$\tilde{H}_{MF} = U_P H_{MF} U_P^\dagger = \sum_{j=1}^{N}\frac{\tilde{\omega}_{eg}^{(j)}}{2}\sigma_z^{(j)} + \sum_{l=1}^{M}\nu_l a_l^\dagger a_l + \sum_{j,k,l}\nu_l\eta_{jl}\eta_{kl}\sigma_z^{(j)}\sigma_z^{(k)} , \tag{4.136}$$

where the creation and annihilation operators transform as

$$a_l \to a_l - \sum_j \eta_{jl}\sigma_z^{(j)} \equiv \tilde{a}_l , \qquad a_l^\dagger \to a_l^\dagger - \sum_j \eta_{jl}\sigma_z^{(j)} \equiv \tilde{a}_l^\dagger . \tag{4.137}$$

From these transformations, it follows that the original Hamiltonian can be rewritten in terms of the transformed operators $\tilde{a}_l^\dagger$ and $\tilde{a}$ as

$$H_{MF} = \sum_{j=1}^{N} \frac{\tilde{\omega}_{eg}^{(j)}}{2} \sigma_z^{(j)} + \sum_l \nu_l \tilde{a}_l^\dagger \tilde{a}_l - \sum_{j,k,l} \nu_l \eta_{jl} \eta_{kl} \sigma_z^{(j)} \sigma_z^{(k)} \ , \tag{4.138}$$

demonstrating that the motional component of the Hamiltonian corresponds to a harmonic oscillator in the new operator's basis. Consequently, the transformed operators $\tilde{a}_l^\dagger$ and $\tilde{a}_l$ provide a picture in which the original Hamiltonian exhibits the form of a harmonic oscillator with an energy shift $\mathfrak{E}$ that depends on the instantaneous electronic states of the ions. Specifically, for an ion chain in the electronic state $\left|s^{(1)} \cdots s^{(n)}\right\rangle$, where $s^{(j)} \in \{g^{(j)}, e^{(j)}\}$, the energy shift is given by

$$\mathfrak{E} = \sum_{j,k,l} (-1)^{s_j + s_k + 1} \nu_l \eta_{jl} \eta_{kl} \ , \tag{4.139}$$

where $s_p = 0$ if $s^{(p)} = e^{(p)}$ and $s_p = 1$ if $s^{(p)} = g^{(p)}$.

In this transformed picture, the motional component of the eigenstates of H_{MF} are Fock states with respect to the transformed ladder operators. These states are defined by the condition $\tilde{a}_l \left|\tilde{n}_l = 0\right\rangle = 0$, where $\left|\tilde{n}_l = 0\right\rangle$ represents the vacuum state in the transformed basis. Crucially, these Fock states in the transformed basis do not directly correspond to the Fock states of the original motional oscillators. This arises from the spin-motion coupling present in the original Hamiltonian. In the original basis, the annihilation operator a_l does not annihilate the state $\left|\tilde{n}_l = 0\right\rangle$, *i.e.* $a_l \left|\tilde{n}_l = 0\right\rangle \neq 0$ (but $a_l \left|n_l = 0\right\rangle = 0$). Using Eq. (4.137), we find instead

$$a_l \left|\tilde{n}_l = 0\right\rangle = \sum_j \eta_{jl} \sigma_z^{(j)} \left|\tilde{n}_l = 0\right\rangle \ . \tag{4.140}$$

This equation reveals that the state $\left|\tilde{n}_l = 0\right\rangle$ in the transformed basis acts as an eigenstate of the original annihilation operator a_l. This implies that $\left|\tilde{n}_l = 0\right\rangle$ corresponds to a coherent state $\left|\sum_j \eta_{jl} \sigma_z^{(j)}\right\rangle$ in the original Fock state basis, which is, indeed, a direct consequence of the polaron transformation. As previously discussed, the polaron transformation acts as a displacement operator on the motional states. Therefore, it is expected that Fock states in the transformed basis will correspond to coherent states in the original basis. This relationship holds more generally, as any excited Fock state in the transformed frame, $\left|\tilde{n}_l\right\rangle$ — and not only the vaccum — corresponds to a displaced state in the original basis, $D_l\left(\sum_j \eta_{jl} \sigma_z^{(j)}\right) \left|n_l\right\rangle$.

Another consequence of the action of the displacement manifests in the expected position of the ions. Specifically, the displacement of ion j depends on the electronic state of the whole chain. Thus, when the ions are in the electronic state $\left|s^{(1)} \cdots s^{(n)}\right\rangle$, where $s^{(j)} \in \{g^{(j)}, e^{(j)}\}$, the displacement of ion j relative to its equilibrium position in the absence of the magnetic

field gradient is given by

$$\left\langle s^{(1)}\cdots s^{(n)}\right|\tilde{\xi}_j-\xi_j\left|s^{(1)}\cdots s^{(n)}\right\rangle=2\sum_{l=1}^{M}\sum_{p=1}^{N}(-1)^{s_p+1}z_{l,0}\chi_{jl}\eta_{pl}\ , \tag{4.141}$$

where $s_p = 0$ if $s^{(p)} = e^{(p)}$ and $s_p = 1$ if $s^{(p)} = g^{(p)}$. Thus, for example, when all ions are the ground state $\left|g^{(1)}\cdots g^{(n)}\right\rangle$, the relative displacement of ion j is given by $2\sum_{l=1}^{M}\sum_{p=1}^{N} z_{l,0}\chi_{jl}\eta_{pl}$, while for all ions in the excited state $\left|e^{(1)}\cdots e^{(n)}\right\rangle$, the displacement is in the opposite direction, $-2\sum_{l=1}^{M}\sum_{p=1}^{N} z_{l,0}\chi_{jl}\eta_{pl}$.

This provides a complete picture of the transformed basis. In the new frame, the Hamiltonian H_{MS} can be understood as describing harmonic oscillators with an energy shift $\mathfrak{E}$ that depends explicitly on the spin states of the ions. Moreover, the motional state associated with each oscillator corresponds to a coherent state displaced in position space by an amount $2\sum_{l=1}^{M}\sum_{p=1}^{N}(-1)^{s_p+1}z_{l,0}\chi_{jl}\eta_{pl}$ depending on the collective spin state of the ion chain. This result builds upon the observations in Fig. 4.5(a), revealing that the displaced oscillators and corresponding energy shifts are now influenced by the collective spin state of the ion chain, rather than the individual spin states of each ion.

Another significant feature of Eq. (4.136) is the final term, $\sum_{j,k,l}\nu_l\eta_{jl}\eta_{kl}\sigma_z^{(j)}\sigma_z^{(k)}$, which represents a *spin-spin entangling interaction*. This term, absent in single-ion systems, emerges naturally from the interaction with the magnetic field gradient and provides a promising mechanism for generating entanglement [130]. Notably, this approach is particularly attractive because it relies solely on the magnetic field gradient, potentially eliminating the need for external electromagnetic fields [95]. While experimental demonstrations have successfully utilized this term to generate entanglement in ion chains [131], a significant drawback is the relatively weak coupling strength between ion pairs. This coupling strength is determined by the sum $\sum_l \nu_l\eta_{jl}\eta_{kl}$, which exhibits a quadratic dependence on the magnetic field gradient $\partial_z B\Big|_{z=0}$ and inverse dependence on the trapping frequency ν, (*i.e.*, $\propto\left(\partial_z B\Big|_{z=0}\right)^2/\nu$). Consequently, achieving fast gate operation times requires sufficiently strong magnetic field gradients. To date, generating entangled states using this approach within competitive timescales compared to entangling gates based on photon momentum kicks has proven challenging due to limitations in achieving the necessary magnetic field gradients [131].

For this reason, in most practical implementations, the spin-spin entangling term

$$\sum_{j,k,l}\nu_l\eta_{jl}\eta_{kl}\sigma_z^{(j)}\sigma_z^{(k)} \tag{4.142}$$

is typically treated as a perturbative contribution. Instead, entangling gates are implemented using sideband transitions, analogous to laser-based gates. In this context, the entangling term is often regarded as an error source, which can be mitigated using techniques such as dynamical decoupling or pulse shaping [95, 131].

To enable such gates, the system is subjected to a magnetic field gradient in the presence of an additional oscillating electromagnetic field of frequency ω_M, tuned close to the qubit resonance frequencies $\omega_{eg}^{(j)}$. Crucially, this oscillating field can operate at low frequencies (and thus long wavelengths), allowing the long-wavelength approximation to be employed. Under this approximation, terms like $e^{i\vec{k}_M\cdot\vec{r}}$, which would otherwise introduce photon momentum effects, can be safely neglected [130]. This simplification facilitates the design of gate protocols while maintaining compatibility with the magnetic gradient coupling mechanism.

Adapting the expression from Eq. (4.143), the interaction Hamiltonian in the presence of this field is given by

$$H_{\text{light-matter}} = \sum_{j=1}^{N}\left(\frac{\Omega_{eg}^{(j)}}{2}\sigma_+^{(j)} + \frac{\Omega_{gg}^{(j)}}{2}\left|g^{(j)}\right\rangle\!\left\langle g^{(j)}\right| + \frac{\Omega_{ee}^{(j)}}{2}\left|e^{(j)}\right\rangle\!\left\langle e^{(j)}\right|\right)\cdot\left(e^{-i(\omega t-\phi)} + e^{i(\omega t-\phi)}\right) + \text{h.c.}\,, \tag{4.143}$$

where the states $\left|g^{(j)}\right\rangle$ and $\left|e^{(j)}\right\rangle$ are in the original frame. In the frame of the polaron transformation, this interaction Hamiltonian takes the form

$$\tilde{H}_{\text{light-matter}} = \sum_{j=1}^{N}\left(\frac{\Omega_{eg}^{(j)}}{2}\sigma_+^{(j)}e^{2\sum_l(a_l^\dagger - a_l)\eta_{jl}} + \frac{\Omega_{gg}^{(j)}}{2}\left|g^{(j)}\right\rangle\!\left\langle g^{(j)}\right| + \frac{\Omega_{ee}^{(j)}}{2}\left|e^{(j)}\right\rangle\!\left\langle e^{(j)}\right|\right) \cdot\left(e^{-i(\omega_M t-\phi)} + e^{i(\omega_M t-\phi)})\right) + \text{h.c.}\,. \tag{4.144}$$

The complete Hamiltonian is therefore composed of $\tilde{H}_{MS} + \tilde{H}_{\text{light-matter}}$. Here, the entangling term in $\tilde{H}_{MS}$ is treated as negligible, such that $\sum_{j,k,l}\nu_l\eta_{jl}\eta_{kl}\sigma_z^{(j)}\sigma_z^{(k)} \approx 0$. To isolate the effects of the interaction, we move to the interaction picture with respect to $\tilde{H}_{MS}$. Applying the rotating wave approximation (RWA) to neglect terms oscillating at frequencies ω_M and $\omega_M + \omega_{eg}^{(j)}$, the interaction Hamiltonian simplifies to

$$\tilde{H}'_{\text{light-matter}} = \sum_{j=1}^{N}\left(\frac{\Omega_{eg}^{(j)}}{2}e^{i(\delta_j t+\phi)}e^{2\sum_l(a_l^\dagger \exp(i\nu_l t) - a_l\exp(-i\nu_l t))\eta_{jl}}\sigma_+^{(j)}\right) + \text{h.c.}\,, \tag{4.145}$$

with $\delta_j = \omega_{eg}^{(j)} - \omega_M$. From this expression, the Lamb-Dicke approximation can be applied by expanding the exponential term containing the ladder operators to first order in η_{jl}. This leads to a Hamiltonian analogous to those used in photon momentum-based implementations (Eq. (4.100)).

Chapter 5

Quantum Control without Quantum States

CONTRIBUTIONS

All the work in this Chapter was conducted in collaboration with Dr. Nguyen H. Le and Florian Mintert. I, along with Florian, led the theoretical development and I performed some of the numerical calculations, while Nguyen H. Le handled the majority of the numerical work and contributed to several of the proofs. The results presented here were also published in Ref. [1].

5.1 Introduction

The rapid development of well-controlled quantum systems has opened unprecedented opportunities for leveraging quantum phenomena across diverse applications, from quantum simulation of complex materials and chemical processes [132, 133, 134] to fault-tolerant quantum computation [135, 136, 137]. At the heart of these prospects lies the exponential growth of the Hilbert space with the number of quantum degrees of freedom. This scaling implies that even modestly sized quantum systems could surpass classical computational capabilities for specific tasks, such as simulating quantum many-body dynamics or solving optimization problems [135, 68]. While this potential has driven remarkable progress in quantum hardware development — evidenced by demonstrations of quantum advantage [138, 139, 140, 141] — it simultaneously exposes a critical challenge: the *curse of dimensionality* [142] makes exact classical simulations of quantum dynamics intractable for even moderate system sizes [143].

This tension between quantum advantage and classical simulability profoundly impacts strategies for controlling quantum systems. Existing approaches often rely on exact analytical or numerical methods restricted to small-scale systems [144, 145], approximate

heuristics for scaling to larger regimes [146, 63], or specialized techniques tailored to systems with inherent symmetries or geometric constraints [147, 148]. While such methods provide valuable insights, they struggle to generalize to arbitrary quantum architectures, leaving a gap between theoretical control paradigms and the demands of real-world quantum devices.

As briefly mentioned in Sec. 3.5, a promising avenue to circumvent these limitations lies in the identification of quantum states that admit efficient descriptions. For instance, states with low entanglement entropy can be represented compactly using tensor networks [149] or machine learning-inspired ansatz [150], bypassing the need for explicit Hilbert-space parametrization. A particularly elegant framework for implicit state characterization is the stabilizer formalism, where quantum states are defined not by their wavefunctions but by the operators that stabilize them [78, 151]. This approach underpins fault-tolerant quantum error correction and measurement-based quantum computation, where complex entangled states like cluster states are succinctly specified by their stabilizer generators [152].

Similarly, ground states of many-body Hamiltonians — such as those exhibiting topological order [153, 154] — further exemplify the power of implicit descriptions. While their explicit wavefunction representations are intractably complex, these states are compactly defined by the interaction geometry and parameters of their parent Hamiltonian. Such implicit specifications, requiring only polynomial resources, form the foundation of adiabatic quantum computation (AQC) [79], where solutions are encoded in the ground state of a problem-specific Hamiltonian. By adiabatically evolving from a trivial initial state, AQC avoids explicit tracking of the wavefunction — relying instead on the adiabatic theorem, which ensures the system remains in the ground state if the evolution is sufficiently slow.

However, AQC's reliance on adiabatic timescales introduces a critical limitation: computational runtime is dictated by the Hamiltonian's spectral gap, which typically shrinks with system size or problem complexity. This constraint not only limits computational speed but also exacerbates vulnerability to decoherence. While AQC circumvents explicit state representations, its dependence on slow evolution highlights a broader challenge: reconciling the exponential complexity of Hilbert space with the need for scalable, robust quantum control.

This work addresses these challenges by unifying implicit state characterization with optimal control theory. We introduce an operator-centric framework that avoids explicit quantum state representations while operating beyond adiabatic constraints. By encoding control objectives directly in the dynamics of operators, the method avoids the exponential overhead of state-vector simulations. This enables precise solutions to control problems that are classically intractable under conventional approaches, such as high-fidelity manipulation of large-scale entangled systems or error-resilient gate design in many-body architectures. Crucially, the framework operates without approximations or restrictive adiabatic assumptions, combining the scalability of implicit descriptions with the rigor of optimal control.

The framework builds on the concept of quantum invariants (see Sec. 3.5) — Hermitian operators that act as constants of motion in the sense of Eq. (3.21). In the Schrödinger picture, invariants evolve according to the equation of motion in Eq. (3.23), and they possess a crucial property for quantum control: their time-dependent eigenvectors $|\Psi(t)\rangle$, which satisfy

$$\mathcal{I}(t)\,|\Psi(t)\rangle = \gamma\,|\Psi(t)\rangle \ , \tag{5.1}$$

with a *time-independent* eigenvalue γ, generate *expanding modes* [83]. These modes generalize the notion of adiabatic eigenstates to non-adiabatic timescales, providing a powerful tool for controlling quantum systems under rapidly changing Hamiltonians. To illustrate this, consider a system initialized in the instantaneous ground state of a time-dependent Hamiltonian $H(t)$. Under adiabatic evolution, the system remains in the instantaneous eigenstate of $H(t)$ at all times. In contrast, if the system is initialized in an expanding mode of the invariant $\mathcal{I}(t)$, it will remain in that evolving mode even under rapid (non-adiabatic) changes to $H(t)$, as highlighted in the discussion following Eq. (3.47). Crucially, these expanding modes need not align with the instantaneous eigenstates of $H(t)$; they may instead span multiple eigenstates of the adiabatic basis. This property enables robust state control without requiring slow parameter variation, circumventing the limitations of traditional adiabatic protocols [155].

Physically, this implies that expanding modes provide a dynamical pathway for the system to evolve in a controlled manner, even when the Hamiltonian changes rapidly. This is particularly useful in scenarios where adiabaticity is impractical, such as in systems with short coherence times or when fast operations are required. The ability to remain in an expanding mode under rapid changes suggests that these modes are resilient to perturbations and can be harnessed for high-fidelity quantum control.

Existing applications of quantum invariants in optimal quantum control rely on identifying analytical time-dependent forms of operators that satisfy Eq. (3.23) for specific types of Hamiltonians. For example, such invariants have been successfully derived for systems like the driven harmonic oscillator (see Eqs. (3.41) and (3.45)) and a single driven spin [83, 156, 157]. Once an analytical invariant is found, it provides an elegant way to design time-dependent Hamiltonians that generate desired dynamics. However, this approach is limited to simple systems, as finding analytical invariants becomes impractical for quantum systems with many interacting subsystems

To overcome this limitation, the goal of this Chapter is to develop a new framework for quantum control that leverages the advantages of invariant-based methods without requiring analytical expressions for invariants. Traditional invariant-based approaches depend on closed-form solutions, which are rarely available for complex or interacting systems. Our approach addresses this challenge by combining ideas from invariant-based quantum control [155] with established numerical techniques typically applied to state vectors or propagators [132, 158].

At the core of our methodology is the iterative numerical refinement of a time-dependent Hamiltonian. Unlike conventional methods that numerically integrate the Schrödinger equation, our framework integrates the equation of motion for quantum invariants (Eq. (3.23)). This shift eliminates the need for analytical invariants while preserving their dynamical benefits. Importantly, this approach extends invariant-based control to interacting quantum systems — where analytical methods often fail — by working directly with the invariant's evolution equation rather than its explicit form.

In this operator-centric formulation of quantum control, control targets are not defined in terms of state vectors or propagators, nor are they included in the cost functions to be minimized, as is common in standard approaches (see Sec. 3.2). Instead, the control objectives are formulated directly in terms of the time-dependent operators $\mathcal{I}(t)$ that satisfy the invariant equation of motion, Eq.(3.23). This eliminates the need to track quantum states, avoiding the exponential computational cost typically associated with their evolution. As demonstrated through explicit examples, this approach remains computationally manageable for interacting quantum systems, even in cases where state-based methods would become intractable.

5.2 Implicit quantum control

Traditional approaches to quantum dynamics typically involve the direct numerical propagation of the time-dependent Schrödinger equation for a state vector $|\psi(t)\rangle$. In contrast, the proposed method, termed *Implicit Quantum Control* (IQC), focuses on propagating an operator $\mathcal{I}(t)$ governed by Eq. (3.23). While the eigenvalue relation Eq. (5.1) inherently encodes full information about the quantum state $|\psi(t)\rangle$, this information remains implicit as long as $\mathcal{I}(t)$ is not explicitly diagonalised. This operator-centric framework shifts computational effort from state vector dynamics to the propagation of $\mathcal{I}(t)$, enabling novel strategies for control and optimization.

To apply this framework for control, we define a target operator $\mathcal{I}_T$ that guides the evolution of $\mathcal{I}(t)$ under Eq. (3.23). Control objectives are translated into constraints on $\mathcal{I}(T)$, allowing standard numerical pulse-shaping techniques to be applied directly to the operator dynamics. The resulting time-dependent Hamiltonian $H(t)$, derived from this process, inherently generates the desired quantum dynamics in the underlying Schrödinger equation. This approach generalizes control problems from state-based formulations to the Liouville-von Neumann equation Eq. (3.23), which governs operator evolution. While this translation does not universally improve computational efficiency, specific cases — such as systems with Hamiltonians of the form in Eqs. (5.36) and (5.37), and others detailed in Sec. 5.5 — achieve exponential efficiency gains by reducing the effective dimensionality of the problem.

5.2.1 Operator expansion

Conventional quantum control involves two key steps: (i) specifying an equation of motion and (ii) defining initial conditions and control targets. These are typically expressed either as a set of initial and final states (for state preparation or transfer) or as a target unitary operator (for quantum simulation). In our framework, the equation of motion is given by Eq. (3.23), while the initial conditions and control targets are specified in terms of initial and final operators — or equivalently, a desired unitary.

The advantage of the operator formulation lies in the efficient propagation of the invariant operator $\mathcal{I}(t)$. This efficiency is determined by the dimension d of the operator space in which $\mathcal{I}(t)$ evolves — that is, the span of operators generated by evolving the initial operator $\mathcal{I}(0)$ under Eq. (3.23). Naturally, the dimension d will depend on the choice of $\mathcal{I}(0)$. To ensure the control problem is well-posed, the initial operator $\mathcal{I}(0)$ must be chosen so that its ground state corresponds to the initial state $|\psi(0)\rangle$ of the system, *i.e.*

$$\mathcal{I}(0)\,|\psi(0)\rangle = \lambda_0\,|\psi(0)\rangle \ , \tag{5.2}$$

with $\lambda_0 = \min\{\lambda_i \mid \mathcal{I}(0)\,|\phi_i\rangle = \lambda_i\,|\phi_i\rangle\}$. Indeed, while one can formulate the control problem by transferring any nondegenerate eigenstate of the invariant (*i.e.* also excited states), we focus here on the ground state because it is typically easier to characterize. Moreover, since multiple choices for $\mathcal{I}(0)$ may satisfy the ground-state condition, one can optimize this choice to minimize the propagation space's dimension d, thereby improving computational efficiency.

To formalize the preceding discussion, we first define the system Hamiltonian. Without lost of generality, the Hamiltonian is expressed as a linear combination of a fixed set of d_0 basis operators $\{\mathfrak{h}_j\}_{j=1}^{d_0}$ with time-dependent scalar coefficients,

$$H(t) = \sum_{j=1}^{d_0} h_j(t)\mathfrak{h}_j \ , \tag{5.3}$$

where some coefficients may be constant (representing the drift Hamiltonian, denoted by H_0 in Eq. (3.1)) and others are tunable (representing the control Hamiltonian).

We propose an ansatz for the invariant operator $\mathcal{I}(t)$ in the form

$$\mathcal{I}(t) = \sum_{j=1}^{d} a_j(t)\mathfrak{a}_j \ , \tag{5.4}$$

with a set of d time-independent operators $\{\mathfrak{a}_j\}_{j=1}^{d}$ and time-dependent scalar expansion coefficients $a_j(t)$. This expansion provides a general solution to the equation of motion (Eq. (3.23)) for $\mathcal{I}(t)$ provided that the operators $\mathfrak{a}_j$ form a closed algebra under commutation with the Hamiltonian basis operators. Specifically, we require that for every

$j \in \{1, \cdots, d\}$ and $k \in \{1, \cdots, d_0\}$,

$$[\mathfrak{a}_j, \mathfrak{h}_k] = -i \sum_{l=1}^{d} \lambda_{lj}^k \mathfrak{a}_l \ , \tag{5.5}$$

where the coefficients λ_{lj}^k are real. This relation ensures that the evolution of $\mathcal{I}(t)$ remains confined to the span of $\{\mathfrak{a}_j\}$.

If the initial choice for the operator set $\{\mathfrak{a}_j\}$ does not yield a closed algebra — that is, if for some j_0 and k_0 the commutator $[\mathfrak{a}_{j_0}, \mathfrak{h}_{k_0}]$ lies outside the span of $\{\mathfrak{a}_j\}_{j=1}^d$ — then the set can be enlarged. In this case, one defines a new operator

$$\mathfrak{a}_{d+1} = i[\mathfrak{a}_{j_0}, \mathfrak{h}_{k_0}] \ , \tag{5.6}$$

thereby increasing the dimension of the operator space by one. This iterative process is continued until the closed commutator condition of Eq. (5.5) is satisfied for all pairs ($\mathfrak{a}_j$, $\mathfrak{h}_k$).

In practice, the construction may start with a single operator $\mathfrak{a}_1$, *i.e.* with $d = 1$, and the final dimension d will depend on the initial choice of $\mathcal{I}(0)$ and the structure of the Hamiltonian. Since the computational effort required to integrate the evolution equation (Eq. (3.23)) increases with d, it is beneficial to identify the smallest operator basis that satisfies the closed commutator algebra. However, even with an optimal choice of $\mathcal{I}(0)$, the effective dimension d generally exceeds d_0, reflecting the increased complexity of the operator dynamics.

5.2.2 Relation with Lie algebras

The construction of the operator set $\{\mathfrak{a}_j\}$ described above is closely related to — but distinct from — the standard construction of a Lie algebra. In a conventional Lie algebra, one considers a set of d operators $\{\mathfrak{h}_j\}_{j=1}^d$ satisfying a closed commutator relation

$$[\mathfrak{h}_j, \mathfrak{h}_k] = -i \sum_{l=1}^{d} \lambda_{lj}^k \mathfrak{h}_l \tag{5.7}$$

for all $j, k \in \{1, \cdots, d\}$, with real structure constants λ_{lj}^k. Often, one begins with a smaller set of d_0 operators (with $d_0 < d$) and then systematically enlarges the set until all commutators between the elements close within the expanded set.

In our approach, however, the closure condition is imposed on the operator being propagated rather than on the Hamiltonian's generators. In other words, the set $\{\mathfrak{a}_j\}$ is chosen so that the time-evolution of the operator $\mathcal{I}(0)$ remains confined to its span. This has subtle implications: it is possible that the Lie algebra generated by the Hamiltonian operators is much larger than the minimal algebra needed to satisfy the closure relation (Eq. (5.5)). In such cases, the dynamics of $\mathcal{I}(t)$ occur in a considerably smaller subspace, which can yield computational advantages.

In the explicit examples provided in Secs. 5.3 and 5.4, the time-dependent operator $\mathcal{I}(t)$ is expanded using the Lie algebra generated by the Hamiltonian operators $\{\mathfrak{h}_j\}_{j=1}^{d_0}$, that is, we set the propagation basis $\{\mathfrak{a}_j\}_{j=1}^{d}$ equal to the full Lie algebra $\{\mathfrak{h}_j\}_{j=1}^{d}$. However, to minimize the effective propagation space — and thus enhance computational efficiency — it can be beneficial to consider operator sets that extend beyond the Lie algebra framework, as further illustrated in Sec. 5.6.2.

5.2.3 Equations of motion

By expanding the time-dependent operator $\mathcal{I}(t)$ in terms of the operator sets $\{\mathfrak{a}_j\}$ and $\{\mathfrak{h}_k\}$, the equation of motion (Eq. (3.23)) becomes [159]

$$\frac{\partial \mathcal{I}}{\partial t} = i \sum_{j,k} a_j(t) h_k(t) [\mathfrak{a}_j, \mathfrak{h}_k] = \sum_{j,k,l} a_j(t) h_k(t) \lambda_{lj}^k \mathfrak{a}_l \ . \tag{5.8}$$

Given that the operators $\mathfrak{a}_j$ are linearly independent (*i.e.* no operator in the set can be written as a linear combination of the others), this leads to the differential equation

$$\dot{a}_l(t) = \sum_{j,k} \lambda_{lj}^k a_j(t) h_k(t) \ , \tag{5.9}$$

which can be written compactly in matrix form as

$$\dot{\mathbf{a}}(t) = K(t)\mathbf{a}(t) \ , \tag{5.10}$$

with the vector $\mathbf{a}$ and a matrix K with elements

$$K_{lj}(t) = \sum_k h_k(t) \lambda_{lj}^k \ . \tag{5.11}$$

If we choose the Hermitian operators $\mathfrak{a}_j$ to be mutually orthonormal (*i.e.* to satisfy $\mathrm{Tr}(\mathfrak{a}_j \mathfrak{a}_k) = \delta_{jk}$), then Eq. (5.5) implies

$$\lambda_{lj}^k = i \, \mathrm{Tr}([\mathfrak{a}_j, \mathfrak{h}_k]\mathfrak{a}_l) \ . \tag{5.12}$$

Invariance of the trace under cyclic permutation implies

$$\lambda_{lj}^k = i \, \mathrm{Tr}([\mathfrak{a}_l, \mathfrak{a}_j]\mathfrak{h}_k) = -\lambda_{jl}^k \ . \tag{5.13}$$

In this case, the matrix K is real and anti-symmetric [156] such that the induced dynamics is orthogonal, *i.e.* unitary and real.

5.2.4 Reachability

In quantum control theory, the concept of reachability (defined in Sec. 3.1) concerns the set of quantum operations or states attainable from a given initial condition under the time-dependent dynamics governed by a Hamiltonian $H(t)$. While standard reachability

analysis aims to determine if any target operation or state can be reached, this work adopts a different perspective. Our primary objective is not to guarantee universal reachability, but rather to optimize the efficiency of control methods for solving specific quantum tasks. As a result, we do not require the ability to reach any arbitrary target, but rather prioritize the ability to achieve a desired target effectively.

A foundational requirement for universal reachability is that the operator set $\{a_j\}$ used in the expansion of the control operator $\mathcal{I}(t)$ spans the entire space of Hermitian operators. For an n-qubit system, this would imply a dimensionality of $d = 4^n$. Satisfying this condition would replicate the complexity associated with full density matrix propagation and offers no computational advantage over standard state-vector propagation, which scales as 2^n. Crucially, universal reachability is not only computationally prohibitive but also unnecessary for our framework, which targets specific control objectives. By restricting $\mathcal{I}(t)$ to a low-dimensional subspace of operators, we bypass the exponential overhead of full operator-space propagation while retaining the ability to solve practical control problems efficiently.

To further understand the achievable set of operators for a given Hamiltonian $H(t)$, it is important to recognize that the propagator generated by $H(t)$ (Eq. (5.3)) is *not* generally expressible in the simple form

$$U(t) = \exp\left(-i\sum_{j=1}^{d_0} b_j(t)\mathfrak{h}_j\right) , \tag{5.14}$$

where $b_j(t)$ are scalar functions and $\{\mathfrak{h}_j\}_{j=1}^{d_0}$ are the operators appearing explicitly in $H(t)$. Rather, because the time-evolution operator involves series of nested commutators (see Eq. (2.53)), contributions from additional operators (*i.e.* for indices $j > d_0$) typically arise. Indeed, the full Lie algebra $\{\mathfrak{h}_j\}_{j=1}^{d}$ is required to correctly capture the evolution. This highlights an important point: a relatively small set of operators $\{\mathfrak{h}_j\}_{j=1}^{d_0}$ can generate a remarkably rich landscape of evolutions, resulting in a diverse set of accessible target operators and dynamics. Thus, even a small set of generators can significantly expand the available control options, making it possible to achieve the desired control objectives efficiently without resorting to universal reachability.

A direct consequence of this structure is that propagators of the form

$$U = \exp(-iK) , \tag{5.15}$$

where the operator K cannot be expressed as a linear combination of the elements in the Lie algebra of $H(t)$ (*i.e.* if no set of coefficients $\{c_j\}$ exists such that $K = \sum_{j=1}^{d} c_j\mathfrak{h}_j$), are fundamentally *unreachable* under the dynamics induced by $H(t)$. This reflects a key structural constraint: the set of accessible transformations is strictly limited to those generated by the Lie algebra of $H(t)$. While this restricts universal controllability, it does not undermine our objective. Rather, it aligns with our priority of optimizing efficiency for targeted

control over arbitrary reachability. In practice, many relevant quantum operations reside within a much smaller subspace of the full operator space, making exhaustive reachability unnecessary for achieving the desired control goals.

5.2.5 Formulation of the control problem

When expressed in terms of Eq. (5.10) rather than the underlying Schrödinger equation, the effective dimensionality of the control problem is determined by the number of operators in the set $\{\mathfrak{a}_j\}$, d, rather than by the dimension of the Hilbert space itself.

In general, d can be quadratically larger than the Hilbert space dimension. However, as we will illustrate, there are several practically relevant cases where d is significantly smaller. The key objective of the following discussion is to exploit this reduced dimensionality to enhance the efficiency of optimal control strategies.

While standard control problems are typically formulated in terms of achieving a target state or implementing a target quantum gate, the present framework requires defining a control objective for the operator, denoted by $\mathcal{I}_\mathcal{T}$, and defining this requires some care. In the following sections, we will address this formulation explicitly for two fundamental tasks: state preparation and realization of propagators.

A. State preparation

State preparation is a natural application for this operator-based framework due to a fundamental asymmetry in quantum mechanics: while Hamiltonians for interacting systems can often be specified efficiently (*e.g.*, through sparse matrix representations or local interaction terms), their eigenstates — such as highly entangled many-body states or fractional quantum Hall ground states [160] — are often challenging to describe explicitly. By reframing control objectives in terms of parent Hamiltonians (operators for which the target state is an eigenstate), the framework bypasses direct state manipulation and leverages the Hamiltonian's inherent efficiency of representation.

In conventional state-preparation protocols, the target is a specific quantum state, and the natural choice for the target functional is one explicitly defined in terms of this state (see Sec. 3.2), which requires full knowledge of the state — a prohibitive demand for complex systems. The present approach leaves much more freedom, since there are many operators $\mathcal{I}_T$ that have a given target state as ground state. There are thus many conceivable choices for $\mathcal{I}_T$ and a good choice is a central part of the control problem within the present approach.

In state preparation, the goal is to design a time-dependent Hamiltonian $H(t)$ that drives the system from the ground state of an initial operator H_I to the ground-state of a final operator H_T. A seemingly natural approach is to set the initial condition as $\mathcal{I}(0) = H_I$ and the control target $\mathcal{I}_T = H_T$. However, unitary dynamics impose a critical constraint: the spectrum of $\mathcal{I}(t)$ is preserved over time. Thus, H_I and H_T must share identical spectra — a severe restriction that rules out the target $\mathcal{I}_T = H_T$ to transfer states separated by

quantum phase transitions (*e.g.*, crossing a critical point to reach a topologically ordered phase). This spectral rigidity highlights the need for a different target $\mathcal{I}_T$ that encodes the target state without making it coincide with the final Hamiltonian H_T.

Moreover, even when H_I and H_T share spectra, achieving the desired transformation depends on the dynamical Lie algebra $\mathfrak{g}$ generated by the control operators $\{\mathfrak{h}_j\}$ in the Hamiltonian (Eq. 5.3). If $\mathfrak{g}$ is not full rank (*i.e.*, it fails to span the entire operator space excluding the identity), the system is not fully controllable, as certain unitary propagators cannot be realized within the constraints of the available control fields, as discussed in Sec. 5.2.4. This limitation implies that even when spectral constraints are satisfied, an operator $\mathcal{I}(t)$ initialized as $\mathcal{I}(0) = H_I$ may not be able to evolve toward the desired final value $\mathcal{I}(T) = H_T$, *i.e.* the target $\mathcal{I}_T = H_T$ is not reachable.

As an explicit example, consider a two-qubit system where the goal is to prepare the entangled Bell state, which corresponds to the ground state of the target Hamiltonian

$$H_T = \frac{1}{2}\left(X_1X_2 + Y_1Y_2\right) \ . \tag{5.16}$$

The system is governed by the control Hamiltonian

$$H(t) = f_1(t)X_1 + f_2(t)X_2 \ , \tag{5.17}$$

and the initial state is the separable state $|11\rangle$, which corresponds to the ground-state of the initial operator

$$\mathcal{I}(0) = \frac{1}{2}\left(Z_1 + Z_2\right) \ . \tag{5.18}$$

Although both $\mathcal{I}(0)$ and H_T share the same eigenvalues ($\{-1, 0, 0, 1\}$), the target $\mathcal{I}_T = H_T$ is not reachable under this control scheme. Intuitively, this is because the initial state — the ground-state of $\mathcal{I}(0)$—is separable, while the target state — the ground state of H_T — is entangled. Generating entanglement requires a unitary transformation that acts simultaneously on both qubits, but $H(t)$ is restricted to local rotations (single-qubit X operations). Mathematically, the Lie algebra generated by $H(t)$ acting on $\mathcal{I}(0)$ consists only of single-qubit Pauli operators (*i.e.*, $\mathfrak{g} = \{X_1, Y_1, Z_1, X_2, Y_2, Z_2\}$). Any reachable target operator $\mathcal{I}_T$ must be expressible in terms of this algebra, implying that only separable ground states can be achieved.

Further examples demonstrating when specific targets can or cannot be achieved within this framework are discussed in Sec. 5.3.2.

Step-by-step formulation

Box 1: IQC Framework for State Preparation

Given an initial Hamiltonian H_I and a target Hamiltonian H_T, the following steps are required to apply the invariant-based quantum control (IQC) framework to a problem of state preparation:

Step 1: Choose a compatible initial operator.
Select an initial operator $\mathcal{I}(0)$ such that the initial state $|\Psi_I\rangle$ (an eigenstate of H_I) satisfies:

$$\mathcal{I}(0)\,|\Psi_I\rangle = \gamma\,|\Psi_I\rangle\,,$$

where γ is a *non-degenerate* eigenvalue of $\mathcal{I}(0)$.

Insights: In most control problems, the initial Hamiltonian H_I is chosen to be non-interacting—typically a sum of single-qubit (or more generally, single-particle) terms. Consequently, $\mathcal{I}(0)$ can also be designed as a non-interacting operator. If the single-qubit components of $\mathcal{I}(0)$ are non-degenerate, the operator will have a unique, non-degenerate ground state. The corresponding eigenvalue γ is simply the sum of the ground-state eigenvalues of the individual terms. However, when $\mathcal{I}(0)$ includes interacting components, verifying ground-state non-degeneracy becomes non-trivial. One practical approach is to demonstrate unitary equivalence between $\mathcal{I}(0)$ and a non-degenerate, non-interacting operator. This ensures that the ground state remains unique and well-defined.

Step 2: Define a compatible control target.
Construct a control target $\mathcal{I}_T$ such that the target state $|\Psi_T\rangle$ (an eigenstate of H_T) is also an eigenstate of $\mathcal{I}_T$ with the *same* eigenvalue γ:

$$\mathcal{I}_T\,|\Psi_T\rangle = \gamma\,|\Psi_T\rangle\,.$$

This condition ensures compatibility with the preserved spectral properties of $\mathcal{I}(t)$.

Insights: There is a general approach to numerically construct targets $\mathcal{I}_T$ when the operator set $\{\mathfrak{a}_j\}$ spans the Lie algebra generated by the Hamiltonian operators $\{\mathfrak{h}_j\}$ in Eq. (5.3).
Given an initial condition $\mathcal{I}(0)$, one can numerically evolve $\mathcal{I}(t)$ under a Hamiltonian that adiabatically interpolates between H_I and H_T (as demonstrated in Sec. 5.3.2). This requires integrating Eq. (5.10) numerically, but crucially, the computational complexity scales polynomially with the operator space dimension d, rather than the exponentially large Hilbert space. The final operator $\mathcal{I}(T)$ obtained this way:

- preserves the spectrum of $\mathcal{I}(0)$ due to unitarity,
- has a ground state corresponding to that of H_T by adiabaticity, and
- is reachable through the dynamics of the system Hamiltonian.

Step 3: Ensure dynamic reachability.
Verify that the control target $\mathcal{I}_T$ is dynamically reachable, meaning there exists a time-dependent Hamiltonian $H(t)$ within the allowed control parameters such that the evolution governed by

$$\dot{a}_l(t) = \sum_{j,k} \lambda_{lj}^k a_j(t) h_k(t)$$

can transform $\mathcal{I}(0)$ into $\mathcal{I}_T$.

Insights: Given Eq. (5.10), the question of reachability of an operator $\mathcal{I}_T$ from an initial operator $\mathcal{I}(0)$ is equivalent to the reachability of a coefficient vector $\mathbf{a}(t)$. Specifically, if $\mathcal{I}(t)$ is expanded as in Eq. (5.4), the evolution of $\mathbf{a}(t)$ is governed by a linear differential equation involving the time-dependent matrix $K(t)$ (Eq. (5.11)). Thus, the problem of operator reachability is mapped onto a standard vector reachability problem under linear dynamics — analogous to state control governed by the Schrödinger equation [161].
The requirements (i), (ii), and (iii) for operator reachability do not uniquely determine the initial condition $\mathcal{I}(0)$ or the target $\mathcal{I}_T$. This flexibility can be leveraged to select an operator $\mathcal{I}(0)$ that expands in a small operator set $\{\mathfrak{a}_j\}$ while ensuring closed commutation relations (Eq. (5.5)).
Practical implementations often rely on numerically constructing control targets through simulated adiabatic dynamics (Sec. 5.3). While this approach is generally applicable, there are also cases where analytic target definitions are possible, as exemplified in Secs. 5.3.2 and 5.3.2.

Objective function for state transfer

Once a consistent definition for the initial condition $\mathcal{I}(0)$ and control target $\mathcal{I}_T$ has been established, a natural objective function to minimize is the infidelity

$$\mathcal{J} = 1 - \frac{\mathrm{Tr}(\mathcal{I}(T)\,\mathcal{I}_T)}{\mathrm{Tr}(\mathcal{I}_T^2)}\ , \tag{5.19}$$

where T is the final time at which the goal of the control problem is intended to be reached. This infidelity measure quantifies the deviation of the evolved operator $\mathcal{I}(T)$ from the target operator $\mathcal{I}_T$ and, crucially, can be equivalently expressed in terms of the vector representations $\boldsymbol{a}(T)$ and $\boldsymbol{a}_T$ of $\mathcal{I}(T)$ and $\mathcal{I}_T$, respectively,

$$\mathcal{J} = 1 - \frac{\boldsymbol{a}(T)\cdot\boldsymbol{a}_T}{\|\boldsymbol{a}_T\|^2}\ . \tag{5.20}$$

This highlights that the effort to evaluate the infidelity scales with the dimension d and not with the dimension of system's Hilbert space.

If $\mathcal{I}(T)$ coincides exactly with the control target $\mathcal{I}_T$, the system state is guaranteed to coincide with the desired non-degenerate eigenstate of $\mathcal{I}_T$, *i.e.* the target state $|\Psi_T\rangle$.

Moreover, since both the state infidelity and the operator infidelity defined in Eq. (5.19) are continuous functions, a vanishing operator infidelity $\mathcal{J}$ for $\mathcal{I}(T)$ guarantees that the state infidelity will also approach zero. This continuity ensures that small deviations in the operator translate to small deviations in the state, providing a robust foundation for control protocols.

While the operator infidelity $\mathcal{J}$ provides a useful measure of control performance, practical applications often require a more direct assessment of the achieved state fidelity. To derive such a measure, we decompose the final state $|\Psi(T)\rangle$ into its overlap with the target state $|\Psi_T\rangle$ (*i.e.* the ground-state of H_T) and its projection onto the excited states of H_T,

$$|\Psi(T)\rangle = \langle\Psi_T|\Psi(T)\rangle\,|\Psi_T\rangle + P_e\,|\Psi(T)\rangle \ , \tag{5.21}$$

where P_e is the projector onto the subspace spanned by the excited states of H_T, and we have used the completeness relation $\mathbb{I} = P_e + |\Psi_T\rangle\langle\Psi_T|$.

The expectation value of H_T with respect to $|\Psi(T)\rangle$ reads

$$\langle\Psi(T)|\,H_T\,|\Psi(T)\rangle = |\,\langle\Psi_T|\Psi(T)\rangle\,|^2 E_0 + \langle\phi|\,H_T\,|\phi\rangle \ , \tag{5.22}$$

with $|\phi\rangle = P_e\,|\Psi(T)\rangle$ and the ground state energy E_0 of H_T. From the completeness relation, we have

$$\langle\Psi(T)|\,P_e\,|\Psi(T)\rangle = 1 - |\,\langle\Psi_T|\Psi(T)\rangle\,|^2 \ . \tag{5.23}$$

This implies that the norm of $|\phi\rangle$ is directly related to the state fidelity $F = |\,\langle\Psi_T|\Psi(T)\rangle\,|^2$ as

$$\langle\phi|\phi\rangle = 1 - F \ . \tag{5.24}$$

Rearraging Eq. (5.22) and using Eq. (5.24) ,

$$\frac{E_0 - \langle\Psi(T)|\,H_T\,|\Psi(T)\rangle + \langle\phi|\,H_T\,|\phi\rangle}{E_0} = \langle\phi|\phi\rangle \ . \tag{5.25}$$

It follows that

$$\frac{\langle\phi|\,H_T\,|\phi\rangle}{\langle\phi|\phi\rangle} = \frac{\langle\Psi(T)|\,H_T\,|\Psi(T)\rangle - E_0}{1-F} + E_0 \ , \tag{5.26}$$

where we substituted $\langle\phi|\phi\rangle$ in the denominator of the right-hand side. With the inequality

$$\frac{\langle\phi|\,H_T\,|\phi\rangle}{\langle\phi|\phi\rangle} \geq E_1 \ , \tag{5.27}$$

in terms of the energy E_1 of the first excited state of H_T, and rearranging, we obtain

$$E_1 \leq \frac{\langle\Psi(T)|\,H_T\,|\Psi(T)\rangle - E_0}{1-F} + E_0 \ . \tag{5.28}$$

Hence, rearranging this expression, we arrive at an upper bound on the state infidelity

$$1 - F \leq \frac{\langle \Psi(T)| H_T |\Psi(T)\rangle - E_0}{E_1 - E_0} \ . \tag{5.29}$$

The state infidelity $1 - F$ can thus be bounded in terms of the ground state energy E_0, the first excited state energy E_1 of the Hamiltonian H_T and the expectation value $\langle \Psi(T)| H_T |\Psi(T)\rangle$. While it might initially appear that calculating this expectation value necessitates explicitly constructing the final state vector $|\Psi(T)\rangle$, this is not the case. Instead, we can leverage the unitary dynamics of the system to evaluate the expectation value efficiently.

Since the state vector $|\Psi(t)\rangle = U(t)|\Psi(0)\rangle$ evolves according to the unitary dynamics induced by the system Hamiltonian, the expectation value can be rewritten as

$$\langle \Psi(T)| H_T |\Psi(T)\rangle = \langle \Psi(0)| U^\dagger(T) H_T U(T) |\Psi(0)\rangle \ . \tag{5.30}$$

The right-hand side shows that the expectation value can be computed equivalently by evolving the operator H_T backward in time, rather than evolving the state forward. Specifically, the transformed operator $U^\dagger(T)H_T U(T)$ represents the backward-evolved version of H_T under the dynamics described by Eq. (3.23).

A key advantage of this approach is that if H_T can be expressed as a linear combination of the basis operators $\{\mathfrak{a}_j\}_{j=1}^d$, this backward propagation can be computed with the same $\mathcal{O}(d)$ effort required to evolve $\mathcal{I}(t)$. Moreover, as long as expectation values with respect to the initial state $|\Psi(0)\rangle$ can be specified efficiently — which is typically the case in problems such as state preparation, adiabatic quantum computation, and quantum approximate optimization algorithms, where initial states are product states [162, 79, 163] — the state fidelity F can be efficiently bounded using Eq. (5.29).

B. Quantum simulation

The framework of IQC can also be applied to quantum simulation, particularly in the context of analog quantum simulation (AQS) (see Sec. 3.4.2). The goal here is to realize a specific unitary transformation $\mathcal{U}_T$, which is generated by a complex many-body target Hamiltonian H_T that may not be directly implementable or controllable in an experimental setting.

This scenario contrasts with the state preparation problem discussed in the previous section. There, for a given initial condition $\mathcal{I}(0)$, multiple operators can have the target state as their ground state, so there is no unique choice for the control target $\mathcal{I}_T$. For AQS, however, no such freedom exists. The control target corresponding to the initial condition $\mathcal{I}(0)$ must be uniquely given by

$$\mathcal{I}_T = \mathcal{U}_T \mathcal{I}(0) \mathcal{U}_T^\dagger \ . \tag{5.31}$$

This equation suggests that if the operator $\mathcal{I}(0)$ evolved via Eq. (3.23) reaches $\mathcal{I}_T$ at the final time T, then the propagator $\mathcal{U}_T$ has been implemented. However, the situation is more subtle. If there exists a unitary V that commutes with the target operator $\mathcal{I}_T$, *i.e.* $[V, \mathcal{I}_T] = 0$, then also the relation

$$\mathcal{I}_T = V\mathcal{I}_T V^\dagger = V\mathcal{U}_T\mathcal{I}(0)\mathcal{U}_T^\dagger V^\dagger \tag{5.32}$$

holds. In this case, reaching the target $\mathcal{I}_T$ does not necessarily confirm that the specific propagator $\mathcal{U}_T$ has been realized, since an alternative unitary $V\mathcal{U}_T$ would produce the same target operator.

In summary, while evolving the operator $\mathcal{I}(t)$ from the initial condition $\mathcal{I}(0)$ toward the target $\mathcal{I}_T = \mathcal{U}_T\mathcal{I}(0)\mathcal{U}_T^\dagger$ is necessary for simulating the desired dynamics, it does not by itself guarantee that the intended unitary $\mathcal{U}_T$ has been implemented.

Thus, just as a faithful objective function in quantum control is defined using a set of initial and final states, the present approach requires a set of initial conditions $\mathcal{I}_j(0)$ and corresponding targets

$$\mathcal{I}_{Tj} = \mathcal{U}_T\mathcal{I}_j(0)\mathcal{U}_T^\dagger \tag{5.33}$$

to construct an objective function that is minimized exactly when the desired unitary $\mathcal{U}_T$ is realized. Unlike standard gate characterization methods, which typically require an exponentially large set of input and output states [164, 165], this operator-based formulation often requires only a small number of initial conditions [166].

Objective function for quantum simulation

A possible choice for a faithful objective function is given by

$$\mathcal{J}_{\mathcal{U}_T} = 1 - \frac{1}{N_c}\sum_{j=1}^{N_c} \frac{\mathrm{Tr}(\mathcal{I}_j(T)\,\mathcal{U}_T\mathcal{I}_j(0)\mathcal{U}_T^\dagger)}{\mathrm{Tr}((\mathcal{I}_j(0))^2)}\ , \tag{5.34}$$

with a sufficiently large number N_c of initial conditions $\mathcal{I}_j(0)$. These initial conditions can, for example, always be chosen as a minimal set of operators from $\{\mathfrak{a}_j\}$ such that there is no operator in $SU(2^n)$ that commutes with all the transformed operators $\mathcal{U}_T\mathcal{I}_j(0)\mathcal{U}_T^\dagger$. This ensures that minimizing $\mathcal{J}_{\mathcal{U}_T}$ unambiguously verifies the implementation of $\mathcal{U}_T$.

Since each summand in Eq. (5.34) can be evaluated analogously to Eq. (5.19), the objective function $\mathcal{J}_{\mathcal{U}_T}$ can indeed be evaluated with polynomial effort as

$$\mathcal{J}_{\mathcal{U}_T} = 1 - \frac{1}{N_c}\sum_{j=1}^{N_c} \frac{\boldsymbol{a}_j(T)\cdot\boldsymbol{a}_{j,T}}{\|\boldsymbol{a}_j(0)\|^2}\ . \tag{5.35}$$

5.2.6 Numerical propagation and optimization

Numerical propagation in the IQC framework is performed entirely within the d-dimesional space spanned by the basis operators $\{\mathfrak{a}_j\}$. This implies that the state of the operator $\mathcal{I}(t)$ at any time t can be completely reconstructed from the expansion coefficients $a_j(t)$ (as defined in Eq. (5.4)). Once a control target $\mathcal{I}_T$ and an objective function — such as $\mathcal{J}$ (Eq. (5.19)) or $\mathcal{J}_{\mathcal{U}_T}$ (Eq. (5.34)) — are specified, any numerical pulse-shaping algorithm (*e.g.*, [132]) can be employed to design a time-dependent Hamiltonian that steers the system from $\mathcal{I}(0)$ to $\mathcal{I}(T)$, at a final time T, that is close to $\mathcal{I}_T$. Since Eq.(5.10) describes dynamics governed by an antisymmetric matrix K, it preserves orthogonality, leading to real and unitary evolution. Consequently, numerical algorithms designed for solving the Schrödinger equation — such as Krotov [167], GRAPE [144] or CRAB [63] — can be applied directly. Additionally, standard techniques for computing gradients with respect to control parameters naturally extend to Eq. (5.10), enabling efficient optimization. Appendix F.2 provides a detailed discussion of gradient computation, along with strategies to enhance optimization performance and achieve optimal values more effectively.

The complete algorithm is detailed in Box 2.

Box 2: A Birdseye View on the Algorithm of IQC

The core algorithm of IQC, which involves finding the optimal time-dependent Hamiltonian for solving state preparation or quantum simulation problems, can be summarized as follows:

Given:

1. A time-dependent Hamiltonian (Eq. (5.3))

2. A set of operators $\{\mathfrak{a}_j\}$ satisfying the closed commutator relations in Eq. (5.5).

Algorithm Steps:

Step 1: Define the initial condition
Choose an initial operator

$$\mathcal{I}(0) = \sum_j a_j(0)\mathfrak{a}_j$$

with a non-degenerate ground state $|\psi(0)\rangle$ that can be easily prepared experimentally (*e.g.* a product state). This ensures that the preparation is feasible and that the optimal pulses can be applied in a real experimental setting.

Step 2: Define the target
Determine a control target $\mathcal{I}_T$ encoding the desired quantum state $|\psi_T\rangle$ as its ground state, and ensure that $\mathcal{I}_T$ is dynamically reachable from $\mathcal{I}(0)$.

Step 3: Optimize the Hamiltonian's time dependence
Design time-varying parameters (in Eq. (5.3)) to minimize an objective function that compares $\mathcal{I}(T)$ and $\mathcal{I}_T$, expressed in terms of the expansion coefficients of $\mathcal{I}(T)$ and $\mathcal{I}_T$ in the operator set $\{\mathfrak{a}_j\}$. Apply any suitable optimal control algorithms for linear

differential equations (*e.g.* GRAPE) to optimize the dynamics described by Eq. (5.10), ensuring the objective function is minimized.

Outcome:
Under the optimized Hamiltonian, the system evolves from the ground state of $\mathcal{I}(0)$ to the ground state of $\mathcal{I}_T$.

Extension to quantum simulations:
To implement a unitary evolution $\mathcal{U}_T$ that mimics the dynamics of a target complex Hamiltonian H_T, several modifications are necessary:

Step 1:
Requires multiple distinct initial conditions $\mathcal{I}_j(0)$, though their eigenstates do not need to be easily prepared experimentally.

Step 2:
Requires multiple distinct control targets $\mathcal{I}_{Tj}$ to uniquely specify the target gate $\mathcal{U}_T$.

5.3 State preparation in a driven spin chain

The control framework introduced in Section 5.2 applies universally to any operator set satisfying Eq. (5.5), though its practical utility crucially depends on the dimension d the operator algebra $\{\mathfrak{a}_j\}$. While no general algebraic theory currently exists (to our knowledge) for identifying system Hamiltonians with operator sets substantially smaller than the Hilbert space dimension, concrete evidence for such systems emerges through explicit constructions.

Section 5.5 presents several spin systems with polynomial-sized operator sets ($d \sim \mathcal{O}(n^k)$, for spin number n), though these technical examples benefit from contextualization. To demonstrate the framework's implementation, we focus subsequent analysis on the paradigmatic case of a linear spin chain with nearest-neighbor interactions — a minimal model shown schematically in Figure 5.1. This illustrative case study will clarify both the method's core principles and its operational requirements.

The system dynamics in this configuration are governed by the Hamiltonian

$$H(t) = g\sum_{j=1}^{n-1} X_j X_{j+1} + \sum_{j=1}^{n} f_j(t) Z_j + \sum_{j\in\{1,n\}} w_j(t) X_j \ , \tag{5.36}$$

which combines three key components:

(i) a static nearest-neighbor interaction term ($g\sum_{j=1}^{n-1} X_j X_{j+1}$) with Pauli-$X$ operators,

(ii) time-dependent local control fields ($f_j(t)Z_j$) acting via Pauli-Z operators, and

(iii) boundary control terms ($w_j(t)X_j$) targeting the chain's end spins (see Fig. 5.1) via Pauli-X operators.

Figure 5.1: A linear spin chain of n qubits with nearest-neighbor XX interactions. Single-qubit Z-driving and X-driving oon the end qubits facilitate the efficient preparation of various quantum states, such as GHZ and cluster states, and enable the realization of effective dynamics involving multi-qubit interactions.

This structure generalizes the conventional Ising model—recovered when $w_j(t) = 0$—while introducing critical differences. The standard Ising model conserves parity symmetry, restricting the achievable dynamics and possible state transitions, while enabling fermionic mapping techniques [168] to mitigate exponential simulation costs. By contrast, the generalized Hamiltonian in Eq. (5.36) breaks these limitations: for $g \neq 0$ and arbitrary time-dependent functions $f_j(t)$ and $w_j(t)$, no non-trivial conserved quantities exist. Formally, no operator A (except scalar multiples of the identity) commutes with all components of $H(t)$, including the single qubit drivings Z_j, the boundary terms X_1, X_n, and the interaction term $\sum_{j=1}^{n-1} X_j X_{j+1}$ (see Appendix F.1 for the proof).

The Lie algebra generated by nested commutators of the individual terms in the Hamiltonian (Eq. (5.36)) contains $d = 2n^2 + 3n + 1$ terms as discussed in Sec. 5.5.1, and they are given by

$$Z_i \ , \tag{5.37a}$$

with $i \in [1, n]$,

$$X_j Z_{jk} X_{j+k+1} \ , \tag{5.37b}$$
$$Y_j Z_{jk} Y_{j+k+1} \ , \tag{5.37c}$$
$$X_j Z_{jk} Y_{j+k+1} \ , \tag{5.37d}$$
$$Y_j Z_{jk} X_{j+k+1} \ , \tag{5.37e}$$

with $j \in [1, n-k-1]$, $k \in [0, n-2]$, and the short-hand notation $Z_{jk} = \prod_{i=1}^{k} Z_{i+j}$,

$$Z_{0j} X_{j+1} \ , \tag{5.37f}$$
$$Z_{0j} Y_{j+1} \ , \tag{5.37g}$$
$$X_{n-j} Z_{(n-j)j} \ , \tag{5.37h}$$
$$Y_{n-j} Z_{(n-j)j} \ , \tag{5.37i}$$

with $j \in [0, n-1]$, and finally

$$\prod_{i=1}^{n} Z_i \ . \tag{5.37j}$$

While the system Hamiltonian (Eq. (5.36)) includes only two-body interactions (X_jX_{j+1}) and single-qubit terms (Z_j, X_1 and X_n), the operator $\mathcal{I}(t)$ needs to be expanded in terms of the full set of Eq. (5.37) to satisfy the commutator closure condition (Eq. (5.5)) and ensure the ansatz in Eq. (5.4) remains general enough for integrating the equations of motion (Eq. (5.8)).

Since Eq. (5.37) contains a quadratic number of terms, the present framework reduces a control problem in an exponentially large Hilbert space to a problem in a vector space of quadratic growth. Thanks to this quadratic scaling, it is possible to design optimal control protocols for spin chains of lengths that are inaccessible for approaches based on quantum states.

The following examples are motivated by typical problems of quantum simulation and state preparation or stabilisation. They exploit the fact that the Lie algebra given in Eq. (5.37) contains three-body interactions such as $X_jZ_{j+1}X_{j+2}$ or even n-body interactions that cannot be realised by static means.

In Secs. 5.3.1 and 5.4.1 , we address this gap by designing time-dependent controls $f_j(t)$ and $w_j(t)$ in the system Hamiltonian $H(t)$ (Eq. (5.36)) that ensure that the system dynamics, governed solely by two-body interactions, effectively facilitate preparation of states or realization of propagators that require higher-order multi-spin couplings.

5.3.1 Target Hamiltonians

Building on the framework established in Sec. 5.2.5, we aim to design time-dependent control parameters $f_j(t)$ and $w_j(t)$ in the system Hamiltonian $H(t)$ (Eq. (5.36)), such that the system evolves from an initial state to a desired final state. Typical choices for an initial state are given by separable states that can be specified efficiently, but final states of interest are often highly entangled states. The following discussion will thus avoid the explicit specification of a state vector, but both the initial state and the final state to be realized will be specified in terms of a Hamiltonian to which they are the ground state.

A natural choice of non-interacting Hamiltonian based on Eq. (5.36) is given by the initial conditions $f_j(0) = f_k(0)$ for all j, k, $f_j(0) \gg g$ and $w_j(0) = 0$ for all j, *i.e.* non-interacting spins with single-spin-Z Hamiltonian.

Crucially, the Hamiltonians defining the final state to be realized do not need to be of the form of the system Hamiltonian in Eq. (5.36). Instead, any Hamiltonian constructed from the operators in Eqs. (5.37) — including those that incorporate three-spin interactions or even couplings among more than three spins — is a viable choice. This flexibility arises because, given a sufficiently long evolution time, the dynamics induced by Eq. (5.36) will generate any element of the Lie algebra.

The discussion of target Hamiltonians includes several key examples, each chosen to high-

light distinct aspects of the control framework. The first is the Hamiltonian

$$H_G = -\sum_{j=1}^{n-1} X_j X_{j+1} - \prod_{i=1}^{n} Z_i \ , \tag{5.38}$$

whose ground state is a GHZ state. GHZ states are of broad interest across quantum technologies, playing a central role in quantum sensing [169], quantum communication protocols [170, 171], and foundational studies of macroscopic quantum phenomena [172]. Their experimental realization has been a major focus in recent years [173, 174], further motivating their inclusion as a target state.

A second example is the Hamiltonian

$$H_C = Z_1 X_2 + \sum_{j=1}^{n-2} X_j Z_{j+1} X_{j+2} + X_{n-1} Z_n \ , \tag{5.39}$$

whose ground state corresponds to the one-dimensional n-qubit cluster state — a resource state for measurement-based quantum computation [175]. Cluster states are particularly notable for their role in enabling universal quantum computing through local measurements alone.

Finally, to demonstrate the generality of the approach, we consider the Hamiltonian

$$H_D = H_C + \sum_{j=1}^{n-1} X_j X_{j+1} \ , \tag{5.40}$$

which, unlike the examples H_G and H_C above, lacks an analytically constructible target operator. In particular, this example illustrates that the framework does not rely on the existence of analytic solutions, a key advantage over methods such as matrix product state-based optimal control [63], which fail for systems like H_D due to its vanishing spectral gap in the thermodynamic limit $n \to \infty$.

5.3.2 Control targets

As outlined in Sec. 5.2.5, a natural initial condition for the operator $\mathcal{I}(0)$ is

$$\mathcal{I}_0 = \sum_j Z_j \ , \tag{5.41}$$

a choice well-suited for the problem at hand. This selection is motivated by the fact that (i) each Z_j belongs to the operator algebra $\{\mathfrak{a}_j\}$, ensuring compatibility with the framework's algebraic structure; and (ii) the ground state of $\mathcal{I}(0)$ is non-degenerate and straightforward to prepare experimentally.

However, defining the corresponding control target requires careful consideration and must be addressed separately for the three distinct control problems defined by the Hamiltonians H_G, H_C and H_D.

Control target for GHZ-state Hamiltonian

Although it is generally not possible to define the control target $\mathcal{I}_T$ directly in terms of the Hamiltonian whose ground state is to be realized, this is feasible for H_G. Specifically, since H_G can be expressed as

$$H_G = W_G^\dagger \mathcal{I}_0 W_G \ , \tag{5.42}$$

with

$$W_G = \left(\prod_{k=1}^{n-1} e^{-i\frac{\pi}{4}(X_k Y_{k+1})} \right) e^{i\frac{\pi}{4}(X_1 - X_n)} \ , \tag{5.43}$$

where the factors in the product are in increasing order in the index k, the two operators H_G and $\mathcal{I}_0$ have the same spectrum. Since every factor in W_G is induced by elements of the Lie Algebra (Eq. (5.37)), it follows that the unitary W_G can indeed be realized with the Hamiltonian $H(t)$ in Eq. (5.36). The control target $\mathcal{I}_G = H_G$ is thus a valid choice for the task of realising the ground state of H_G.

Control target for cluster-state Hamiltonian

The construction of the control target $\mathcal{I}_C$ for the task of realising the ground state of H_C is very similar to the case of H_G above. H_C can be expressed as

$$H_C = W_C^\dagger \mathcal{I}_0 W_C \tag{5.44}$$

with

$$W_C = \left(\prod_{k=1}^{n-1} e^{(-1)^k i\frac{\pi}{4}(X_k X_{k+1})} \right) e^{i\frac{\pi}{4}(X_1 + X_n)} \ . \tag{5.45}$$

Also here, all the terms in W_C are induced by elements of the Lie Algebra (Eq. (5.37)). Since W_C is unitary, the control target $\mathcal{I}_C = H_C$ is thus a valid choice for the task of realising the ground state of H_C starting from the ground state of $\mathcal{I}_0$.

Control target for H_D

Unlike the cases of H_G and H_C, the control target for H_D cannot be defined analytically and requires a numerical construction. This is because $\mathcal{I}_D = H_D$ is unreachable from $\mathcal{I}(0)$ with unitary dynamics. Instead, a numerical target $\mathcal{I}_D$ sharing the same ground state as H_D must be constructed.

One approach to construct such an $\mathcal{I}_D$ is to propagate $\mathcal{I}(t)$ from $\mathcal{I}(0)$, which naturally yields operators reachable within the available dynamics. By choosing a Hamiltonian $H_a(t)$ with adiabatically slow time dependence, one can identify an operator $\mathcal{I}_a(T_a)$ whose ground state matches that of $H_a(T_a)$ at the end of the adiabatic evolution.

The following example is based on the choice

$$H_a(t) = \left(1 - \frac{t}{T_a}\right) H_I + \frac{t}{T_a} H_D + \frac{t}{T_a} \left(1 - \frac{t}{T_a}\right) H_B \ , \tag{5.46}$$

where the last term with

$$H_B = \sum_j Z_j + \sum_{j=1}^{n-1} X_j X_{j+1} + X_1 + X_n \tag{5.47}$$

vanishes at the initial and final point in time ($t = 0$ and $t = T_a$), but turns some level crossings into avoided crossings, so that adiabatic dynamics does indeed ensure transfer from the ground-state of H_I to the ground-state of H_D.

By choosing a sufficiently large adiabatic evolution time T_a, a viable control target $\mathcal{I}_D = \mathcal{I}_a(T_a)$ can be constructed numerically. In our examples, we chose $T_a = 2500\tau_g$, where τ_g is the characteristic timescale set by the pairwise interaction strength g.

In an ideal adiabatic process, every eigenstate of $\mathcal{I}(0)$ would evolve into a corresponding eigenstate of H_D, ensuring that $\mathcal{I}(T_a)$ commutes with H_D. To verify this commutativity, one can propagate $\mathcal{I}(t)$ with H_D for an additional random duration $T_b \in [50\tau_g, 100\tau_g]$. In the ideal adiabatic limit, since $\mathcal{I}(T_a)$ commutes with H_T, further evolution should leave the system unchanged, yielding $\mathcal{I}(T_a + T_b) = \mathcal{I}(T_a)$. Any deviation from this equality is a measure of adiabatic error, and the infidelity

$$1 - \frac{\mathrm{Tr}(\mathcal{I}(T_a)\mathcal{I}(T_a + T_b))}{\mathrm{Tr}(\mathcal{I}(T_a)^2)} \tag{5.48}$$

can be used as an estimate of this error.

This adiabatic construction of target operators leverages the quadratic scaling of computational effort associated with the dimension of the Lie algebra (Eq. (5.37)), bypassing the exponential complexity associated with the Hilbert space. Once the control target $\mathcal{I}_D$ is defined in this fashion, it can be used to design a time-dependent Hamiltonian $H(t)$ that achieves the target state transfer *diabatically* — that is, within a finite protocol duration T —, avoiding the impractical requirement of asymptotically slow adiabatic evolution.

5.3.3 Results – State transfer

Fig. 5.2 depicts the infidelity $\mathcal{J}$ (Eq. (5.19)) in realizing the ground states of the target Hamiltonians using numerically optimized time-dependent Hamiltonians for spin chains of length $n = 5$ to 50. Results are shown for three target states (discussed in Sec. 5.3.1): the GHZ-state of the Hamiltonian H_G (Eq. (5.38), red diamonds), the cluster-state of H_C (Eq. (5.39), blue squares) and the ground-state of the gapless Hamiltonian H_D (Eq. (5.40), black triangles). The optimisations for H_G and H_C are intentionally stopped when infidelities fall below 10^{-6}, while the optimization for H_D requires longer runtime and is therefore terminated once a maximum number of iterations, around 10^3, is reached.

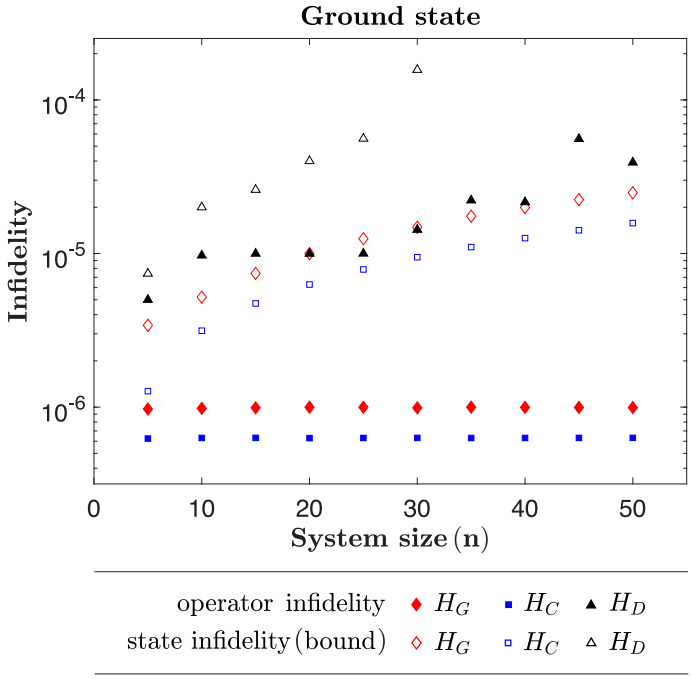

Figure 5.2: Infidelities (on a logarithmic scale) associated with preparing the ground states of H_G, H_C and H_D using optimized control pulses, plotted as a function of system size n for a linear spin chain governed by the Hamiltonian in Eq. (5.36). Solid shapes represent operator infidelities $\mathcal{J}$ (Eq. (5.19)). Open diamonds and squares indicate theoretical upper bounds on the corresponding state infidelities (Eq. (5.29)), open triangles represent state infidelities calculated using matrix product state representations. As result of the optimization, the values of the infidelities $\mathcal{J}$ are largely independent of the system size n. Although state infidelities do grow with system size, they remain well below 10^{-3} across the entire range studied, and can be further reduced with refined pulse shaping.

The empty red diamonds and empty blue squares depict the bound of Eq. (5.29) on the state fidelity for the ground states of H_G and H_C. The gap between the infidelities for the operators and the bounds on the state infidelity grows approximately linearly with the number of qubits (for more details, see Appendix F.3). However, this growing gap does not appear to pose a significant limitation in practical implementations, as state infidelities on the order of 10^{-5} are well below typical experimental noise levels, even for small system sizes [176].

The Hamiltonian H_D is gap-less, *i.e.*, the gap between the ground state and the first excited state vanishes in the thermodynamic limit. For finite-size chains, this gap gets progressively smaller with increasing system size, making the bound of Eq. (5.29) unsuited for H_D. The state fidelity in this case is thus estimated from numerical propagations with matrix product states[1] (see Sec. 3.4.3) for qubit numbers $n \leq 30$, as depicted by the empty triangles in Fig. 5.2. Despite the efficient MPS representation of the initial and final states, the states at in-between times created by the controlled dynamics for $n \geq 35$ require bond dimensions exceeding 500, rendering numerical propagation impractical. Both

[1]The ground state of H_D is computed with DMRG, and the final state is obtained by evolving the initial state $|\Psi_0\rangle$ with the MPO (matrix product operator) W^{II} method [177], where each time bin is further divided into 20 smaller steps to reduce error. All MPS calculations are done using the Tenpy package [178].

operator infidelities (Eq. (5.19)) and state infidelities are larger than for H_G and H_C. This is mostly due to the closing gap of H_D that results in increasing errors in the adiabatic evolution used to obtain the target $\mathcal{I}_D$. The optimization of the control pulses is made consistent with the estimated error of $\mathcal{I}_D$, *i.e.* the optimization algorithm is terminated when infidelities of the order of the accuracy of $\mathcal{I}_D$ are reached. For finite systems, this error can be further minimized if desired.

The state fidelities achieved across all cases in Fig. 5.2 demonstrate that optimal control remains effective for system sizes where direct state manipulation proves impractical. Any deviations from perfect fidelity are attributed to finite numerical accuracy. In the figure, the chosen accuracy does not exceed typical experimental tolerances, but higher precision can be achieved if technological advances demand more accurate solutions.

Interestingly, because of the constant interaction term g in the system Hamiltonian, there is a minimal time required for the state transfer, also referred to as quantum speed limit [179]. In order to obtain infidelities as low as in Fig. 5.2, the duration of the controlled dynamics needs to increase with the system size, but a modest approximately linear increase $\sim n\tau_g/4$ for H_G and H_C, and $\sim n\tau_g/2$ for H_D, with the qubit number n and the timescale $\tau_g = 2\pi/g$ given by the interaction constant g in Eq. (5.36), is sufficient for the ground state transfer. The time-dependence in the system Hamiltonian is parametrized in terms of piecewise constant pulses that are suitable for numerical optimization algorithms. To maintain a linear scaling of gate time with system size while keeping the control duration per time bin constant, the number of time bins in the pulse must also scale linearly with the system size n. For the results shown in Fig. 5.2, pulses were constructed with $10n$ time bins, except for H_G which required $20n$ bins to achieve the desired precision. The exact number of bins, however, can be adjusted based on the target infidelity, allowing for flexibility in balancing computational effort and control accuracy.

Despite the challenging goal of realizing eigenstates of Hamiltonians beyond pairwise interactions, the necessary control pulses do not exhibit undesired characteristics like excessively high amplitudes or frequencies. Even optimizations without penalty for high amplitudes do not yield amplitudes exceeding the coupling strength g by a factor of 2. The spectral width obtained with a standard optimization (see Appendix F.2) is not excessive, but it is broader than necessary. It is thus possible to smooth pulses with only a moderate increase in infidelity, and to use these smoothed pulses as initial condition for further optimization.

Fig. 5.3 displays the optimized control pulses for a 50-spin chain, showing the time-dependent amplitudes of the Z-drive terms $f_i(t)$ (for each qubit $i = 1, \cdots, 50$) and the boundary X-drive $w(t)$ (applied equally to both ends of the chain, $w_1 = w_n = w$). The heat-map organizes the controls vertically, with each row corresponding to a specific control parameter $u_k(t)$, color-coded from approximately -2 (blue) to 2 (red). The horizontal axis represents normalized time in units of the interaction timescale τ_g, tracing the evolution of each control $u_k(t)$ from protocol start to finish.

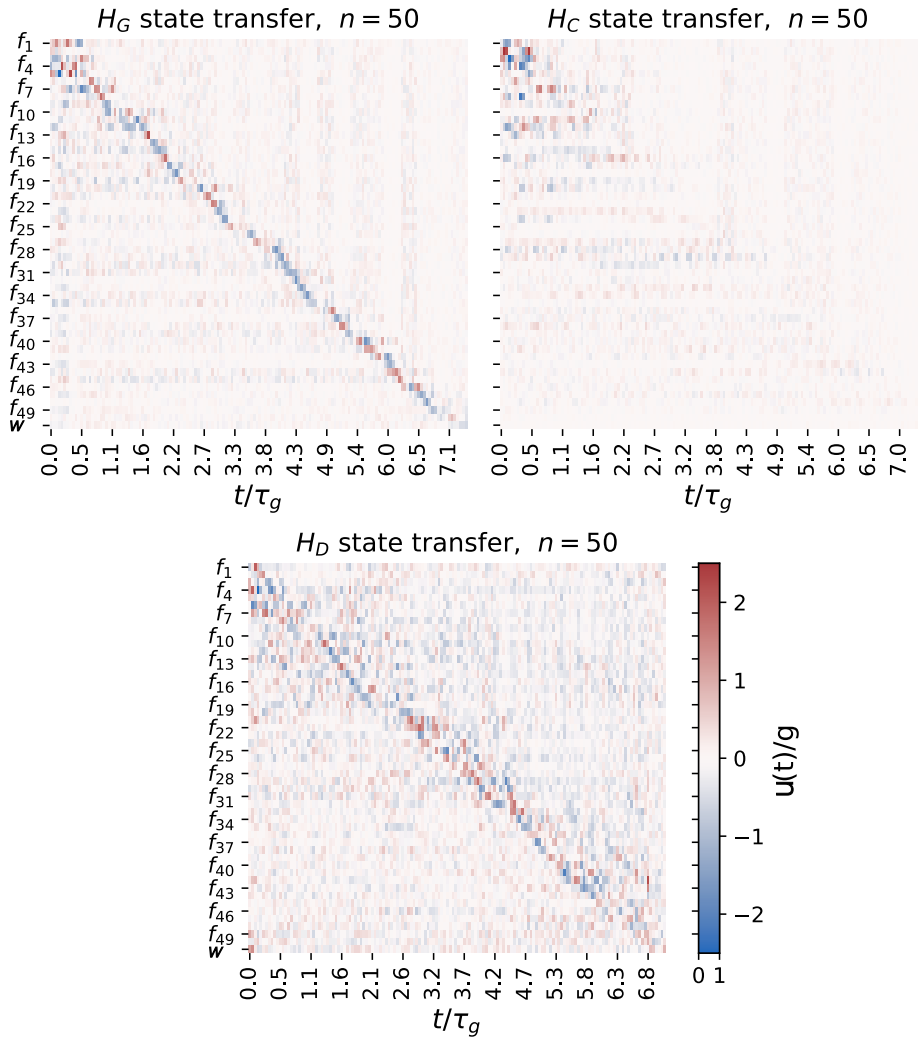

Figure 5.3: Optimal control amplitudes used for state preparation in a spin chain with $n = 50$ qubits. The figure is divided into three panels, each corresponding to one of the control problems: preparation of the ground states of H_G, H_C and H_D. It depicts $f_i(t)$ (for $i = 1, \cdots, 50$) and $w(t)$ (where the boundary X-terms are driven equally, *i.e.* $w_i = w$ for all i) for the Hamiltonian $H(t)$ in Eq. (5.36). The heat-map organizes the controls along the y-axis, with each row representing a specific control $u_k(t)$ and its amplitude ranging approximately from -2 to 2 (from blue to red). The x-axis represents the protocol time, normalized to the interaction timescale τ_g. Thus, for each row, moving from left to right traces the time evolution of a single control $u_k(t)$.

For the GHZ state (top left panel), the Z-drive pulses $f_i(t)$ exhibit a sequential activation pattern: spins at the chain's left end (lower indices j) peak first, followed progressively by spins toward the right. This diagonal structure in the heat-map suggests a wave-like propagation of control across the chain. In contrast, the cluster state (top right panel) requires intense Z-drive activity concentrated in the first third of the protocol, predominantly involving a subset of spins, followed by weak but essential driving (faint heat-map coloring) to achieve high fidelity.

The preparation of H_D's ground state (bottom panel) demands the most intricate control profile. While a sequential activation akin to the GHZ case is faintly visible, nearly

all Z-drive terms $f_i(t)$ remain active throughout the protocol, reflecting the heightened complexity of preparing states governed by gapless Hamiltonians.

The pulse shapes for smaller chains exhibit qualitatively similar structures, but both the duration and the number of time bins scale approximately proportionally to the system size. The pulse data for all spins and system sizes ranging from 5 to 50 is provided in Ref. [180].

5.4 Realization of propagators

The preparation of eigenstates for Hamiltonians with tailored interactions plays a pivotal role in computational problems such as quantum optimization and adiabatic algorithms [181, 182]. In quantum simulation, however, it is of interest to explore the dynamics induced by a given Hamiltonian. Such applications require — in addition to an initial state preparation and a final measurement — the realization of propagators (see Sec. 3.4 for a detailed discussion on the topic). Realizing propagators governed by Hamiltonians beyond pairwise interactions — such as H_G, H_C, H_D discussed above in Sec. 5.3.1 — is inherently infeasible using static interactions alone. Such multi-spin couplings can only be achieved through time-dependent control, making IQC well-suited for this task. To this end, we design time-dependent control functions $f_j(t)$, $w_1(t)$ and $w_n(t)$ in the system Hamiltonian $H(t)$ (Eq. (5.36)), such that the resultant propagator is of the form $\exp(-iH_T T)$ with a Hamiltonian including more-than-pairwise interactions at a given time T.

The realization of such effective Hamiltonians is commonly pursued based on Floquet theory [183] and the present approach allows us to go beyond the common perturbative treatment that is typically required [184].

The realization of desired propagators is exemplified here in more detail for

$$U_G = \exp\Big(-i\frac{\pi}{8}H_G\Big)\ , \qquad U_C = \exp\Big(-i\frac{\pi}{8}H_C\Big)\ , \qquad U_D = \exp\Big(-i\frac{\pi}{8}H_D\Big)\ , \tag{5.49}$$

where H_G, H_C and H_D are the Hamiltonians defined in Eqs. (5.38), (5.39), and (5.40), respectively. These propagators are to be implemented through the system dynamics governed by the time-dependent Hamiltonian $H(t)$ in Eq. (5.36).

5.4.1 Objective function

As discussed in Sec. 5.2.5, implementing a deterministic quantum gate typically requires more than a single pair of initial and final operators, $\{\mathcal{I}(0), \mathcal{I}_T\}$. Instead, multiple pairs $\{\mathcal{I}_j(0), \mathcal{I}_{Tj}\}$ must be considered to evaluate the infidelity $\mathcal{J}_{U_T}$ in Eq. (5.34). The key challenge, which ultimately dictates the computational cost, is determining how many and which initial conditions $\mathcal{I}_j(0)$ are necessary to construct a reliable objective function.

In the present case, for the initial conditions

$$\mathcal{I}_j(0) = Z_j \ , \qquad \text{for } j \in [1, n] \ , \tag{5.50a}$$

$$\mathcal{I}_{j+n}(0) = X_j X_{j+1} \ , \qquad \text{for } j \in [1, n-1] \ , \tag{5.50b}$$

$$\mathcal{I}_{2n}(0) = X_1 + X_n \ , \tag{5.50c}$$

the infidelity $\mathcal{J}_{U_T}$ in Eq. (5.34) vanishes exactly for the target gate $\mathcal{U}_T$, provided $\mathcal{U}_T$ is realizable with the Hamiltonian $H(t)$ in Eq. (5.36). That is to say that the relation $U\mathcal{I}_j(0)U^\dagger = \mathcal{U}_T\mathcal{I}_j(0)\mathcal{U}_T^\dagger$ can be simultaneously satisfied for all these choices $\mathcal{I}_j(0)$ only if $U = \mathcal{U}_T \exp(i\varphi)$, where $\exp(i\varphi)$ is a global phase factor. To see that this is indeed the case, it is helpful to notice that the set of relations $U\mathcal{I}_j(0)U^\dagger = \mathcal{U}_T\mathcal{I}_j(0)\mathcal{U}_T^\dagger$ is equivalent to the set of commutation relations

$$[\mathcal{U}_T^\dagger U, \mathcal{I}_j(0)] = 0 \ . \tag{5.51}$$

As shown in Sec. F.1 of the Appendix, the only operators that commute with each of the operators in Eq. (5.50) are multiples of the identity, which leaves $\mathcal{U}_T^\dagger U = \exp(i\varphi)\mathbb{I}$ as the only solution. While this provides a faithful objective function, its use in an optimisation implies the evaluation of $2n$ summands in Eq. (5.34) at any step in the optimisation. For the sake of efficiency, it can be preferable to use the objective functional $\mathcal{J}_{\mathcal{U}_T}$ with only five initial conditions

$$\mathcal{I}_1(0) = \sum_k Z_{2k+1} \ , \tag{5.52a}$$

$$\mathcal{I}_2(0) = \sum_k Z_{2k} \ , \tag{5.52b}$$

$$\mathcal{I}_3(0) = \sum_k X_{2k+1}X_{2k+2} \ , \tag{5.52c}$$

$$\mathcal{I}_4(0) = \sum_k X_{2k}X_{2k+1} \ , \tag{5.52d}$$

$$\mathcal{I}_5(0) = X_1 + X_n \ . \tag{5.52e}$$

While the initial conditions given by Eq. (5.52) theoretically permit minimization of the objective function with propagators other than the target $\mathcal{U}_T$, in practice, numerical optimizations do not appear to converge to such solutions. Since verification requires only a single propagation, it is numerically advantageous to use this objective function (with Eqs. (5.52) as initial conditions) for the optimisation, and eventually use the faithful objective function (with Eqs. (5.50) as initial conditions) only for verification of the final solution.

5.4.2 Results – Propagators

Fig. 5.4 depicts the infidelities $\mathcal{J}_{\mathcal{U}_T}$, defined in Eq. (5.34), using the initial conditions in Eq. (5.50), as function of system size n. The solid red diamonds, blue squares, and black triangles correspond to the target unitaries $U_G = \exp(-i\pi/8\, H_G)$, $U_C = \exp(-i\pi/8\, H_C)$

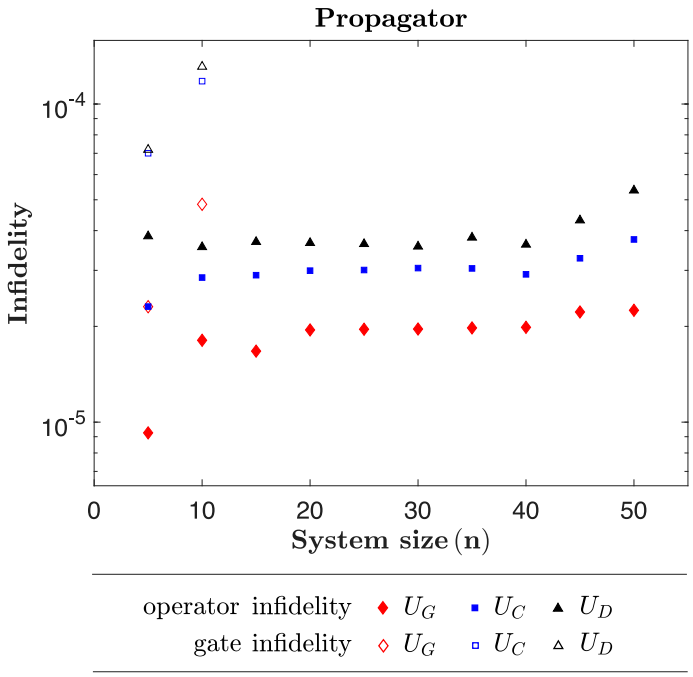

Figure 5.4: Infidelities (on a logarithmic scale) associated with simulating the quantum gates U_G, U_C and U_D using optimized control pulses, plotted as a function of system size n for a linear spin chain governed by the Hamiltonian in Eq. (5.36). Solid shapes represent operator infidelities $\mathcal{J}_{U_T}$ (Eq. (5.34)), while empty shapes depict gate infidelities. As result of the optimization, the values of the infidelities $\mathcal{J}_{U_T}$ are largely independent of the system size n. Although gate infidelities do increase with system size, they remain below the error threshold necessary for fault-tolerant quantum computation.

and $U_D = \exp(-i\pi/8\, H_D)$, respectively. The optimized protocols employ piecewise constant pulses with durations $\sim n\tau_g$ (using $20n$ time bins) for U_G, and $\sim \tau_g$ (using $10n$ bins) for U_C and U_D.

The empty shapes in the figure show actual gate infidelities, $1 - \left|\mathrm{tr}\left(U^\dagger(T)\mathcal{U}_T\right)\right|^2/2^{2n}$, obtained with numerically exact integration of the Schrödinger equation. Since this type of verification is limited by the exponential scaling of the Hilbert space, actual gate infidelities are shown for up to $n = 10$ only. Within what is numerically achievable, the gate infidelities do confirm the success of the control protocols designed with the present framework, and similarly to the task of state preparation, the realisation of desired propagators is achieved with infidelities far below of what could be experimentally resolved with existing technology [136, 137].

Also, the duration of controlled dynamics required for the realization of a desired propagator has a fundamental limit given by the physical timescale $\tau_g = 2\pi/g$. The numerically observed minimal time required to implement the unitaries induced by H_C and H_D is independent of the system size, but the minimal time required to implement the unitary induced by H_G scales linearly in the number of qubits. Given that H_C and H_D contain at most three-body interactions, whereas H_G contains an n-body interaction — where the interaction range increases with the system size n — the observed scaling of the minimal

durations for controlled dynamics appears consistent with the complexity of the underlying problem. This consistency suggests that the obtained solutions are likely close to the true global optimum of the control problem.

Fig. 5.5 depicts optimized driving patterns $f_i(t)$ and $w(t)$ (with $w_1(t) = w_2(t) = w(t)$ for simplicity), obtained using the same smoothing and reoptimization procedure as in the state preparation protocols. The optimal driving pattern for U_G (top left panel) reveals a two-phase structure. During the first half of the evolution ($t \in [0, 25\tau_g]$), all Z-drives $f_i(t)$ and X-drives $w(t)$ are activated uniformly across qubits, while the second half ($t \in [25\tau_g, 50\tau_g]$), is dominated by uncontrolled dynamics under the always-on XX couplings. This suggests that the initial controlled dynamics prepares the system into a state that evolves naturally under XX-interactions toward the target state. The full duration of $50\tau_g$ appears essential for achieving high fidelity, highlighting the intricate interplay between controlled and uncontrolled dynamics.

The driving patterns for U_C (top right panel) exhibit a distinct profile. Here, the Z- and X-drives $f_i(t)$, $w(t)$ follow a slowly decaying sinusoidal profile, oscillating between $-4g$ to $4g$ initially and gradually narrowing to $-g$ to g over time. This low-frequency modulation contrasts sharply with the uniform activation seen in U_G.

Finally, the driving profiles for U_D resemble those of U_C, featuring similar sinusoidal oscillations with decaying amplitude. This similarity suggests that the additional XX-coupling term $\sum_k X_k X_{k+1}$ in H_G (compared to H_C) requires only minor adjustments to the optimal pulses designed for U_C, along with a slightly longer gate duration.

Crucially, the notably longer duration required for U_G ($50\tau_g$), compared to U_C and U_D (both of which are shorter than $\tau_g/2$), arises from the inherent difficulty of simulating the n-body interaction $\prod_{i=1}^{n} Z_i$ (see Eq. (5.38)) using a Hamiltonian restricted to pairwise couplings $X_j X_{j+1}$ and single-qubit terms (X_j, Z_j). To see why, consider how effective multi-spin interactions are synthesized iteratively through commutators of the available terms.

When two noncommuting operations A and B are applied sequentially for a short time Δt, the combined effect is not merely $A + B$, but includes a correction from their nested commutators. Specifically, the BCH expansion gives

$$e^{-iA\Delta t} e^{-iB\Delta t} = \exp\left(-i(A+B)\Delta t - \frac{1}{2}[A,B]\Delta t^2 + \mathcal{O}(\Delta t^3) \right) , \tag{5.53}$$

which reflects the leading correction is proportional to $[A, B]$, appearing at order $\mathcal{O}(\Delta t^2)$. For example, starting with the two-qubit operators $X_j X_{j+1}$ (naturally present in the Hamiltonian) and $Y_{j+1} X_{j+2}$ (which arises via the commutator $[X_{j+1} X_{j+2}, Z_{j+1}]$), their nested commutator produces a three-qubit interaction

$$[X_j X_{j+1}, Y_{j+1} X_{j+2}] \propto X_j Z_{j+1} X_{j+2} , \tag{5.54}$$

which emerges after a total duration of $2\Delta t$, and with an effective strength proportional to Δt^2.

Building on this concept, synthesizing an n-body interaction requires iteratively constructing higher-order commutators. Each additional step introduces another factor of Δt, such that an n-body interaction term emerges at order $(\Delta t)^{n-1}$. This scaling implies a total required evolution time of approximately

$$(n-1)\Delta t \sim n\Delta \ . \tag{5.55}$$

To ensure the generated interaction strength is physically meaningful within the system Hamiltonian $H(t)$ in Eq. (5.36), the elementary time step Δt must be comparable to the natural timescale τ_g (*i.e.* $\Delta t \sim \tau_g$). Substituting this, we conclude that the total duration required to synthesize the n-body interaction $\prod_{i=1}^{n} Z_i$ scales as $\sim n\tau_g$, consistent with the observed $\sim 50\tau_g$ for $n = 50$.

Finally, pulse data for smaller system sizes, ranging from $n = 5$ to 50 are provided in Ref. [180], with the optimal solutions exhibiting the same qualitative behavior.

5.5 More sets of operators with polynomial scaling

While the discussion in Secs. 5.3 and 5.4 is meant to exemplify the use of IQC for actual control problems, a similarly detailed discussion for further examples would be repetitive. The goal of this section is thus to provide further insight into sets of operators for which the present approach provides an advantage over treatments in terms of state vectors. In the following, a few exemplary algebras with polynomial scaling are provided for different interaction geometries. The corresponding commutation relations are available at Ref. [180].

5.5.1 Spin chain

The Lie algebra defined in Eq. (5.37) (discussed in Section 5.3) corresponds to that of an extended one-dimensional Ising model. While the elements of this Lie algebra are listed in that section, we now provide a detailed analysis of how its dimension scales with the number of qubits n. The system Hamiltonian includes

$$\mathfrak{h}_j = Z_j \ , \tag{5.56a}$$

with $j \in [1, n]$,

$$\mathfrak{h}_{j+n} = X_j X_{j+1} \ , \tag{5.56b}$$

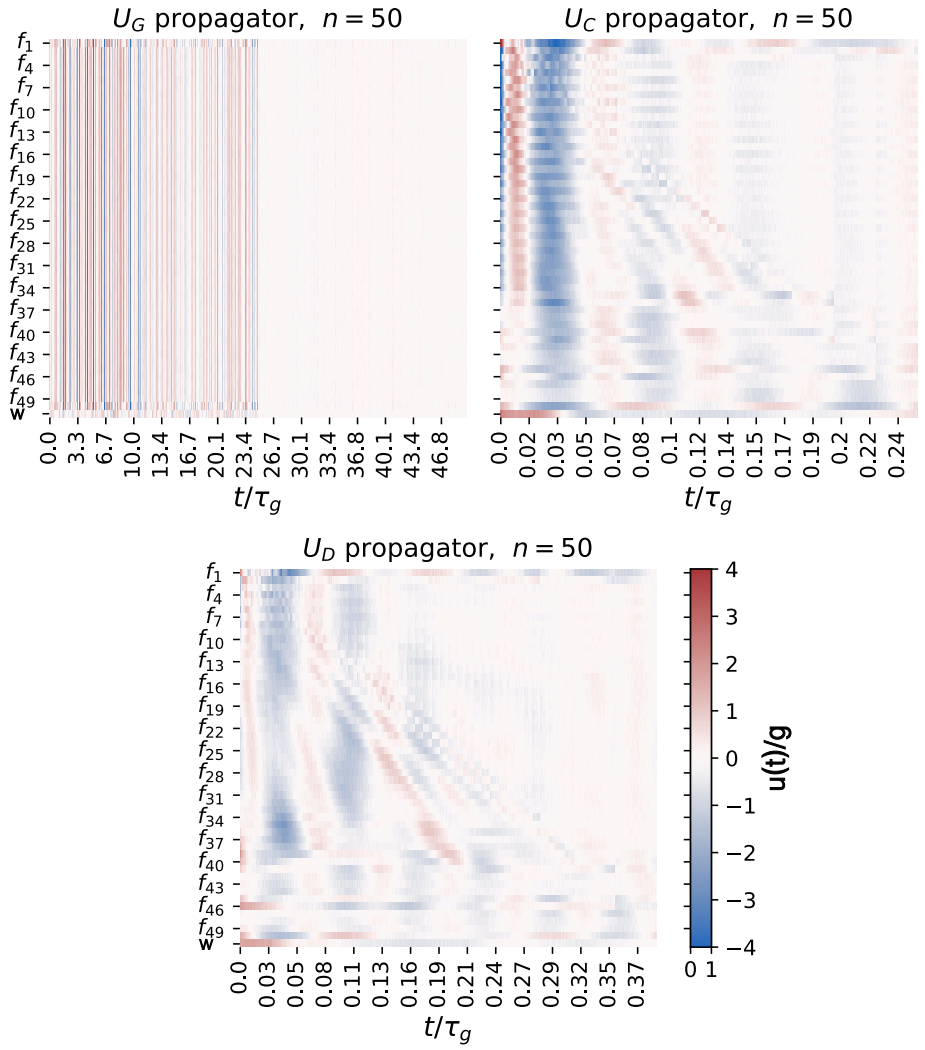

Figure 5.5: Optimal control amplitudes used for quantum simulation in a spin chain with $n = 50$ qubits. The figure is divided into three panels, each corresponding to one of the control problems: simulation of the gates U_G, U_C and U_D. It depicts $f_i(t)$ (for $i = 1, \cdots, 50$) and $w(t)$ (where the boundary X-terms are driven equally, *i.e.* $w_i = w$ for all i) for the Hamiltonian $H(t)$ in Eq. (5.36). The heat-map organizes the controls along the y-axis, with each row representing a specific control $u_k(t)$ and its amplitude ranging approximately from -2 to 2 (from blue to red). The x-axis represents the protocol time, normalized to the interaction timescale τ_g. Thus, for each row, moving from left to right traces the time evolution of a single control $u_k(t)$.

with $j \in [1, n-1]$, and

$$\mathfrak{h}_{2n} = X_1 \ , \tag{5.56c}$$

$$\mathfrak{h}_{2n+1} = X_n \ . \tag{5.56d}$$

Commutators between terms in Eq. (5.56a) and terms in Eq. (5.56b) yield operators of the form $X_j Y_{j+1}$ and $Y_j X_{j+1}$, and commutators between those and terms in Eq. (5.56a) yields operators of the form $Y_j Y_{j+1}$. The Lie algebra thus contain the terms

$$X_j X_{j+1} \ , \ X_j Y_{j+1} \ , \ Y_j X_{j+1} \ , \ Y_j Y_{j+1} \ . \tag{5.57}$$

Commutators between such terms yield operators of the form $A_j Z_{j+1} B_{j+2}$ (with A and $B \in \{X, Y\}$), and nested commutators with several terms of Eq. (5.57) yield operators of the form

$$A_j Z_{j+1} \dots Z_{j+k} B_{j+k+1} \ . \tag{5.58}$$

Commutators between these k+2–body interactions and the terms X_1 and X_n (Eqs. (5.56c) and (5.56d)) yields the terms

$$Z_1 \dots Z_l A_{l+1} \ , \tag{5.59a}$$

$$A_{n-l} Z_{n-l+1} \dots Z_n \ , \tag{5.59b}$$

and

$$Z_1 \dots Z_n \ . \tag{5.59c}$$

Those are exactly the terms specified in Eq. (5.37), and they do indeed form a closed Lie algebra.

With n terms in Eq. (5.56a), $2n(n-1)$ terms in Eq. (5.58) (that include Eq. (5.56b) and Eq. (5.57) as special cases), $2n-1$ terms from Eqs. (5.59a) and (5.59b) each, as well as one term in Eqs. (5.56c), Eqs. (5.56d) and (5.59c) respectively, the total number of elements in the Lie algebra is $d = 2n^2 + 3n + 1$.

5.5.2 Driven spin comb

The interaction geometry shown in Fig. 5.6(a) — a comb-shaped lattice — generates a Lie algebra whose dimension scales quadratically with the number of qubits n. This structure, inspired by protocols for topologically protected quantum information processing [185], comprises two interconnected chains: a primary chain of $m = n/2$ qubits with nearest-neighbor interactions, and a secondary chain of m qubits, each coupled exclusively to its corresponding qubit on the primary chain. Within this geometry, Pauli operators are labeled with two indices: the lower index denotes the qubit's position within its chain, while the upper index distinguishes the chain itself, with 1 assigned to the primary chain and 2 to the secondary chain. For example, the operator X_j^1 acts on the j-th qubit of the primary chain, whereas Z_j^2 acts on the j-th qubit of the secondary chain.

The elementary Hamiltonian terms $\mathfrak{h}_i$ (for the definition of a system Hamiltonian in Eq. (5.3)) are given by

$$\mathfrak{h}_j = Z_j^1 Z_j^2 \ , \tag{5.60a}$$

with $j \in [1, m]$,

$$\mathfrak{h}_{j+m} = X_j^2 \ , \tag{5.60b}$$

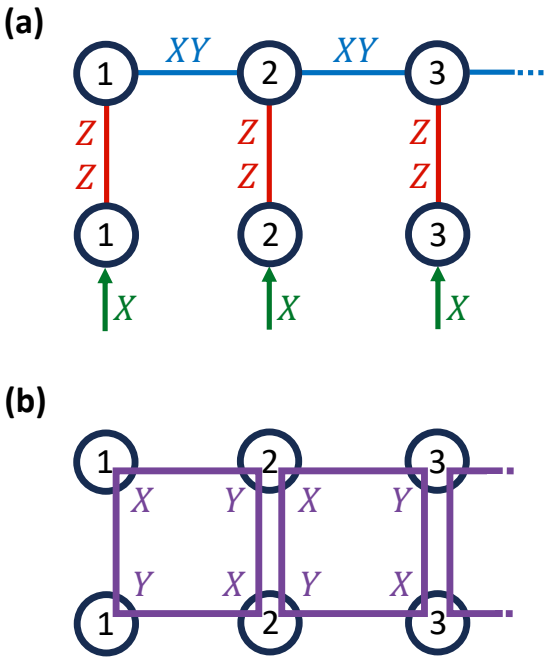

Figure 5.6: Spin comb with nearest-neighbor XY interactions in the top chain and ZZ interactions between spins of different chains (inset (a)). Single-spin X-driving (inset (a)) enables the realization of effective dynamics with four-spin interactions matching the Toric-code plaquette operators Eq. (5.63) (inset (b)).

with $j \in [1, m]$, and

$$\mathfrak{h}_{j+2m} = X^1_j Y^1_{j+1} \ , \tag{5.60c}$$

with $j \in [1, m-1]$.

In order to understand the Lie algebra generated by Eqs. (5.60), and, in particular its scaling with m, it is instructive to start with the Lie algebra generated by the terms in Eq. (5.60c) only. The terms in Eq. (5.60c) form a subset of the terms in Eq. (5.57), and similarly to the discussion in Sec. 5.5.1 the resultant Lie algebra is comprised of the terms

$$X^1_j Z_{jk} Y^1_{j+k+1} \ , \tag{5.61}$$

with $j + k + 1 \leq m$ and the short-hand notation $Z_{jk} = \prod_{i=1}^{k} Z^1_{i+j}$.

Commutation between the terms in Eq. (5.61) and the terms in Eq. (5.60a) yields the terms

$$Y^1_j Z_{jk} Y^1_{j+k+1} \ Z^2_j \ , \tag{5.62a}$$
$$X^1_j Z_{jk} X^1_{j+k+1} \ Z^2_{j+k+1} \ , \tag{5.62b}$$
$$Y^1_j Z_{jk} X^1_{j+k+1} \ Z^2_j Z^2_{j+k+1} \ . \tag{5.62c}$$

With $m(m-1)/2$ terms in Eq. (5.61) (that includes the elements in Eq. (5.60c)), 3 terms

in Eq. (5.62), and m elements in Eq. (5.60a), the Lie algebra generated by the terms in Eq. (5.60a) and Eq. (5.60c) thus contain $2m^2 - m$ terms.

Commutation with the terms in Eq. (5.60b) yields terms of similar structure to the terms in Eq. (5.62), but with operators Z_j^2 and/or Z_{j+k+1}^2 replaced by the corresponding operator of X or Y type. The number of operators of the type in Eqs. (5.62a) and (5.62b) is thus increased by a factor of 3, and the number of operators of the type in Eq. (5.62c) is increased by a factor of 9. The Lie algebra generated by all the terms in Eq. (5.60) thus has $3m(3m-1)/2$ terms. Within this Lie algebra are terms of the form

$$Q_j = X_j^1 Y_{j+1}^1 \, Y_j^2 X_{j+1}^2 \ , \tag{5.63}$$

corresponding to a four-body interaction on four spins forming a square as depicted in Fig. 5.6(b). The operators Q_j and Q_{j+1} act on two different quartets of spins with an overlap on two spins (with index $j+1$). The factor of Q_j on these spins is given by $Y_{j+1}^1 X_{j+1}^2$, and the factor of Q_{j+1} on these spins is given by $X_{j+1}^1 Y_{j+1}^2$. All the operators Q_j are thus mutually commuting, even though their single-spin factors on overlapping spins are not mutually commuting. The present example is thus suitable for the realization of a ribbon of plaquette operators of the toric code [153].

5.5.3 Hexagonal spin ladder

Fig. 5.7 depicts a spin-ladder with hexagonal structures, similar the Kitaev honeycomb model [153], but with the two interactions of the spin at the bottom of each hexagon commuting with each other. This interaction geometry results in a Lie-algebra of dimension $(25n^2 - 40n + 12)/32$ with $n = 4n_h + 2$ spins, where n_h is the number of hexagons. In contrast, the interaction geometry of the original Kitaev honeycomb model scales exponentially $(2^{n_h} n\,(n-1)\,/2)$.

The individual operators $\mathfrak{h}_j$ entering the system Hamiltonian read

$$\mathfrak{h}_j = Y_{2j-1}^1 Y_{2j}^1 \ , \tag{5.64a}$$
$$\mathfrak{h}_{j+(m-1)/2} = Z_{2j}^1 Z_{2j+1}^1 \ , \tag{5.64b}$$
$$\mathfrak{h}_{j+m-1} = X_{2j}^2 X_{2j+1}^2 \ , \tag{5.64c}$$
$$\mathfrak{h}_{j+(3m-3)/2} = Z_{2j-1}^2 X_{2j}^2 \ , \tag{5.64d}$$
$$\mathfrak{h}_{l+2m-2} = X_{2l-1}^1 Y_{2l-1}^2 \ , \tag{5.64e}$$

with $m = n/2$, $j \in [1, (m-1)/2]$, $l \in [1, (m+1)/2]$. The corresponding Lie algebra can be constructed systematically, following a similar approach to the discussion in Sec. 5.5.1. However, due to the more intricate interaction geometry, the explicit form of its elements is more complex. For clarity, the full derivation is provided in Appendix F.4.

Crucially, the Lie algebra contains the 6-body plaquette operators

$$P_j = Z_{2j-1}^1 X_{2j}^1 Y_{2j+1}^1 Y_{2j-1}^2 X_{2j}^2 Z_{2j+1}^2 \ , \tag{5.65}$$

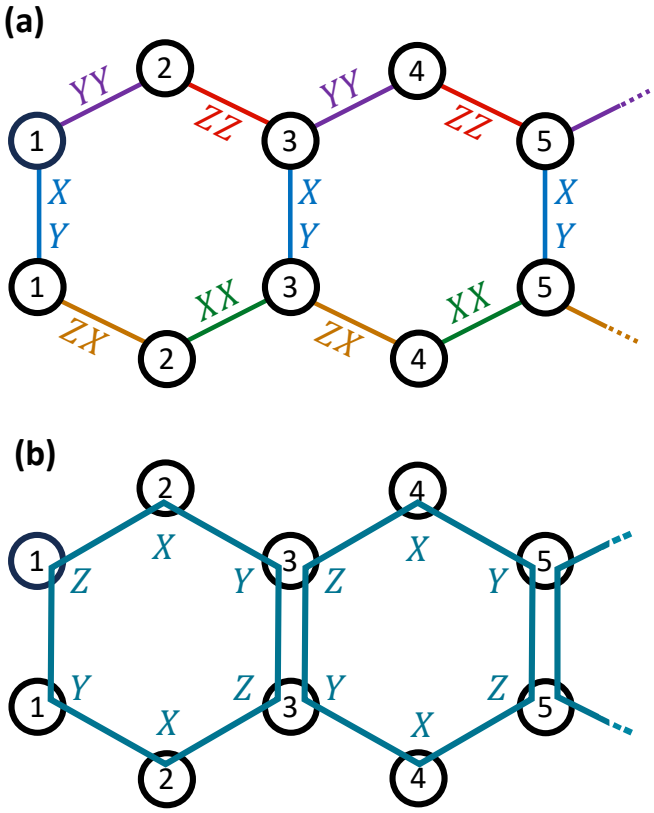

Figure 5.7: A spin-ladder with hexagonal structures, where each spin interacts with its nearest neighbors. In contrast to the Kitaev honeycomb model, that includes only mutually non-commuting interactions for any spin, there is one spin (at the bottom of each hexagon) that has two commuting interactions (inset (a)). This interaction geometry results in a Lie algebra of quadratic size with elements including the plaquette operators (Eq. (5.65), inset (b)) that are crucial in the field of topological stabilizer codes.

which are depicted schematically in Fig. 5.7b. These operators, that commute with the Kitaev honeycomb Hamiltonian [153], form a central part in the realization of error-correcting surface codes on hexagonal lattices [186, 187]. In particular, plaquette operators together with two-body operators like $X^1_{2l-1}Y^2_{2l-1}$, can form the basis for stabilizer operators, as exemplified by the XYZ^2 topological stabilizer code [188]. The present framework can thus be used to aid the realization of quantum error correction.

5.6 Beyond Lie algebras

In the examples discussed so far, the operator sets $\{\mathfrak{a}_j\}$ used to expand the operator $\mathcal{I}(t)$ have been chosen to coincide with the Lie algebra generated by the elements of the system Hamiltonian $\{\mathfrak{h}_j\}$. However, this alignment is not a strict requirement. In fact, in many cases, the Lie algebra associated with $\{\mathfrak{h}_j\}$ grows exponentially or with a high polynomial degree in the system size, making it impractical for expanding $\mathcal{I}(t)$. Despite this, it is still possible to construct a set $\{\mathfrak{a}_j\}$ of polynomial size that can be effectively used for IQC, and in the following we present a systematic approach for this construction.

5.6.1 Block diagonalization of the structure constant matrices

This section formalizes a systematic procedure to decompose a set of operators into dynamically independent subsets under the action of a Hamiltonian. The objective is to identify substructures within the operator algebra that evolve independently, allowing the dynamics of $\mathcal{I}(t)$ to be analyzed within lower-dimensional, decoupled subspaces, thereby simplifying the overall complexity of the simulation. Consider a physical system governed by the Hamiltonian with generators $\{\mathfrak{h}_k\}_{k=1}^{d_0}$, and let $\{\mathfrak{a}_j\}_{j=1}^{d}$ be a set of operators representing the basis of expansion for $\mathcal{I}(t)$. The dynamics of $\mathcal{I}(t)$ are encoded in the commutation relations

$$[\mathfrak{a}_j, \mathfrak{h}_k] = -i \sum_{l=1}^{d} \lambda_{lj}^{k} \mathfrak{a}_l \ . \tag{5.66}$$

To isolate independent dynamical sectors, we introduce a linear transformation defined by an invertible $d \times d$ matrix $M \in GL(d, \mathbb{C})$ that maps the original operators $\{\mathfrak{a}_j\}_{j=1}^{d}$ to a new set new operators $\{\mathfrak{b}_j\}_{j=1}^{d}$, such that

$$\mathfrak{b}_j = \sum_{p=1}^{d} M_{jp} \mathfrak{a}_p \ , \tag{5.67}$$

with the inverse transformation given by

$$\mathfrak{a}_p = \sum_{j=1}^{d} [M^{-1}]_{pj} \mathfrak{b}_j \ . \tag{5.68}$$

The objective is to select M such that the transformed operators $\{\mathfrak{b}_j\}$ partition into disjoint subsets $\{\mathfrak{b}_j^{(1)}\}, \{\mathfrak{b}_j^{(2)}\}, \cdots$, each satisfying closed commutation relations within their respective subsets. For a subset labeled by s, the commutation relations take the form

$$[\mathfrak{b}_j^{(s)}, \mathfrak{h}_k] = -i \sum_{l=1}^{w_s} \tilde{\lambda}_{lj}^{k(s)} \mathfrak{b}_l^{(s)} \ , \tag{5.69}$$

with $w_s \leq d$, and $\tilde{\lambda}_{lj}^{k(s)}$ are subset-specific structure constants. When all subsets are combined, the full set $\{\mathfrak{b}_j\}$ satisfies

$$[\mathfrak{b}_j, \mathfrak{h}_k] = -i \sum_{l=1}^{d} \tilde{\lambda}_{lj}^{k} \mathfrak{b}_l \ , \tag{5.70}$$

with the structure constants matrix $\tilde{\Lambda}^k$ assuming a block-diagonal form

$$\tilde{\Lambda}^k = \begin{pmatrix} \tilde{\Lambda}^{k(1)} & 0 & \cdots & 0 \\ 0 & \tilde{\Lambda}^{k(2)} & \cdots & 0 \\ \vdots & \vdots & \ddots & \vdots \\ 0 & 0 & \cdots & \tilde{\Lambda}^{k(r)} \end{pmatrix} \ , \tag{5.71}$$

where each block $\tilde{\Lambda}^{k(s)}$ corresponds to the structure constants of subset s.

The transformation matrix M is determined by enforcing the block-diagonal structure of $\tilde{\Lambda}^k$. Substituting the expressions for $\mathfrak{b}_j$ and $\mathfrak{a}_p$ into the commutation relations, we derive the conditions that M must satisfy. Specifically, inserting Eq. (5.67) into Eq. (5.70) yields

$$\sum_{p=1}^{d} M_{jp}[\mathfrak{a}_p, \mathfrak{h}_k] = -i \sum_{l=1}^{d} \sum_{q=1}^{d} \tilde{\lambda}_{lj}^{k} M_{lq} \mathfrak{a}_q \ . \tag{5.72}$$

Applying Eq. (5.66) to the left-hand side leads to

$$\sum_{p=1}^{d} \sum_{m=1}^{d} M_{jp} \lambda_{mp}^{k} \mathfrak{a}_m = \sum_{l,q=1}^{d} \sum_{q=1}^{d} \tilde{\lambda}_{lj}^{k} M_{lq} \mathfrak{a}_q \ . \tag{5.73}$$

Using the antisymmetry of the structure constants, $\lambda_{mp}^{k} = -\lambda_{pm}^{k}$, on both sides, we obtain

$$\sum_{p=1}^{d} \sum_{m=1}^{d} M_{jp} \lambda_{pm}^{k} \mathfrak{a}_m = \sum_{l=1}^{d} \sum_{q=1}^{d} \tilde{\lambda}_{jl}^{k} M_{lq} \mathfrak{a}_q \ , \tag{5.74}$$

which implies the relation in matrix form

$$M\Lambda^k = \tilde{\Lambda}^k M \ , \quad \text{for all } k \ , \tag{5.75}$$

or equivalently

$$\tilde{\Lambda}^k = M\Lambda^k M^{-1} \ , \quad \text{for all } k \ . \tag{5.76}$$

This equation reveals that M acts as a similarity transformation, conjugating the original structure constant matrices Λ^k into the block-diagonal form $\tilde{\Lambda}^k$. Each block $\tilde{\Lambda}^{k(s)}$ in $\tilde{\Lambda}^k$ corresponds to a subset $\{\mathfrak{b}_j^{(s)}\}$, ensuring that the commutation relations within a subset depend only on its own operators. The physical significance of this decomposition lies in the decoupling of dynamical evolution. Operators within a subset $\{\mathfrak{b}_j^{(s)}\}$ evolve independently of those in other subsets, effectively partitioning the system into non-interacting subsystems. This mirrors the concept of normal modes in classical and quantum mechanics, where collective coordinates diagonalize the equations of motion.

The problem of finding a matrix M that simultaneously block-diagonalizes a set of matrices $\{\Lambda^k\}$ has been explored in various fields, particularly in mathematical programming and semidefinite programming (SDP), and has been subjected to both numerical and analytical treatments. In order to determine the matrix M, it will prove useful to consider a Hermitian matrix X that commutes with Λ^k [189], *i.e.*

$$\left[\Lambda^k, X\right] = 0 \ , \quad \text{for all } k \ . \tag{5.77}$$

Since X is Hermitian, it admits a spectral decomposition of the form

$$X = PDP^\dagger \ , \tag{5.78}$$

which, when rearranged, gives

$$D = P^\dagger X P \ , \tag{5.79}$$

where $D = \mathrm{diag}(\sigma_1, \ldots, \sigma_d)$ is a diagonal matrix with real entries (potentially with some repeated eigenvalues σ_i), and P is a unitary matrix whose columns correspond to the eigenvectors of X. If Eq. (5.77) holds, then

$$P^\dagger \left(\Lambda^k P P^\dagger X - X P P^\dagger \Lambda^k \right) P = 0 \ . \tag{5.80}$$

Using Eq. (5.78), this simplifies to

$$\left(P^\dagger \Lambda^k P \right) D - D \left(P^\dagger \Lambda^k P \right) = 0 \ . \tag{5.81}$$

Expanding in components,

$$\sum_j [P^\dagger \Lambda^k P]_{ij} D_{jk} = \sum_m D_{im} [P^\dagger \Lambda^k P]_{mk} \ , \tag{5.82}$$

which, since D is diagonal, implies

$$[P^\dagger \Lambda^k P]_{ik} D_{kk} = D_{ii} [P^\dagger \Lambda^k P]_{ik} \ . \tag{5.83}$$

Substituting $D_{aa} = \sigma_a$, we obtain

$$[P^\dagger \Lambda^k P]_{ik} (\sigma_k - \sigma_i) = 0 \ . \tag{5.84}$$

This equation implies that whenever $\sigma_i \neq \sigma_k$, we must have $[P^\dagger \Lambda^k P]_{ik} = 0$, meaning that $P^\dagger \Lambda^k P$ must be block-diagonal, with blocks corresponding to eigenspaces of X.

If two indices a, b correspond to the same eigenvalue, $\sigma_a = \sigma_b$, then the corresponding elements $[P^\dagger \Lambda^k P]_{ab}$ may be nonzero, indicating that the matrix has nontrivial structure within the degenerate subspaces. The dimension of each invariant subspace is determined by the multiplicity of its associated eigenvalue: higher multiplicities correspond to larger subspaces.

Thus, we conclude that P block-diagonalizes Λ^k, leading to the final form

$$P^\dagger \Lambda^k P = \begin{pmatrix} \Lambda_1^k & 0 & \cdots & 0 \\ 0 & \Lambda_2^k & \cdots & 0 \\ \vdots & \vdots & \ddots & \vdots \\ 0 & 0 & \cdots & \Lambda_r^k \end{pmatrix} \ , \tag{5.85}$$

where each block Λ_j^k corresponds to a different eigenspace of X. The size of each block is determined by the degeneracy of the corresponding eigenvalue of X.

Hence, the problem of finding a matrix that simultaneously diagonalizes all the matrices Λ^k can be reformulated as finding a matrix X that commutes with every Λ^k, *i.e.* Eq. (5.77). However, this commutation relation does not directly yield X. To address this, we introduce the concept of *vectorization*.

For an operator $A = \sum_{i,j} A_{ij} |i\rangle\langle j|$ acting on a d-dimensional Hilbert space, its vectorization, denoted by $|A\rangle\rangle$, is a d^2 -dimensional vector defined by

$$|A\rangle\rangle = \sum_{i,j} A_{ij} |j\rangle \otimes |i\rangle \ , \tag{5.86}$$

where $\{|i\rangle\}$ is an orthonormal basis. A key property of the vectorization operation is its effect on operator products. For two operators A and B, the vectorized form of its product is

$$|AB\rangle\rangle = \sum_{i,j,k} A_{ik} B_{kj} |j\rangle \otimes |i\rangle = \sum_k \sum_j B_{kj} |j\rangle \otimes \sum_i A_{ik} |i\rangle \ . \tag{5.87}$$

Noting that

$$A |k\rangle = \sum_j |j\rangle\langle j| A |k\rangle = \sum_j A_{jk} |j\rangle \ , \tag{5.88}$$

$$B^T |k\rangle = \sum_j |j\rangle\langle j| B^T |k\rangle = \sum_j B_{kj} |j\rangle \ , \tag{5.89}$$

this implies the following useful identity

$$|AB\rangle\rangle = \sum_k B^T |k\rangle \otimes \sum_i A_{ik} |i\rangle = (B^T \otimes \mathbb{I}) \sum_{i,k} A_{ik} |k\rangle \otimes |i\rangle = (B^T \otimes \mathbb{I}) |A\rangle\rangle \ , \tag{5.90}$$

or, alternatively,

$$|AB\rangle\rangle = \sum_k \sum_j B_{kj} |j\rangle \otimes A |k\rangle = (\mathbb{I} \otimes A) \sum_{j,k} B_{kj} |j\rangle \otimes |k\rangle = (\mathbb{I} \otimes A) |B\rangle\rangle \ . \tag{5.91}$$

Hence, if we apply the vectorization to both terms in the commutator Eq. (5.77), we obtain

$$\left|\Lambda^k X\right\rangle\rangle = \left(\mathbb{I} \otimes \Lambda^k\right) |X\rangle\rangle \ , \tag{5.92}$$

$$\left|X \Lambda^k\right\rangle\rangle = \left(\left(\Lambda^k\right)^T \otimes \mathbb{I}\right) |X\rangle\rangle \ , \tag{5.93}$$

and thus the linear equation

$$\left[\left(\mathbb{I} \otimes \Lambda^k\right) - \left(\left(\Lambda^k\right)^T \otimes \mathbb{I}\right)\right] |X\rangle\rangle = 0 \ , \quad \text{for all } k \ . \tag{5.94}$$

Eq. (5.94) implies that the d^2-vector $|X\rangle\rangle$ corresponding to the matrix X must lie in the null space of the $d^2 \times d^2$ matrix

$$\mathbb{M}_k \equiv \left(\mathbb{I} \otimes \Lambda^k\right) - \left(\left(\Lambda^k\right)^T \otimes \mathbb{I}\right) \ . \tag{5.95}$$

Thus, finding a solution X reduces to computing the null space of $\mathbb{M}_k$ for each k, a task that can be efficiently handled using standard numerical techniques. However, a key point to note is that a vector $|X\rangle\rangle$ satisfying Eq. (5.94) does not necessarily correspond to a Hermitian matrix. To guarantee that the resulting matrix is Hermitian, we need an additional constraint. Specifically, the solution $|X\rangle\rangle$ must also satisfy the analogous condition for the Hermitian conjugate $\left(\Lambda^k\right)^\dagger$,

$$\mathbb{M}_k \, |X\rangle\rangle = 0 \ , \quad \tilde{\mathbb{M}}_k \, |X\rangle\rangle = 0 \ , \tag{5.96}$$

where

$$\tilde{\mathbb{M}}_k \equiv \left(\mathbb{I} \otimes \left(\Lambda^k\right)^\dagger\right) - \left(\left(\Lambda^k\right)^* \otimes \mathbb{I}\right) \ , \tag{5.97}$$

and we have used the identity $\left(\left(\Lambda^k\right)^\dagger\right)^T = \left(\Lambda^k\right)^*$. When these two conditions are satisfied, the symmetrized form $\mathrm{Herm}(X) \equiv (X + X^\dagger)/2$ is a valid Hermitian solution to Eq. (5.94). This follows because

$$\left[\Lambda^k, \mathrm{Herm}(X)\right] = \frac{1}{2}\left[\Lambda^k, X\right] + \frac{1}{2}\left[\Lambda^k, X^\dagger\right] = \frac{1}{2}\left[\Lambda^k, X\right] - \frac{1}{2}\left[\left(\Lambda^k\right)^\dagger, X\right] = 0 \ , \tag{5.98}$$

where we used $\left[A, B^\dagger\right] = AB^\dagger - B^\dagger A = (BA^\dagger)^\dagger - (A^\dagger B)^\dagger = -\left[A^\dagger, B\right]$, and the conditions in Eq. (5.96) ensure that both commutators vanish (*i.e.*, $\left[\Lambda^k, X\right] = 0$ and $\left[\left(\Lambda^k\right)^\dagger, X\right] = 0$).

To find a Hermitian matrix $\mathrm{Herm}(X)$ that commutes with all Λ^k, we must identify a vector $|X\rangle\rangle$ that satisfies both conditions in Eq. (5.96) for all k. A practical approach is to combine the conditions by constructing the following positive semidefinite Hermitian matrix

$$\mathbb{L} = \sum_k \mathbb{M}_k^\dagger \mathbb{M}_k + \tilde{\mathbb{M}}_k^\dagger \tilde{\mathbb{M}}_k \ . \tag{5.99}$$

Since $\mathbb{L}$ is a sum of positive semidefinite matrices, its null space consists of the vectors $|X\rangle\rangle$ that simultaneously satisfy both conditions in Eq. (5.96). The eigenvectors of $\mathbb{L}$ satisfy the eigenvalue equation

$$\mathbb{L} \, |v_i\rangle = \epsilon_i \, |v_i\rangle \ , \tag{5.100}$$

and those corresponding to zero eigenvalues span the null subspace

$$\mathbb{L} \left|v_j^{(0)}\right\rangle = 0 \ . \tag{5.101}$$

Any vector in this null space provides a solution to the simultaneous commutator conditions. In particular, a general solution can be constructed as a linear combination of these zero-eigenvalue eigenvectors

$$|u\rangle = \sum_j a_j \left|v_j^{(0)}\right\rangle \ , \tag{5.102}$$

where the coefficients a_j satisfy the normalization condition $\sum_j |a_j|^2 = 1$. This vector defines a Hermitian matrix $\mathrm{Herm}(X)$ through the relation $|X\rangle\rangle = |u\rangle$.

To see why any vector in the null space of $\mathbb{L}$ satisfies the required conditions, observe that if $|u\rangle$ is in the null space, we have

$$\begin{aligned} 0 &= \langle u|\, \mathbb{L}\, |u\rangle \\ &= \sum_k \langle u|\, \mathbb{M}_k^\dagger \mathbb{M}_k\, |u\rangle + \langle u|\, \tilde{\mathbb{M}}_k^\dagger \tilde{\mathbb{M}}_k\, |u\rangle \\ &= \sum_k \|\mathbb{M}_k\, |u\rangle\, \|^2 + \|\tilde{\mathbb{M}}_k\, |u\rangle\, \|^2 \ . \end{aligned} \tag{5.103}$$

Since each term in the sum is nonnegative, the only way for the total to be zero is if every individual term vanishes

$$\mathbb{M}_k\, |u\rangle = 0 \ , \quad \tilde{\mathbb{M}}_k\, |u\rangle = 0 \ , \quad \text{for all } k \ , \tag{5.104}$$

which is precisely the condition required by Eq. (5.96). Therefore, any vector $|u\rangle$ in the null space of $\mathbb{L}$ corresponds to a Hermitian matrix $\mathrm{Herm}(X)$ that commutes with all Λ^k. For a step-by-step description of the Block-diagonalization process, refer to Box 3.

Box 3: High-Level View of the Algorithm for Block-diagonalization

The following algorithm outlines the process for transforming the structure constant matrices Λ^k into a form $\tilde{\Lambda}^k$ with potentially disjoint subspaces:

Step 1: Define Operators

- Identify the operators $\{\mathfrak{h}_j\}$ defining the Hamiltonian.
- Select the basis $\{a_k\}$ for expanding the invariant operator $\mathcal{I}(t)$.

Step 2: Compute Structure Constants

- Compute the structure constant matrices Λ^k.
- Determine their adjoints $\left(\Lambda^k\right)^\dagger$.

Step 3: Compute Auxiliary Matrices

- Use Eqs. (5.95) and (5.97) to obtain the matrices $\mathbb{M}_k$ and $\tilde{\mathbb{M}}_k$.

Step 4: Construct Aggregate Matrix

- Form the matrix $\mathbb{L}$ as defined in Eq. (5.99).

Step 5: Solve for Null Subspace

- Solve Eq. (5.101) to find the null subspace of $\mathbb{L}$.
- Construct the vector $|u\rangle$ from the null-space solution.

Step 6: Reshape Solution

- Reshape $|u\rangle$ into a matrix X such that $|u\rangle = |X\rangle\rangle$.

Step 7: Compute Hermitian Form

- Construct the Hermitian version of X, given by $\mathrm{Herm}(X)$.

Step 8: Eigendecomposition

- Compute the eigendecomposition of $\mathrm{Herm}(X)$ as in Eq. (5.78).
- The resulting eigenvectors define the unitary matrix P.

Step 9: Transform Structure Constants

- Apply Eq. (5.85) to transform Λ^k into its block-diagonal form.
- Identify the disjoint subspaces.

5.6.2 Examples beyond Lie algebras

While the previous examples in Sec. 5.5 demonstrate that certain Lie-algebras, generated by the Hamiltonian operators $\{\mathfrak{h}_i\}$, have dimensions that scale polynomially with the number of qubits n, the following example illustrate sets of operators $\{\mathfrak{a}_i\}$ that form a small (polynomial-sized) algebra under the action of the Hamiltonian, even if the Lie-algebra associated to the Hamiltonian scales unfavourably.

For example, consider the spin ladder depicted in Fig. 5.8 with the set of Hamiltonian operators

$$\mathfrak{h}_i \in \{Z_{2k-1}Z_{2k+1},\ Y_{2k-1}Y_{2k},\ Z_{2k}Z_{2k+2}\} \text{ with } k \in [1, \frac{n}{2} - 1] \tag{5.105}$$

and open boundary conditions. The corresponding Lie algebra has $2^{\frac{n}{2}}\left(n^2 - n\right)/8$ elements, *i.e.* it is exponentially large. It is, however, possible to find a set of operators $\{\mathfrak{a}_i\}$ with linear scaling that satifies the required commutation relation $[\mathfrak{a}_j, \mathfrak{h}_k] = -i\sum_{l=1}^{d} \lambda_{jl}^k \mathfrak{a}_l$.

This construction follows the algorithm outlined in Box 3. Because the method requires handling high-dimensional matrices $\mathbb{L}$ (see Eq. (5.99)), it is computationally practical only for systems with a limited number of qubits. However, the solutions obtained for small systems reveal a systematic way to construct the operators $\mathfrak{a}_k$ for any number of qubits. Once the underlying structure of these operators is identified, the full set can be generated sequentially for an arbitrary n. The procedure begins by selecting an initial operator, $\mathfrak{a}_1$, from which the remaining operators are obtained iteratively through nested commutators with $\mathfrak{h}_k$. This recursive construction starts with

$$\mathfrak{a}_1 = \sum_{k=0}^{(n-2)/4} X_1 Z_{4k}^s \ , \tag{5.106}$$

where Z_{4k}^s denotes the symmetric sum over all permutations of the product of $2k$ pairs

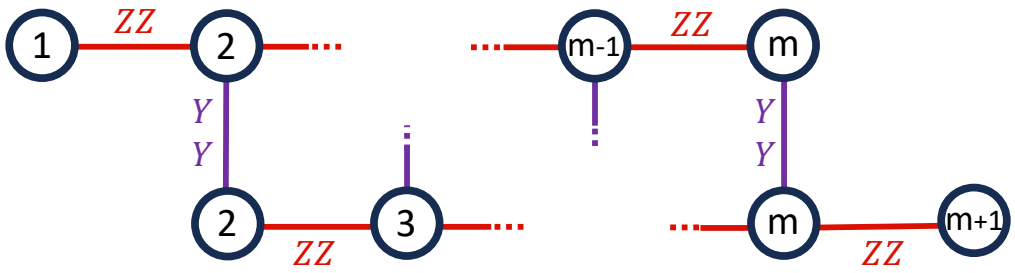

Figure 5.8: A driven spin ladder with nearest-neighbor ZZ interactions in the top and bottom chains and YY interactions between spins of different chains.

$Z_{2j}Z_{2j+1}$ of Pauli Z operators on spins 2 to n. For instance, for $n = 10$, those read

$$\begin{aligned} Z_0^s &= \mathbb{I} \\ Z_4^s &= Z_2Z_3Z_4Z_5 + Z_2Z_3Z_6Z_7 + Z_2Z_3Z_8Z_9 + Z_4Z_5Z_6Z_7 + Z_4Z_5Z_8Z_9 + Z_6Z_7Z_8Z_9 \\ Z_8^s &= Z_2Z_3Z_4Z_5Z_6Z_7Z_8Z_9 \end{aligned} \tag{5.107}$$

In general, $\mathfrak{a}_1$ is a sum over $2^{(n-4)/2}$ individual operators. The second operator can be readily constructed noting that $\mathfrak{a}_1$ commutes with all the elements $\mathfrak{h}_i$ of the Hamiltonian except for Z_1Z_3. In particular, one can define

$$\mathfrak{a}_2 \propto \sum_k [X_1 Z_{4k}^s, Z_1Z_3] \ , \tag{5.108}$$

which now commutes with all the elements $\mathfrak{h}_i$ in the Hamiltonian except for Z_1Z_3 and Y_2Y_3. This defines the third element

$$\mathfrak{a}_3 \propto [\mathfrak{a}_2, Y_2Y_3] \ , \tag{5.109}$$

that, since anti-commutes with Y_2Y_3, Z_2Z_4 and Z_3Z_5 defines the fourth element

$$\mathfrak{a}_4 \propto [\mathfrak{a}_3, Z_2Z_4] = [\mathfrak{a}_3, Z_3Z_5] \ . \tag{5.110}$$

In turn, $\mathfrak{a}_4$ anti-commutes with Z_2Z_4, Z_3Z_5 and Y_4Y_5 and determines

$$\mathfrak{a}_5 \propto [\mathfrak{a}_4, Y_4Y_5] \ . \tag{5.111}$$

This process can be repeated until the last element is derived:

$$\mathfrak{a}_n \propto [\mathfrak{a}_{n-1}, Z_{n-2}Z_n] \ . \tag{5.112}$$

Since this operator only anti-commutes with $Z_{n-2}Z_n$, it follows that the algebra $\{\mathfrak{a}_1, \ldots, \mathfrak{a}_n\}$ is closed under the Hamiltonian's action and, specifically, is of n size.

Within the set of elements $\{\mathfrak{a}_i\}$, the n-body operator (after the appropriate relabeling)

$$\sum_{k=0}^{\lfloor (n-4)/4 \rfloor} Z_1 (X_{4k+2} Y_{n-4k-4})^s Z_n \ , \tag{5.113}$$

with $(X_{4k+2}Y_{n-4-4k})^s$ being the symmetric sum over all permutations of the product of $2k$ pairs $X_{2j}X_{2j+1}$ and $(n-2k-4)$ pairs $Y_{2l}Y_{2l+1}$ is composed of mutually commuting operators and of interest for the implementation surface codes. For $n = 10$, those read

$$\begin{aligned}(X_2Y_6)^s &= X_2X_3Y_4\cdots Y_9 + Y_2Y_3X_4X_5Y_6\cdots Y_9 + Y_2\cdots Y_5X_6X_7Y_8Y_9 + Y_2\cdots Y_7X_8X_9 \\ (X_6Y_2)^s &= Y_2Y_3X_4\cdots X_9 + X_2X_3Y_4Y_5X_6\cdots X_9 + X_2\cdots X_5Y_6Y_7X_8X_9 + X_2\cdots X_7Y_8Y_9 \ .\end{aligned} \tag{5.114}$$

5.7 Conclusions

The techniques developed in this Chapter expand the toolbox of quantum optimal control by addressing a critical limitation of traditional invariant-based methods: the reliance on analytically derived dynamical invariants $\mathcal{I}_a(t)$. For systems governed by Hamiltonians such as $H(t)$ (Eq. (5.36)), constructing such invariants requires enforcing strict compatibility conditions to ensure the dynamics involve only experimentally accessible terms — Z_j ($j \in [1,n]$), X_1, X_n and the nearest-neighbor interaction $\sum_{j=1}^{n} X_jX_{j+1}$ — while rigorously excluding nonphysical terms like those listed in Eq. (5.37). Deriving these invariants is exceptionally challenging, as they must satisfy both the equation of motion (Eq. (5.8)) and the algebraic constraints of the hardware. By replacing the need for explicit analytic invariants with numerical optimization, our approach avoids these challenges entirely. Instead, it leverages the closed commutation relations of the system's operators (Eq. (5.5)) to generate control fields that keep dynamics confined to the desired interaction space. This ensures that the resulting protocols are both numerically exact and experimentally feasible, bypassing the impractical step of deriving invariants while preserving the Hamiltonian's physical realizability.

This methodology contrasts with counterdiabatic driving (CD) [190, 191, 192, 193], which mimics adiabatic dynamics by adding terms like those in Eq. (5.37) to the Hamiltonian. However, these terms often involve interactions (*e.g.*, three-body couplings or higher nonlocal spin operators) that cannot be directly implemented in platforms such as superconducting qubits or trapped ions. While other CD methods approximate these terms using time-dependent modulation or perturbative expansions [190], such approximations introduce errors that limit fidelity. Our framework circumvents this issue by exploiting the system's inherent algebraic structure (Eq. (5.5)), enabling exact control without unphysical terms. Similarly, Floquet engineering [194, 195] — which synthesizes effective Hamiltonians via periodic driving — relies on perturbative methods and stroboscopic approximations, restricting its utility to systems with periodic modulation. Our approach generalizes this by enabling exact propagator design (Sec. 5.4) for arbitrary time-dependent Hamiltoni-

ans, opening avenues for controlling aperiodic processes like quantum quenches or non-equilibrium dynamics.

A key strength of this framework lies in its compatibility with diverse quantum control algorithms. While we employ the GRAPE algorithm [144] for gradient-based optimization, the mathematical equivalence between our dynamical equations (Eq. (5.10)) and the Schrödinger equation allows seamless integration of advanced methods. For instance, recent gradient computation techniques [196] could accelerate optimization in high-dimensional systems, while parametrizing control fields as Gaussian pulses [63] might improve noise robustness. Gradient-free approaches [197] could further enhance experimental applicability where gradient measurements are impractical. This flexibility ensures adaptability to evolving hardware capabilities and algorithmic advancements.

The exponential scaling of Hilbert space dimensionality presents a fundamental challenge in controlling composite quantum systems, as the resources required to simulate or manipulate such systems grow rapidly with the number of qubits. However, this challenge can be alleviated in certain cases by utilizing operator sets with favorable scaling properties. In platforms such as superconducting qubits [198], trapped ions, and Rydberg atom arrays [199], the native interaction geometries enable control protocols to exploit the hardware's intrinsic connectivity. This allows for efficient use of the available qubit count — now reaching up to 256 in state-of-the-art devices [199] — without resorting to long gate sequences that amplify decoherence and accumulate errors. By tailoring control strategies to these interaction geometries, our approach minimizes the need for complex gate decompositions, preserving coherence and enhancing the overall fidelity of quantum operations.

At the same time, verifying the functionality of quantum devices remains a significant challenge, particularly as systems scale beyond the limits of classical simulation [200]. Here, the invariant-based description of quantum dynamics offers a powerful tool for experimental validation. By providing precise predictions for the expected dynamics, our framework enables direct comparison with measured observables, helping to identify discrepancies caused by unmodeled noise, calibration errors, or hardware imperfections. This predictive capability not only aids in debugging and optimizing quantum devices but also establishes a feedback loop between theory and experiment, fostering iterative improvements in both control protocols and hardware design.

The emergence of multi-body interactions in the dynamics governed by the spin Hamiltonian (Eq. (5.36)) further underscores the versatility of our approach. These interactions, such as three- and four-body terms, naturally arise in systems with native coupling geometries and can be harnessed to implement error-correcting codes [201, 202] and topologically protected quantum operations [185]. For instance, in platforms like Rydberg atom arrays, where interactions can be tuned to create complex entanglement structures, our control framework enables the direct realization of stabilizer operations or non-Abelian anyons without the overhead of decomposing them into elementary gates. This capability is par-

ticularly valuable as quantum devices grow in size and complexity, pushing beyond the limits of classical simulation [199] and demanding control techniques with efficient scaling.

Moreover, the ability to optimize control sequences within this framework reduces the need for costly experimental tuning [173, 203], accelerating the development of high-fidelity protocols. By minimizing trial-and-error optimization, our approach not only saves time and resources but also enhances reproducibility across different experimental setups. Finally, the capacity to engineer quantum states at the Heisenberg limit — enabled by precise control over entanglement and coherence — positions this framework as a valuable tool for quantum sensing applications. From magnetic field detection to gravitational wave observation, the ability to create highly sensitive quantum states could transform metrology, underscoring the broader impact of this work on the development of quantum technologies.

Chapter 6

Quantum Control of Trapped Ions' Motion

CONTRIBUTIONS

All the work in this Chapter was carried out by me, under the supervision of Florian Mintert. Some of the numerical tests were inpired by the experimental challenges suggested by Selwyn Simsek, Sahra A. Kulmiya, Samuel J. Hile and Winfried K. Hensinger. The results were also published in Ref. [2].

The development of quantum technologies has reached a pivotal stage where scalability is no longer a distant goal but an immediate challenge. While early proof-of-principle demonstrations of quantum information processing relied primarily on controlling discrete degrees of freedom — such as qubits — scalable architectures demand mastery over motional quantum states as well [96]. This shift is particularly evident in trapped-ion systems, a leading platform for quantum computing [204], where scalability hinges on modular architectures with ions partitioned into interconnected clusters [205]. To perform quantum operations across these clusters, individual ions must be shuttled between trapping zones with high precision.

To meet these demands, experimental platforms increasingly aim to realize two-dimensional (2D) arrangements of trapped ions, moving beyond linear chains to planar configurations that offer greater flexibility and parallelism. These 2D layouts are achieved using various techniques. In RF Paul traps, anisotropic confinement can enable planar Coulomb crystals under strong radial confinement [206]; in Penning traps, a combination of static magnetic and electric fields stabilizes rotating 2D ion lattices [207]; and in surface-electrode traps, tailored control voltages create trapping potentials above a chip surface, allowing for reconfigurable 2D arrays of individually addressable ions [208, 109]. These architectures enable critical capabilities like junction crossings, ion reordering, and parallel operations — features essential for scalable quantum processing.

However, these added capabilities introduce significant control challenges. Trapped-ion logic gates — especially entangling operations — require ions to remain near their motional ground state, as excess energy leads to reduced gate fidelity due to breakdowns in the Lamb-Dicke approximation [209] (see Sec. 4.1.4). While adiabatic shuttling protocols can maintain low motional excitation, they are too slow to be compatible with the finite coherence times of trapped-ion qubits [32]. On the other hand, diabatic transport offers much faster operation but often induces motional excitations, especially in multidimensional trapping environments where multiple vibrational modes can couple non-trivially [210]. Although ground-state transport has been demonstrated in one-dimensional geometries [211], generalizing these results to large-scale 2D architectures remains an outstanding experimental and theoretical hurdle.

This challenge has driven the development of *shortcuts to adiabaticity (STA)*, a class of techniques designed to achieve the outcomes of adiabatic processes in significantly shorter times [155]. Among STA strategies, quantum dynamical invariants — particularly the Ermakov-Lewis invariant [212] defined in Eq. (3.45) — have proven to be powerful tools [80]. These invariants enable the inverse engineering of control Hamiltonians and have been successfully applied to a broad range of theoretical and experimental problems, including atom cooling [83], fast ion separation [84], and one-dimensional transport in harmonic traps [213]. Moreover, when combined with variational methods or integrated into master equation formalisms, invariants have addressed problems that defy standard treatments, such as transport in anharmonic potentials [214] or population inversion in atomic states [215]. Their versatility extends to mitigating experimental imperfections, such as control parameter fluctuations and environmental noise, making them indispensable for practical quantum control [216].

Despite these successes, a critical limitation remains: most invariant-based protocols have been developed for systems with a single motional degree of freedom [155]. Yet, real-world applications — such as the shuttling of ions in multidimensional trapping potentials — demand invariants capable of handling multiple degrees of freedom simultaneously.

In this Chapter, we tackle this problem by utilizing the recently developed Gaussian invariant for multidimensional systems [157], which we introduced in Sec. 3.5.5. We examine its potential for quantum optimal control through theoretical examples inspired by current ion shuttling experiments, showing how it can aid designing fast, precise, and efficient control protocols for complex geometries. Ultimately, by extending the invariant framework to higher dimensions, we aim to facilitate the translation of theoretical control strategies into practical solutions for scalable quantum technologies.

6.1 Quantum dynamics in quadratic Hamiltonians

Although real-world trapping potentials are never perfectly harmonic, they can often be approximated as quadratic near equilibrium for sufficiently cooled and spatially confined ions. This approximation generally holds during shuttling protocols, where the ion's mo-

tion remains tightly localized within the potential well. Under these conditions, the ion's dynamics along a d-dimensional trajectory $\vec{r}(t)$ are governed by the time-dependent Hamiltonian in Eq. (4.28) — which is expressed in terms of phase-space variables in Eq. (3.52). This Hamiltonian depends critically on two parameters:

- The trapping matrix $\mathbf{M}(t)$, a $d \times d$ positive-definite matrix derived from the Hessian of the pseudopotential (Eq. (4.27)), which encodes the effective harmonic frequencies of the trap.

- The restoring force $\vec{F}(t)$, a time-dependent vector that drives the ion toward the instantaneous trap center $\vec{C}(t) = \frac{1}{m}\mathbf{M}^{-1}(t)\vec{F}(t)$, corresponding to the potential minimum.

Unlike static traps (Sec. 4.1.1), shuttling requires explicit time dependence in $\mathbf{M}(t)$ and $\vec{F}(t)$ (or equivalently $\vec{C}(t)$). These parameters are dynamically modulated through controlled variations in the confining electromagnetic fields, enabling precise ion transport with minimal heating.

For initial quantum states that are Gaussian — such as the ground state of Eq. (3.52) — the time evolution preserves Gaussianity. This simplifies the description of the system's dynamics to two essential quantities: the classical phase-space trajectory $\vec{Z}$, which represents the expectation values of the position and momentum operators, and the covariance matrix $\mathbf{\Sigma}$, which encodes all variances and covariances of the phase-space operators $\vec{X}$ (defined in Eq. (3.49)). Specifically,

$$\vec{Z}(t) = \mathrm{Tr}[\rho(t)X] \ , \tag{6.1a}$$

$$\mathbf{\Sigma}(t) = \mathrm{Tr}\Big[\rho(t)\Big\{(X-\vec{Z}),(X-\vec{Z})^T\Big\}\Big] \ , \tag{6.1b}$$

where $\{A, B\} = AB + BA$ is the anticommutator. Explicitly distinguishing the position and momentum components, we express the phase-space trajectory as

$$\vec{Z}(t) = (\vec{r}_c(t), m\dot{\vec{r}}_c(t)) \ , \quad \text{with} \quad \vec{r}_c(t) = \mathrm{Tr}[\rho(t)r] \ , \tag{6.2}$$

which is given in terms of the classical position $r_c(t)$ and classical momentum $m\dot{\vec{r}}_c(t)$ of the particle. In the Heisenberg picture (see Appendix B.2), $\vec{Z}(t)$ and $\mathbf{\Sigma}(t)$ evolve in time, following the equations of motion

$$\dot{\vec{Z}} = \mathbb{S}\boldsymbol{K}\vec{Z} + \mathbb{S}\vec{V} \ , \tag{6.3a}$$

$$\dot{\mathbf{\Sigma}} = \mathbb{S}\boldsymbol{K}\mathbf{\Sigma} - \mathbf{\Sigma}\boldsymbol{K}\mathbb{S} \ , \tag{6.3b}$$

where $\mathbb{S}$ is the symplectic matrix (defined in Eq. (3.51)), and $\boldsymbol{K}$ and $\vec{V}$ are the matrices defined in Eqs. (3.53) and (3.54), respectively.

6.2 Invariant-based ion shuttling

The central challenge in ion shuttling is designing a time-dependent control protocol for the Hamiltonian $H(t)$ in Eq. (3.52) that transports an ion — initially in the motional ground state of a Hamiltonian H_I — to the ground state of a *distinct* final Hamiltonian H_T. This requires addressing two critical differences between H_I and H_T:

- Spatial displacement: The trap center shifts from the initial position $\vec{C}_I$ to the final position $\vec{C}_T$.
- Trap reconfiguration: The shape of the confining potential may change, reflected in the differing trapping matrices $\mathbf{M}_I$ (initial) and $\mathbf{M}_T$ (final), which encode the harmonic frequencies.

The objective is to minimize motional excitation during the transport process, ensuring that the ion ends up in the final ground state with no residual phonon excitation. While this can be framed as an optimization problem — searching for parameter trajectories $\boldsymbol{M}(t)$ and $\vec{F}(t)$ that minimize excitations — a more elegant approach leverages quantum invariants. These invariants offer a direct and analytic method for engineering $H(t)$, ensuring that the system's quantum state is transferred from the initial ground state to the final ground state, even during rapid trap displacements.

In this invariant-based approach, the focus shifts to identifying an invariant operator $\mathcal{I}(t)$ with respect to the time-dependent Hamiltonian $H(t)$ in Eq. (3.52). For $\mathcal{I}(t)$ to be a valid invariant, it must satisfy the equation of motion in Eq. (3.23). The eigenstates of this invariant operator provide the framework for quantum state transfer.

A ground-state-to-ground-state transfer is achieved when the quantum state of the ion evolves along a non-degenerate eigenstate $|\lambda;t\rangle$ of the invariant that smoothly interpolates between the ground states of the initial and final Hamiltonians. That is, the eigenstate coincides with the ground state the initial Hamiltonian $|g_I\rangle$ at $t = 0$ (*i.e.*, $|\lambda;0\rangle = |g_I\rangle$) and with the ground state of the final Hamiltonian $|g_F\rangle$ at the end of the protocol $t = T$ (*i.e.*, $|\lambda;T\rangle = |g_F\rangle$). Crucially, at intermediate times, the eigenstate $|\lambda;t\rangle$ may involve a superposition of excited states of the instantaneous Hamiltonian $H(t)$, allowing transitions that overcome the limitations of adiabaticity. This feature provides a pathway to shuttling the ion efficiently, bypassing the slow time scales typically required in adiabatic processes.

To ensure this behavior, the boundary conditions must be satisfied

$$[\mathcal{I}(0), H(0)] = [\mathcal{I}(T), H(T)] = 0 \ . \tag{6.4}$$

These commutation relations guarantee that $\mathcal{I}(0)$ and $H(0)$ share a common eigenbasis, as do $\mathcal{I}(T)$ and $H(T)$. Consequently, if the initial quantum state of the ion is in the ground state of $H(0)$ — which is typically the case in an experimental setting — this initial state must also be the ground state of $\mathcal{I}(0)$, due to the commutation relation. Similarly, at the final time $t = T$, if the quantum state is in the ground state of $\mathcal{I}(T)$, it will also be in the

ground state of $H(T)$.

Furthermore, since the eigenstates of the invariant have time-independent eigenvalues, the ground state of $\mathcal{I}(0)$ will deterministically evolve into the ground state of $\mathcal{I}(T)$, which is to say that the quantum state of the system will be transferred from the ground-state of $H(0)$ to the ground-state of $H(T)$.

A shuttling protocol can thus be formulated in terms of the dynamical invariant $\mathcal{I}(t)$, where Eq. (3.23) serves as the defining condition for determining a time-dependent Hamiltonian $H(t)$ that implements the desired protocol. However, it is crucial to ensure that, when defining $\mathcal{I}(t)$, the resulting Hamiltonian takes the form specified in Eq. (3.52), comprising both a kinetic-energy term and a time-dependent potential. This ensures experimental feasibility, rather than yielding an operator that is physically impractical. The relationship between a Hamiltonian and its induced dynamics is nonlinear, and as such, identifying conditions on $\mathcal{I}(t)$ that guarantee an experimentally realizable Hamiltonian remains an open problem, with only a few known solutions, which are inherently unintuitive.

One such solution is the multidimensional quantum invariant $\mathcal{I}(t)$ introduced in Sec. 3.5.5, which is explicitly given in Eq. (3.57) in terms of a time-dependent matrix $\mathbf{\Gamma}(t)$ and vector $\vec{W}(t)$. These quantities evolve according to Eq. (3.58), with $\mathbf{\Gamma}(t)$ fully determined by a freely chosen matrix $\boldsymbol{R}(t)$ (Eq. (3.59)). Thus, constructing a suitable invariant $\mathcal{I}(t)$ amounts to selecting appropriate functions for $\boldsymbol{R}(t)$ and $\vec{W}(t)$. Once these are specified, one can inverse-engineer the corresponding Hamiltonian: the trapping matrix $\boldsymbol{M}(t)$ is obtained from Eq. (3.62), while the restoring force $\vec{F}(t)$ follows from Eq. (3.63). This approach directly links the mathematical structure of the invariant to experimentally tunable parameters, enabling the design of shuttling protocols that achieve rapid ion transport while suppressing motional excitations.

The physical interpretation of $\boldsymbol{R}(t)$ and $\vec{W}(t)$ emerges from their connection to the quantum state's dynamics. Specifically, $\vec{W}(t)$ coincides with the classical phase-space trajectory $\vec{Z}(t)$ defined in Eq. (6.1a) (see also Eq. (3.58b)), which describes the expectation values of the ion's position and momentum. Substituting $\vec{W}(t) = \vec{Z}(t)$ into the invariant's structure reveals that the restoring force $\vec{F}(t)$ satisfies the *vector Newton equation*

$$\vec{F}(t) = m\Big(\boldsymbol{M}(t)\vec{r}_c(t) + \ddot{\vec{r}}_c(t)\Big) \,, \tag{6.5}$$

where $\vec{r}_c(t)$ and $\ddot{\vec{r}}_c(t)$ are the classical displacement and acceleration of the ion as given in Eq. (6.2). This equation mirrors the classical equation of motion for a particle in a harmonic potential, establishing a direct correspondence between the quantum invariant's parameters and the ion's macroscopic trajectory.

Equally significant is the role of $\boldsymbol{R}(t)$ in quantifying quantum fluctuations. The matrix $\boldsymbol{R}(t)$ is directly related to the covariance matrix $\mathbf{\Sigma}(t)$, which encodes the positional and momentum uncertainties of the ion's Gaussian wavepacket. In particular, the spatial submatrix of $\mathbf{\Sigma}(t)$ is equal to $\frac{1}{2}\boldsymbol{R}^2(t)$, making $\boldsymbol{R}(t)$ a dynamical measure of the wavefunction's

spatial spreading during transport. This relationship becomes especially intuitive in the slow-modulation regime, where $\boldsymbol{R}(t)$ varies adiabatically ($\dot{\boldsymbol{R}} \approx 0$). Here, $\boldsymbol{R}(t) \approx \boldsymbol{M}^{-1/4}(t)$, linking the trapping potential's curvature $\boldsymbol{M}(t)$ to the wavepacket's instantaneous width. This approximation offers a simple method to estimate motional heating during transport without solving the full nonlinear dynamics — though by design, the final heating remains zero.

Hence, for $\mathcal{I}(t)$ in Eq. (3.57) to be an invariant of motion for the quadratic Hamiltonian $H(t)$ in Eq. (3.52), $\boldsymbol{\Gamma}(t)$ must satisfy Eq. (3.59), and $\vec{W}(t)$ must correspond to the phase-space trajectory $\vec{Z}(t)$. The freedom to choose $\boldsymbol{R}(t)$ and $\vec{Z}(t)$ thus allows for the construction of infinitely many valid invariants. Given a choice of $\boldsymbol{R}(t)$ and $\vec{Z}(t)$, one can then inverse-engineer a Hamiltonian $H(t)$ that is compatible with the chosen time-dependency in the invariant. This Hamiltonian is specified by $\boldsymbol{K}(t)$ and $\vec{V}(t)$, according to Eq. (3.52). $\boldsymbol{K}(t)$ is obtained by first calculating $\boldsymbol{M}(t)$ from $\boldsymbol{R}(t)$ using Eq. (3.62), while $\vec{V}(t)$ is determined by Eq. (3.54), with $\vec{F}(t)$ given by in Eq. (6.5).

The Hamiltonian obtained in this fashion is guaranteed to yield a time evolution that preserves the structure of the chosen invariant, ensuring that the system follows the prescribed phase-space dynamics. This framework thus provides a systematic way to construct dynamically invariant protocols for quadratic systems, enabling precise control over the motion by appropriately selecting $\boldsymbol{R}(t)$ and $\vec{Z}(t)$. In particular, by tailoring $\boldsymbol{R}(t)$, one can shape the effective potential landscape in a nontrivial yet controlled manner, while $\vec{Z}(t)$ dictates the desired phase-space trajectory within this landscape.

However, not all choices of $\boldsymbol{R}(t)$ and $\vec{Z}(t)$ are suitable for realizing ground-to-ground state transfer. To ensure that the system transitions between the ground states of the initial and final Hamiltonians, the boundary conditions in Eq. (6.4) must be satisfied. The necessary commutativity between the invariant and the Hamiltonian at any instant t is achieved if the following relations hold

$$\vec{r}_c(t) = \vec{C}(t) \ , \qquad \dot{\vec{r}}_c(t) = \ddot{\vec{r}}_c(t) = \vec{0} \ , \tag{6.6a}$$

$$\boldsymbol{R}(t) = \boldsymbol{M}^{-1/4}(t) \ , \qquad \dot{\boldsymbol{R}}(t) = \ddot{\boldsymbol{R}}(t) = \mathbb{O} \ . \tag{6.6b}$$

Physically, the first set of conditions ensures that the classical trajectory of the ion coincides with the position of the trap center, and that both its velocity and acceleration vanish. The second set of conditions guarantees that the Gaussian state is consistent with the Hessian of the potential, while the trapping potential remains at rest, with zero velocity and acceleration.

If these boundary conditions are satisfied at $t = 0$ and at $t = T$, with $\vec{C}(0)$, $\vec{C}(T)$, $\boldsymbol{M}(0)$ and $\boldsymbol{M}(T)$ determined by the initial and final Hamiltonian, then the time-dependent ground state of the invariant indeed defines a shuttling protocol in which an ion evolves from the ground state of an initial Hamiltonian towards the ground state of a final Hamiltonian.

6.3 Optimal control with the multidimensional invariant

Beyond the constraints imposed by the boundary conditions (Eqs. (6.6)), the flexibility in choosing the time evolution of $\vec{r}_c(t)$ and $\boldsymbol{R}(t)$ allows for a wide range of possible dynamics. This non-uniqueness in the compatible Hamiltonians enables the identification of protocols that are optimal in a sense to be defined. To achieve this, a variational analysis over $\vec{r}_c(t)$ and $\boldsymbol{R}(t)$ must be performed while ensuring consistency with the boundary conditions given by Eqs. (6.6).

For this purpose, it is convenient to introduce a set of $N_a + 1$ basis functions $\{\vec{z}_i(t)\}_{i=0}^{N_a}$, where $\vec{z}_0(t)$ satisfies the boundary conditions specified in Eq. (6.6) (*i.e.* $\vec{z}_0(0) = \vec{C}(0)$ and $\vec{z}_0(T) = \vec{C}(T)$), while each function $\vec{z}_i(t)$ with $i > 0$ satisfies the homogeneous boundary conditions, *i.e.* Eqs. (6.6) with vanishing right-hand sides. The parameterization

$$\vec{r}_c(t) = \vec{z}_0(t) + \sum_{i=1}^{N_a} a_i \vec{z}_i(t) \tag{6.7}$$

then guarantees that the boundary conditions are satisfied for any choice of the N_a expansion coefficients a_i.

A parametrization of the matrix $\boldsymbol{R}(t)$ can be constructed analogously, using a reference matrix $\boldsymbol{R}_0(t)$ that satisfies the inhomogeneous boundary conditions and a set of matrices $\{\boldsymbol{R}_i(t)\}_{i=1}^{N_b}$ that satisfy the homogeneous version of Eqs. (6.6). This ensures that the parameterized form

$$\boldsymbol{R}(t) = \boldsymbol{R}_0(t) + \sum_{i=1}^{N_b} b_i \boldsymbol{R}_i(t) \tag{6.8}$$

automatically satisfies the boundary conditions for any choice of the N_b free parameters b_i. Ensuring the positivity of $\boldsymbol{R}(t)$, however, requires additional considerations. Imposing that all matrices $\boldsymbol{R}_i(t)$, including $\boldsymbol{R}_0(t)$, are positive and restricting the coefficients b_i to be non-negative does not fully explore the space of positive matrices within the spanning set. Therefore, in the optimizations that follow, no explicit constraints are placed on the coefficients b_i, and the positivity of $\boldsymbol{R}(t)$ is instead verified numerically using subdeterminants (via Sylvester's criterion [217]), moments, or numerically computed eigenvalues.

For a detailed discussion on the specific form of the vectors $\vec{z}_i(t)$ and matrices $\boldsymbol{R}_i(t)$, please refer to Appendix G.1.

6.4 Applications

To illustrate the advantages of this invariant-based control framework, we analyze three distinct control scenarios with clear experimental motivations, each addressing key limitations currently hindering progress in ion shuttling.

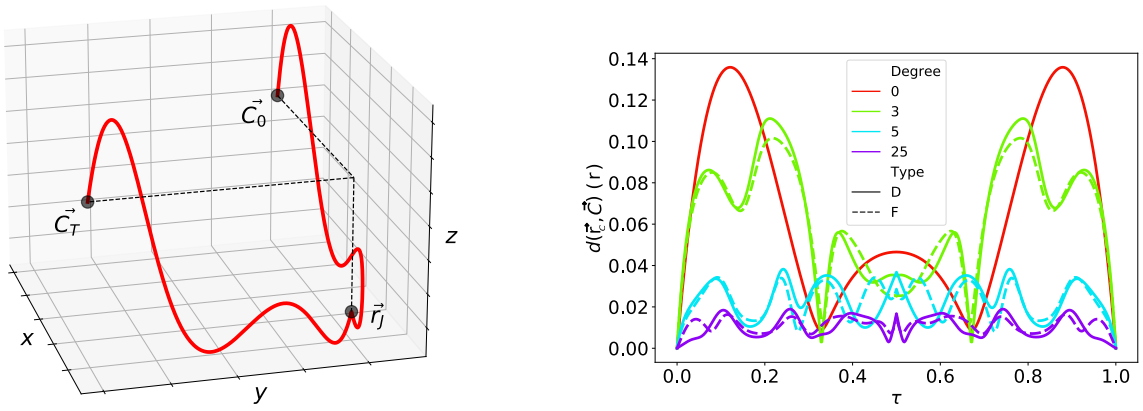

(a) (b)

Figure 6.1: (a) Example of a corner trajectory (red solid line) from $\vec{C}_0$ to $\vec{C}_T$ constrained to pass through $\vec{r}_J$. Dashed black lines are drawn to facilitate the three-dimensional view of the problem. (b) Displacement d as a function of normalized time ($\tau = t/T$). Solid lines represent optimal solutions using a diagonal form (D) of $\boldsymbol{R}(t)$, while dashed lines correspond to the optimization of all entries of $\boldsymbol{R}(t)$ (F). Colors indicate different numbers of control functions (*i.e.*, free parameters) used in the optimization.

6.4.1 Three-dimensional shuttling with reduced displacement from the potential center

Achieving fast, diabatic shuttling necessitates strong acceleration and deceleration at the beginning and end of the transport process. The simplest way to implement such rapid changes in velocity often involves allowing the ion to undergo significant displacement from the center of the trapping potential. However, in practical setups, large displacements can push the ion into regions where the trapping potential exhibits substantial anharmonicity, leading to unwanted excitations or loss of control. Consequently, minimizing the ion's deviation from the potential center is a crucial optimization goal.

As a concrete example, we consider the problem of minimizing the ion's maximum displacement while it is transported around a corner in a structured potential landscape (see Fig. 6.1a). The initial and final positions are specified by the vectors

$$\vec{C}_0 = (0, r, h) \qquad \text{and} \qquad \vec{C}_T = (r, 0, h)\ . \tag{6.9}$$

Additionally, an intermediate boundary condition,

$$\vec{r}_J(t = T/2) = (r, r, h) \tag{6.10}$$

is introduced to account for the fact that, in realistic experimental implementations, the ion's trajectory may not always maintain a strictly constant z-coordinate throughout the motion. This constraint ensures that the ion's path aligns with the structural limitations imposed by the trapping potential.

The potential landscape governing the ion's motion is described through the time-dependent matrix $M(t)$, defined in accordance with Eq. (3.52), and constrained by the boundary con-

ditions

$$\boldsymbol{M}_0 = \begin{pmatrix} \omega_t^2 & 0 & 0 \\ 0 & \omega_r^2 & 0 \\ 0 & 0 & \omega_r^2 \end{pmatrix} \quad \text{and} \quad \boldsymbol{M}_T = \begin{pmatrix} \omega_r^2 & 0 & 0 \\ 0 & \omega_t^2 & 0 \\ 0 & 0 & \omega_r^2 \end{pmatrix} , \tag{6.11}$$

with an axial frequency ω_t that is substantially smaller than the radial frequency ω_r, so that the preferred direction of motion is initially along the x-axis and, finally, along the y-axis. Since the displacement required for acceleration or deceleration can be arbitrarily reduced by increasing the confining potential along the relevant axis, the optimization is subject to the constraints

$$\boldsymbol{M}_{xx} \leq \min(\boldsymbol{M}_{yy}, \boldsymbol{M}_{zz}) \leq 2\omega_r , \quad \text{for } t < T/2 , \tag{6.12a}$$

$$\boldsymbol{M}_{yy} \leq \min(\boldsymbol{M}_{xx}, \boldsymbol{M}_{zz}) \leq 2\omega_r , \quad \text{for } t \geq T/2 . \tag{6.12b}$$

These constraints ensure that, during the first half of the transport, the strongest confinement remains in the y-z plane while allowing modulation of $\boldsymbol{M}_{xx}$. In the second half, the role of x and y is switched, maintaining symmetry in the optimization process. The upper bound of $2\omega_r$ prevents the potential from becoming excessively stiff, which could introduce technical limitations in control hardware.

Under these conditions, adiabatic shuttling — where the transport duration T is long enough for the ion to remain in its motional ground state throughout — can achieve near-perfect transport fidelities ($F > 99\%$) for shuttling times $T > 200/\omega_t$. However, in many practical scenarios, such long durations are undesirable, as they limit the overall speed of quantum operations and increase susceptibility to decoherence.

Here, we focus on *diabatic* transport, where shuttling is performed significantly faster than the adiabatic limit. Specifically, a protocol with a duration of $T = 10/\omega_t$ is considered, corresponding to an order-of-magnitude reduction in transport time compared to the adiabatic regime. Unlike in adiabatic transport, where the ion remains in the motional ground state throughout the process, diabatic transport generally induces motional excitation. However, by ensuring that the ion follows the ground state of the invariant rather than the instantaneous ground state of the Hamiltonian, it is guaranteed to return to the motional ground state upon completion of the transport.

As described above, both the classical trajectory of the ion $\vec{r}_c$ and the matrix $\boldsymbol{R}(t)$ can be parameterized such that the boundary conditions are satisfied for any value of the expansion coefficients. To illustrate the capability of the proposed framework in solving control problems under constraints on achievable potentials, two distinct parameterizations of $\boldsymbol{R}(t)$ are considered:

- Case 1: Diagonal $\boldsymbol{R}(t)$ (no coupling between spatial dimensions): In this case, $\boldsymbol{R}(t)$ is constrained to remain diagonal at all times, with only the three diagonal elements subject to optimization. This ensures that the principal axes of the trapping poten-

tial remain aligned with the x, y and z directions, allowing only modulation of the confinement strength along each axis. While this constraint simplifies implementation, it limits flexibility, as the potential cannot rotate to optimally align with the ion's trajectory.

- Case 2: Fully optimized $\boldsymbol{R}(t)$ (potential coupling between spatial dimensions allowed): Here, all elements of $\boldsymbol{R}(t)$ are treated as free parameters, allowing for both strength modulation and dynamic rotation of the trapping potential. This additional degree of freedom enables continuous adaptation of the potential to the ion's motion, reducing motional excitation and improving transport performance. By dynamically reshaping the potential, this approach can mitigate unwanted excitations more effectively.

Fig. 6.1b illustrates the ion's displacement $d = \|\vec{d}\|$, where $\vec{d} = \vec{r}_c(t) - \vec{C}(t)$, from the center of the potential as a function of normalized time ($\tau = t/T$) for various optimization strategies. The color code corresponds to the number of control functions included in the optimization, while the line styles distinguish between solutions where the matrix $\boldsymbol{R}(t)$ is restricted to a diagonal (D) form or fully optimized (F). The red curve represents the unoptimized solution. For $\tau \leq 0.15$, the ion is progressively separated from the trap center, reaching a maximum displacement of approximately $0.14r$. This initial displacement occurs as the ion is accelerated away from the center, where the potential gradient is steep. Following this, the ion is decelerated and begins moving back towards the trap center, before experiencing another phase of separation. Due to the symmetry in trap geometry and time dependence of the invariant, the trajectory is symmetric around the instant $\tau = 1/2$.

The large displacements observed in the early and late stages of the protocol are physically anticipated. Strong acceleration and deceleration are required at the beginning and end of the shuttling process to minimize the duration of the protocol. These forces are most effectively applied when the ion is located further from the center of the trap, where the potential is less harmonic and the trapping forces are stronger. Consequently, the ion experiences more significant forces, enabling faster motion during these phases.

Achieving strong acceleration and deceleration without significant displacement from the trap center requires a carefully designed time dependence in the shuttling protocol. The green curves represent a numerically optimized protocol using three control functions for each independent component of $\vec{r}_c(t)$ and $\boldsymbol{R}(t)$. Both forms of $\boldsymbol{R}(t)$ lead to a reduction in the maximum displacement compared to the initial unoptimized solution. However, rotating the trapping potential by using the full $\boldsymbol{R}(t)$ matrix (dashed line) provides a slight improvement over the diagonal form.

Further optimization using five control functions (light blue curves) yields an even more significant improvement, with the maximum displacement reduced to below $0.04r$. Additionally, allowing for the rotation of the principal axes of the trapping potential (dashed line) leads to a further enhancement in the solution. To achieve even smaller displacements,

a substantial increase in the number of control functions is necessary. Optimizing up to 25 control functions (*i.e.*, 225 free parameters when using the full $\boldsymbol{R}(t)$ matrix, and 150 when using the diagonal $\boldsymbol{R}(t)$ matrix) results in a maximum displacement smaller than $0.02r$ (dashed purple line). In this case, the effect of allowing for rotation in the trapping potential becomes minimal.

Notably, for any given number of control functions per matrix element, the maximum displacement obtained in the optimization with a general $\boldsymbol{R}(t)$ matrix is slightly smaller than that in the corresponding optimization with a diagonal $\boldsymbol{R}(t)$ matrix. However, optimizations with a diagonal $\boldsymbol{R}(t)$ matrix can outperform those with a full $\boldsymbol{R}(t)$ matrix if the number of control functions in the diagonal case is only moderately larger than in the full-matrix case. This suggests that constraints on the experimentally realizable rotating potentials can be mitigated by introducing an additional temporal degree of freedom in the tunable trapping parameters, which provides an effective means to improve the transport protocol without the need for more complex experimental setups.

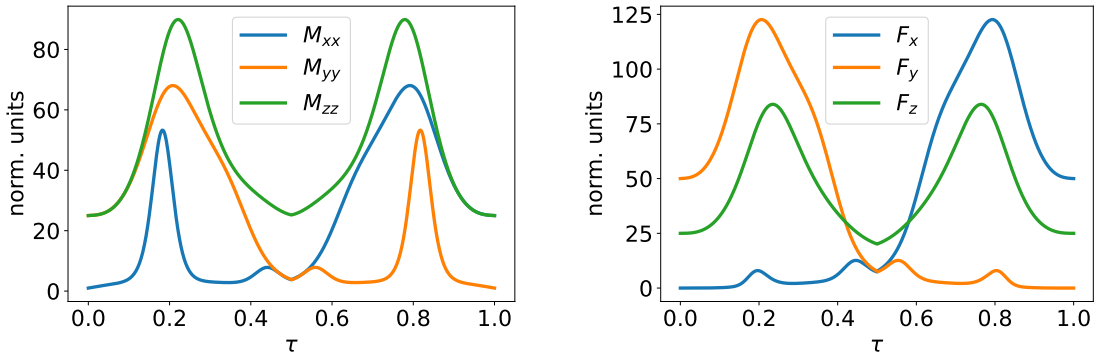

(a) (b)

Figure 6.2: (a) Optimal time evolution of (a) M_{xx}, M_{yy}, M_{zz} and (b) F_x, F_y and F_z, in units of $\sqrt{1/(m\omega_t)}$, for $\omega_r/\omega_t = 5$ and $\omega_t T = 10$, based on 25 control functions and $\boldsymbol{R}(t)$ in diagonal form.

While the discussion has thus far focused on optimizing the trajectory of the ion, achieving a true motional ground-state-to-ground-state protocol requires more than just minimizing displacement. The covariances of the Gaussian state must also evolve to their correct values throughout the shuttling process. This is critical because, for the ion to remain in the motional ground state at the end of the protocol, the uncertainties in its position and momentum must be in accordance with the final Hamiltonian.

Fig. 6.2 provides insight into this aspect of the process by depicting the time-dependent components of the trapping potential, M_{xx}, M_{yy}, and M_{zz} (Fig. 6.2a), alongside the corresponding linear force (Fig. 6.2b). Initially, the trapping potential provides weak confinement along the x-axis, followed by weak confinement along the y-axis at the final stage. Between these phases, two periods of increased confinement occur. These intervals are necessary to accelerate or decelerate the ion sufficiently to reach the target positions. The strength of the trapping potential during these periods directly influences the forces expe-

rienced by the ion, as shown in Fig. 6.2b. In particular, the force is concentrated in the directions in which the ion is being moved: along the y- and z-axes in the first half of the protocol, and along the x- and z-axes in the second half.

However, simply increasing the confinement throughout the protocol to ease control over the ion's trajectory is not a viable strategy. Excessive confinement would cause undesirable dynamics in the covariances, preventing the ion from reaching the ground state of the final Hamiltonian. To achieve optimal control, the protocol must therefore balance strong confinement and weak confinement. Strong confinement should only be applied during the phases of the protocol that require significant acceleration or deceleration, while weak confinement is necessary during the remaining intervals to allow the ion's motional state to evolve smoothly into the desired final configuration.

So far, the primary goal has been to minimize the ion's displacement. However, in practical applications, the maximum allowable displacement is often constrained by experimental limitations rather than being a freely tunable parameter. Since the ion's acceleration is directly related to its displacement from the center of the potential, imposing a limit on the displacement introduces a corresponding constraint on the protocol's duration. As the displacement increases, the ion's motion can be slowed or accelerated more, but this can only be sustained for a limited period. Therefore, achieving perfect motional ground-state fidelity is only feasible within specific timescales, a concept that will be explored further in the subsequent analysis.

To formalize this relationship, consider the Hamiltonian $H(t)$ expressed in terms of the trap center $\vec{C}(t)$, as in Eq. (4.26). The ion's classical acceleration can be derived from Hamilton's equations of motion as follows

$$\ddot{\vec{r}}_c(t) = \frac{-1}{m}\frac{\partial H(t)}{\partial \vec{r}_c} = -\boldsymbol{M}(t)(\vec{r}_c(t) - \vec{C}(t)) = -\boldsymbol{M}(t)\vec{d}(t) \ , \tag{6.13}$$

and thus depends linearly on the ion's displacement $\vec{d}$ and the inverse of the trapping potential's curvature.

Next, we introduce a constraint on the ion's displacement. We assume that for all times t within the shuttling duration $[0, T]$, the maximum displacement is bounded by a value ϵ, *i.e.* $\|\vec{d}\| \leq \|\vec{\epsilon}\|$[1]. In some cases, $\vec{\epsilon}$ may depend on the spatial position of the ion, *i.e.* $\vec{\epsilon} \equiv \vec{\epsilon}(\vec{r}_c)$, reflecting variations in the trap landscape. Such variations could arise from inhomogeneities in the trapping potential, control limitations, or the need to account for experimental constraints, such as noise or imperfect calibration. In this case, we take the minimum value of $\vec{\epsilon}$ along the trajectory $\vec{r}_c(t)$, *i.e.* $\vec{\epsilon} \equiv \min_{\vec{r}_c(t)} \vec{\epsilon}\,(\vec{r}_c)$.

Assuming that the trapping frequencies $\boldsymbol{M}(t)$ are bounded from above, *i.e.*, $\|\boldsymbol{M}(t)\| <$

[1]While one could analyze this constraint component-wise along each spatial dimension, we consider the norm of the displacement for simplicity.

M_{max}, we can derive a constraint on the acceleration from Eq. (6.13)

$$\|\ddot{\vec{r}}_c(t)\| < M_{max}\|\vec{\epsilon}\| \ . \tag{6.14}$$

This inequality provides a limit on the minimum time required to achieve perfect motional state fidelity during the transfer of the ion over a distance greater than zero. Specifically, we find that

$$T > \sqrt{\frac{2\Delta}{M_{max}\|\vec{\epsilon}\|}} \ , \tag{6.15}$$

where Δ represents the distance to be traveled.

Thus, if the transport protocol does not satisfy this inequality, some residual motional excitation will inevitably persist at the conclusion of the protocol. In other words, the ion's motional state will not perfectly match the ground state of the final Hamiltonian but will instead remain in a superposition that includes excited states. Importantly, a larger allowable displacement $\|\vec{\epsilon}\|$ enables faster transport by permitting greater accelerations. Likewise, stronger trapping potentials (higher M_{max}) allow for increased accelerations even when the maximum permitted displacement is more restricted.

6.4.2 Narrow wave packets in weak confinement

The spatial extent of the wave packet in diabatic dynamics is dictated by the strength of the confining potential. In a weak potential, the wave packet naturally broadens, making it more susceptible to anharmonicities in the potential landscape. However, during diabatic shuttling, the wave packet does not necessarily expand to match the equilibrium width dictated by the local trapping potential. This is because the timescale of the transport can be fast enough to prevent significant broadening, limiting the extent to which the wave packet can adjust to the local confinement.

More importantly, by carefully preparing the initial wave packet shape, one can exploit the system's natural dynamics to counteract broadening. If the wave packet is squeezed before entering a region of weak confinement — while still under strong control from the trapping potential — its narrow profile can persist for a longer duration, effectively delaying the impact of weak trapping on its spatial spread. This controlled evolution allows the wave packet to navigate through regions of varying confinement without excessive distortion, reducing the influence of anharmonic effects.

To illustrate this concept, consider the problem of dynamically reducing the spatial width $\Sigma_{xx}(t)$ of a wave packet — where $\Sigma_{xx}(t) = \mathrm{Tr}\big[\rho(t)\big\{(\vec{r}-\vec{r}_c),(\vec{r}-\vec{r}_c)^T\big\}\big]$ denotes the spatial component of the covariance matrix $\mathbf{\Sigma}(t)$ associated with the Gaussian state. The wave packet is confined by a time-dependent trapping frequency $\omega(t)$, which must satisfy the boundary conditions $\omega(0) = \omega(T) = \omega_0$, ensuring that the wave packet evolves from the ground state of the initial Hamiltonian to the ground state of the final Hamiltonian. During the intervals $0 \leq t \leq T/4$ and $3T/4 \leq t \leq T$, the trapping frequency can be modulated

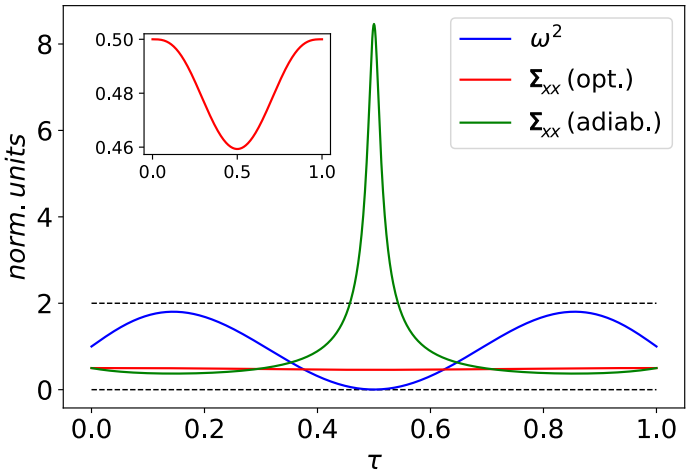

Figure 6.3: Squared trapping frequency $\omega^2(t)$ and spatial uncertainty Σ_{xx} of the quantum state as a function of normalized time τ. The red curve shows the evolution of Σ_{xx} under the optimal protocol, while the green curve corresponds to adiabatic transport. Dashed black lines mark the upper and lower frequency limits. All quantities are expressed in units of $\sqrt{\frac{1}{m\omega_0}}$, with $\omega_0 T = 1$ in this case.

up to a maximum value of $\sqrt{2}\omega_0$, whereas in the central interval $T/4 \leq t \leq 3T/4$, it is constrained to a maximum of ω_0. The goal of the optimization involves minimizing a weighted average of the maximum wave packet width $\Sigma_{xx}(t)$ and the maximum trapping frequency $\omega(t)$. Specifically, the cost function to be minimized is defined as

$$C = \alpha \max_t \left(\Sigma_{xx}(t)\right) + (1-\alpha) \max_t \left(\omega(t)\right) \tag{6.16}$$

for $T/4 < t < 3T/4$, where α determines the relative importance of reducing the wave packet width versus minimizing the trapping frequency within the constrained interval.

The protocol depicted in Fig. 6.3 involves the optimization of 25 control functions. The left panel shows the evolution of the squared trapping frequency ω^2 (in blue) as a function of normalized time. The optimal trajectory of $\omega^2(t)$ begins by increasing the trapping strength to approximately twice its initial value, followed by a gradual reduction in confinement. During the central time window, $T/4 < t < 3T/4$, the trapping potential weakens. The squared trapping frequency reaches a minimum close to zero at $t = T/2$, after which it exhibits a symmetric evolution relative to this time.

The red curve in the figure illustrates the temporal evolution of the wave packet's spatial width $\Sigma_{xx}(t)$ under this optimal time-dependent trapping potential. Notably, the uncertainty in the wave packet's position does not increase during the protocol; instead, it even slightly decreases in the central region where the confinement is weakest (see inset). The minimum uncertainty occurs at $t = T/2$, coinciding with the point of minimal confinement. This highlights an intriguing result: in weakly confined potentials, the wave packet can achieve a minimum width, but only under non-adiabatic conditions.

In contrast, if the protocol duration is increased by a factor of 10, *i.e.* $T' = 10T$, radically different results are obtained. In this case, the uncertainty evolves inversely proportional to the confinement, as indicated by the green curve in Fig. 6.3. In the first quarter of the protocol, the wave packet width slightly decreases due to stronger confinement. However, as the potential strength weakens, the wave packet broadens, reaching its maximum width in the central time window. As the confinement is increased again in the second half of the protocol, the wave packet re-localizes before settling into the final motional ground state.

6.4.3 Shuttling based on null control over the curvature of the potential

The challenge of shuttling around a corner, as discussed in Sec. 6.4.1, illustrates how constraints on realizable trapping potentials can be mitigated by leveraging temporal degrees of freedom. More generally, limitations in control over certain system parameters can often be compensated by precisely tuning others. This principle is exemplified in the following scenario, where only the linear force terms can be dynamically controlled, while the curvature of the potential remains fixed, allowing only the trap center to be adjusted.

Crucially, although the potential's curvature is time-independent, the curvature experienced by the ion depends on its position along the trajectory. In realistic settings, trapping potentials are typically anharmonic, resulting in position-dependent curvature variations. Since the ion's trajectory determines which regions of the potential it explores, it effectively modulates the confinement it experiences. By carefully designing the trajectory, one can thus compensate for restrictions on direct control over the trap's confinement strength.

This effect is illustrated by considering the potential

$$V(t) = \frac{1}{2}m\left(\omega_x^2 \frac{yx^2}{y_c} + \omega_y^2 (y - y_0(t))^2\right) , \tag{6.17}$$

which describes a tapered trap where the confinement in the x-direction varies along the y-axis. The trapping parameters ω_x, ω_y, and y_c remain fixed, while only the trap center $y_0(t)$ can be dynamically controlled. Importantly, the local confinement in the x-direction is governed by the frequency $\omega_x\sqrt{\frac{y(t)}{y_c}}$, which depends on the particle's trajectory. Since $y(t)$ can be controlled in terms of the trap center $y_0(t)$, this allows for effective modulation of the confinement strength in the x-direction, despite the absence of direct tunability.

Since the quadratic components of the trapping potential are not directly controllable, the current invariant-based control framework does not inherently guarantee ground-state-to-ground-state shuttling. Applying the framework without modification results in an overdetermination of the quadratic potential term, represented by $\boldsymbol{M}(t)$ in Eq. (3.52). Specifically, $\boldsymbol{M}(t)$ is constrained by two distinct and potentially conflicting conditions:

(i) **Framework prescription**: The standard control framework defines $\boldsymbol{M}(t)$ through a designated matrix $\boldsymbol{R}(t)$, according to Eq. (3.61).

(ii) **Physical potential curvature**: The actual trapping potential (Eq. (6.17)) imposes a curvature constraint along the ion trajectory $(x(t), y(t))$:

$$\boldsymbol{M}(x(t), y(t)) = \frac{m}{y_c} \begin{pmatrix} \omega_x^2 y(t) & \omega_x^2 x(t) \\ \omega_x^2 x(t) & \omega_y^2 y_c \end{pmatrix} . \tag{6.18}$$

While the framework prescription via Eq. (3.61) is intended to ensure that the ion remains in the ground state of the invariant operator throughout the shuttling process, the physical curvature defined by Eq. (6.17) governs the actual forces experienced by the ion. The lack of inherent compatibility between these two constraints means that achieving ground-state-to-ground-state transfer is not guaranteed by the framework alone.

Nevertheless, the discrepancy between these constraints can be mitigated by numerically optimizing the ion's trajectory $(x(t), y(t))$ to ensure that the curvature of the physical potential along the path closely matches a quadratic term $\boldsymbol{M}(t)$ that remains compatible with a matrix $\boldsymbol{R}(t)$ prescribed by the invariant. If an optimized trajectory exists such that the resulting $\boldsymbol{M}(t)$ satisfies both the curvature constraint imposed by the potential and the compatibility condition with $\boldsymbol{R}(t)$, then a viable shuttling protocol is achieved. In this case, the ion remains in the ground state of the invariant operator throughout the transport, ensuring a successful ground-state-to-ground-state transfer.

To illustrate this, consider the control problem of moving the trap center from its initial position $y_0(0) = y_i$ to its final position $y_0(T) = y_f$ ensuring that the particle evolves from the ground state of the initial Hamiltonian to that of the final Hamiltonian. The specific parameter values chosen for this example are $y_i = 10y_c$, $y_f = 1000y_c$, and $\omega_y = 10\omega_x$. In this setting, adiabatic transport corresponds to protocol durations $T > 70/\omega_y$, yielding a fidelity $F > 99\%$ or, equivalently, a final motional occupation $\bar{n} < 10^{-2}$. The results presented here correspond to a significantly shorter duration, $T = 3/\omega_y$, where an adiabatic approach would instead lead to $\bar{n} = \mathcal{O}(10^3)$.

Fig. 6.4a shows the optimal trajectory of the trap center $y_0(t)$ in black ($x_0(t) = 0$ for all t), derived from the optimal choices of the matrix $\boldsymbol{R}(t)$ and vector $\vec{r}_c(t)$. The resulting trap center exhibits oscillations well beyond the spatial interval through which the ion is intended to be transported. However, the ion trajectory (red) remains confined within this interval. The ion moves relatively slowly during the first 60% of the total transport duration, with the majority of the displacement occurring within a brief window — approximately 20% of the total time — before slowing down again during the final 10% of the protocol.

As a consequence of this motion, the confinement along the x-direction remains relatively weak during the first half of the transport and increases toward its final value only later, as shown in Fig. 6.4b (red). The time-dependent confinement required for perfect ground-state-to-ground-state transfer, as derived from the invariant framework, is shown in blue. The deviation between the two remains small — in fact, the protocol achieves an infidelity below 0.02% (corresponding to a final motional excitation of $\bar{n} < 10^{-4}$) — indicating

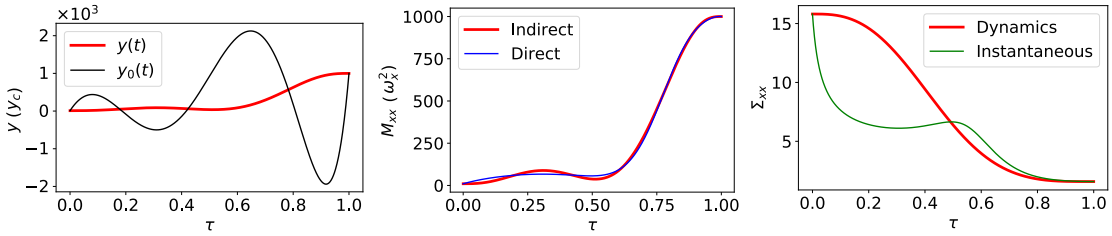

(a) (b) (c)

Figure 6.4: (a) Trajectory of the ion along the y-axis as a function of time, following the optimal temporal evolution (red) and the corresponding trajectory of the trap center y_0 (black). (b) The red curve shows the indirect modulation due to the position-dependent curvature of the tapered trap, while the blue curve represents the curvature required for perfect ground-state transfer, achieved through direct dynamic control. (c) Wave-packet spread in x (in normalized units) as a function of time. The red line shows the dynamics resulting from following the trajectory $y(t)$ (with the appropriate velocity), while the green curve represents the instantaneous spread corresponding to the trajectory's curvature M_{xx}, ignoring the dynamics of the full trajectory.

that the ion's dynamics closely approximate those of an ideal ground-state-to-ground-state transport, even in the absence of direct control over the potential curvature.

The near-perfect fidelity of the shuttling protocol also suggests that the ion's covariances evolve toward values characteristic of the ground state of the final Hamiltonian. This is illustrated in Fig. 6.4c, where the evolution of the covariance matrix is compared between the adiabatic limit and the diabatic, fast protocol. The green curve represents the evolution of the instantaneous spatial covariance during slow, adiabatic transport actual trajectory of the ion (shown in red in Fig. 6.4a). In this adiabatic limit, the ion's quantum state continuously evolves along the ground states of the instantaneous Hamiltonian.

In contrast, the red curve depicts the dynamics of $\Sigma_{xx}(t)$ along the same trajectory, but accounting for the actual velocity of the ion during the fast transport. Despite the strong accelerations the ion experiences, as indicated by the high amplitudes of the trap centre in Fig. 6.4a, and the intervals of slow dynamics that result in plateaus in the instantaneous covariance (green curve in Fig. 6.4c), the dynamics of the Σ_{xx} exhibit a remarkable simplicity. The wave packet width decreases monotonically, reaching its desired final value at the end of the shuttling process. Therefore, the covariance evolves exactly as it would in an adiabatic protocol, even though the protocol operates far outside the adiabatic regime.

6.5 Conclusions

In Chapter 5, we introduced an operator-based formulation of quantum control designed to mitigate the exponential complexity of solving system dynamics. While this approach does not require analytical solutions, such solutions can offer major advantages when available. For instance, in the case of a multidimensional harmonic Hamiltonian for a single ion, the solution can be embedded directly into the control formulation, provided the constraint equation (Eq. (3.62)) and boundary conditions (Eq. (6.6)) are satisfied. This enables efficient exploration of remaining degrees of freedom in the invariant for refining state transfer in meaningful ways.

Looking forward, incorporating more realistic effects into the framework will be important for practical applications. For example, models of decoherence and dissipation would account for interactions between the ion and its environment, such as collisions with background gas or thermal fluctuations. This would improve predictions of ion dynamics in noisy settings, enabling protocols that compensate for these effects. Similarly, expanding noise models to multidimensional traps — where anisotropic forces influence motion — would enhance accuracy in advanced architectures with complex geometries. Such extensions are vital for modern traps, which increasingly use intricate electrode layouts to manipulate multiple ions or degrees of freedom.

While invariants provide a rigorous foundation for protocol design, practical implementation requires balancing theoretical principles with experimental constraints. For instance, the physical layout of trap electrodes restricts the range of achievable electric fields, making some mathematically optimal protocols impractical. Constructing invariants tailored to arbitrary trap geometries remains challenging, but our approach minimizes deviations between idealized models and experimentally feasible solutions. By focusing on optimizations that align with hardware limitations — such as refining the timing of potential changes rather than their amplitude — we bring theoretical insights closer to practical implementation. This adaptability ensures that protocols remain viable in real-world quantum processors, where factors like fabrication tolerances and control bandwidth limitations must be accounted for.

In summary, analytic invariants offer a compelling strategy for precise, efficient, and robust ion transport. By combining solid theory with practical flexibility, we move closer to scalable quantum technologies that can operate reliably under real-world conditions. Future work will focus on extending the framework to incorporate environmental effects and multi-ion shuttling, ensuring its continued relevance as quantum hardware grows in complexity.

Chapter 7

Generally Noise-Resilient Quantum Gates for Trapped Ions

CONTRIBUTIONS

This work was carried out in collaboration with Wasim Rehman, under the supervision of Florian Mintert. Wasim contributed to the initial development of high-fidelity entanglement for two non-identical species, while I generalized the approach to arbitrarily long chains and motional modes, incorporating the effects of environmental decoherence and operational imperfections, and conducted the numerical tests. The results are available in Ref. [3].

Resilience to noise is a critical requirement for the practical viability of quantum devices. While proof-of-principle experiments, such as those in trapped-ion systems, often rely on time-intensive cooling and meticulous calibration to achieve idealized conditions like ground-state operation [126, 115], real-world applications cannot afford frequent recalibration or re-cooling once a task begins. Practical implementations must inherently tolerate deviations from theoretical ideals, such as imperfect ground-state cooling or finite-strength interactions, which are unavoidable in experimental settings [218, 219, 220]. Optimal control techniques provide a pathway to engineer such resilience by tailoring quantum dynamics to suppress sensitivity to specific noise sources [221, 222, 4, 223]. However, as quantum systems scale toward practical utility, the number of fluctuating parameters — such as laser intensities, trap frequencies, or environmental couplings — grows rapidly [96, 223]. A key challenge lies in ensuring that efforts to mitigate one source of imperfection do not inadvertently amplify sensitivity to others. Achieving robust performance thus demands a unified control framework that addresses multiple noise sources simultaneously, rather than solving isolated optimization problems [224].

In this Chapter, we address this challenge for trapped-ion systems, where entangling gate fidelity is threatened by anharmonic trap dynamics, fluctuations in laser control fields,

and thermal excitations. While our explicit solutions focus on trapped ions, the principles underlying these imperfections — such as parameter drift, environmental decoherence, and nonlinear system responses — are shared across quantum platforms. For instance, superconducting qubits face analogous issues with flux noise and charge fluctuations [102], while neutral atom arrays contend with laser intensity variations and positional inhomogeneities [225]. By developing protocols that balance robustness across multiple noise channels, we advance not only trapped-ion technologies but also provide a blueprint for error-resilient quantum control in diverse architectures. This approach underscores the necessity of harmonizing theoretical models with the imperfections inherent to real-world hardware, ensuring scalability without compromising performance.

7.1 Trapped-ion quantum gates

Geometric phase gates are a cornerstone of trapped-ion quantum computing, leveraging the shared motional modes of ions to mediate entangling interactions through precisely controlled laser fields. In Sec. 7.1, we introduced the fundamental principles of trapped-ion quantum computing, and discussed in Sec. 4.1.4 the implementation of geometric gates, including the MS gate (Eq. (4.115)), which has demonstrated fidelities exceeding 99% in both optical and hyperfine qubits [226, 227, 131, 228]. These gates exploit the accumulated geometric phase of the ions' internal states as they traverse closed trajectories in phase space, offering intrinsic robustness against certain types of noise [115, 75]. However, despite these advantages, current implementations remain susceptible to a range of experimental imperfections that limit their fidelity and scalability.

One of the primary challenges in implementing high-fidelity entangling gates is the coupling of qubit states to motional degrees of freedom. While geometric gates are designed to be insensitive to the initial motional state, they remain vulnerable to motional heating and mode-frequency fluctuations, both of which degrade gate performance [229, 230]. Additionally, systematic errors arising from laser intensity fluctuations, detuning drifts, and phase instability introduce further sources of infidelity [231, 75]. The interplay among these error sources presents a fundamental challenge: optimizing gate parameters to mitigate one type of error often exacerbates another. For instance, increasing laser power can reduce the gate duration and improve resilience to detuning errors, yet it also enhances off-resonant coupling to carrier transitions, introducing additional decoherence [229, 232]. Similarly, in multi-ion systems, strategies to suppress motional mode cross-talk by slowing down gate operations can lead to reduced coherence times and imperfect coupling [233, 234].

Beyond these technical limitations, geometric gates face additional challenges when scaling to larger ion chains. As the number of ions increases, the motional mode structure becomes increasingly complex, with coupling strengths varying across the chain and different modes becoming comparable in magnitude [235, 236, 237]. This complexity makes it difficult to selectively address a single mode without inadvertently exciting spectator modes, leading to residual spin-motion entanglement and degraded gate fidelities [234]. The need for robust control strategies that can suppress these effects is therefore essential for scalable

implementations of geometric gates in trapped-ion quantum processors.

Several approaches have been proposed to enhance the robustness of entangling gates. One strategy involves shaping the phase-space trajectory of the ions by modulating the sideband field parameters — such as phase, frequency, or amplitude — to minimize susceptibility to motional heating [238, 239]. Another approach employs multi-tone driving schemes, where carefully detuned fields are applied to engineer interference effects that suppress unwanted motional excitations [240]. While these techniques have demonstrated improved resilience against motional noise, they remain constrained by the requirements of the Lamb–Dicke regime, where weak laser-ion interactions are necessary to maintain high fidelity. This constraint not only limits gate speeds but also necessitates near-ground-state cooling of the motional modes, posing a scalability bottleneck for architectures that rely on active ion shuttling [205, 2].

Moving beyond the Lamb–Dicke regime presents an alternative path toward more robust and scalable entangling operations. In this regime, stronger spin-motion coupling enables faster gate times, reducing sensitivity to decoherence and allowing for high-fidelity operations even with elevated motional states. One approach in this direction involves employing complex pulse sequences to induce state-dependent kicks that exceed the motional frequencies, effectively accelerating the gate operation [241]. While this technique achieves significant speed improvements, it introduces new challenges related to experimental complexity and unwanted coupling to additional motional modes. Another method relies on higher-order sideband transitions, carefully engineered to cancel undesired contributions from the non-linear spin-motion coupling effects that arise beyond the Lamb–Dicke approximation [240]. While promising, these approaches require careful balancing of additional sideband excitations, which may introduce increased sensitivity to motional heating.

Another significant challenge faced by current entangling gates involves scaling to larger ion chains with a complex multi-mode structure [235, 236, 237]. This scaling not only amplifies noise sensitivity due to increased crosstalk between ions [234], but also significantly complicates control protocols, particularly when operating far from the Lamb-Dicke regime. In these larger systems, the coupling strength for each motional mode becomes comparable, and it varies across different ions in the chain. Selectively driving a single mode in such a system inevitably triggers higher-order phonon exchange processes, unintentionally coupling non-targeted spectator modes to the qubit states. This makes achieving high-fidelity gates more difficult and necessitates control strategies that differ from those used in systems with fewer modes, where precise control over individual modes is typically sufficient.

To address these challenges, this Chapter presents a gate scheme that integrates multiple strategies to mitigate various error sources in trapped-ion quantum computing. Our control framework ensures high-fidelity entanglement with hot trapped ions in a multi-mode system, demonstrating resilience against motional heating and improved robustness against fluctuations in both qubit frequencies and normal-mode frequencies. This is achieved through a polychromatic driving field that includes tones near-resonant with the first-

order sideband of a designated central mode, which serves as the primary driver for the gate, as well as second-order sidebands of both central and spectator modes. By expanding the interaction Hamiltonian to higher-order terms in the Lamb-Dicke parameter η, we derive specific driving functions that guarantee purely entangling dynamics, eliminating residual spin-motion coupling and unwanted spin-flip processes.

7.1.1 Hamiltonian model

The dynamics of a system composed of N[1] trapped ions and their M collective vibrational modes are governed by the Hamiltonian H_0, as defined in Eq. (4.91). This Hamiltonian contains two distinct contributions: the first describes the energy splitting of the electronic states of the ions, while the second accounts for the quantized collective motion of the ion chain, which is modeled as M independent harmonic oscillators with frequencies ν_l.

When the system is subjected to an external electromagnetic field — such as a laser — the interaction between the field and the ions simultaneously excites both the internal and motional degrees of freedom. As discussed in Sec. 4.1.3, this coupling arises from terms in the multipole expansion of the field-matter interaction, including electric dipole, magnetic dipole, and higher-order contributions. For classical fields with sinusoidal time dependence (Eq. E.11), the interaction can be transformed into the interaction picture with respect to H_0, yielding an effective interaction Hamiltonian of the form given in Eq. (4.143), which encapsulates the coupling between the ions' spin states and their collective motion induced by the external field.

Modern experimental techniques extend beyond simple sinusoidal driving fields. By engineering temporally modulated electromagnetic fields, it is possible to synthesize waveforms with arbitrary time dependence. For instance, the electric field can be decomposed into a superposition of plane waves

$$\vec{E}(\vec{r},t) = \mathrm{Re}\left[\sum_p E_p e^{i(\vec{k}_p\cdot\vec{r}-\omega_p t+\phi_p)}\right] , \tag{7.1}$$

where each component is characterized by its amplitude E_p, wavevector $\vec{k}_p$, frequency ω_p and phase ϕ_p. Such multichromatic fields enable precise control over the system's dynamics by leveraging interference effects between frequency components.

A critical regime for scalable quantum control arises when the wavevectors of the applied fields approximately align (*i.e.* $\vec{k}_p \approx \vec{k}$). This alignment ensures a uniform spatial phase profile across all field components, effectively decoupling the spatial and temporal dynamics of the interaction. Under this condition, the electric field (Eq. (7.1)) simplifies to

$$\vec{E}(\vec{r},t) = e^{i\vec{k}\cdot\vec{r}} f(t) \; + \; \text{h.c.} \; , \tag{7.2}$$

[1]Note that in this chapter, N represents the number of ions, replacing the lowercase n used in previous chapters to refer to the system's constituents. This change ensures that n is reserved for labeling the Fock-state occupations of the motional modes.

where $f(t) = \sum_p \frac{E_p}{2} e^{-i(\omega_p t - \phi_p)}$. By synthesizing a sufficiently broad spectrum of tones, $f(t)$ can approximate arbitrary time-dependent functions through spectral engineering, enabling Fourier-synthesized waveforms. This capability is central to quantum optimal control, where $f(t)$ is dynamically optimized to enhance gate fidelity, suppress decoherence, or minimize operation times.

Modern trapped-ion platforms further extend this paradigm by enabling site-selective control of individual ions. Through tightly focused laser beams or frequency-space multiplexing, distinct time-dependent modulations $f_j(t)$ can be applied to each ion. This programmability generalizes the interaction Hamiltonian Eq. (4.97) to

$$\begin{aligned} H'_{\text{light-matter}} = \sum_{j=1}^{N} \frac{\Omega_{eg}^{(j)}}{2} \Bigg(& f_j(t) e^{i\omega_{eg}^{(j)} t} \prod_{l=1}^{M} \exp\Big(i\eta_{jl} (a_l e^{-i\nu_l t} + a_l^\dagger e^{i\nu_l t}) \Big) \\ & + f_j^*(t) e^{i\omega_{eg}^{(j)} t} \prod_{l=1}^{M} \exp\Big(-i\eta_{jl} (a_l e^{-i\nu_l t} + a_l^\dagger e^{i\nu_l t}) \Big) \Bigg) \sigma_+^{(j)} \\ + \sum_{j=1}^{N} \sum_{m \in \{g,e\}} \frac{\Omega_{mm}^{(j)}}{2} \Bigg(& f_j(t) \prod_{l=1}^{M} \exp\Big(i\eta_{jl} (a_l e^{-i\nu_l t} + a_l^\dagger e^{i\nu_l t}) \Big) \\ & + f_j^*(t) \prod_{l=1}^{M} \exp\Big(-i\eta_{jl} (a_l e^{-i\nu_l t} + a_l^\dagger e^{i\nu_l t}) \Big) \Bigg) \left| m^{(j)} \right\rangle\!\left\langle m^{(j)} \right| \\ & + \text{h.c.} \,. \end{aligned} \tag{7.3}$$

The first summation in $H'_{\text{light-matter}}$ describes coherent transitions between the internal states $\left|g^{(j)}\right\rangle \leftrightarrow \left|e^{(j)}\right\rangle$ of each ion j, driven by a site-dependent modulation function $f_j(t)$. These transitions are mediated by the interaction between the ions and the collective motional modes, with a coupling strength proportional to the Rabi frequency $\Omega_{eg}^{(j)}$. The modulation function $f_j(t)$, which encodes the applied electromagnetic field, dynamically controls the amplitude and phase of the interaction, enabling tunable, site-selective driving.

The second summation accounts for AC Stark shifts, which induce energy level shifts in $\left|g^{(j)}\right\rangle$ and $\left|e^{(j)}\right\rangle$ due to off-resonant couplings to the motional modes. These shifts depend on the Rabi frequencies $\Omega_{mm}^{(j)}$ and contribute an effective state-dependent potential, modifying the internal energy landscape of each ion.

The products $\prod_{l=1}^{M} \exp\Big(\pm i\eta_{jl} (a_l e^{-i\nu_l t} + a_l^\dagger e^{i\nu_l t}) \Big)$ in Eq. (7.3) represent the multimode displacement operators, entangling the internal state of ion j with all M motional modes. Here, ν_l denotes the frequency of the l-th motional mode, and $\eta_{jl} = \chi_{jl}\Lambda$ is the Lamb-Dicke parameter quantifying the spin-motion coupling strength. The parameter χ_{jl} corresponds to the normalized eigenvector component of ion j in mode l (see Eq. (4.40)), reflecting the spatial structure of the collective vibrations, while $\Lambda = \frac{2\pi}{\lambda}\sqrt{\frac{1}{2m\nu}}$ is the intrinsic coupling factor. This factor depends on the laser wavevector $k = 2\pi/\lambda$ and the ion mass m.

Expanding $f_j(t)$ as a Fourier series with non-negative frequency components $\omega_{jp} \geq 0$, the terms $f_j^*(t) e^{i\omega_{eg}^{(j)} t}$ introduce oscillatory contributions at frequencies $\omega_{jp} + \omega_{eg}^{(j)}$, while terms

proportional to $f_j(t)$ oscillate at ω_{jp}. When the frequency components ω_{jp} are tuned close to the qubit resonance frequencies, *i.e.* $\omega_{jp} \approx \omega_{eg}^{(j)}$, the RWA can be applied to eliminate rapidly oscillating terms at ω_{jp} and $\omega_{jp} + \omega_{eg}^{(j)}$, which vary rapidly compared to the interaction timescale, retaining only terms oscillating at $\omega_{jp} - \omega_{eg}^{(j)}$. This reduces the interaction Hamiltonian to

$$H'_{\text{light-matter}} = \sum_{j=1}^{N} g_j(t) e^{i\omega_{eg}^{(j)} t} \sigma_+^{(j)} \prod_{l=1}^{M} \exp\Big(i\eta_{jl} (a_l e^{-i\nu_l t} + a_l^\dagger e^{i\nu_l t}) \Big) \; + \text{h.c.} \,, \tag{7.4}$$

where $g_j(t) = \frac{\Omega_{eg}^{(j)}}{2} f_j(t)$ defines the effective time-dependent coupling strength.

To express the interaction Hamiltonian in a more convenient form, the BCH formula (Eq. (2.84)) can be applied to expand the exponential term in Eq. (7.4). This allows the expression to be rewritten as the product of two exponentials, each containing only creation or annihilation operators. Expanding these exponentials yields

$$H'_{\text{light-matter}} = \sum_{j=1}^{N} g_j(t) e^{i\omega_{eg}^{(j)} t} e^{\frac{-1}{2}\sum_l \eta_{jl}^2} \sigma_+^{(j)} \prod_{l=1}^{M} \sum_{p,q=0}^{\infty} e^{i(p-q)\nu_l t} (i\eta_{jl})^{p+q} \frac{(a_l^\dagger)^p a_l^q}{p!q!} \; + \text{h.c.} \,. \tag{7.5}$$

By introducing a new index $m = p - q$, this expression can be rewritten more concisely as

$$H'_{\text{light-matter}} = \sum_{j=1}^{N} g_j(t) e^{i\omega_{eg}^{(j)} t} e^{\frac{-1}{2}\sum_l \eta_{jl}^2} \sigma_+^{(j)} \prod_{l=1}^{M} \sum_{m=-\infty}^{\infty} \sum_{q=0, q\geq -m}^{\infty} e^{im\nu_l t} (i\eta_{jl})^{2q+m} \frac{(a_l^\dagger)^{q+m} a_l^q}{(q+m)!q!} + \text{h.c.} \,, \tag{7.6}$$

where the constraint $q \geq -m$ in the second sum ensures that the exponent of the creation operator $(a_l^\dagger)^{q+m}$ remains non-negative.

To further clarify the structure of the Hamiltonian, it can be expressed in terms of operators that directly describe the creation and annihilation of phonons in each motional mode. These operators are defined as

$$\mathcal{D}_{l,m}(\eta) = \sum_{q=0, q\geq -m}^{\infty} (i\eta)^{2q+m} \frac{a_l^{\dagger q+m} a_l^q}{(q+m)!q!} \,, \tag{7.7}$$

and satisfy the relation

$$\mathcal{D}_{l,-m}(\eta) = (-1)^m \mathcal{D}_{l,m}^\dagger(\eta) \,, \tag{7.8}$$

for $m \geq 0$. These operators encapsulate all processes involving the creation ($m > 0$) and annihilation ($m < 0$) of m phonons in mode l, providing a compact notation for describing

motional dynamics. Using this formalism, the interaction Hamiltonian takes the form

$$H'_{\text{light-matter}}(t) = \sum_{j=1}^{N} \tilde{g}_j(t)\sigma_+^{(j)} \prod_{l=1}^{M} \sum_{m=-\infty}^{\infty} e^{im\nu_l t}\mathcal{D}_{l,m}(\eta_{jl}) + \text{h.c.} \,, \tag{7.9}$$

where

$$\tilde{g}_j(t) = e^{\frac{-1}{2}\sum_{l=1}^{M}\eta_{jl}^2} e^{i\omega_{eg}^{(j)}t} g_j(t) \tag{7.10}$$

represents a renormalized driving function.

The operators $\mathcal{D}_{l,k}$ capture the k-th order sideband transitions of the motional mode l. To realize a coherent gate operation that relies on excitations of phonons, it is beneficial to define driving functions $\tilde{g}_j(t)$ that enable the spectral selection of specific processes. This can be achieved by parameterizing the driving pattern as follows

$$g_j(t) = -ie^{\frac{1}{2}\sum_{l=1}^{M}\eta_{jl}^2} \sum_l \frac{1}{\eta_{jl}} \sum_k F_{l,k}^{(j)}(t) e^{-i(k\nu_l + \omega_{eg}^{(j)})t} \,, \tag{7.11}$$

where the factors $e^{-i(k\nu_l+\omega_{eg}^{(j)})t}$ introduce the time-dependence necessary to achieve resonance with a specific sideband transition. The functions $F_{l,k}^{(j)}(t)$ exhibit a slow time-dependence compared to the motional frequencies ν_l and account for finite detuning and temporal modulation that can be used to achieve the desired robustness. Finally, the factor η_{jl}^{-1} reflects the fact that weaker interaction (smaller η_{jl}) requires proportionally stronger driving fields to maintain constant interaction strength.

Substituting Eq. (7.11) into Eq. (7.9) yields

$$\begin{aligned} H'_{\text{light-matter}}(t) = -i \sum_{j,j'=1}^{N} \Bigg(& \sigma_+^{(j)} e^{\frac{1}{2}\sum_{l=1}^{M}(\eta_{j'l}^2 - \eta_{jl}^2)} e^{i(\omega_{eg}^{(j)} - \omega_{eg}^{(j')})t} \\ & \times \sum_{l'} \frac{1}{\eta_{j'l'}} \sum_k \prod_{l=1}^{M} \sum_{m=-\infty}^{\infty} e^{i(m\nu_l - k\nu_{l'})t} F_{l',k}^{(j')}(t)\, \mathcal{D}_{l,m}(\eta_{jl}) \Bigg) \\ & + \text{h.c.} \,, \end{aligned} \tag{7.12}$$

which represents the exact generator of the dynamics induced by the light-matter interaction.

Notably, the derivation of Eq. (7.12) does not assume *a priori* individual addressing of ions, meaning that residual cross-talk terms naturally emerge. These terms arise from the summation over j', accounting for unintended couplings where a laser addressing ion j also interacts with ion j'. These undesired couplings, however, are strongly suppressed because the spatial profile of the driving fields ensures that the amplitudes $F_{l',k}^{(j)}(t)$ decay rapidly for ions $j' \neq j$ outside the targeted region, a consequence of the Gaussian intensity distribution of focused laser beams.

Furthermore, the structure of Eq. (7.12) reveals multiple distinct timescales governing the dynamics. The factors $e^{i(\omega_{eg}^{(j)}-\omega_{eg}^{(j')})t}$ oscillate at the frequency differences of the qubit transitions, which are significant only when the ions belong to different species. In addition, the exponential $e^{i(m\nu_l-k\nu_{l'})t}$ introduces vibrational frequencies, with resonant processes occurring when $m = k$ and $l = l'$; other combinations lead to rapidly oscillating, off-resonant terms. Finally, the driving functions $F_{l',k}^{(j')}(t)$ vary on a much slower timescale, as they are engineered to only contribute with a small detuning from the resonant transitions.

To simplify the analysis, we employ a RWA, which neglects terms in Eq. (7.12) that oscillate with frequencies ν_l and/or $\omega_{eg}^{(j)}$, while retaining the time dependence of the driving functions $F_{l,k}^{(j)}(t)$. The resulting resonant Hamiltonian thus reads

$$H'_{\text{light-matter}}(t) = -i\sum_{j=1}^{N}\left(\sigma_+^{(j)}\sum_{l,k}\frac{F_{l,k}^{(j)}(t)}{\eta_{jl}}\mathcal{D}_{l,k}(\eta_{jl})\prod_{l'\neq l}^{M}\mathcal{D}_{l',0}(\eta_{jl})\right) + \text{h.c.}\,, \tag{7.13}$$

where the operator

$$\mathcal{D}_{l,0}(\eta) = \sum_{n=0}^{\infty}\frac{(i\eta)^{2n}}{n!^2}a_l^{\dagger n}a_l^n \tag{7.14}$$

describe phonon-conserving, but phonon-number-dependent energy shifts. At first order, these shifts correspond to carrier transitions, while higher-order terms involve processes where phonons are temporarily created and annihilated, resulting in no net change in the phonon number.

This approximation is justified by the significant separation of timescales in the system: the phonon frequencies ν_l, which scale with the trap frequency ν, are typically orders of magnitude smaller than the qubit resonance frequencies $\omega_{eg}^{(j)}$ of the ions [96]. The quality of the rotating-wave approximation is thus determined by the ratio of the trap frequency ν to the characteristic frequency in the functions $F_{l,k}^{(j)}(t)$. In typical experiments this ratio is of the order 1/100 to 1/1000 [96, 242, 131, 130, 243], so that the employed approximations are consistent with currently targeted fidelities of entangling gates.

To rigorously validate this approach, we provide a quantitative error analysis in Section 7.1.4. By explicitly calculating contributions from far off-resonant terms omitted under the RWA, we demonstrate that their impact on gate fidelity is suppressed to levels below 10^{-5} — consistent with fault-tolerant quantum computing requirements.

7.1.2 Driving patterns

To implement a coherent quantum gate based on the Hamiltonian in Eq. (7.13), the functions $F_{l,k}^{(j)}(t)$ must be carefully designed to ensure that the motional state is unaffected by the internal state of the ions. This is achieved with driving patterns in which the driving amplitude $F_{l,-k}^{(j)}$ for any blue sideband transition ($k > 0$) is given by the driving amplitude

$F_{l,k}^{(j)}$ for the corresponding red sideband transition following the relation

$$F_{l,-k}^{(j)} = (-1)^k \left(F_{l,k}^{(j)}\right)^* \ , \tag{7.15}$$

where the factor $(-1)^k$ has its origin in Eq. (7.8).

With any such driving pattern, the interaction Hamiltonian Eq. (7.13) reduces to

$$H'_{\text{light-matter}}(t) = \sum_{j=1}^{N} \sigma_y^{(j)} \sum_{l,k>0} \frac{F_{l,k}^{(j)}(t)}{\eta_{jl}} \mathcal{D}_{l,k} \prod_{l' \neq l} \mathcal{D}_{l',0} \ + \text{h.c.} \ , \tag{7.16}$$

with the Pauli-Y operator $\sigma_y^{(j)} = i(\sigma_-^{(j)} - \sigma_+^{(j)})$. This simplified Hamiltonian provides the foundation for engineering the desired quantum gate dynamics. With the sideband symmetry constraint (Eq. (7.15)) now enforced, the remaining task reduces to designing the time-dependent profiles of $F_{l,k}^{(j)}(t)$ (for $k > 0$) to engineer the unitary transformation that generates entanglement in the electronic states of the ions.

Crucially, not all motional modes of the ion chain are required for entanglement generation. Only a subset of these modes, along with a finite number of their sideband transitions, play a crucial role. This selective coupling is central to many quantum gate schemes, as it enables targeted state manipulation while minimizing decoherence from unnecessary mode interactions. For example, the MS entangling gate achieves entanglement by selectively driving only the first sideband of a specific motional mode or a targeted group of modes.

As we have seen in Sec. 4.1.4, the implementation of this approach relies on operating in the weak coupling regime or restricting motional states to be near their ground states. In this regime, the displacement operators for the driven modes d can be approximated to the lowest order in η (see Eq. (4.100)) as

$$\mathcal{D}_{d,1} \approx i\eta_d a_d^\dagger \ , \tag{7.17}$$

while the displacement operators for the spectator modes effectively reduce to the identity,

$$\mathcal{D}_{l',0} \approx \mathbb{I} \ . \tag{7.18}$$

This first-order approximation implies that spectator modes remain effectively decoupled from the driven modes (see Eq. (7.16)), allowing them to be safely neglected in the dynamics. As a result, the interaction Hamiltonian simplifies to the form derived in Eq. (4.117) (in the case of global driving)

$$H_{MS}(t) = iS_y \sum_d \left(F_d(t) a_d^\dagger - F_d^*(t) a_d\right) \ , \tag{7.19}$$

where the collective spin operator is given by $S_y = \sum_j \sigma_y^{(j)}$. Together with suitable driving functions $F_d(t)$ (see Sec. 4.1.4), this effective Hamiltonian enables implementation of the entangling gate $U = e^{i\phi_T \sum_{j,k} \sigma_y^{(j)} \sigma_y^{(k)}}$ across all ion pairs (see Eq. (4.118)) .

Non-identical ion species and multi-mode systems

Although the Hamiltonian H_{MS} provides a conceptually simple framework for generating entangled states, its practical implementation faces key limitations. While a global driving field ($f_j(t) = F(t)$ for all ions j) works for identical ion species, two key challenges arise when dealing with non-identical ions.

First, non-identical ions possess different resonance frequencies $\omega_{eg}^{(j)}$, causing them to accumulate distinct phase factors $e^{i\omega_j t}$ during their evolution. This frequency mismatch disrupts the coherent buildup of entanglement, requiring additional control mechanisms to compensate for phase discrepancies. Second, ions with different internal structures experience varying coupling strengths to the shared motional modes, characterized by their Lamb-Dicke parameters η_{jl}. These variations lead to different scaling factors $e^{\frac{1}{2}\eta_{jl}^2}$ appearing in the interaction Hamiltonian (Eq. (7.9)), making it difficult to obtain uniform entangling interactions across the system.

While these challenges can be addressed through refined individual addressing techniques or frequency stabilization schemes, a more fundamental limitation arises from the very foundation of the MS gate: the Lamb-Dicke approximation. This approximation, which underpins the derivation of the simplified first-order Hamiltonian H_{MS}, is only valid in the weak coupling regime or when motional states remain close to their ground state. This restriction is formalized by the inequality $(\eta_{jl}^2/2)n_l \ll 1$ [244, 240], where n_l represents the phonon occupation number in mode l. If this condition is not met — such as in systems with higher phonon excitations or strong ion-motion coupling — the standard MS formulation breaks down, necessitating alternative approaches for robust high-fidelity quantum operations.

Beyond the Lamb-Dicke approximation

Moving beyond the Lamb-Dicke approximation — whether due to stronger ion-motion interactions or the presence of higher motional excitations — fundamentally alters the structure of the interaction Hamiltonian. In this regime, the displacement operators in Eq. (7.7) must incorporate higher-order phonon-exchange processes, leading to more intricate spin-motion interactions. For a driven motional mode, this results in an expansion of the form

$$\mathcal{D}_{l,k}(\eta) \approx \frac{(i\eta)^k}{k!} a_l^{\dagger k} + \frac{(i\eta)^{k+2}}{(k+1)!} a_l^{\dagger(k+1)} a_l + \cdots \,. \tag{7.20}$$

Crucially, this breakdown of the lowest-order approximation introduces indirect couplings between driven and spectator modes, as seen in the expansion

$$\mathcal{D}_{l,k} \prod_{l' \neq l} (\mathbb{I} - \eta_{jl'}^2 a_{l'}^\dagger a_{l'} + \cdots) \tag{7.21}$$

appearing in Eq. (7.16). These terms highlight an intricate interplay between different collective vibrational modes that is absent in the standard Lamb-Dicke treatment.

This inter-mode coupling fundamentally changes how the system evolves under the interaction Hamiltonian. A notable example occurs in a two-ion system, where driving the first sideband of the center-of-mass mode induces not only the expected first-order phonon process $\eta_{j1}a_1$ but also higher-order terms such as $(\eta_{j1}^3/2)a_1^{\dagger 2}a_1$, which become significant for larger values of η_{jl}. Even when the stretch mode is not directly addressed, it still contributes dynamically through these indirect couplings, introducing additional phonon-exchange terms like $\eta_{j2}^2 a_2^\dagger a_2$. Consequently, spectator modes are no longer passive; they become entangled with the driven modes in a nontrivial way, potentially impacting the fidelity of entangling operations.

To design high-fidelity entangling gates beyond the Lamb-Dicke regime, these higher-order phonon processes must be explicitly accounted for in the extended interaction Hamiltonian $H(t)$. This refined description exposes additional phonon-mediated exchange terms that are neglected in the standard treatment, revealing new error channels that can degrade gate performance. Thus, developing robust entangling gates in this regime requires a carefully crafted control strategy: rather than simply selecting a driving field that targets a single motional mode, the approach must actively suppress unwanted phonon couplings while ensuring that only the desired processes contribute to entanglement.

A systematic gate design strategy begins with the selection of an appropriate set of driven motional modes L and the corresponding sidebands $K(l)$ that will be resonantly driven. These choices define the dominant phonon processes shaping the interaction. The next crucial step is engineering the time-dependent driving functions $F_{l,k}^{(j)}$ to achieve entanglement at the desired gate time T while actively suppressing the unwanted processes and maximizing the gate's overall robustness.

Driven sidebands for entanglement generation

The specific construction presented here enables the implementation of an entangling gate in a multi-mode system of N trapped ions with high motional states and offers enhanced resilience against both motional heating and combined errors in qubit and vibrational frequencies. While alternative choices exist, the proposed configuration minimizes the number of driven sidebands required for achieving the desired robustness, offering a practical advantage for experimental implementation.

In a system with M motional modes, the proposed gate implementation involves simultaneous driving of all modes ($L = M$). The first-order sideband ($k = 1$) of a designated central mode, typically chosen for its stronger spin-motion coupling, acts as the primary bus mode of the entangling process. Meanwhile, other modes (together with the central one) contribute through second-order sidebands ($k = 2$) to actively suppress unwanted contributions arising from higher-order terms in the Hamiltonian.

With such choice, the Hamiltonian in Eq. (7.16) simplifies to

$$H_c(t) = \sum_{j=1}^{N} \sigma_y^{(j)} \left(\frac{F_{1,1}^{(j)}}{\eta_{j1}} \mathcal{D}_{1,1} D_1 + \sum_{l=1}^{M} \frac{F_{l,2}^{(j)}}{\eta_{jl}} \mathcal{D}_{l,2} D_l \right) + \text{h.c.}, \tag{7.22}$$

with $D_k = \prod_{l' \neq k} \mathcal{D}_{l',0}$ being the product of phonon-conserving operators in the spectator modes.

The specific time-dependence of the driving functions $F_{1,1}^{(j)}$ and $F_{l,2}^{(j)}$ plays a crucial role in shaping the system's dynamics. These functions dictate how the spin-motion coupling in Eq. (7.22) evolves over time, ultimately determining whether entanglement between the electronic states of the ions can be robustly generated. Designing an appropriate modulation strategy for these driving functions is therefore essential for achieving high-fidelity quantum operations. To obtain the required time dependence, we analyze the time-evolution operator generated by Eq. (7.22), applying two successive approximations:

- **Hamiltonian truncation**: The displacement operators $\mathcal{D}(\eta_{jl})$, which involve an unbounded sum of phonon creation and annihilation operators, make $H_c(t)$ formally an infinite series. To resolve this, we perform a perturbative expansion in the Lamb-Dicke parameter η, truncating at third order (η^3). This truncation is physically justified by the rapid convergence of the series: each term scales as η^k, making higher orders negligible for $\eta \ll 1$. For typical experimental values ($\eta = 0.05$), the ratio of the η^4 term to the η^3 term is only $\mathcal{O}(5\%)$, while the η^5 effects are $\mathcal{O}(0.25\%)$. Thus, truncating at η^3 introduces errors well below standard gate error tolerances ($10^{-3} - 10^{-4}$), while retaining all nonlinear features up to cubic order in η. With this approximation, the truncated Hamiltonian becomes

$$H_c(t) = \sum_j \left[i F_{1,1}^{(j)} \sigma_y^{(j)} a_1^\dagger \left(\mathbb{I} - \frac{1}{2} \eta_{j1}^2 a_1^\dagger a_1 - \sum_{l=2}^{M} \eta_{jl}^2 a_l^\dagger a_l \right) - \frac{1}{2} \sum_{l=1}^{M} \eta_{jl} F_{l,2}^{(j)} \sigma_y^{(j)} a_l^{\dagger 2} \right] + \text{h.c.}\,, \tag{7.23}$$

  where $a_1^\dagger$ and a_1 denote the creation and annihilation operators for the designated central motional mode. Terms proportional to η and η^2 reflect the inclusion of higher-order motional effects, which contribute to non-trivial modifications of the gate dynamics beyond the standard first-order theory, while η^3 terms do not appear in this expression due to the intrinsic η^{-1} scaling of the driving fields (see Eq. (7.11)).

  Compared to first-order models (*e.g.*, MS gates), this third-order expansion significantly improves fidelity by capturing nonlinear dynamics critical for modern trapped-ion experiments, where first-order approximations often prove insufficient.

- **Time evolution via Magnus expansion**: Even with the truncated form of $H_c(t)$, solving the time-evolution operator $U(T) = \mathcal{T} \exp\left(-i \int_0^T dt H_c(t)\right)$ remains challenging due to the explicit time dependence and non-commutativity of $H_c(t)$. To address

this, we use the Magnus expansion [42] (see Sec. 2.0.4), which approximates $U(T)$ as a single exponential of a series of nested commutators. Truncating the Magnus expansion at third order in η, we write $U(t) = \exp\left(\sum_{i=1}^{4} \Omega_i(t)\right)$, where the operators $\Omega_i(t)$ (defined in Eq. (2.54)) encapsulate contributions from increasingly complex integrals of $H_c(t)$.

The validity of this approximation relies on three crucial considerations that ensure convergence of the Magnus expansion. First, the Lamb-Dicke parameters must satisfy $\eta < 1$, which guarantees that higher-order terms remain perturbatively small — a condition automatically met in typical light-matter interaction scenarios. Second, the time-dependent driving functions $F_{1,1}^{(j)}$ and $F_{l,2}^{(j)}$ must maintain smooth, well-behaved temporal profiles to prevent uncontrolled growth of higher-order terms, a requirement naturally fulfilled by our chosen parametrization. Finally, the integration time T must be sufficiently short to keep the Hamiltonian's integrated norm below the critical threshold in Eq. (2.55), thereby avoiding series divergence — a condition that presents no practical limitation for entangling gate operations.

The Magnus expansion results in a unitary evolution operator $U(T)$ that can be written as the exponential of a sum of operators. Each of these operators can be written in the form

$$\Theta(T) \left(\prod_l a_l^{\dagger p_l} a_l^{q_l} \right) \left(\sigma_y^{(1)} \right)^r \left(\sigma_y^{(2)} \right)^s \ , \tag{7.24}$$

where p_l, q_l, r, s are integers, and $\Theta(T)$ is a function dependent on nested integrals of the time-dependent driving functions $F_{l,k}^{(j)}(t)$.

Crucially, not all terms in $U(T)$ contribute to the desired entangling operation. To achieve pure entanglement at the gate time T, the driving functions $F_{l,k}^{(j)}$ must be meticulously chosen to eliminate all terms except the entangling term $i\phi_T \sigma_y^{(1)} \sigma_y^{(2)}$. This selective elimination imposes a set of constraints on the driving functions (via the functions $\Theta(T)$), which have been provided in electronic format for convenience [245].

A direct verification confirms that the following monochromatic driving functions satisfy the required constraints, effectively eliminating any undesired processes

$$F_{1,1}^{(1)} = F_{1,1}^{(2)} = \Omega e^{2i\delta t} \ , \tag{7.25a}$$

$$F_{l,2}^{(1)} = s_{1l} \Omega \frac{\tilde{\eta}_l}{\eta_{1l}} e^{i\delta t} \ , \tag{7.25b}$$

$$F_{l,2}^{(2)} = s_{1l} \Omega \frac{\tilde{\eta}_l}{\eta_{2l}} e^{i\delta t} \ , \tag{7.25c}$$

where $l = 1, \cdots, M$ refers to the motional mode, $s_{jl} = \text{sign}(\eta_{jl})$ and $\tilde{\eta}_l := \frac{\sqrt{2}}{2}\sqrt{\eta_{1l}^2 + \eta_{2l}^2}$. Furthermore, to achieve entanglement at the gate time $T = 2\pi/\delta$ for any chosen detuning

δ or Rabi frequency Ω, the following entangling condition must be satisfied

$$-3\left(\frac{\Omega}{\delta}\right)^4\left(\sum_j \eta_{j1}^2\right)+\left(\frac{\Omega}{\delta}\right)^2\left(2+\sum_{l,j}\eta_{jl}^2\right)=\frac{\phi_T}{\pi}\ . \tag{7.26}$$

This condition implies that as long as the ratio Ω/δ fulfills Eq. (7.26), the specific values of δ and Ω can be chosen freely. This flexibility allows for independent tuning of the gate time T and the drive amplitud Ω, though with a tradeoff: lower power consumption (*i.e.*, smaller Ω), requires a longer gate time, as a smaller δ is needed to satisfy Eq. (7.26). Conversely, stronger driving fields shorten the required interaction time to achieve the desired coupling.

The time-dependent drives in Eq. (7.25) define an optimal driving strategy for generating entangled states by leveraging interactions with the electromagnetic field. However, the solution is not unique — various alternative strategies, such as driving higher-order sideband transitions or employing different modulation schemes, could also achieve entanglement.

In the following, we refine this driving scheme to enhance its robustness against experimental noise sources. This refinement ensures that the advantages of achieving a high-fidelity solution are preserved even when the system is subject to realistic imperfections, thereby making the entanglement protocol more resilient to practical implementation challenges.

To achieve this, we first construct a Hamiltonian model that accounts for the system's interaction with its environment.

Lindblad master equation

While the drivings in Eq. (7.25) facilitate high-fidelity entangling gates under ideal coherent dynamics, in practical implementations, the motional modes inevitably couple to the environment, leading to processes such as heating and dephasing that degrade gate fidelity.

A convenient way to model these effects is through the master equation formalism [44], introduced in Sec. 2.0.4 (see Eq. (2.80)),

$$\dot{\rho}=-i[H_c(t),\rho]+\mathcal{L}_D(\rho)\ , \tag{7.27}$$

where ρ is the system density matrix, $H_c(t)$ the Hamiltonian in Eq. (7.16), and $\mathcal{L}_D$ represents dissipative processes through the Lindbladian (see Eq. (2.80))

$$\begin{aligned}\mathcal{L}_D(\rho)=&\sum_l \gamma_+^{(l)}\left(a_l^\dagger\rho a_l-\frac{1}{2}\{a_l a_l^\dagger,\rho\}\right)+\sum_l\gamma_-^{(l)}\left(a_l\rho a_l^\dagger-\frac{1}{2}\{a_l^\dagger a_l,\rho\}\right)\\&+\sum_l\gamma_d^{(l)}\left(n_l\rho n_l-\frac{1}{2}\{n_l^2,\rho\}\right)\ .\end{aligned} \tag{7.28}$$

Here, $a_l^\dagger$ and a_l are the creation and annihilation operators for phonon mode l, and $n_l=a_l^\dagger a_l$ is the corresponding number operator. The terms with rates $\gamma_+^{(l)}$ and $\gamma_-^{(l)}$ describe phonon

creation and annihilation due to thermal fluctuations. When the trap electrodes are at room temperature while the ions are laser-cooled, the environmental temperature can be approximated as infinite, making $\gamma_+^{(l)}$ and $\gamma_-^{(l)}$ coincide. The final term in Eq. (7.28) accounts for dephasing, where phase coherence is lost without introducing motional excitations.

While the optimal pulse sequences derived in the following Sec. 7.1.2 and the overall entangling framework will be applicable for any combination of decay rates, our numerical simulations in Sec. 7.1.3 will, for simplicity, assume uniform dissipation across all motional modes, *i.e.*

$$\gamma_+^{(l)} = \gamma_-^{(l)} = \gamma_d^{(l)} = \gamma \ . \tag{7.29}$$

This assumption, while simplifying the numerical analysis, does not limit the generality of the derived solutions. The essential physical behavior of the system is preserved under this simplification, allowing for a clearer understanding of the impact of decoherence without the need to analyze each noise source individually.

Robustness to motional heating

The master equation Eq. (7.28) describes the system's dynamics when interacting with its environment. Motional heating and dephasing can reduce gate fidelity, but careful design of the driving functions $F_{l,k}^{(j)}(t)$ can mitigate these effects and improve gate performance.

In the absence of dissipation (*i.e.* with $\mathcal{L}_D = 0$ in Eq. (7.28)), the target gate U is perfectly implemented and thus transforms the initial state $\rho(0)$ into the desired final state $\rho(T) = U\rho(0)U^\dagger$. However, in the presence of motional heating and dephasing, the implemented gate deviates from the ideal unitary transformation. This deviation is captured by the non-unitary map $\tilde{\mathcal{E}} : \rho \to \tilde{\mathcal{E}}(\rho)$, which is influenced by the evolution of the motional state (following Eq. (7.27)), making the choice of driving functions $g_j(t)$ in Eq. (7.4) crucial for the gate's resilience to dissipative effects. The MS gate is particularly vulnerable to motional heating due to its non-centered phase-space trajectories, but alternative choices of the driving functions $F_{l,k}^{(j)}(t)$ (which then define $g_j(t)$) can significantly enhance gate's resilience to heating [231].

In the time-dependent frame defined by the target unitary $U(T) = \mathcal{T}\exp\Big(-i\int_0^T dt H_c(t)\Big)$, and assuming the drivings $F_{l,k}^{(j)}(t)$ are chosen as described in Sec. (7.1.2), the coherent evolution reduces to the identity $\mathbb{I}$. Consequently, the master equation (Eq. (7.27)), in this frame, becomes purely dissipative

$$\dot{\rho} = \tilde{\mathcal{L}}_D(\rho) \ . \tag{7.30}$$

In the interaction picture defined by the unitary $U(T)$, the jump operators $a_l, a_l^\dagger$ and n_l become time-dependent, transforming as $\tilde{a}_l(T) = U^\dagger(T) a_l U(T)$, with analogous transformations for the other operators. Due to the generally complex structure of $U(T)$, the

resulting time-dependent expressions for the jump operators involve intricate combinations of operators and nested integrals of the driving functions $F_{l,k}^{(j)}(t)$. For convenience, their explicit expressions up to third order in η are provided in electronic format at Ref. [245].

Assuming that the decay rates are much smaller than the typical gate timescales (*i.e.* $\gamma T \ll 1$), the system's dynamics can be accurately approximated to first order using the propagator $e^{\tilde{\mathcal{L}}_D t} \approx \mathbb{I} + \int_0^t dt' \tilde{\mathcal{L}}_D(t')$. This implies that the spin state evolves to a final state that, tracing out the motion, can be expressed as $\rho_S(T) = \rho_S(0) + \Delta\rho_S$, with

$$\Delta\rho_S = \mathrm{Tr}_M \int_0^T dt' \tilde{\mathcal{L}}_D(t')[\rho_S \otimes \rho_M] \ , \tag{7.31}$$

where Tr_M denotes the partial trace over the motional degrees of freedom, and the initial state is assumed to be a tensor product of spin and motional states, $\rho(0) = \rho_S \otimes \rho_M$. While Eq. (7.31) vanishes in the ideal, dissipation-free scenario, motional heating and dephasing introduce a non-zero correction $\Delta\rho_S$ modifying the spin state. In general, this correction can be expressed in a form analogous to the Kraus representation (Eq. (2.20))

$$\Delta\rho_S = \sum_{m,n} \chi_{mn} A_m \rho_S(0) A_n^\dagger \ , \tag{7.32}$$

where the operators A_m belong to the set $\{\ \mathbb{I}, \sigma_y^{(j)}, \sigma_y^{(j)}\sigma_y^{(k)}\}$. Here, χ_{mn} are the process matrix elements whose norm characterizes the infidelity of the gate and depend on the motional properties of the state (*e.g.* $\langle n_l \rangle$), as well as on the temporal shaping of the driving functions $F_{l,k}^{(j)}(t)$. Therefore, since each element χ_{mn} is weighted with a factor of η, it is possible to devise schemes that are robust to a particular order of η. Formulated as an optimisation problem, this entails determining the form of the drivings $F_{l,k}^{(j)}(t)$ that minimize a set of constraints.

Resilience to order η

The first-order-in-η contributions to the motional heating and dephasing are found to be functionals of the driving functions $F_{1,1}^{(j)}(t)$ (with $j = \{1, 2\}$) associated with the central motional mode. In particular, optimizing the drive requires minimizing the cost function

$$\mathcal{C} = \mathcal{F}(c_1, \cdots, c_9) \ , \tag{7.33}$$

where $\mathcal{F}$ is a chosen function (*e.g.* $\max, \sum$) such that minimizing $\mathcal{C}$ yields the optimal solution, and the individual terms c_i are defined as

$$\begin{aligned}
&c_1 = \{\alpha_i\} \ , && c_2 = \{\alpha_i^2\} \ , && c_3 = \{\alpha_i \alpha_j\} \ , \\
&c_4 = \{|\alpha_i|^2 \alpha_j\} \ , && c_5 = \{\alpha_i^2 \alpha_j^{*2}\} \ , && c_6 = \{|\alpha_i|^2\} \ , \\
&c_7 = \{\alpha_i \alpha_j^*\} \ , && c_8 = \{|\alpha_i|^2 |\alpha_j|^2\} \ , && c_9 = \{\alpha_i^2 \alpha_j^*\} \ ,
\end{aligned} \tag{7.34}$$

with $i \neq j$, $\alpha_j := \{F_{1,1}^{(j)}\}$ and with the short-hand notation $\{f\} = \int_0^T dt' f(t')$ to indicate time-integrated functionals.

To identify the optimal drive that minimizes motional heating and dephasing, it is useful to express the driving functions $F_{l,k}^{(j)}(t)$ in terms of a Fourier series of the form

$$F_{l,k}^{(j)}(t) = \sum_m A_{l,k,m}^{(j)} e^{i\omega_{l,k,m}^{(j)} t} \ , \tag{7.35}$$

where $A_{l,k,m}^{(j)}$ and $\omega_{l,k,m}^{(j)}$ represent the amplitudes and frequencies, respectively, which are to be determined. Crucially, by imposing the constraint

$$\sum_m \left(A_{1,1,m}^{(j)} \prod_{n \neq m} \omega_{1,1,n}^{(j)} \right) = 0 \ , \tag{7.36}$$

on the functions $F_{1,1}^{(j)}$ we ensure that all terms c_i, except for c_6 and c_8, vanish. This simplification allows us to achieve optimal motional heating resilience at first order in η by minimizing a cost function that depends solely on c_6 and c_8, *i.e.* $C = \mathcal{F}(c_6, c_8)$. In our optimization, we choose $\mathcal{F}$ to correspond to the maximum function.

Resilience to order η^2 and η^3

Contributions to motional resilience beyond first order in η involve a significantly larger number of functional constraints. These higher-order contributions become appreciable primarily in the regime of large Lamb-Dicke parameters or with highly excited motional states.

The number of independent conditions required to enforce motional robustness grows dramatically with order. In a two-ion system, there are 186 distinct conditions c_i, at second order, while at third order, this number rises to 2543. These conditions, analogous in structure to those in Eq. (7.34), ensure that unwanted motional excitations and dephasing effects remain suppressed at progressively higher orders. Given the number and complexity of these constraints, their explicit expressions are provided in electronic format in Ref. [245] for convenience and ease of reference.

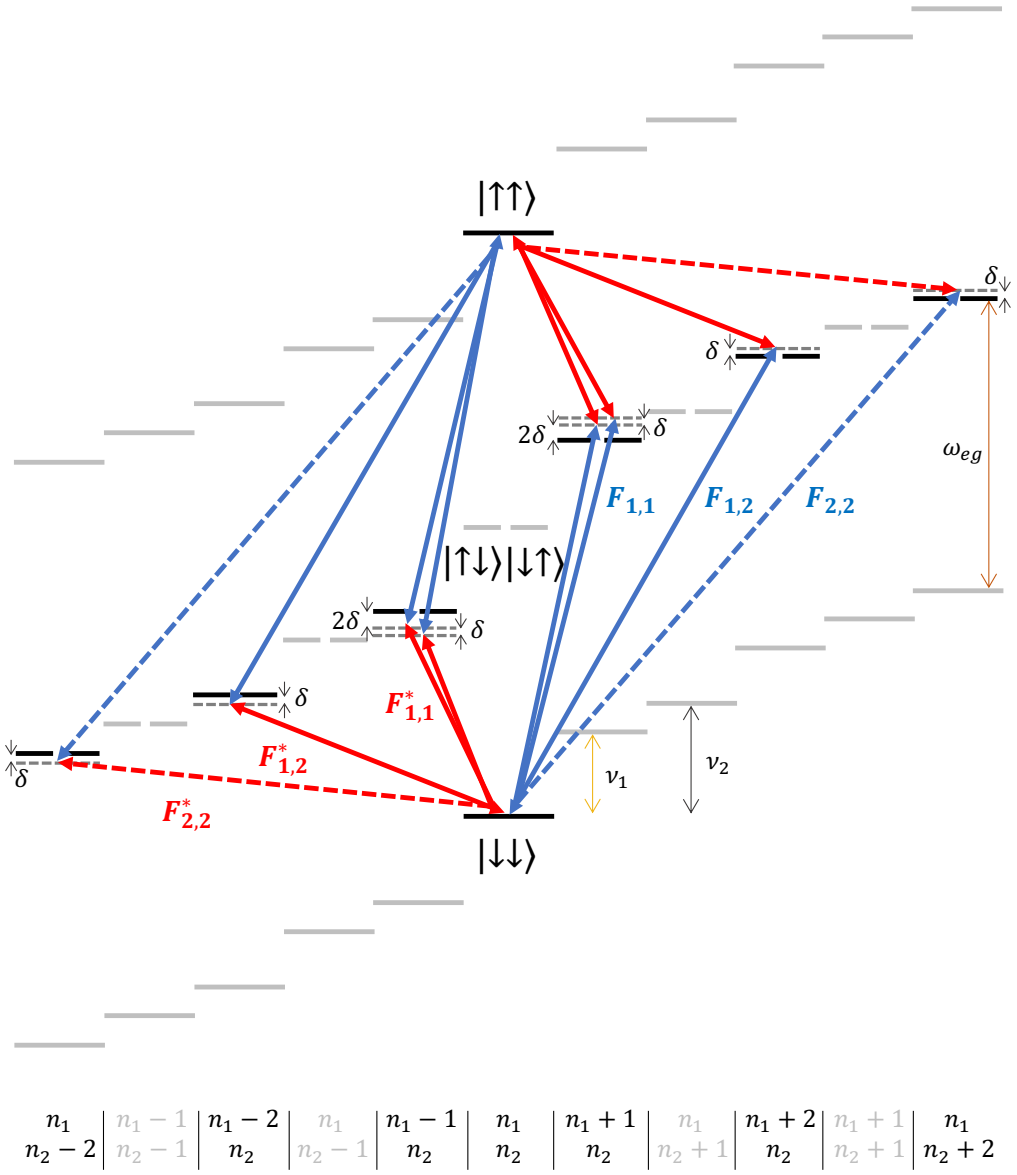

Figure 7.1: Energy level diagram for two identical ions and two motional modes. Solid blue (red) sidebands represent transitions with a phonon gain (loss) in motional mode 1. Dashed blue (red) sidebands represent similar processes for motional mode 2. Levels depicted with grey lines are highly off-resonant, while those shown with black lines are driven nearly resonantly by multiples of the detuning δ, as defined in Eq. (7.37). For clarity, the deviations from the exact resonance δ have been exaggerated, as they are significantly smaller than the energy spacing between oscillator levels.

Driven sidebands for entanglement generation and robustness

Achieving robustness against motional heating and dephasing requires a more intricate driving scheme. Typically, this involves either driving additional sidebands or implementing more complex time dependencies in the modulation of each sideband. Balancing the trade-off between complexity and feasibility, we introduce a scheme that is resilient to decoherence effects up to first order in η, specifically minimizing the nine functionals defined in Eq. (7.34). The corresponding driving functions are given by

$$F_{1,1}^{(1)} = F_{1,1}^{(2)} = \Omega\left(e^{2i\delta t} - \frac{3}{2}e^{3i\delta t}\right) \tag{7.37a}$$

$$F_{l,2}^{(1)} = s_{1l}\Omega\frac{\tilde{\eta}_l}{\eta_{1l}}e^{i\delta t} \tag{7.37b}$$

$$F_{l,2}^{(2)} = s_{1l}\Omega\frac{\tilde{\eta}_l}{\eta_{2l}}e^{i\delta t} \tag{7.37c}$$

where $l = 1, \cdots, M$ labels the motional modes and the effective Lamb-Dicke parameter is defined as $\tilde{\eta}_l := \frac{\sqrt{5}}{2}\sqrt{\eta_{1l}^2 + \eta_{2l}^2}$. The parameter δ defines the gate duration $T = 2\pi/\delta$, and can be freely chosen within experimental constraints

Beyond enabling fast gate operation, increasing δ also mitigates the impact of off-resonant transitions. However, as in the previous driving scheme (Eq. (7.25)), larger values of δ require stronger driving fields, imposing practical limitations. In an experimental setting, the optimal choice of δ is thus determined by the maximum achievable drive strength while maintaining gate fidelity.

To understand the specific implementation of this robust driving scheme, consider a pair of ions selected for entanglement generation within the N-ion chain. According to Eq. (7.37a), both ions receive identical bichromatic modulation with detunings 2δ and 3δ ions targeting the first sideband of the primary motional mode (see Fig. 7.1 for the case of two *identical* ions). This bichromatic modulation is crucial for enhancing resilience against motional heating, while the specific detuning ratio optimizes gate speed.

Eqs. (7.37b) and (7.37c) specify different driving fields for each ion within the pair, targeting second-order sidebands of all vibrational modes (see Fig. 7.1). These additional drives suppress unwanted processes arising from higher-order (in η) contributions to the system's dynamics. Notably, the amplitudes of these drives are mode-dependent, compensating for the varying coupling strengths across the different modes.

Finally, the Rabi amplitude Ω is determined by solving the equation

$$-6\frac{\Omega^4}{\delta^4}\left(\sum_j \eta_{j1}^2\right) + \frac{\Omega^2}{\delta^2}\left(2 + \sum_{l,j}\eta_{jl}^2\right) = \frac{2\phi_T}{5\pi}\ , \tag{7.38}$$

for a specified detuning δ, which ensures the desired entangling phase ϕ_T in the unitary gate U.

As the solution to Eq. (7.38) depends on the specific coupling strengths η_{jl}, the amplitude Ω is generally a function of these parameters. In the weak-coupling regime, where $\eta_{jl} \ll 1$, Eq. (7.38) reduces to $\frac{\Omega^2}{\delta^2} = \frac{\phi_T}{5\pi}$ whereas the corresponding condition for the conventional MS gate reads $\frac{\Omega^2}{\delta^2} = \frac{\phi_T}{8\pi}$. For any given value of δ, the value of Ω in the present case is thus larger by a factor of $2\sqrt{2/5}$ than with conventional gates, but with stronger coupling, *i.e.* larger values of η_{jl}, the value of Ω decreases.

While Ω directly corresponds to the Rabi frequency of the driving fields in the conventional MS, the maximal Rabi frequency in the present case, following Eq. (7.37a), is given by $5/2\ |\Omega|$. In the weak-coupling limit, this maximum Rabi frequency is $\sqrt{10}$ times larger than the constant Rabi frequency of the MS gate. However, this ratio decreases to approximately ~ 2.5 for stronger spin-motion coupling (see Appendix H.1).

The key distinction between the two gate schemes lies in the inclusion of drives on second-order sidebands in the present approach. As defined by Eqs. (7.37b) and (7.37c), the Rabi frequencies of these second-order sidebands are slightly larger than Ω, but remain smaller than those of the first-order sidebands. Consequently, the present scheme generally requires only slightly stronger driving fields compared to the conventional MS gate (see Appendix H.1 for more details).

7.1.3 Results

The proposed control strategy enables high-fidelity entangling gates for trapped ions, even in noisy environments. It fully accounts for all collective vibrational modes of the ion chain and does not rely on the Lamb-Dicke approximation. As a result, it remains effective even at high motional excitations, reducing the need for extensive cooling.

Gate performance can be quantified using the gate fidelity, which is given by

$$F(\rho_M) = \frac{1}{d^2} \sum_{\alpha,\beta=1}^{d} \langle\alpha|U^\dagger \operatorname{Tr}_M \left(\mathcal{E}(|\alpha\rangle\langle\beta| \otimes \rho_M)\right) U|\beta\rangle\,, \tag{7.39}$$

where the states $|\alpha\rangle\,, |\beta\rangle$ span the d-dimensional Hilbert space of spin states (with $d = 2^N$), ρ_M is the initial density matrix of motional states, U represents the target unitary and $\mathcal{E}(\cdot)$ the actual (potentially non-unitary) channel corresponding to the implemented gate.

In practical settings, the motional states of ions are rarely Fock states, which are required to evaluate Eq. (7.39). Instead, they typically correspond to thermal states, defined as

$$\rho_{th} = \frac{\exp\left(-\beta \sum_k \nu_k a_k^\dagger a_k\right)}{\operatorname{Tr}\left[\exp\left(-\beta \sum_k \nu_k a_k^\dagger a_k\right)\right]}\,, \tag{7.40}$$

with $\beta = 1/k_B T$, where k_B is the Boltzmann constant and T is the *temperature* of the ion trap. Given this, it is useful to derive an expression for the gate fidelity adapted to thermal states.

To do so, we first express the thermal state as a sum over Fock states,

$$\rho_{th} = \sum_{n_1,\cdots,n_M=0}^{\infty} P(n_1,\cdots,n_M)\,|n_1,\cdots,n_M\rangle\langle n_1,\cdots,n_M|\ , \tag{7.41}$$

where the probability distribution is given by

$$\begin{aligned} P(n_1,\cdots,n_M) &= \frac{\exp(-\beta(\nu_1 n_1+\cdots+\nu_M n_M))}{\sum_{m_1,\cdots,m_M=0}^{\infty}\exp(-\beta\sum_k \nu_k m_k)} \\ &= \frac{\exp(-\beta(\nu_1 n_1+\cdots+\nu_M n_M))}{\left(\sum_{n_1=0}^{\infty} e^{-\beta\nu_1 n_1}\right)\cdots\left(\sum_{n_M=0}^{\infty} e^{-\beta\nu_M n_M}\right)} \\ &= \frac{\exp(-\beta(\nu_1 n_1+\cdots+\nu_M n_M))}{\left(\frac{1}{1-\exp(-\beta\nu_1)}\right)\cdots\left(\frac{1}{1-\exp(-\beta\nu_M)}\right)} \\ &= \prod_k \left(1-e^{-\beta\nu_k}\right) e^{-\beta(\nu_1 n_1+\cdots+\nu_M n_M)}\ . \end{aligned} \tag{7.42}$$

To simplify this further, we note that the mean phonon number in each mode l is given by

$$\begin{aligned} \bar{n}_l &= \mathrm{Tr}[\rho\ n_l] \\ &= \sum_{n_1,\cdots,n_M=0}^{\infty} \langle n_1,\cdots,n_M|\, n_l P(n_1,\cdots,n_M)\,|n_1,\cdots,n_M\rangle \\ &= \prod_k \left(1-e^{-\beta\nu_k}\right) \sum_{n_1,\cdots,n_M=0}^{\infty} e^{-\beta(\nu_1 n_1+\cdots+\nu_M n_M)}\,\langle n_1,\cdots,n_M|\, n_l\,|n_1,\cdots,n_M\rangle \\ &= \frac{\prod_k\left(1-e^{-\beta\nu_k}\right)}{\prod_{k\neq l'}\left(1-e^{-\beta\nu_k}\right)} \sum_{n_l=0}^{\infty} e^{-\beta\nu_l n_l} n_l \\ &= (1-e^{-\beta\nu_l}) \sum_{n_l=0}^{\infty} e^{-\beta\nu_l n_l} n_l \\ &= (1-e^{-\beta\nu_l}) \frac{-1}{\nu_l}\frac{\partial}{\partial\beta} \sum_{n_l=0}^{\infty} e^{-\beta\nu_l n_l} \\ &= (1-e^{-\beta\nu_l}) \frac{-1}{\nu_l}\frac{\partial}{\partial\beta} (1-e^{-\beta\nu_l})^{-1} \\ &= (e^{\beta\nu_l}-1)^{-1}\ , \end{aligned} \tag{7.43}$$

which implies that $e^{-\beta\nu_l} = \frac{\bar{n}_l}{\bar{n}_l+1}$. Substituting this into $P(n_1,\cdots,n_M)$ yields

$$\begin{aligned} P(n_1,\cdots,n_M) &= \prod_{k=1}^{M}\left(\frac{1}{\bar{n_k}+1}\right)\left(\frac{\bar{n}_1}{\bar{n_1}+1}\right)^{n_1}\cdots\left(\frac{\bar{n}_M}{\bar{n_M}+1}\right)^{n_M} \\ &= \prod_{k=1}^{M}\frac{\bar{n}_k^{n_k}}{(\bar{n}_k+1)^{n_k+1}}\ . \end{aligned} \tag{7.44}$$

Consequently, a thermal state can be conveniently rewritten as

$$\rho_{th} = \sum_{n_1,\cdots,n_M=0}^{\infty} \left(\prod_{k=1}^{M} \frac{\bar{n}_k^{n_k}}{(\bar{n}_k+1)^{n_k+1}} \right) |n_1,\cdots,n_M\rangle\langle n_1,\cdots,n_M| \ . \tag{7.45}$$

This decomposition represents a thermal state as a statistical mixture of Fock states, each weighted by its thermal occupation probability. Since gate fidelity is a linear function of the density matrix, it follows that the fidelity of a thermal state can be directly obtained as a weighted sum of the fidelities for individual Fock states

$$\begin{aligned} F(\rho_M) &= \sum_{n_1,\cdots,n_M=0}^{\infty} P(n_1,\cdots,n_M) F(n_1,\cdots,n_M) \ , \quad \text{with} \\ F(n_1,\cdots,n_M) &= \frac{1}{d^2} \sum_{\alpha,\beta=1}^{d} \langle\alpha|U^\dagger \, \mathrm{Tr}_M \Big(\mathcal{E}(|\alpha\rangle\langle\beta| \otimes |n_1,\cdots,n_M\rangle\langle n_1,\cdots,n_M|) \Big) U|\beta\rangle \ , \end{aligned} \tag{7.46}$$

where we exploited the linearity of both the trace and the quantum map, and $P(n_1,\cdots,n_M)$ is the thermal occupation probability given in Eq. (7.44). This formulation not only simplifies the fidelity calculation but also provides direct physical insight: understanding the behavior of the gate fidelity for Fock states is sufficient to characterize its performance for a thermal state. The final expression further reveals that for small thermal occupations (low $\bar{n}_k$), the vacuum components ($n_k = 0$) dominate, making the fidelity approach that of the ideal Fock-state scenario. Conversely, as thermal excitations increase, higher-n_k states contribute more significantly, leading to a reduction in the average fidelity and emphasizing the growing impact of motional fluctuations.

To gain deeper insight into the gate performance, the following discussion examines the dependence of the fidelity $F(\rho)$ on experimentally relevant parameters. Specifically, we explore the role of system size N, the initial motional occupations $|n_1,\cdots,n_M\rangle$, and the effects of non-idealities such as motional heating and frequency shifts. The latter include both errors in the vibrational mode frequencies ϵ_ν and fluctuations in the spin transition frequencies ϵ_ω, which can degrade fidelity by introducing unwanted phase shifts and decoherence. Understanding these dependencies is crucial for optimizing gate performance in realistic implementations.

Multi-mode systems with no dissipation or frequency errors

Unlike simpler two-ion systems, designing entangling gates for larger, multi-mode, systems requires accounting for variations in coupling strengths η_{jl} across ion pairs. This key challenge is directly addressed by the proposed control scheme. Fig. 7.2(a) exemplifies this point by depicting the infidelity $1 - F$ of the present gate in a 4-ion system under ideal conditions (no dissipation or frequency errors). The x-axis represents the initial motional Fock state $|n\rangle^{\otimes 4}$, but it is important to emphasize that the driving patterns are *not* tailored to a specific initial motional state. Instead, all infidelities correspond to the same fixed

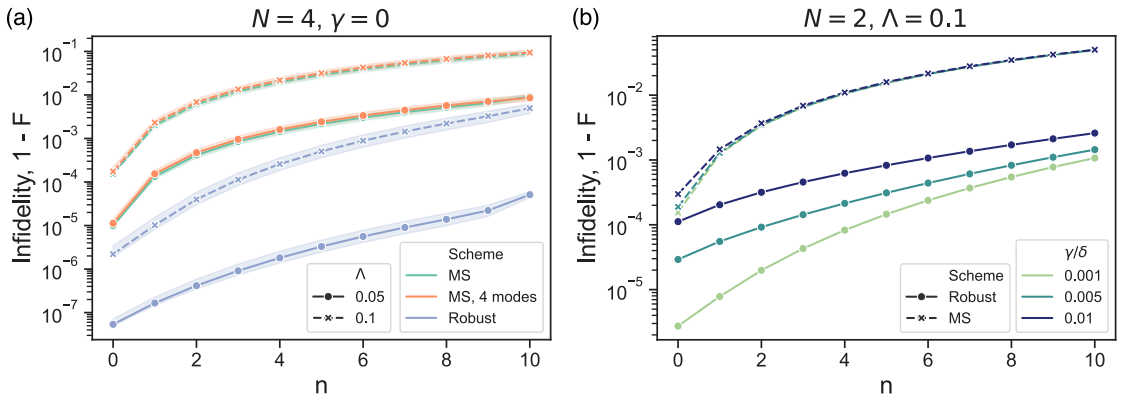

Figure 7.2: Infidelity $1 - F$ of the entangling gate as a function of the initial Fock state occupation n for a 4-qubit (left panel) and 2-qubit (right panel) systems (where $n_l = n$ for all modes l). The left panel illustrates coherent dynamics, and each data point represents the average infidelity across all qubit pairs, with the shaded area showing the range of values found across the different pairs. The infidelity is compared for the standard MS gate (green), the MS gate with the interaction mediated by all four modes (orange), and the present gate (blue). Different values of the coupling strength Λ are shown with different markers. The right panel depicts the impact of heating and dephasing on the dynamics of the motional modes according to the Lindbladian Eq. (7.28). All results in the right panel use fixed spin-motion coupling $\Lambda = 0.1$, and varying rates γ (Eq. (7.29)) for the dissipative processes of the phonon modes, specified in units of the detuning δ and thus gate time $T = 2\pi/\delta$. Marker styles differentiate the standard MS gate (crosses) from the proposed robust scheme (circles). In all simulations, the amplitude of the driving fields in the present scheme is limited to match the amplitude of the MS gate, ensuring a fair comparison.

driving sequence. The shaded region indicates the spread of infidelities across different ion pairs, with marker points showing the average value. Different marker styles further distinguish the results for varying coupling strengths Λ, highlighting the robustness of the scheme against inhomogeneities in ion coupling.

To assess the performance of the proposed gate (shown in blue in Fig. 7.2(a)), it is compared to two alternative approaches. The first approach is the standard MS implementation (depicted in green), which achieves spin-spin coupling by driving only the first sideband transition of a selected motional mode, with the remaining modes acting as spectators. The second approach (depicted in orange) extends the MS drives to all available modes (four in this case), employing a scheme that excites the first sideband transition of each mode with the same frequency and half the amplitude ($\Omega/2$) used in the standard MS gate. This adjustment distributes power equally among the four modes while preserving the total Rabi angle Ω^2 [237].

Crucially, under ideal conditions, the present gate consistently outperforms both MS variants across all initial states and coupling strengths. This advantage is particularly evident in weak-coupling regimes ($\Lambda = 0.05$, circles). Even with high motional states ($n = 10$), it achieves infidelities below 10^{-4}, a remarkable two orders of magnitude lower than any MS variant. Notably, this performance is independent of the specific ion pair within the four-

ion system, demonstrating its robustness across various configurations, a crucial feature for practical applications.

While the current analysis is limited to Fock states with $n = 10$ for a four-ion system, numerical evidence suggests this trend persists for significantly higher levels of motional excitation, indicating the gate's high performance even under substantial thermal noise. In fact, fidelities exceeding 99% remain achievable even at mean phonon occupations as high as $\bar{n} \sim 100$, as demonstrated in App. H.2 for a two-ion system using the same driving scheme as in Fig. 7.2(b). This highlights the gate's ability to maintain high performance well beyond the low-temperature regime, making it highly relevant for experimental settings where motional heating is a concern.

Motional heating and dephasing

The previous results demonstrate that the proposed entangling protocol enables high-fidelity gates even in the absence of near-ground-state motional cooling, making it particularly beneficial in systems with weak spin-phonon coupling. However, a crucial question is whether this advantage comes at the expense of increased sensitivity to motional decoherence due to the additional sideband driving.

A key feature of this protocol is its resilience to motional heating, which is achieved through the temporal modulation of the driving fields in Eq. (7.37). Specifically, the bichromatic driving terms in $F_{1,1}^{(1)}$ and $F_{1,1}^{(2)}$ are designed to suppress the leading-order effects of motional noise. This suppression arises because the modulation ensures that motional excitations induced by heating do not accumulate coherently over the gate duration. Instead, the drive structure counteracts these incoherent processes to first order in η, as discussed in Sec. 7.1.2. Physically, this means that while motional heating may still introduce small errors, their impact remains bounded rather than growing uncontrollably with time. Further enhanced robustness could be achieved by implementing a polychromatic version for all drivings in Eq. (7.37), although at the cost of a more intricate driving scheme.

Fig. 7.2(b) illustrates the performance of the proposed gate in the presence of motional heating and dephasing for a two-ion system of identical species. The infidelity $1 - F$ is represented as a function of the motional occupation for a fixed coupling strength $\Lambda = 0.1$ and different decay rates γ (Eq. (7.29)), obtained by numerically solving the Lindblad master equation Eq. (7.28). The crosses correspond to the performance of the MS gate applied to the center-of-mass mode, while circles represent solutions derived from the parametrization in Eq. (7.37). The results demonstrate a significant performance advantage of the present scheme over the MS approach across all decay rates, particularly in low-dissipative environments. This enhanced robustness achieved with bichromatic driving enables fidelities close to 10^{-3} for motional occupations of up to $n = 10$ in low and medium dissipative environments ($\gamma \leq 0.01$), compared to an infidelity close to 10^{-1} for the MS gate. Notably, while this improved performance typically requires individual addressing of the ions, the specific symmetry of the two-ion system ($\eta_{11} = \eta_{21}$ and $\eta_{12} = -\eta_{22}$) implies that the driving functions in Eq. (7.10) are identical for both ions ($f_1 = f_2$) and, hence,

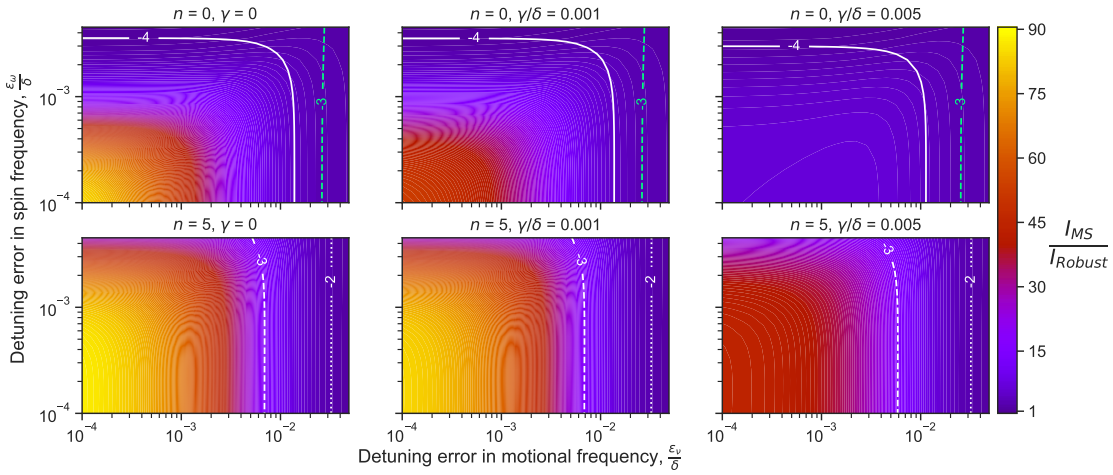

Figure 7.3: Combined impact of vibrational and spin frequency errors on the performance of the present entangling scheme (robust) compared to the standard MS gate in a two-ion system. Each panel shows the ratio of MS gate infidelity to the infidelity of the robust scheme I_{MS}/I_{Robust} for a specific initial motional state $|n, n\rangle$ and a fixed coupling strength $\Lambda = 0.1$. Panels from left to right show results for increasing heating and dephasing, as modeled by the master equation Eq. (7.28). Coherent motional dynamics correspond to a decay rate $\gamma = 0$, while increasing dissipation is captured by higher decay rates γ (Eq. (7.29)), which are expressed in terms of the detuning δ of the driving fields. The x-axis represents (in log scale) errors in vibrational frequency ϵ_ν, while the y-axis depicts symmetric errors in spin frequencies ϵ_ω, both scaled by the detuning δ. Contour lines reveal actual fidelities achievable by each method. Solid lines enclose regions where infidelities remain below 10^{-4}, dashed lines correspond to 10^{-3} and dotted lines to 10^{-2}. Green lines represent the MS gate, while white ones represent the robust scheme.

that both ions can be driven collectively using a global field.

Detuning errors

Even small deviations in vibrational and spin frequencies can substantially impact gate fidelity. These errors, though typically minor relative to the resonant frequencies (*i.e.*, $\epsilon \ll \omega$), can be modeled as frequency shifts of the form $\omega \to \omega + \epsilon$. Specifically, errors in motional frequencies appear as shifts in each vibrational mode, $\nu_l \to \nu_l + \epsilon_\nu$, while (symmetric) spin frequency errors are modeled as $\omega_j \to \omega_j + \epsilon_\omega$, affecting spin transition resonances. Such drifts introduce a mismatch between the actual transition frequencies and the intended driving frequencies in Eq. (7.11), effectively generating an unwanted detuning that alters the system dynamics and can degrade performance.

Importantly, the same properties that suppress the effects of motional heating — namely, closed phase-space trajectories and vanishing time-integrated displacement (see Sec. 7.1.2) — also play a key role in mitigating errors from motional detuning [230]. As a result, the proposed gate is inherently robust against such detuning effects. While it is not specifically designed to counteract spin frequency errors, it still exhibits notable resilience to them, as demonstrated in Fig. 7.3.

Fig. 7.3 depicts the combined impact of detuning errors in vibrational and spin frequencies for a two-ion system also experiencing motional heating and dephasing. Each panel represents the ratio in infidelities between the MS gate (mediated by the center-of-mass mode) and the present robust protocol, I_{MS}/I_{Robust}, using a color code ranging from purple (similar performance) to yellow (significant improvement). The panels vary across different initial motional states $|n, n\rangle$ and decay rates γ; and the x and y axes correspond to errors in the vibrational ϵ_ν (assumed to be the same across all modes for simplicity) and spin frequencies ϵ_ω, respectively.

The first row of panels shows the infidelity ratio for the initial motional ground state ($n = 0$) with increasing decay rates from left to right. Here, the present scheme (robust) exhibits substantial improvement over the MS gate for small and moderate errors in motional frequencies ($\epsilon_\nu/\delta < 0.5\%$), even with spin frequency shifts of up to $\epsilon_\omega/\delta < 0.1\%$. Notably, reductions in infidelity of up to two orders of magnitude are achieved in the case with no motional heating and small frequency errors (yellow region in leftmost panel). While this advantage diminishes with increasing motional heating (moving right within the first row), the present scheme maintains superior performance across all decay rates depicted, within the studied range of frequency errors.

Overall, when restricting motional frequency errors to a maximum of 1.5% of the detuning δ, the proposed gate achieves fidelities exceeding 99.99% (as delimited by the green contour line), which represents an improvement of at least a factor of five, and up to two orders of magnitude, over the standard MS approach.

Moving to higher motional states ($n = 5$), the present scheme demonstrates a more significant advantage. The region with very substantial improvement (in red and yellow tones) expands to encompass larger errors across both axes. This improvement also decays more gradually with higher decay rates compared to the case with motional ground states (first row). Importantly, the MS gate fails to achieve fidelities exceeding 99% for any frequency error within the studied range. In contrast, the robust scheme maintains high fidelities exceeding 99% within a broad range of errors (up to $\epsilon_\nu/\delta < 3\%$ and $\epsilon_\omega/\delta < 2\%$) and even achieves exceptional fidelities exceeding 99.9% with frequency errors of any type of up to 0.7% of the detuning δ. This advantage persists even for high motional occupations ($n \sim 100$), where the robust scheme still maintains fidelities exceeding 99% with moderate frequency errors.

7.1.4 Quantifying off-resonant contributions

While the results in Sec. 7.1.3 demonstrate significant improvements in gate fidelity for both ideal and dissipative environments, a critical question remains: *do these gains persist when the underlying approximations are relaxed?* In particular, off-resonant terms neglected under the rotating-wave approximation (RWA) could potentially accumulate phase errors or induce spurious transitions during the gate operation. These terms oscillate at frequencies $\sim \pm k\nu_l$ and were neglected in deriving the effective Hamiltonian in Eq. (7.13) from Eq. (7.12).

In this section, we establish rigorous bounds on their impact by analyzing the critical ratio ν/δ, where ν is the trap frequency and δ is the detuning of the driving fields from the qubit transition frequency, which sets the characteristic timescale of the gate.

To ensure consistency with the perturbative framework used to derive optimal control solutions (which truncates the Lamb-Dicke expansion at third order in η), we expand the full Hamiltonian in Eq. (7.12) to the same order, as detailed in Appendix H.4. This expansion reveals residual off-resonant interactions arising from higher-order sideband processes and nonlinear couplings.

Off-resonant processes stem from terms in the expanded Hamiltonian in Eq. (H.2) with time-dependencies on the motional frequencies ν_l. These include off-resonant carrier transitions that induce spin-flips σ_+ and σ_- without altering the motional state, corresponding to processes of the form

$$-i\sigma_+^{(j)} \sum_p \mathfrak{f}_p^{(j)} \ + \text{h.c.} \ , \tag{7.47}$$

with $\mathfrak{f}_p^{(j)}$ defined in Eq. (H.3).

Sideband transitions involve spin-flips accompanied by phonon excitations or de-excitations in motional modes near-resonant with the driving fields, with the dominant process given by

$$\sigma_+^{(j)} \left[\sum_{l' \neq 1} \frac{\eta_{jl'}}{\eta_{j1}} \left(f_{1,1}^{(j)} e^{-i\Delta_{l'}t} a_{l'}^\dagger - f_{1,1}^{*(j)} e^{i\Delta_{l'}t} a_{l'} \right) + \sum_{p,l'} \frac{\eta_{jl'}}{\eta_{jp}} \left(f_{p,2}^{(j)} e^{-i\upsilon_{pl'}t} a_{l'}^\dagger + f_{p,2}^{*(j)} e^{i\upsilon_{pl'}t} a_{l'} \right) \right] , \tag{7.48}$$

where $\Delta_{l'} = \nu_1 - \nu_{l'}$ and $\upsilon_{pl'} = 2\nu_p - \nu_{l'}$ are non-zero detunings.

Other off-resonant processes, involving multiple phonon exchanges, can be similarly identified and included in the off-resonant Hamiltonian. These terms, oscillating at frequencies that are linear combinations of the motional frequencies $\sum_m c_m \nu_m$, contribute to the effective Hamiltonian on timescales scaling as inverse powers of the trap frequency ν^{-1}. Given that the gate time is dictated by the detunings δ (as discussed in the following sections), off-resonant processes, evolving on the slower timescale of the trap frequency ν^{-1}, can be neglected when $\nu \gg \delta$, as they average out over the gate duration.

For the two-ion case, Fig. 7.4 shows the gate infidelity of the proposed scheme as a function of the trap frequency ν on a log scale. Grey dots represent data from numerical simulations using the full system Hamiltonian, with all off-resonant contributions, and specific values of ν in the range $[1, 300]$ with step size of 0.1. The black dashed line, depicting the ν^{-2} scaling, serves as an upper bound for infidelity across the entire frequency range. This scaling can be understood through a perturbative analysis, as the factors $e^{-i\nu_l t}$ induce a perturbation on the state with dependence of the form $\int dt e^{-i\nu_l t} \propto \nu_l^{-1}$. Given that infidelity is bilinear in the state, this translates to the overall ν^{-2} scaling of the infidelity.

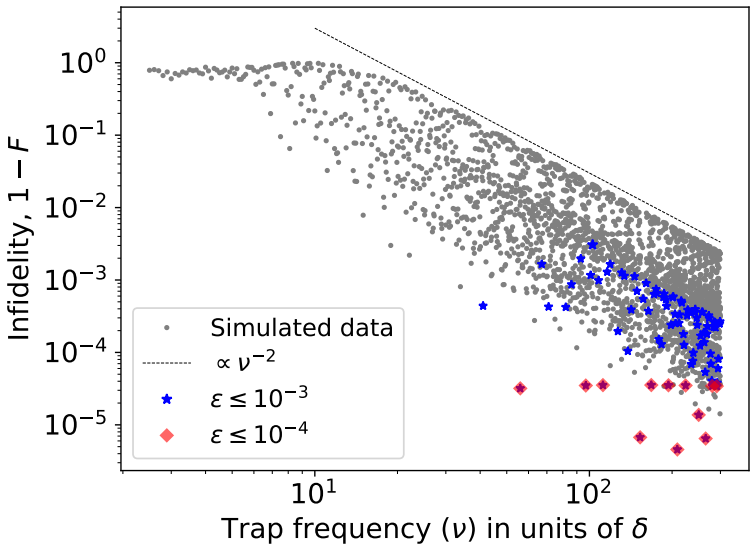

Figure 7.4: Gate infidelity, including all off-resonant terms, for the two-ion gate as a function of trap frequency ν, in units of the detuning δ. Grey dots show infidelities for specific values of ν in the range $[1, 300]$ with a step size of 0.1, while the black dashed line represents the ν^{-2} scaling that bounds the infidelity. Blue stars highlight specific values of the ratio ν/δ that satisfy Eq. (7.51) with an error tolerance $\epsilon \leq 10^{-3}$, while the red diamonds highlight those that satisfy the same equation with a tighter tolerance of $\epsilon \leq 10^{-4}$.

While this bound provides insights into the ratio ν/δ required for specific fidelity levels, it is desirable to identify practical conditions on gate parameters that enable high-fidelity gates without excessively large ratios ν/δ. This can be achieved by minimizing the influence of off-resonant terms in Eq. (H.2) on the effective Hamiltonian.

Carrier transitions (Eq. (7.47)) vanish at first order when

$$\nu_l T = 2\pi k_l^{(1)} , \quad l \in [1, M] \tag{7.49}$$

for any integers $k_l^{(1)}$. Similarly, vanishing first-order off-resonant sideband transitions (Eq. (7.48)) requires

$$(\nu_1 - \nu_l)T = 2\pi k_l^{(2)} , \quad l \in [2, M] , \tag{7.50a}$$

$$(2\nu_p - \nu_l)T = 2\pi k_{pl}^{(3)} , \quad p, l \in [1, M] , \tag{7.50b}$$

for integers $k_l^{(i)}, k_{pl}^{(i)}$.

Similar constraints can be derived for the remaining off-resonant terms in Eq. (H.2). Notably, to simultaneously satisfy all these conditions and the gate time constraint $\delta T = 2\pi k_0$, only the following relation must hold

$$\left| \frac{\nu_l}{\delta} - \frac{k_l}{k_0} \right| \leq \epsilon , \tag{7.51}$$

System Size	Smallest ratio ν/δ for varying ϵ			
(N)	$\epsilon = 10^{-1}$	$\epsilon = 10^{-2}$	$\epsilon = 10^{-3}$	$\epsilon = 10^{-4}$
2	3	11	41	56
3	3	15	71	485
4	3	22	212	765
5	3	31	201	1534
6	3	34	157	1362
7	5	29	292	1791
8	5	31	318	2280
9	5	44	288	1437
10	5	33	328	2385

Table 7.1: Smallest ratios ν/δ of trap frequency ν to detuning δ required to satisfy Eq. (7.51) for different system sizes N, subject to a maximum error tolerance ϵ and the constraint $\delta T = 2\pi$.

for integers k_l, k_0, with $\epsilon \approx 0$. While exact cancellation of off-resonant effects requires $\epsilon = 0$, a sufficiently small ϵ can be enough to achieve low infidelity in practice.

To exemplify this, Fig. 7.4 depicts the ratios ν/δ (in different colored shapes) required to satisfy Eq. (7.51) for two precision levels ϵ in a two-ion system. Blue stars represent solutions satisfying Eq. (7.51) with a tolerance of $\epsilon = 10^{-3}$, while red diamonds correspond to a tighter tolerance of $\epsilon = 10^{-4}$. The looser tolerance of $\epsilon = 10^{-3}$ allows for numerous solutions for ν/δ, generally yielding infidelities below 10^{-3}, which is sufficient for most applications. However, with the tighter tolerance of $\epsilon = 10^{-4}$ infidelities even lower than 10^{-5} can be achieved. Notably, all the required ratios ν/δ are well within experimental reach.

Optimizing gate fidelity for larger systems requires adjusting the ratios ν/δ. Table 7.1 presents the minimum ratio ν/δ required to solve Eq. (7.51) with a given tolerance ϵ for up to 10 ions (with the motional mode frequencies listed in Table H.1 for convenience). However, the framework can be extended to arbitrary system sizes by solving Eq. (7.51) to the desired precision ϵ.

As demonstrated in this section, while the resonant Hamiltonian employed in Eq. (7.13) does not impose specific conditions on the detunings δ or trap frequencies ν, constraining the ratio ν/δ, enables the elimination of off-resonant contributions with arbitrary precision.

7.2 Conclusions

Trapped-ion quantum computation has emerged as a leading candidate for scalable quantum information processing, yet the realization of high-fidelity entangling gates continues to pose significant challenges. Existing gate schemes, while effective at mitigating specific error mechanisms, are limited by their inability to address the interplay of thermal excitations, control field imperfections, and environmental decoherence. These factors introduce unwanted spin-motion couplings, detuning instabilities, and motional heating, which degrade gate performance and require highly controlled environments and sophisticated control techniques, even to achieve moderate entanglement fidelities with small ion chains.

In this Chapter, we have presented a robust entangling gate protocol designed to suppress multiple error mechanisms simultaneously. By leveraging a multi-sideband driving strategy, the scheme dynamically cancels inhomogeneous spin-motion interactions across all available motional modes, significantly enhancing fidelity even in large ion chains. Crucially, the approach remains effective under substantial thermal excitations — a key advantage for scalability, as thermal noise becomes increasingly problematic with system size. Moreover, the protocol demonstrates resilience against motional heating, vibrational frequency fluctuations, and detuning errors, easing experimental constraints and improving feasibility.

Future work should focus on experimental validation across different trapped-ion hardware configurations, considering variations in ion species, trap geometries, and motional mode structures. Integration with quantum error correction and exploration of multi-qubit extensions will be crucial for fault-tolerant architectures. Further refinements could optimize driving parameters for specific experimental constraints, such as laser power limitations or mode-frequency crowding, enhancing practical implementation. Additionally, assessing the protocol's compatibility with real-time feedback and dynamic circuit execution will be essential for its role in algorithm-driven quantum processing.

Beyond its immediate application to trapped ions, this method offers insights for error mitigation in other quantum platforms, such as superconducting qubits and neutral atom arrays, where control imperfections similarly impact performance. By reducing dependence on extreme cooling and highly isolated environments, the protocol enables more flexible and modular quantum architectures, bringing us closer to the realization of practical quantum computers.

Chapter 8

Entangling Gates of Trapped Ions Mediated by Spectrally Crowded Modes

CONTRIBUTIONS

All the work in this Chapter was carried out by me, under the supervision of Florian Mintert.

8.1 Introduction

In trapped-ion quantum computing, the implementation of quantum gates typically follows one of two main approaches: laser-based control or magnetic-field-based control. Laser-driven gates — such as the MS gate discussed in earlier sections — exploit the coupling between internal qubit states and the collective vibrational modes of an ion chain, mediated by focused laser beams. These gates typically rely on the Lamb-Dicke approximation [246, 3], which assumes the ions' motional amplitudes are small compared to the laser wavelength, simplifying the interaction Hamiltonian and enabling analytical solutions. However, as previously discussed, this approximation imposes strict operational constraints: ions must be laser-cooled to their motional ground states [209], and the qubit-motion coupling must remain weak to prevent excitations beyond the Lamb-Dicke regime [96].

In the previous Chapter, we proposed a control scheme that mitigates many of these issues by selecting specific sidebands and modulating the time-dependence of driving fields. However, a significant scalability challenge arises from the laser infrastructure itself. As the number of ions increases, the complexity of the optical system grows exponentially [204]. Individual addressing of ions in long chains necessitates tightly focused laser beams with rapid reconfiguration or frequency multiplexing [95], both of which introduce technical noise and crosstalk. Additionally, maintaining laser phase stability and uniform power across

the ion chain becomes increasingly difficult, which affects gate fidelity [232]. The heating of ion motion from electric field noise in trap electrodes further exacerbates these issues, as residual thermal motion reduces the coherence of phonon-mediated interactions [210].

In contrast, magnetic-field-controlled gates, such as those using a magnetic field gradient [129], employ microwave or radiofrequency fields to induce qubit-motion coupling. These methods replace complex laser systems with global microwave fields to manipulate qubits, as seen in scalable architectures like the "Blueprint" ion trap design [205]. The gradient creates a position-dependent Zeeman shift, enabling spin-motion coupling proportional to the ion's displacement [227] (see Sec. 4.1.4). This approach doesn't require the Lamb-Dicke approximation, as coupling strength is linearly related to displacement[129], enabling operations with larger motional amplitudes and reducing cooling requirements while improving robustness against heating effects [131].

However, practical magnetic field gradients—on the order of 100 T/m from microfabricated wires or permanent magnets [229]—result in weaker coupling strengths compared to optical dipole forces, leading to slower gate times. These typically range from microseconds to milliseconds, while laser-driven gates operate in the nanosecond to microsecond range [96]. Although high-fidelity entangling gates have been demonstrated with magnetic gradients [131], scalability is still limited by the need to maintain gradient uniformity over large ion arrays and mitigate decoherence during prolonged gate durations [205]. Recent advancements, such as cryogenic trap integration to reduce thermal noise [247] and dynamic gradient modulation [248], aim to address these challenges.

Both laser and magnetic-field gates rely on coupling qubits via shared motional modes, acting as a quantum bus. To entangle specific ion pairs, control pulses are tailored to resonantly drive selected modes while suppressing off-resonant excitations [209]. For laser-driven gates, frequency combs synchronized to mode frequencies are used [228], while magnetic-field gates employ oscillating gradients modulated at mode frequencies [130]. However, as the ion count increases, the vibrational mode spectrum becomes densely packed, with mode frequencies scaling inversely with the square root of the ion number [249]. This spectral crowding complicates the resolution of individual modes without crosstalk, necessitating longer gate times to preserve spectral selectivity [250]. As a result, most high-fidelity gates to date have been limited to two-ion crystals or small chains with well-separated modes [251].

In this Chapter, we propose a novel control strategy that completely eliminates the need for spectral mode selection. By applying a time-dependent magnetic field gradient with a carefully designed temporal profile, we can engineer the interaction between qubits and motional modes to accumulate a geometric phase proportional to the collective displacement of ions, irrespective of the motional mode structure. This is achieved by shaping the gradient waveform to impart a spin-dependent force that does not require selectively driving specific sideband transitions and instead can simultaneously use all available modes of vibration.

8.2 Hamiltonian model

The Hamiltonian for a set of trapped ions and motional degrees of freedom, coupled via a constant magnetic field gradient of the form in Eq. (4.124), is given by the Hamiltonian in Eq. (4.133). In the following, however, it will be convenient to consider a more general magnetic field with a constant offset but a gradient that can be modulated in time, *i.e.*

$$B(z_j, t) = B(z = 0) + f(t)\frac{\partial B}{\partial z}\Big|_{z=0} z_j \ , \tag{8.1}$$

where z_j is the axial position of the j-th ion and $f(t)$ is the time-dependent gradient (in the static case, $f = 1$). Consider the magnetic field gradient to be bounded by a maximum value $\partial B/\partial z$, so that $-1 \leq f(t) \leq 1$ for any time t. The interaction Hamiltonian takes the form

$$H = \sum_j \frac{\tilde{\omega}_{eg}^{(j)}}{2}\sigma_z^{(j)} + \sum_k \nu_k a_k^\dagger a_k + f(t)\sum_{j,l}\nu_l \eta_{jl}(a_l + a_l^\dagger)\sigma_z^{(j)} \ , \tag{8.2}$$

where $\tilde{\omega}_{eg}^{(j)}$ is the qubit frequency for ion j, accounting for the Zeeman shift due to the magnetic field (defined in Eq. (4.132)), and $\sigma_z^{(j)}$ the corresponding Pauli Z-operator. The terms $a_l^\dagger$ and a_l are the creation and annihilation operators for the harmonic oscillator modes with frequency ν_l, and the coupling strength η_{jl} between ion j and motion in normal mode l is given by Eq. (4.134) and we reproduce here for convenience

$$\eta_{jl} = \frac{\gamma_s \chi_{jl} z_{l,0}}{2\nu_l}\partial_z B\Big|_{z=0} \ . \tag{8.3}$$

The time-dependent function $f(t)$ controls the amplitude of the magnetic field gradient and, since it is challenging to engineer independent gradients for each ion, this modulation affects all ions uniformly, manifesting as a global prefactor in the interaction Hamiltonian.

In the case of a static field gradient (*i.e.* time-independent f), the qubit-motion interaction $(a_l + a_l^\dagger)\sigma_z^{(j)}$ results in an effective qubit-qubit interaction in terms of a polaron transformation that accounts for the qubit-state-dependent displacement of the trapping potential center [129]. This interaction can be used for entangling quantum gates, but since the interaction constant is quadratic in f and thus in the magnetic field gradient, it is typically weaker than effective interactions realised with additional driving or in laser-driven gates.

The gate speed can be increased with a periodic modulation of the gradient [130]. If the frequency of this modulation is close to the eigenfrequency of one of the motional modes, then the effective interaction is amplified by a factor $1/\delta$, where δ is the detuning between the modulation frequency and the eigenfrequency. The requirement that motional and qubit degrees of freedom are uncorrelated after the gate operation requires the gate time to be an integer multiple of $2\pi/\delta$. By setting the detuning proportional to the coupling strength of a selected driven mode l, $\delta \propto \eta_{kl}\nu_l$, it becomes possible to engineer an effective interaction between a pair of ions i, j that scales linearly with the gradient, $(\eta_{il}\eta_{jl}\eta_{kl}^{-1})\sigma_z^{(i)}\sigma_z^{(j)} \propto (\partial_z B)\sigma_z^{(i)}\sigma_z^{(j)}$, rather than quadratically. Given typical restrictions to

system parameters, most notably the magnetic field gradient, effective interactions induced by an oscillating field gradient can thus be stronger than with a static gradient [130].

This enhanced spin-spin interaction, however, comes with certain limitations. The driving fields are tuned near the resonance of a selected motional mode, which serves as the mediator for the gate operation. The detuning from these resonances determines the gate timescale, and processes occurring on significantly faster timescales are neglected under the rotating-wave approximation, which imposes upper limits on achievable fidelities and restricts the method to slower gate operations. Furthermore, the mode-specific nature of this approach limits its scalability. The increasing spectral density of motional modes in larger chains makes it difficult to target specific modes without unintentionally driving others. Also, the decreasing interaction strength between each qubit and each motional mode with increasing ion number (scaling roughly as $\propto 1/\sqrt{n}$) implies that fast gates necessarily require several motional modes participating actively, rather than relying on a single one as the mediator.

In order to overcome these limitations, we aim at a treatment that takes into account the qubit motion interaction $(a_l + a_l^\dagger)\sigma_z^{(j)}$ exactly without resort to any rotating wave approximation that is the basis for spectral selection of individual motional modes.

Similar to the case of a static field gradient, the Hamiltonian can be diagonalized with a polaron transformation (see Eq. (4.135)), but a time-dependent gradient requires a time-dependent transformation. For this purpose, we adopt the specific time-dependent polaron transformation

$$U_P = \exp\left(i \sum_{j,l} \left(g_l^*(t) a_l + g_l(t) a_l^\dagger \right) \eta_{jl} \sigma_z^{(j)} \right) , \tag{8.4}$$

where $g_l(t)$ are time-dependent functions to be determined. The transformed Hamiltonian is given by $\tilde{H} = U_P H U_P^\dagger + i\dot{U}_P U_P^\dagger$. After expanding and reorganizing terms by their operator structure, $\tilde{H}$ simplifies to

$$\begin{aligned} \tilde{H} = & \sum_l \nu_l a_l^\dagger a_l \\ & + \sum_{j,l} \left(\nu_l f + i\nu_l g_l^* - \dot{g}_l^* \right) a_l \eta_{jl} \sigma_z^{(j)} + \sum_{j,l} \left(\nu_l f - i\nu_l g_l - \dot{g}_l \right) a_l^\dagger \eta_{jl} \sigma_z^{(j)} \\ & + \sum_{l,j,j'} \left(\nu_l g_l^* g_l + i\nu_l f (g_l^* - g_l) - \frac{i}{2} \left(g_l^* \dot{g}_l - g_l \dot{g}_l^* \right) \right) \eta_{jl} \eta_{j'l} \sigma_z^{(j)} \sigma_z^{(j')} . \end{aligned} \tag{8.5}$$

The central aim of this transformation is to decouple the spin degrees of freedom from the motional modes. This decoupling is achieved only if the coefficients of the spin-motion coupling terms $a_l \sigma_z^{(j)}$ and $a_l^\dagger \sigma_z^{(j)}$ vanish identically. Enforcing this condition leads to a set of first-order differential equations for $g_l(t)$

$$\dot{g}_l(t) + i\nu_l g_l(t) = \nu_l f(t) , \tag{8.6}$$

which mirror the classical equations of motion for a driven harmonic oscillator. The formal solution to Eq. (8.6),

$$g_l(t) = e^{-it\nu_l}\left(g_l(0) + \nu_l \int_0^t d\tau e^{i\nu_l\tau} f(\tau)\right) , \tag{8.7}$$

encodes the interplay between the global driving field $f(t)$ and the vibrational mode's natural dynamics. The first term, $e^{-it\nu_l}g_l(0)$, represents free evolution of the mode under its intrinsic frequency ν_l, while the integral term describes the cumulative phase-space displacement driven by $f(t)$. This structure mirrors the response of a classical harmonic oscillator to an external force: the displacement $ig_l(t)$ arises from the resonant interplay between the driving field $f(t)$ and the mode's oscillation at ν_l.

Crucially, $g_l(t)$ acts as a spin-dependent displacement in phase space. The displacement magnitude depends on the collective electronic (spin) state of the ions via the Pauli operators $\sigma_z^{(j)}$ in the polaron transformation U_P. For example, in a two-ion system, the displacement becomes conditional on the ions' spin states ($|ee\rangle, |eg\rangle, |ge\rangle, |gg\rangle$), as seen in the matrix representation of U_P ,

$$\begin{aligned} U_P = \prod_l \Big(& \mathcal{D}\left(ig_l(t)(\eta_{1l} + \eta_{2l})\right) |ee\rangle\langle ee| \\ & + \mathcal{D}\left(ig_l(t)(\eta_{1l} - \eta_{2l})\right) |eg\rangle\langle eg| \\ & + \mathcal{D}\left(ig_l(t)(-\eta_{1l} + \eta_{2l})\right) |ge\rangle\langle ge| \\ & + \mathcal{D}\left(ig_l(t)(-\eta_{1l} - \eta_{2l})\right) |gg\rangle\langle gg| \Big) . \end{aligned} \tag{8.8}$$

Here, $\mathcal{D}(\alpha) = \exp\left(\alpha a^\dagger - \alpha^* a\right)$ is the displacement operator, which shifts the motional state in phase space by an amount α. This conditional displacement is central to entanglement. As the ions are displaced along spin-dependent paths, they accumulate phases proportional to their trajectories in phase space. When two ions are subjected to such state-dependent forces simultaneously, their relative phases become correlated through the shared motional mode. Over time, this correlation transfers entanglement from the motional state to the internal spin states of the ions. By carefully choosing $g_l(t)$, the motional states are steered back to their original configurations at the end of the operation, eliminating any residual motion and leaving behind purely entangled spin states.

With $g_l(t)$ chosen to satisfy the constraints, the transformed Hamiltonian $\tilde{H}$ simplifies to

$$\tilde{H}(t) = \sum_j \frac{\tilde{\omega}_{eg}^{(j)}}{2}\sigma_z^{(j)} + \sum_k \nu_k a_k^\dagger a_k + \sum_{ij} \alpha_{ij}\sigma_z^{(i)}\sigma_z^{(j)} , \tag{8.9}$$

with coupling elements $\alpha_{ij}(t) = \sum_l \eta_{il}\eta_{jl}\Phi_l(t)$ given in terms of the real functions

$$\Phi_l(t) = \nu_l f(t)\mathfrak{Im}(g_l(t)) , \tag{8.10}$$

with the $\mathfrak{Im}(g_l(t))$ denoting the imaginary component of $g_l(t)$. Although the Hamiltonian $\tilde{H}(t)$ is generally time-dependent, the commutator $[\tilde{H}(t_1), \tilde{H}(t_2)] = 0$ holds for all t_1 and t_2. This property ensures that the time-evolution operator $\tilde{U}(t)$ induced by $\tilde{H}(t)$ is of the simple form

$$\tilde{U}(t) = \exp\left(-i \int_0^t d\tau \tilde{H}(\tau)\right) , \tag{8.11}$$

eliminating the need for time-ordering.

The evolution governed by $\tilde{U}(t)$ accumulates a phase $\int_0^T \Phi_l(t)dt$, determined by the oscillator mode l's trajectory in phase space. To uncover the physical origin of this phase, we express the displacement function as $g_l(t) = X_l(t) + iP_l(t)$, where $X_l(t)$ and $P_l(t)$ are the real canonical quadrature components (normalized such that they form a conjugate pair). The accumulated phase then becomes

$$\int_0^T \Phi_l(t)dt = \nu_l \int_0^T f(t)P_l(t)dt \ . \tag{8.12}$$

Using the driven-oscillator equation (Eq. (8.6)), we rewrite this as

$$\int_0^T \Phi_l(t)dt = \int_0^T [\dot{X}_l(t) + i\dot{P}_l(t) + i\nu_l X_l(t) - \nu_l P_l(t)]P_l(t)dt \ . \tag{8.13}$$

Taking the real part (since the Hamiltonian and couplings must be Hermitian), we get

$$\mathfrak{Re} \int_0^T \Phi_l(t)dt = \int_0^T \dot{X}_l(t)P_l(t)dt - \nu_l \int_0^T P_l^2(t)dt \ . \tag{8.14}$$

The first term is of geometric origin, representing the area enclosed by the oscillator trajectory in phase space. The second term corresponds to a dynamical phase, dependent on the detailed time dependence of the trajectory. If the oscillator's motion is cyclic over the interval $[0, T]$ (*i.e.* $X_l(0) = X_l(T)$ and $P_l(0) = P_l(T)$), then the geometric contribution simplifies to the closed-loop integral

$$\mathfrak{Re} \int_0^T \Phi_l(t)dt = \oint P_l \ dX_l \ , \tag{8.15}$$

which is the signed area enclosed by the trajectory $(X_l(t), P_l(t))$ in phase space. This geometric phase is central to entanglement generation in trapped-ion systems. In the case of a static gradient (*i.e.*, time-independent g_l), the phase accumulates linearly in time, yielding a contribution proportional to $T\nu_l \frac{\partial B}{\partial z}\Big|_{z=0}$, consistent with a constant displacement in phase space. In contrast, time-dependent driving $g_l(t)$ enables nonlinear trajectories and thus richer phase-space structures and entanglement dynamics.

The polaron transformation captures the displacement of the ion's motional states dependent on the ion's internal states. In the following, we will consider time-independent initial and final Hamiltonian with potentially a finite gradient, but between the initial and final

point in time, the gradient can be time-dependent. In order to ensure that the ions' initial and final motional states differ only in terms of the displacement corresponding to the difference of initial and final gradient, but there are no motional excitations as a result of the oscillating gradients, the boundary conditions

$$g_l(t) = -if(t) \tag{8.16}$$

need to be satisfied at both the initial time $t = 0$ and the final time $t = T$ for all modes l.

Given the ability to implement a suitable driving function $f(t)$, this allows for the realization of n independent phase shifts $D_l = \int_0^T dt\Phi_l(t)$. The most general achievable interaction in the effective qubit dynamics is thus of the form

$$\sum_{ij}[\eta D\eta^T]_{ij}\sigma_z^{(i)}\sigma_z^{(j)} \tag{8.17}$$

with a diagonal matrix D, *i.e.* the manifold of achievable interactions is n-dimensional, whereas the most general case is $n(n-1)/2$ dimensional.

As a consequence, a desired interaction matrix Λ_d can be perfectly realized only if it is diagonalizable by η^T, *i.e.*, if it admits a decomposition of the form

$$\eta^T\Lambda_d\eta = D \ , \tag{8.18}$$

with D being diagonal, and where the diagonal elements of Λ_d can be chosen at will. If this decomposition exists, the diagonal elements of D directly correspond to the phase shifts $\int_0^T \Phi_l(t)$ required to achieve the desired interaction geometry.

While the diagonalizability condition Eq. (8.18) limits the set of achievable matrices Λ_d with a global driving $f(t)$, a more flexible approach combining π-pulses and entangling dynamics with the global drive can enable the realization of arbitrary coupling matrices.

A π-pulse acting on ion k is defined by the operator $P_k^\pi = \exp\Big(-i\pi/2\sigma_x^{(k)}\Big)$. Applying this π-pulse followed by entangling dynamics within a time window $[t_1, t_2]$ yields the unitary transformation

$$U_T(t_2; t_1, \Lambda)U_0(t_2; t_1)P_k^\pi \ , \tag{8.19}$$

where U_0 is the unitary propagator corresponding to the non-interacting dynamics of $H_0 = \sum_j \omega_j/2Z_j + \sum_l \nu_l a_l^\dagger a_l$, and $U_T(t_2; t_1, \Lambda) = \exp\Big(-i\sum_{i,j}\Lambda_{ij}Z_iZ_j\Big)$ the entangling operation with coupling matrix $\Lambda = \int_{t_1}^{t_2} dt\alpha(t)$.

A second π-pulse with opposite phase gives the overall transformation

$$\begin{aligned}\mathcal{U} &= P_k^{-\pi}U_T(t_2; t_1, \Lambda)U_0(t_2; t_1)P_k^\pi \\ &= U_T(t_2; t_1, S_k\Lambda S_k^T)\tilde{U}_0(t_2; t_1) \ ,\end{aligned} \tag{8.20}$$

where the interaction matrix Λ turns into $S_k \Lambda S_k^T$, with a diagonal matrix S_k with -1 at the k-th index and 1 elsewhere. The transformed non-interacting propagator $\tilde{U}_0(t_2; t_1)$ accounts for the energy level shifts of ion k induced by the π-pulse and has no impact in the desired coupling.

Thus, by strategically applying π-pulses to selected ions before and after entangling dynamics, the interaction matrix Λ can be transformed into a new matrix $S\Lambda S^T$, where the signs of specific matrix elements are inverted.

A sequence of such transformations can be concatenated, resulting in an effective entangling matrix Λ_T of the form

$$\Lambda_T = \sum_j S^{(j)} \Lambda^{(j)} (S^{(j)})^T \ . \tag{8.21}$$

In particular, a sequence involving the application of $-\Lambda$, followed by π-pulses on ion k, and subsequent entangling dynamics with interaction matrix Λ results in

$$\Lambda_T = \Lambda + S_k(-\Lambda)S_k^T = 2\Big(\sum_{j \neq k} \Lambda_{kj} \left|k\right\rangle\!\left\langle j\right| + \Lambda_{jk} \left|j\right\rangle\!\left\langle k\right|\Big) \ . \tag{8.22}$$

Given the symmetry $\Lambda_{jk} = \Lambda_{kj}$, the resulting interaction matrix has only $N-1$ independent entries, which are located along row and column k. By adjusting the N Rabi-angles D_l, it is therefore possible to choose all the $N-1$ entries, and the last free parameter can be optimized to minimize the gate time for implementing a given interaction pattern.

This iterative approach enables the construction of any interaction geometry that couples ion k to the other ions in the chain. By iteratively applying this sequential scheme to each ion in the chain, any desired interaction geometry, including the most general form $\sum_{ij} \Lambda_{ij} Z_i Z_j$, can be realised.

However, this sequential approach may not be optimal, as π-pulses are applied to only one ion at a time. Applying π-pulses to multiple ions simultaneously could potentially lead to shorter pulse sequences. According to Eq. (8.22), a single sequence involving a global field $f(t)$, preceded and followed by appropriately chosen π-pulses, is sufficient to produce a desired Λ_d if

$$(S^{(1)}\eta)^T \Lambda_d (S^{(1)}\eta) = D^{(1)} \ , \tag{8.23}$$

where $D^{(1)}$ is diagonal. Otherwise, one can replace $D^{(1)}$ by $D^{(1)} + \epsilon^{(1)}$, where $\epsilon^{(1)}$ contains the off-diagonal elements such that $(S^{(1)}\eta)^T \Lambda_d (S^{(1)}\eta) = D^{(1)} + \epsilon^{(1)}$, and aim at finding a second sequence such that

$$(S^{(2)}\eta)^T (S^{(1)}\eta) \epsilon^{(1)} (S^{(1)}\eta)^T (S^{(2)}\eta) = D^{(2)} \tag{8.24}$$

with $D^{(2)}$ diagonal. If such a decomposition exists, one has found a two-sequence solution involving entangling dynamics with π-pulses before and after to achieve the desired Λ_d.

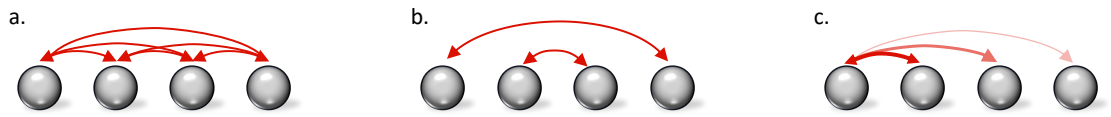

Figure 8.1: Illustration of various entanglement geometries, where arrows indicate interacting elements, and their thickness and color represent interaction strength (thin and light for weak, thick and dark for strong). In (a), uniform coupling is shown across all ions, with equal interaction strength between each pair. In (b), a rainbow-style entanglement geometry is depicted, where symmetric pairs of ions are coupled with equal strength. In (c), distance-dependent coupling is represented, with ion 1 interacting with the rest of the chain, and interaction strength decreasing with distance.

If not, one repeats with a new off-diagonal matrix $\epsilon^{(2)}$. In general, this iterative process continues until a matrix $S^{(j)}$ is found that satisfies

$$(S^{(j)}\eta)^T(S^{(j-1)}\eta)\epsilon^{(j-1)}(S^{(j-1)}\eta)^T(S^{(j)}\eta) = D^{(j)} \ , \tag{8.25}$$

with a diagonal $D^{(j)}$.

8.3 Results

To illustrate the methodology, consider a time-dependent magnetic field gradient with

$$f(t) = \sum_j A_j \cos(\omega_j t + \vartheta_j) \ , \tag{8.26}$$

expressed in terms of real amplitudes A_j, frequencies ω_j and phases ϑ_j. Notably, this parametrization, or any other suitable choice, must offer enough degrees of freedom (A_j, ω_j, ϑ_j) to satisfy the boundary conditions (Eq. (8.16)) and offer flexibility for optimizing the time-dependence to achieve the desired entanglement pattern. For a given motional mode l with frequency ν_l, the boundary conditions are met if

$$0 = \sum_j \frac{A_j\omega_j}{\nu_l^2 - \omega_j^2}\Big[\nu_l \sin(\nu_l T)\sin(\vartheta_j) + \omega_j \cos(\omega_j T + \vartheta_j) - \omega_j \cos(\nu_l T)\cos(\vartheta_j)\Big] \ , \tag{8.27a}$$

$$0 = \sum_j \frac{A_j\omega_j}{\nu_l^2 - \omega_j^2}\Big[\nu_l \cos(\nu_l T)\sin(\vartheta_j) - \nu_l \sin(\omega_j T + \vartheta_j) + \omega_j \sin(\nu_l T)\cos(\vartheta_j)\Big] \ . \tag{8.27b}$$

A natural choice to solve Eq. (8.27) is to use at least $2M$ sets of parameters $(A_j, \omega_j, \vartheta_j)$ for a system with M motional modes, as this provides enough flexibility to solve the constraints. However, introducing additional frequency components in the expansion Eq. (8.26) can further refine the dynamics, allowing better control over entanglement generation and robustness against imperfections.

For a specific example of a four-ion chain, nine sets $(A_j, \omega_j, \vartheta_j)$ are sufficient to satisfy boundary conditions (Eq. (8.16)) and optimize the dynamics as desired, though more optimal choices may exist. With such a decomposition, one can generate a wide range of effective couplings $\sum_{i,j} \Lambda_{ij}\sigma_z^{(i)}\sigma_z^{(j)}$.

To determine which interaction strengths Λ_{ij} are achievable from the field parametrization (Eq. (8.26)), it helps to derive explicit formulas for the accumulated phases D_l, which directly determine the interaction matrices Λ by the congruence transformation of D with η, the matrix of Lamb-Dicke parameters (see Eq. (8.17)). To facilitate this derivation, we first determine the imaginary part of $g_l(t)$

$$\mathfrak{Im}(g_l) = -\sum_j \frac{A_j}{\nu_l^2 - \omega_j^2}\Big[\nu_l^2\cos(\omega_j t + \vartheta_j) - \omega_j^2\cos(\nu_l t)\cos(\vartheta_j) + \omega_j\nu_l\sin(\nu_l t)\sin(\vartheta_j)\Big]\,. \tag{8.28}$$

This expression leads to the derivation of the explicit time-dependent phases for each motional mode l

$$\begin{aligned}\frac{\Phi_l(t)}{\nu_l} = \sum_{j,k}\frac{-A_jA_k}{2(\nu_l^2-\omega_j^2)}\Big[&\nu_l^2\cos((\omega_j+\omega_k)t+\vartheta_j+\vartheta_k) + \nu_l^2\cos((\omega_j-\omega_k)t+\vartheta_j-\vartheta_k)\\ &-\omega_j^2\cos(\vartheta_j)\cos((\nu_l+\omega_k)t+\vartheta_k) - \omega_j^2\cos(\vartheta_j)\cos((\nu_l-\omega_k)t-\vartheta_k)\\ &+\omega_j\nu_l\sin(\vartheta_j)\sin((\nu_l+\omega_k)t+\vartheta_k) + \omega_j\nu_l\sin(\vartheta_j)\sin((\nu_l-\omega_k)t-\vartheta_k)\Big]\,,\end{aligned} \tag{8.29}$$

and, then, the accumulated phases $D_l = \int_0^T \Phi_l(t)$ can be expressed in the closed form

$$\begin{aligned}\frac{D_l}{\nu_l} = \sum_{j,k}\frac{-A_jA_k}{2(\nu_l^2-\omega_j^2)}\Bigg[&\frac{\nu_l^2\sin((\omega_j+\omega_k)T+\vartheta_j+\vartheta_k) - \nu_l^2\sin(\vartheta_j+\vartheta_k)}{\omega_j+\omega_k}\\ &+\frac{\nu_l^2\sin((\omega_j-\omega_k)T+\vartheta_j-\vartheta_k) - \nu_l^2\sin(\vartheta_j-\vartheta_k)}{\omega_j-\omega_k}\\ &-\frac{\omega_j^2\cos(\vartheta_j)\sin((\nu_l+\omega_k)T+\vartheta_k) - \omega_j^2\cos(\vartheta_j)\sin(\vartheta_k)}{\nu_l+\omega_k}\\ &-\frac{\omega_j^2\cos(\vartheta_j)\sin((\nu_l-\omega_k)T-\vartheta_k) - \omega_j^2\cos(\vartheta_j)\sin(-\vartheta_k)}{\nu_l-\omega_k}\\ &-\frac{\omega_j\nu_l\sin(\vartheta_j)\cos((\nu_l+\omega_k)T+\vartheta_k) - \omega_j\nu_l\sin(\vartheta_j)\cos(\vartheta_k)}{\nu_l+\omega_k}\\ &-\frac{\omega_j\nu_l\sin(\vartheta_j)\cos((\nu_l-\omega_k)T-\vartheta_k) - \omega_j\nu_l\sin(\vartheta_j)\cos(-\vartheta_k)}{\nu_l-\omega_k}\Bigg]\,.\end{aligned} \tag{8.30}$$

To exemplify this, consider the task of generating an effective homogeneous Ising interaction $\sum_{i,j} g\sigma_z^{(i)}\sigma_z^{(j)}$, where each pair is coupled with the same strength g (see Fig. 8.1a). Since a decomposition of the form in Eq. (8.18) exists with $\Lambda_d = g\mathbf{J}$ (where $\mathbf{J}$ is the matrix filled with ones), this interaction can be implemented using a single global driving pulse $f(t)$. Fig. 8.2 presents one such pulse, although other solutions are possible. To achieve a uniform coupling strength of $g = \pi/4$, the required gate duration is $T = 94.2111/\nu$, typically corresponding to a few microseconds in practical implementations, and represents the time needed to decouple all motional states.

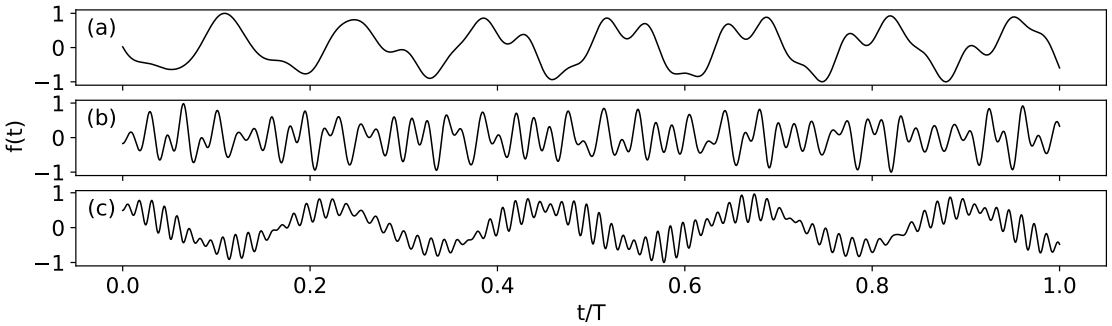

Figure 8.2: Global modulation $f(t)$ of the magnetic field gradient as a function of time t, in fractions of the total gate time T. Panels (a), (b), and (c) illustrate different modulation patterns to engineer specific quantum operations: a uniform Ising interaction ($g = \pi/4$, $T = 8.12556/2\pi\nu$) in (a), a rainbow entanglement pattern ($g = \pi/4$, $T = 134.51/\nu$) in (b), and an entangling gate with decaying coupling strength between the first qubit and the rest of the chain ($g = \pi/4$ in Eq. (8.34), $T = 153.78/\nu$) in (c). Simulations with (a) and (b) assume a magnetic field gradient of 100 T/m and a trap frequency of $\nu/2\pi = 100$ kHz leading to a maximum spin motion coupling of $\eta_{j1} \sim 0.1196$. In (c), the magnetic field gradient is set to 200 T/m, yielding $\eta_{j1} \sim 0.2392$.

The effectiveness of the protocol can be verified with a numerical simulation of the gate using the original system Hamiltonian Eq. (8.2) with the optimal driving $f(t)$.

Considering an initial state $\rho(0) = \rho_S \otimes \rho_M$ composed of spin (ρ_S) and motional (ρ_M) components, and the target gate $U = \exp\left(-ig\sum_{i,j}\sigma_z^{(i)}\sigma_z^{(j)}\right)$, the target spin state is given by $\rho_S(T) = \mathrm{Tr}_M\left(U\rho_S U^\dagger \otimes \rho_M\right)$, where Tr_M denotes the trace over the motional degrees of freedom. Denoting the actual implementation of the gate by the map $\mathcal{E}(\rho(0))$, one can estimate the performance of the protocol with the gate fidelity defined in Eq. (7.39).

By employing the driving field $f(t)$ in Fig. 8.2(a), we achieve a fidelity exceeding $F = 0.9999$. Importantly, this value represents a stopping point in the optimization process; in principle, the infidelity $1 - F$ can be made vanishingly small, approaching arbitrarily close to zero, through systematic refinement of the pulse parameters. The framework avoids common approximations such as the weak-coupling assumption or the rotating wave approximation, ensuring that the solution's accuracy is limited solely by the precision of the numerical pulse-shape optimization — provided the target entangling operation is physically realizable.

Another key advantage of this method is that it eliminates the need to spectrally resolve optical transitions associated with specific mode sidebands. Instead, it enables the simultaneous excitation of all motional modes by fully accounting for both resonant and off-resonant processes. With motional mode frequencies $\{\nu_1, \nu_2, \nu_3, \nu_4\} \sim \{\nu, 1.73\nu, 2.41\nu, 3.05\nu\}$ (where ν is the trap frequency), the optimal driving scheme for generating the Ising interaction utilizes frequencies $\{\omega_1, \omega_2, \ldots, \omega_9\} \sim \{0.88\nu, 1.05\nu, 1.11\nu, 1.86\nu, 2.43\nu, 2.82\nu, 2.86\nu, 2.91\nu, 3.04\nu\}$. These tones are distributed around the characteristic frequencies of the motional modes, with several being near-resonant with specific sideband transitions, particularly those associated with modes 1, 3, and 4, and to a lesser extent, mode 2. This configuration

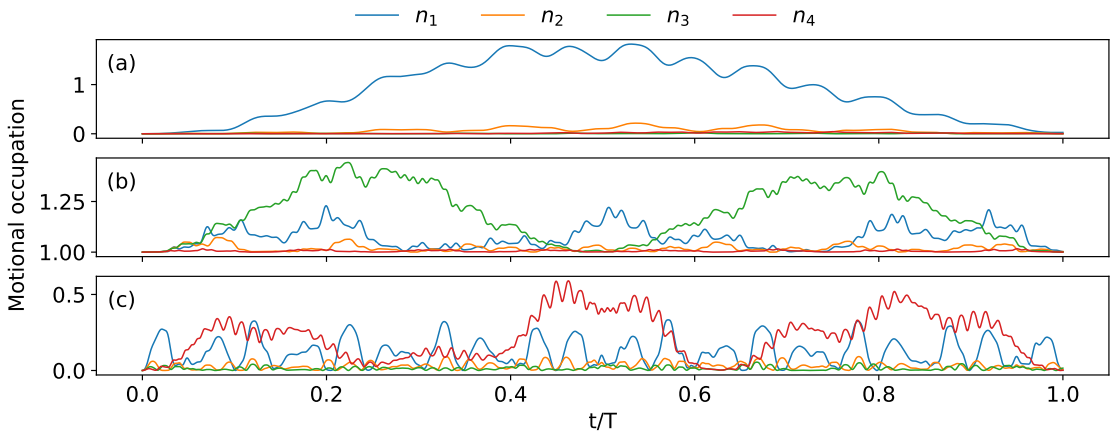

Figure 8.3: Temporal evolution of the mean phonon number $\langle n_l \rangle$ for each motional mode in a four-ion linear chain, ordered by increasing motional frequency. Panels (a), (b), and (c) depict the evolution when engineering different entangling patterns: a uniform Ising interaction, a rainbow entanglement pattern, and an entangling gate with decaying coupling strength between the first qubit and the rest of the chain, respectively. The specific driving pulses used and the simulation parameters are detailed in Fig. 8.2. Importantly, the pulses are determined once and are *independent* of the initial motional state. To illustrate this, the initial motional states for (a) and (c) are chosen as ground states $|0\rangle^{\otimes 4}$ (*i.e.*, $\langle n_l(t=0)\rangle = 0$), while for (b), they are set to $|1\rangle^{\otimes 4}$ (*i.e.*, $\langle n_l(t=0)\rangle = 1$).

show that the optimal dynamics involves the excitation of multiple motional modes.

The impact of this optimal driving is evident in the evolution of the phonon population $\langle n_l \rangle$ across the different modes l during the gate operation (Fig. 8.3(a)). Starting with all modes in the ground state $|0\rangle^{\otimes 5}$, the center-of-mass mode (blue line in Fig. 8.3(a)) is the primary mediator of the gate and gains more than a phonon of excitation. While the remaining modes (orange, green, and red) exhibit mostly virtual excitations due to weaker spin-motion coupling, these virtual excitations cannot be neglected. This is evidenced by the comparable phase shifts across all modes $\vec{D} \sim [52.6, -12.1, -32.7, -66.3]$, which clearly demonstrate the active role of all motional modes in the overall dynamics and generation of entanglement.

An alternative effective coupling, mediated by a global field, can generate the so-called rainbow state [252, 253]. This state describes a one-dimensional chain of N sites (with N even) partitioned into $N/2$ singlet pairs, where each singlet is the maximally entangled state

$$|\psi^-\rangle = \frac{1}{\sqrt{2}} \left(|01\rangle - |10\rangle \right) \ . \tag{8.31}$$

The full rainbow state is then given by the tensor product

$$|\Psi_{rainbow}\rangle = \bigotimes_{j=1}^{N/2} |\psi^-\rangle_{j,\,N-j+1} \ , \tag{8.32}$$

pairing sites symmetrically about the chain's center. Specifically, for each i satisfying $1 \leq i \leq N/2$, a singlet is formed between the site at position $N/2-(i-1)$ and the site at position $N/2+i$ (see Fig. 8.1(b)).

This symmetric pairing has profound implications for entanglement. A bipartition of the chain into two contiguous blocks cuts a number of singlet bonds proportional to the block size, resulting in an entanglement entropy that scales linearly with the subsystem size — a volume law. This contrasts sharply with the area law entanglement typically observed in local, gapped systems. The volume law entanglement of rainbow states makes them a valuable resource for exploring quantum entanglement and its scaling properties.

Notably, these rainbow states can be generated by applying the unitary

$$U = \exp\left(ig \sum_{j=1}^{N/2} \sigma_z^{(j)} \sigma_z^{(N-j+1)} \right) , \tag{8.33}$$

which couples spins in symmetric pairs (see Fig. 8.1b), followed by optimal single-qubit rotations. Since the exponent in U matches the form in Eq. (8.17), this can be achieved using our method. The corresponding optimal driving profile to produce this entangling pattern is shown in Fig. 8.2(b).

Furthermore, the optimal driving profiles determined by our method are completely independent of the initial motional state. For example, the simulation of the gate dynamics shown in Fig. 8.3(b) assumes an initial motional state with one phonon per mode, $|1\rangle^{\otimes 4}$. However, the driving profile remains equally effective for any other initial state. As the figure demonstrates, the desired entangling pattern does not rely predominantly on the center-of-mass mode; rather, multiple motional modes contribute comparably, with significant excitations distributed across several modes during the gate evolution.

While the previous examples can be realized with a single global drive $f(t)$, more complex interaction geometries require a sequential approach involving π-pulses on specific ions. This feature can be exemplified with the generation of an entangling gate that couples the first spin to the other spins in the chain (with no interactions between the other spins), where the coupling strength decays linearly with distance, *i.e.* with a coupling matrix

$$\Lambda_{ij} = 2g \left(\frac{\delta_{i1}}{j} + \frac{\delta_{j1}}{i} \right) , \tag{8.34}$$

and any chosen coupling constant g (see Fig. 8.1c).

This gate can be implemented using the two-step procedure outlined in Eq. (8.20). First, a specific matrix Λ is implemented by applying a set of phase shifts D_l to each mode l. Then, a π-pulse is applied to ion 1, followed by the application of $-\Lambda$. Finally, a π-pulse is applied to ion 1 to complete the gate. With such a sequence, the resulting entangling

matrix reads

$$\Lambda_T = 2\left(\sum_{j=2}^{5}\Big(|1\rangle\langle j| + |j\rangle\langle 1|\Big)\sum_l \eta_{1l}D_l\eta_{jl}\right). \tag{8.35}$$

Each motional mode contributes a specific entry D_l, providing sufficient free parameters to satisfy the conditions

$$[\eta D\eta^T]_{12} = \frac{g}{2}\,, \quad [\eta D\eta^T]_{13} = \frac{g}{3}\,, \quad [\eta D\eta^T]_{14} = \frac{g}{4}\,, \tag{8.36}$$

required to achieve the desired entanglement pattern. Crucially, the factor of 2 in Eq. (8.35) ensures that these conditions indeed reconstruct the coupling matrix in Eq. (8.34)

The driving pulse $f(t)$ shown in Fig. 8.2(c) satisfies these conditions, along with the boundary conditions for $g_l(t)$. Notably, this scheme does not rely on weak spin-motion coupling, allowing the pulse $f(t)$ to be tailored to achieve the desired coupling matrix Eq. (8.34) even with an exceptionally strong magnetic field gradient of $\partial_z B = 200$ T/m (*i.e.*, a very strong spin-motion coupling of $\eta_{j1} \sim 0.2392$).

Numerical simulations of the dynamics driven by this optimal pulse indicate that all motional modes are actively driven (see Fig. 8.3(c)). Interestingly, the mode with the weakest spin-motion coupling appears to be the primary mediator of the gate (see n_4 in Fig. 8.3(c)), and explains the highly oscillatory nature of the required optimal drive (Fig. 8.2(c)).

8.4 Conclusions

The rapid advancement of quantum computing relies on the ability to scale systems while maintaining precise control over qubits, particularly as algorithms demand increasingly complex entanglement patterns. Trapped-ion systems have emerged as a leading candidate due to their long qubit coherence times and high-fidelity operations. However, scaling these systems beyond a few dozen ions has posed significant challenges, primarily due to the difficulty of controllably entangling large arrays without introducing errors or requiring prohibitively complex hardware. Current methods often rely on spectrally selective addressing of individual ions or motional modes, which becomes impractical as the number of qubits grows. These approaches are further constrained by approximations like the rotating wave approximation — which neglects counter-rotating terms in oscillating fields — and the assumption of weak spin-motion coupling, limiting gate speeds and accuracy.

The control scheme we introduced in this Chapter addresses these bottlenecks through the strategic combination of a global, time-dependent magnetic field gradient and π-pulses. Unlike traditional methods that selectively excite specific vibrational (motional) modes via narrowband lasers or microwaves, this approach harnesses all motional degrees of freedom in the ion crystal. By avoiding spectral selectivity, the scheme eliminates the need for finely tuned, frequency-resolved addressing, thereby reducing hardware complexity and mitigating crosstalk errors. Furthermore, by operating outside the constraints of the RWA

and weak-coupling regimes, the method enables faster, stronger interactions between spins and motion. This not only accelerates gate operations but also improves fidelity by preserving the full physical dynamics of the system, which are often oversimplified in conventional models.

The implications of this advancement are profound. First, it simplifies the control infrastructure required for large ion chains, as global magnetic gradients and π-pulses are more straightforward to implement than arrays of frequency-selective actuators. Second, the ability to engineer arbitrary entanglement patterns unlocks the potential for implementing complex algorithms — such as quantum error correction, simulation of correlated materials, or large-scale Shor's and Grover's algorithms — that demand flexible, high-connectivity qubit interactions. Finally, by enhancing gate speeds and fidelities in larger crystals, this method advances the transition from near-term demonstrations to fault-tolerant quantum computing. As trapped-ion systems scale, such techniques will be critical in realizing practical quantum advantage, positioning ion-based platforms at the forefront of the race to build scalable, universal quantum computers.

Chapter 9

Concluding Remarks

The path to scalable quantum computers is fraught with challenges that grow exponentially with system size. At its core lies a fundamental tension: quantum systems must remain isolated enough to preserve coherence, yet be precisely controllable to perform computations. As qubit counts rise, maintaining this balance becomes increasingly difficult. Noise — decoherence, thermal fluctuations, and control imperfections — amplifies, while resource demands for calibration and operation scale unsustainably. Shared physical degrees of freedom, such as collective ion motion or superconducting circuit crosstalk, introduce correlated errors that evade conventional mitigation strategies. These hurdles demand a paradigm shift in control methodologies, emphasizing three pillars: resource efficiency, noise resilience, and hardware-aware design — a framework we have established and validated in this work.

A critical bottleneck in quantum control is the curse of dimensionality, where classical resources scale exponentially with qubit count. To address this, we introduced Implicit Quantum Control (IQC), a framework that leverages the principles of quantum invariants to bypass full state-vector simulations. By parameterizing objectives through operators rather than exponentially large state vectors, IQC enables the design of protocols that suppress excitations during diabatic operations (*e.g.*, ion shuttling) or simulate complex Hamiltonians with minimal overhead. Looking ahead, hybrid frameworks offer a promising avenue to amplify these advantages. Classical optimization, guided by IQC, could design efficient control sequences for problems like combinatorial optimization, while quantum hardware might execute tasks such as ground-state preparation, which are intractable for classical systems. By strategically partitioning roles between classical and quantum resources, such frameworks could circumvent exponential memory demands, potentially enabling scalable solutions to problems that are otherwise classically intractable.

For instance, NP-hard problems like the Shortest Vector Problem (SVP) or Traveling Salesman Problem (TSP) can be encoded as Hamiltonian ground-state searches. While classical methods require exponential resources to solve such problems at scale (despite polynomial-time verification), IQC optimizes control protocols to guide quantum systems

from simple initial states to the desired ground states. Quantum hardware then executes these protocols, revealing solutions that evade classical computation. This synergy between operator-based control and quantum execution highlights a transformative pathway for solving computationally prohibitive problems, with far-reaching implications for cryptography, logistics, and materials science.

Noise resilience is equally critical. Entanglement operations, often mediated by fragile motional or photonic "bus" modes, are particularly vulnerable. Traditional methods, reliant on weak-coupling approximations or idealized hardware, falter at scale. Our protocols, such as multi-sideband driving in trapped ions, dynamically cancel undesired couplings across all motional modes, mitigating thermal noise, frequency instabilities, and initial excitations. As validated in this work, these methods enhance gate fidelities in simulations while reducing sensitivity to imperfections, both features that are essential for scaling. This proactive error suppression, embedded directly into control design, preempts the need for resource-heavy post-correction.

Scalability further demands control schemes aligned with physical constraints. In trapped-ion systems, we demonstrated that global time-dependent fields enable arbitrary entanglement patterns without individual qubit addressing, circumventing a key bottleneck in large ion chains. By harnessing all motional modes and operating beyond weak-coupling regimes, our protocols achieve faster, stronger interactions while eliminating crosstalk and approximations like adiabatic or rotating-wave assumptions. These principles can be broadly applied to other platforms, such as superconducting qubits or neutral atoms, where designs that minimize hardware complexity reduce the reliance on high spectral precision and individual qubit control.

Ultimately, scaling quantum computers involves more than just increasing the qubit count; it requires a fundamental shift in control paradigms to address the challenges posed by noise, complexity, and hardware limitations. The integration of operator-based control, hybrid workflows, and platform-specific optimizations, as outlined in this thesis, offers a strategic framework for advancing quantum technologies. By focusing on robustness, reducing classical overhead, and exploiting the distinctive physics of each platform, these strategies form the foundation for quantum systems that exceed the limitations of current technology. Whether in simulating quantum materials, optimizing complex networks, or securing cryptographic systems, these advances hold the potential to solve classically intractable problems and unlock computational frontiers previously beyond reach.

Bibliography

[1] Modesto Orozco-Ruiz, Nguyen H Le, and Florian Mintert. Quantum control without quantum states. *PRX Quantum*, 5(4):040346, 2024.

[2] Modesto Orozco-Ruiz, Selwyn Simsek, Sahra A Kulmiya, Samuel J Hile, Winfried K Hensinger, and Florian Mintert. Optimal control with a multidimensional quantum invariant. *Phys. Rev. A*, 108(2):022601, 2023.

[3] Modesto Orozco-Ruiz, Wasim Rehman, and Florian Mintert. Generally noise-resilient quantum gates for trapped-ions. *arXiv preprint arXiv:2404.12961*, 2024.

[4] Nguyen H Le, Modesto Orozco-Ruiz, Sahra A Kulmiya, James G Urquhart, Samuel J Hile, Winfried K Hensinger, and Florian Mintert. Amplitude-noise-resilient entangling gates for trapped ions. *arXiv preprint arXiv:2407.03047*, 2024.

[5] Albert Einstein. *Albert Einstein: Philosopher-Scientist*, volume 7. Tudor Publishing Company, 1957.

[6] David J. Griffiths and Darrell F. Schroeter. *Introduction to Quantum Mechanics*. Cambridge University Press, 2019.

[7] J. W. Strutt and Lord Rayleigh. Remarks upon the law of complete radiation. *Philos. Mag.*, 49:539, 1900.

[8] Paul Ehrenfest. Welche züge der lichtquantenhypothese spielen in der theorie der wärmestrahlung eine wesentliche rolle? *Ann. Phys.*, 341(11):91–118, 1911.

[9] Martin J. Klein. Max Planck and the beginnings of the quantum theory. *Arch. Hist. Exact Sci.*, 1:459–479, 1961.

[10] Albert Einstein. Über einen die Erzeugung und Verwandlung des Lichtes betreffenden heuristischen Gesichtspunkt, 1905.

[11] Niels Bohr. On the constitution of atoms and molecules. *Philos. Mag.*, 26(153):476–502, 1913.

[12] Erwin Schrödinger. Quantisierung als Eigenwertproblem. *Ann. Phys.*, 385(13):437–490, 1926.

[13] Werner Heisenberg. *Über quantentheoretische Umdeutung kinematischer und mechanischer Beziehungen*. Springer, 1985.

[14] Paul Adrien Maurice Dirac. *The principles of quantum mechanics*. Number 27. Oxford University Press, 1981.

[15] John Bardeen, Leon N Cooper, and John Robert Schrieffer. Theory of superconductivity. *Phys. Rev.*, 108(5):1175, 1957.

[16] Charles H Townes and Arthur L Schawlow. *Microwave Spectrosc.* Courier Corporation, 2013.

[17] Paul C Lauterbur. Image formation by induced local interactions: examples employing nuclear magnetic resonance. *Nature*, 242(5394):190–191, 1973.

[18] Peter W. Shor. Algorithms for quantum computation: Discrete logarithms and factoring. In *Proc. 35th Annu. Symp. Found. Comput. Sci.*, pages 124–134. IEEE, 1994.

[19] Iulia M. Georgescu, Sahel Ashhab, and Franco Nori. Quantum simulation. *Rev. Mod. Phys.*, 86(1):153–185, 2014.

[20] Yudong Cao, Jhonathan Romero, and Alán Aspuru-Guzik. Potential of quantum computing for drug discovery. *IBM J. Res. Dev.*, 62(6):6–1, 2018.

[21] Markus Reiher, Nathan Wiebe, Krysta M Svore, Dave Wecker, and Matthias Troyer. Elucidating reaction mechanisms on quantum computers. *Proc. Natl. Acad. Sci.*, 114(29):7555–7560, 2017.

[22] Frank Arute, Kunal Arya, Ryan Babbush, Dave Bacon, Joseph C Bardin, Rami Barends, Rupak Biswas, Sergio Boixo, Fernando GSL Brandao, David A Buell, et al. Quantum supremacy using a programmable superconducting processor. *Nature*, 574(7779):505–510, 2019.

[23] Barbara M Terhal. Quantum error correction for quantum memories. *Rev. Mod. Phys.*, 87(2):307–346, 2015.

[24] A Yu Kitaev. Fault-tolerant quantum computation by anyons. *Ann. Phys.*, 303(1):2–30, 2003.

[25] Steffen J Glaser, Ugo Boscain, Tommaso Calarco, Christiane P Koch, Walter Köckenberger, Ronnie Kosloff, Ilya Kuprov, Burkhard Luy, Sophie Schirmer, Thomas Schulte-Herbrüggen, et al. Training Schrödinger's cat: Quantum optimal control: Strategic report on current status, visions and goals for research in europe. *Eur. Phys. J. D*, 69:1–24, 2015.

[26] Navin Khaneja, Timo Reiss, Cindie Kehlet, Thomas Schulte-Herbrüggen, and Steffen J Glaser. Optimal control of coupled spin dynamics: design of NMR pulse sequences by gradient ascent algorithms. *J. Magn. Reson.*, 172(2):296–305, 2005.

[27] A del Campo and MG Boshier. Shortcuts to adiabaticity in a time-dependent box. *Sci. Rep.*, 2(1):648, 2012.

[28] RB Blakestad, C Ospelkaus, AP VanDevender, JM Amini, Joseph Britton, Dietrich Leibfried, and David J Wineland. High-fidelity transport of trapped-ion qubits through an x-junction trap array. *Phys. Rev. Lett.*, 102(15):153002, 2009.

[29] Max Werninghaus, Daniel J Egger, Federico Roy, Shai Machnes, Frank K Wilhelm, and Stefan Filipp. Leakage reduction in fast superconducting qubit gates via optimal control. *npj Quantum Inf.*, 7(1):14, 2021.

[30] Jianwei Wang, Fabio Sciarrino, Anthony Laing, and Mark G Thompson. Integrated photonic quantum technologies. *Nat. Photon.*, 14(5):273–284, 2020.

[31] Juan I Cirac and Peter Zoller. Quantum computations with cold trapped ions. *Phys. Rev. Lett.*, 74(20):4091, 1995.

[32] Christopher J Ballance, Thomas P Harty, Nobert M Linke, Martin A Sepiol, and David M Lucas. High-fidelity quantum logic gates using trapped-ion hyperfine qubits. *Phys. Rev. Lett.*, 117(6):060504, 2016.

[33] Benjamin Harper, Behnam Tonekaboni, Bahar Goldozian, Martin Sevior, and Muhammad Usman. Crosstalk attacks and defence in a shared quantum computing environment. *arXiv preprint arXiv:2402.02753*, 2024.

[34] Peng Zhao, Kehuan Linghu, Zhiyuan Li, Peng Xu, Ruixia Wang, Guangming Xue, Yirong Jin, and Haifeng Yu. Quantum crosstalk analysis for simultaneous gate operations on superconducting qubits. *PRX Quantum*, 3(2):020301, 2022.

[35] Werner Heisenberg. Physics and philosophy. 1958.

[36] Marc-Olivier Renou, David Trillo, Mirjam Weilenmann, Thinh P. Le, Armin Tavakoli, Nicolas Gisin, Antonio Acín, and Miguel Navascués. Quantum theory based on real numbers can be experimentally falsified. *Nature*, 600(7890):625–629, 2021.

[37] Nicolas Brunner, Daniel Cavalcanti, Stefano Pironio, Valerio Scarani, and Stephanie Wehner. Bell nonlocality. *Rev. Mod. Phys.*, 86(2):419–478, 2014.

[38] Angelo Bassi, Kinjalk Lochan, Seema Satin, Tejinder P. Singh, and Hendrik Ulbricht. Models of wave-function collapse, underlying theories, and experimental tests. *Rev. Mod. Phys.*, 85(2):471–527, 2013.

[39] Daniel A. Lidar. Lecture notes on the theory of open quantum systems. *arXiv preprint arXiv:1902.00967*, 2019.

[40] Jun John Sakurai and Jim Napolitano. *Modern Quantum Mechanics*. Cambridge University Press, 2020.

[41] Mario Argeri, Stefano Di Vita, Pierpaolo Mastrolia, Edoardo Mirabella, Johannes Schlenk, Ulrich Schubert, and Lorenzo Tancredi. Magnus and Dyson series for master integrals. *J. High Energy Phys.*, 2014(3):1–32, 2014.

[42] Sergio Blanes, Fernando Casas, Jose-Angel Oteo, and José Ros. The Magnus expansion and some of its applications. *Phys. Rep.*, 470(5-6):151–238, 2009.

[43] Ralph M Wilcox. Exponential operators and parameter differentiation in quantum physics. *J. Math. Phys.*, 8(4):962–982, 1967.

[44] Heinz-Peter Breuer and Francesco Petruccione. *The theory of open quantum systems*. OUP Oxford, 2002.

[45] Fima C Klebaner. *Introduction to stochastic calculus with applications*. World Scientific Publishing Company, 2012.

[46] Kalyanapuram R Parthasarathy. *An introduction to quantum stochastic calculus*. Springer Science & Business Media, 2012.

[47] Jakob Schwichtenberg. *Physics from Symmetry*. Springer, 2018.

[48] David John Simms. *Lie Groups and Quantum Mechanics*, volume 52. Springer, 1968.

[49] Alexander A. Kirillov. *An Introduction to Lie Groups and Lie Algebras*, volume 113. Cambridge University Press, 2008.

[50] Richard Feynman. The character of physical law (1965). *Cox and Wyman Ltd., London*, 1967.

[51] Domenico d'Alessandro. *Introduction to Quantum Control and Dynamics*. CRC Press, 2021.

[52] Daoyi Dong and Ian R. Petersen. Quantum control theory and applications: A survey. *IET Control Theory Appl.*, 4(12):2651–2671, 2010.

[53] Michael A Nielsen and Isaac L Chuang. *Quantum computation and quantum information*. Cambridge university Press, 2010.

[54] Vittorio Giovannetti, Seth Lloyd, and Lorenzo Maccone. Advances in quantum metrology. *Nat. Photon.*, 5(4):222–229, 2011.

[55] Constantin Brif, Raj Chakrabarti, and Herschel Rabitz. Control of quantum phenomena: past, present and future. *New J. Phys.*, 12(7):075008, 2010.

[56] Viswanath Ramakrishna, Murti V Salapaka, Mohammed Dahleh, Herschel Rabitz, and Anthony Peirce. Controllability of molecular systems. *Phys. Rev. A*, 51(2):960, 1995.

[57] J Werschnik and EKU Gross. Quantum optimal control theory. *J. Phys. B*, 40(18):R175, 2007.

[58] John A Nelder and Roger Mead. A simplex method for function minimization. *Comput. J.*, 7(4):308–313, 1965.

[59] Michael JD Powell. An efficient method for finding the minimum of a function of several variables without calculating derivatives. *Comput. J.*, 7(2):155–162, 1964.

[60] Mohammad Reza Bonyadi and Zbigniew Michalewicz. Particle swarm optimization for single objective continuous space problems: a review. *Evol. Comput.*, 25(1):1–54, 2017.

[61] W Keith Hastings. Monte Carlo sampling methods using Markov chains and their applications. 1970.

[62] Rainer Storn and Kenneth Price. Differential evolution–a simple and efficient heuristic for global optimization over continuous spaces. *J. Global Optim.*, 11:341–359, 1997.

[63] Patrick Doria, Tommaso Calarco, and Simone Montangero. Optimal control technique for many-body quantum dynamics. *Phys. Rev. Lett.*, 106(19):190501, 2011.

[64] Shlomo E Sklarz and David J Tannor. Loading a bose-einstein condensate onto an optical lattice: An application of optimal control theory to the nonlinear Schrödinger equation. *Phys. Rev. A*, 66(5):053619, 2002.

[65] Oak Ridge Leadership Computing Facility. Frontier supercomputer. https://www.olcf.ornl.gov/olcf-resources/compute-systems/frontier/, 2025. Accessed: 2025-01-28.

[66] Fujitsu. Fugaku supercomputer. https://www.fujitsu.com/global/about/innovation/fugaku/, 2025. Accessed: 2025-01-28.

[67] Giuseppe Carleo and Matthias Troyer. Solving the quantum many-body problem with artificial neural networks. *Science*, 355(6325):602–606, 2017.

[68] Iulia Buluta and Franco Nori. Quantum simulators. *Science*, 326(5949):108–111, 2009.

[69] Abhinav Kandala, Kristan Temme, Antonio D Córcoles, Antonio Mezzacapo, Jerry M Chow, and Jay M Gambetta. Error mitigation extends the computational reach of a noisy quantum processor. *Nature*, 567(7749):491–495, 2019.

[70] Seth Lloyd. Universal quantum simulators. *Science*, 273(5278):1073–1078, 1996.

[71] Anmer Daskin and Sabre Kais. Decomposition of unitary matrices for finding quantum circuits: application to molecular Hamiltonians. *J. Chem. Phys.*, 134(14), 2011.

[72] Andrew M. Childs, Yuan Su, Minh C. Tran, Nathan Wiebe, and Shuchen Zhu. Theory of trotter error with commutator scaling. *Phys. Rev. X*, 11(1):011020, 2021.

[73] Rene Gerritsma, Gerhard Kirchmair, Florian Zähringer, E Solano, R Blatt, and CF Roos. Quantum simulation of the Dirac equation. *Nature*, 463(7277):68–71, 2010.

[74] Francesco Petiziol, Sandro Wimberger, André Eckardt, and Florian Mintert. Non-perturbative floquet engineering of the toric-code hamiltonian and its ground state. *Phys. Rev. B*, 109(7):075126, 2024.

[75] Anders Sørensen and Klaus Mølmer. Quantum computation with ions in thermal motion. *Phys. Rev. Lett.*, 82(9):1971, 1999.

[76] J Ignacio Cirac, David Perez-Garcia, Norbert Schuch, and Frank Verstraete. Matrix product states and projected entangled pair states: Concepts, symmetries, theorems. *Rev. Mod. Phys.*, 93(4):045003, 2021.

[77] Román Orús. A practical introduction to tensor networks: Matrix product states and projected entangled pair states. *Ann. Phys.*, 349:117–158, 2014.

[78] Daniel Gottesman. *Stabilizer codes and quantum error correction*. California Institute of Technology, 1997.

[79] Tameem Albash and Daniel A Lidar. Adiabatic quantum computation. *Rev. Mod. Phys.*, 90(1):015002, 2018.

[80] H Ralph Lewis Jr and WB Riesenfeld. An exact quantum theory of the time-dependent harmonic oscillator and of a charged particle in a time-dependent electromagnetic field. *J. Math. Phys.*, 10(8):1458–1473, 1969.

[81] RS Kaushal and SC Mishra. Dynamical algebraic approach and invariants for time-dependent hamiltonian systems in two dimensions. *J. Math. Phys.*, 34(12):5843–5850, 1993.

[82] H.J. Korsch. Dynamical invariants and time-dependent harmonic systems. *Phys. Lett. A*, 74(5):294–296, 1979.

[83] Xi Chen, A Ruschhaupt, Sebastian Schmidt, Adolfo del Campo, David Guéry-Odelin, and J Gonzalo Muga. Fast optimal frictionless atom cooling in harmonic traps: Shortcut to adiabaticity. *Phys. Rev. Lett.*, 104(6):063002, 2010.

[84] E Torrontegui, S Ibáñez, Xi Chen, A Ruschhaupt, D Guéry-Odelin, and JG Muga. Fast atomic transport without vibrational heating. *Phys. Rev. A*, 83(1):013415, 2011.

[85] Selwyn Simsek and Florian Mintert. Quantum control with a multi-dimensional gaussian quantum invariant. *Quantum*, 5:409, 2021.

[86] Richard P. Feynman. Simulating physics with computers. In *Feynman and Computation*, pages 133–153. CRC Press, 2018.

[87] Vasileios Mavroeidis, Kamer Vishi, Mateusz D. Zych, and Audun Jøsang. The impact of quantum computing on present cryptography. *arXiv preprint arXiv:1804.00200*, 2018.

[88] Lov K. Grover. A fast quantum mechanical algorithm for database search. In *Proc. 28th Annu. ACM Symp. Theory Comput.*, pages 212–219, 1996.

[89] Michel H. Devoret and Robert J. Schoelkopf. Superconducting circuits for quantum information: An outlook. *Science*, 339(6124):1169–1174, 2013.

[90] H. Jeff Kimble. The quantum internet. *Nature*, 453(7198):1023–1030, 2008.

[91] Sankar Das Sarma, Michael Freedman, and Chetan Nayak. Majorana zero modes and topological quantum computation. *npj Quantum Inf.*, 1(1):1–13, 2015.

[92] Mark Saffman, Thad G Walker, and Klaus Mølmer. Quantum information with rydberg atoms. *Rev. Mod. Phys.*, 82(3):2313–2363, 2010.

[93] Christopher Monroe and Jungsang Kim. Scaling the ion trap quantum processor. *Science*, 339(6124):1164–1169, 2013.

[94] Hartmut Häffner, Christian F Roos, and Rainer Blatt. Quantum computing with trapped ions. *Phys. Rep.*, 469(4):155–203, 2008.

[95] TP Harty, DTC Allcock, CJ Ballance, L Guidoni, HA Janacek, NM Linke, DN Stacey, and DM Lucas. High-fidelity preparation, gates, memory, and readout of a trapped-ion quantum bit. *Phys. Rev. Lett.*, 113(22):220501, 2014.

[96] Colin D. Bruzewicz, John Chiaverini, Robert McConnell, and Jeremy M. Sage. Trapped-ion quantum computing: Progress and challenges. *Appl. Phys. Rev.*, 6(2), 2019.

[97] John Preskill. Quantum computing in the NISQ era and beyond. *Quantum*, 2:79, 2018.

[98] Philip Krantz, Morten Kjaergaard, Fei Yan, Terry P Orlando, Simon Gustavsson, and William D Oliver. A quantum engineer's guide to superconducting qubits. *Appl. Phys. Rev.*, 6(2), 2019.

[99] Terry Rudolph. Why I am optimistic about the silicon-photonic route to quantum computing. *APL photonics*, 2(3), 2017.

[100] C Langer, R Ozeri, John D Jost, J Chiaverini, B DeMarco, A Ben-Kish, RB Blakestad, Joseph Britton, DB Hume, Wayne M Itano, et al. Long-lived qubit memory using atomic ions. *Phys. Rev. Lett.*, 95(6):060502, 2005.

[101] Iulia Georgescu. The DiVincenzo criteria 20 years on. *Nat. Rev. Phys.*, 2(12):666–666, 2020.

[102] Morten Kjaergaard, Mollie E Schwartz, Jochen Braumüller, Philip Krantz, Joel I-J Wang, Simon Gustavsson, and William D Oliver. Superconducting qubits: Current state of play. *Annu. Rev. Condens. Matter Phys.*, 11(1):369–395, 2020.

[103] Dietrich Leibfried, Brian DeMarco, Volker Meyer, David Lucas, Murray Barrett, Joe Britton, Wayne M. Itano, B. Jelenković, Chris Langer, Till Rosenband, et al. Experimental demonstration of a robust, high-fidelity geometric two ion-qubit phase gate. *Nature*, 422(6930):412–415, 2003.

[104] Daniel Loss and David P DiVincenzo. Quantum computation with quantum dots. *Phys. Rev. A*, 57(1):120, 1998.

[105] AH Myerson, DJ Szwer, SC Webster, DTC Allcock, MJ Curtis, G Imreh, JA Sherman, DN Stacey, AM Steane, and DM Lucas. High-fidelity readout of trapped-ion qubits. *Phys. Rev. Lett.*, 100(20):200502, 2008.

[106] Philipp Schindler, Daniel Nigg, Thomas Monz, Julio T Barreiro, Esteban Martinez, Shannon X Wang, Stephan Quint, Matthias F Brandl, Volckmar Nebendahl, Christian F Roos, et al. A quantum information processor with trapped ions. *New J. Phys.*, 15(12):123012, 2013.

[107] Rachel Noek, Geert Vrijsen, Daniel Gaultney, Emily Mount, Taehyun Kim, Peter Maunz, and Jungsang Kim. High speed, high fidelity detection of an atomic hyperfine qubit. *Opt. Lett.*, 38(22):4735–4738, 2013.

[108] Juan M Pino, Jennifer M Dreiling, Caroline Figgatt, John P Gaebler, Steven A Moses, MS Allman, CH Baldwin, Michael Foss-Feig, David Hayes, Karl Mayer, et al. Demonstration of the trapped-ion quantum ccd computer architecture. *Nature*, 592(7853):209–213, 2021.

[109] Karan K Mehta, Colin D Bruzewicz, Robert McConnell, Rajeev J Ram, Jeremy M Sage, and John Chiaverini. Integrated optical addressing of an ion qubit. *Nat. Nanotechnol.*, 11(12):1066–1070, 2016.

[110] Dolev Bluvstein, Simon J Evered, Alexandra A Geim, Sophie H Li, Hengyun Zhou, Tom Manovitz, Sepehr Ebadi, Madelyn Cain, Marcin Kalinowski, Dominik Hangleiter, et al. Logical quantum processor based on reconfigurable atom arrays. *Nature*, 626(7997):58–65, 2024.

[111] David J Griffiths. *Introduction to electrodynamics*. Cambridge University Press, 2023.

[112] Lowell S. Brown and Gerald Gabrielse. Geonium theory: Physics of a single electron or ion in a penning trap. *Rev. Mod. Phys.*, 58(1):233, 1986.

[113] G. Gabrielse, L. Haarsma, and S. L. Rolston. Open-endcap penning traps for high-precision experiments. *Int. J. Mass Spectrom. Ion Process.*, 88(2-3):319–332, 1989.

[114] Ralph F. Wuerker, Haywood Shelton, and R. V. Langmuir. Electrodynamic containment of charged particles. *J. Appl. Phys.*, 30(3):342–349, 1959.

[115] Dietrich Leibfried, Rainer Blatt, Christopher Monroe, and David Wineland. Quantum dynamics of single trapped ions. *Rev. Mod. Phys.*, 75(1):281, 2003.

[116] M. G. Raizen, J. M. Gilligan, James C. Bergquist, Wayne M. Itano, and David J. Wineland. Ionic crystals in a linear Paul trap. *Phys. Rev. A*, 45(9):6493, 1992.

[117] Lawrence Ruby. Applications of the Mathieu equation. *Am. J. Phys.*, 64(1):39–44, 1996.

[118] H. Landa, M. Drewsen, B. Reznik, and A. Retzker. Classical and quantum modes of coupled Mathieu equations. *J. Phys. A*, 45(45):455305, 2012.

[119] Hans G. Dehmelt. Radiofrequency spectroscopy of stored ions I: Storage. In *Adv. At. Mol. Phys.*, volume 3, pages 53–72. Elsevier, 1968.

[120] Caroline Champenois. Dynamics and thermodynamics of trapped ions. *J. Phys. B*, 42(15):154002, 2009.

[121] Selwyn Simsek. *Control of Motional States of Trapped Ions with Quantum Invariants*. PhD thesis, Imperial College London, 2022.

[122] Jonathan P. Home, David Hanneke, John D. Jost, Dietrich Leibfried, and David J. Wineland. Normal modes of trapped ions in the presence of anharmonic trap potentials. *New J. Phys.*, 13(7):073026, 2011.

[123] Gilbert Grynberg, Alain Aspect, and Claude Fabre. *Introduction to Quantum Optics: From the Semi-Classical Approach to Quantized Light*. Cambridge University Press, 2010.

[124] Girish S. Agarwal. *Quantum Optics*. Cambridge University Press, 2012.

[125] Claude Cohen-Tannoudji, Jacques Dupont-Roc, and Gilbert Grynberg. *Atom-photon interactions: basic processes and applications*. John Wiley & Sons, 1998.

[126] Claude N Cohen-Tannoudji. Nobel lecture: Manipulating atoms with photons. *Rev. Mod. Phys.*, 70(3):707, 1998.

[127] Rodney Loudon. *The quantum theory of light*. OUP Oxford, 2000.

[128] Mark Fox. *Optical Properties of Solids*, volume 3. Oxford University Press, 2010.

[129] Florian Mintert and Christof Wunderlich. Ion-trap quantum logic using long-wavelength radiation. *Phys. Rev. Lett.*, 87(25):257904, 2001.

[130] Christian Ospelkaus, Christopher E Langer, Jason M Amini, Kenton R Brown, Dietrich Leibfried, and David J Wineland. Trapped-ion quantum logic gates based on oscillating magnetic fields. *Phys. Rev. Lett.*, 101(9):090502, 2008.

[131] S Weidt, J Randall, SC Webster, K Lake, AE Webb, I Cohen, T Navickas, B Lekitsch, A Retzker, and WK Hensinger. Trapped-ion quantum logic with global radiation fields. *Phys. Rev. Lett.*, 117(22):220501, 2016.

[132] Christiane P. Koch, Ugo Boscain, Tommaso Calarco, Gunther Dirr, Stefan Filipp, Steffen J. Glaser, Ronnie Kosloff, Simone Montangero, Thomas Schulte-Herbrüggen, Dominique Sugny, and Frank K. Wilhelm. Quantum optimal control in quantum technologies. Strategic report on current status, visions and goals for research in Europe. *EPJ Quantum Technol.*, 9(1):1–60, December 2022.

[133] Tomi H Johnson, Stephen R Clark, and Dieter Jaksch. What is a quantum simulator? *EPJ Quantum Technol.*, 1:1–12, 2014.

[134] David Marcos, Peter Rabl, Enrique Rico, and Peter Zoller. Superconducting circuits for quantum simulation of dynamical gauge fields. *Phys. Rev. Lett.*, 111(11):110504, 2013.

[135] Thaddeus D Ladd, Fedor Jelezko, Raymond Laflamme, Yasunobu Nakamura, Christopher Monroe, and Jeremy Lloyd O'Brien. Quantum computers. *Nature*, 464(7285):45–53, 2010.

[136] Mark Horowitz and Emily Grumbling. *Quantum computing: progress and prospects*. National Academies Press, 2019.

[137] Laszlo Gyongyosi and Sandor Imre. A survey on quantum computing technology. *Comput. Sci. Rev.*, 31:51–71, 2019.

[138] Youngseok Kim, Andrew Eddins, Sajant Anand, Ken Xuan Wei, Ewout Van Den Berg, Sami Rosenblatt, Hasan Nayfeh, Yantao Wu, Michael Zaletel, Kristan Temme, et al. Evidence for the utility of quantum computing before fault tolerance. *Nature*, 618(7965):500–505, 2023.

[139] Yulin Wu, Wan-Su Bao, Sirui Cao, Fusheng Chen, Ming-Cheng Chen, Xiawei Chen, Tung-Hsun Chung, Hui Deng, Yajie Du, Daojin Fan, et al. Strong quantum computational advantage using a superconducting quantum processor. *Phys. Rev. Lett.*, 127(18):180501, 2021.

[140] Han-Sen Zhong, Hui Wang, Yu-Hao Deng, Ming-Cheng Chen, Li-Chao Peng, Yi-Han Luo, Jian Qin, Dian Wu, Xing Ding, Yi Hu, et al. Quantum computational advantage using photons. *Science*, 370(6523):1460–1463, 2020.

[141] Lars S Madsen, Fabian Laudenbach, Mohsen Falamarzi Askarani, Fabien Rortais, Trevor Vincent, Jacob FF Bulmer, Filippo M Miatto, Leonhard Neuhaus, Lukas G Helt, Matthew J Collins, et al. Quantum computational advantage with a programmable photonic processor. *Nature*, 606(7912):75–81, 2022.

[142] Warren B Powell. *Approximate Dynamic Programming: Solving the curses of dimensionality*, volume 703. John Wiley & Sons, 2007.

[143] Andrew J Daley, Immanuel Bloch, Christian Kokail, Stuart Flannigan, Natalie Pearson, Matthias Troyer, and Peter Zoller. Practical quantum advantage in quantum simulation. *Nature*, 607(7920):667–676, 2022.

[144] Navin Khaneja, Timo Reiss, Cindie Kehlet, Thomas Schulte-Herbrüggen, and Steffen J. Glaser. Optimal control of coupled spin dynamics: design of NMR pulse sequences by gradient ascent algorithms. *J. Magn. Reson.*, 172(2):296–305, February 2005.

[145] T. Schulte-Herbrüggen, A. Spörl, N. Khaneja, and S. J. Glaser. Optimal control-based efficient synthesis of building blocks of quantum algorithms: A perspective from network complexity towards time complexity. *Phys. Rev. A*, 72(4):042331, October 2005.

[146] Wayne Jordan Chetcuti, Claudio Sanavio, Salvatore Lorenzo, and Tony J. G. Apollaro. Perturbative many-body transfer. *New J. Phys.*, 22(3):033030, March 2020.

[147] Daniel Burgarth, Koji Maruyama, Michael Murphy, Simone Montangero, Tommaso Calarco, Franco Nori, and Martin B. Plenio. Scalable quantum computation via local control of only two qubits. *Phys. Rev. A*, 81:040303, Apr 2010.

[148] N. H. Le, M. Cykiert, and E. Ginossar. Scalable and robust quantum computing on qubit arrays with fixed coupling. *npj Quantum Inf.*, 9(1):1–8, January 2023.

[149] Frank Verstraete, Valentin Murg, and J Ignacio Cirac. Matrix product states, projected entangled pair states, and variational renormalization group methods for quantum spin systems. *Adv. Phys.*, 57(2):143–224, 2008.

[150] Giuseppe Carleo and Matthias Troyer. Solving the quantum many-body problem with artificial neural networks. *Science*, 355(6325):602–606, February 2017.

[151] Scott Aaronson and Daniel Gottesman. Improved simulation of stabilizer circuits. *Phys. Rev. A*, 70(5):052328, November 2004.

[152] Robert Raussendorf, Daniel E Browne, and Hans J Briegel. Measurement-based quantum computation on cluster states. *Phys. Rev. A*, 68(2):022312, 2003.

[153] A.Yu. Kitaev. Fault-tolerant quantum computation by anyons. *Ann. Phys.*, 303(1):2–30, 2003.

[154] Michael A Levin and Xiao-Gang Wen. String-net condensation: A physical mechanism for topological phases. *Phys. Rev. B*, 71(4):045110, 2005.

[155] David Guéry-Odelin, Andreas Ruschhaupt, Anthony Kiely, Erik Torrontegui, Sofia Martínez-Garaot, and Juan Gonzalo Muga. Shortcuts to adiabaticity: Concepts, methods, and applications. *Rev. Mod. Phys.*, 91(4):045001, 2019.

[156] E. Torrontegui, S. Martínez-Garaot, and J. G. Muga. Hamiltonian engineering via invariants and dynamical algebra. *Phys. Rev. A*, 89(4):043408, April 2014.

[157] Selwyn Simsek and Florian Mintert. Quantum control with a multi-dimensional Gaussian quantum invariant. *Quantum*, 5:409, March 2021.

[158] Anthony P Peirce, Mohammed A Dahleh, and Herschel Rabitz. Optimal control of quantum-mechanical systems: Existence, numerical approximation, and applications. *Phys. Rev. A*, 37(12):4950, 1988.

[159] Francesco Iachello. *Lie algebras and applications*, volume 708. Springer, 2006.

[160] Robert B Laughlin. Anomalous quantum hall effect: an incompressible quantum fluid with fractionally charged excitations. *Phys. Rev. Lett.*, 50(18):1395, 1983.

[161] S. G. Schirmer, A. I. Solomon, and J. V. Leahy. Criteria for reachability of quantum states. *J. Phys. A: Math. Gen.*, 35(40):8551, September 2002.

[162] Martin Plesch and Časlav Brukner. Quantum-state preparation with universal gate decompositions. *Phys. Rev. A*, 83(3):032302, 2011.

[163] Edward Farhi, Jeffrey Goldstone, and Sam Gutmann. A quantum approximate optimization algorithm. *arXiv preprint arXiv:1411.4028*, 2014.

[164] Alexei Gilchrist, Nathan K. Langford, and Michael A. Nielsen. Distance measures to compare real and ideal quantum processes. *Phys. Rev. A*, 71:062310, Jun 2005.

[165] Sean Greenaway, Frédéric Sauvage, Kiran E. Khosla, and Florian Mintert. Efficient assessment of process fidelity. *Phys. Rev. Res.*, 3:033031, Jul 2021.

[166] Daniel M. Reich, Giulia Gualdi, and Christiane P. Koch. Minimum number of input states required for quantum gate characterization. *Phys. Rev. A*, 88:042309, Oct 2013.

[167] Michael Goerz, Daniel Basilewitsch, Fernando Gago-Encinas, Matthias G Krauss, Karl P Horn, Daniel M Reich, and Christiane Koch. Krotov: A Python implementation of Krotov's method for quantum optimal control. *SciPost Phys.*, 7(6):080, 2019.

[168] Glen Bigan Mbeng, Angelo Russomanno, and Giuseppe E Santoro. The quantum ising chain for beginners. *arXiv preprint arXiv:2009.09208*, 114, 2020.

[169] Christian L Degen, Friedemann Reinhard, and Paola Cappellaro. Quantum sensing. *Rev. Mod. Phys.*, 89(3):035002, 2017.

[170] Xing-Ri Jin, Xin Ji, Ying-Qiao Zhang, Shou Zhang, Suc-Kyoung Hong, Kyu-Hwang Yeon, and Chung-In Um. Three-party quantum secure direct communication based on GHZ states. *Phys. Lett. A*, 354(1-2):67–70, 2006.

[171] Mark Hillery, Vladimír Bužek, and André Berthiaume. Quantum secret sharing. *Phys. Rev. A*, 59(3):1829, 1999.

[172] F Fröwis and W Dür. Stable macroscopic quantum superpositions. *Phys. Rev. Lett.*, 106(11):110402, 2011.

[173] Ahmed Omran, Harry Levine, Alexander Keesling, Giulia Semeghini, Tout T Wang, Sepehr Ebadi, Hannes Bernien, Alexander S Zibrov, Hannes Pichler, Soonwon Choi, et al. Generation and manipulation of Schrödinger cat states in Rydberg atom arrays. *Science*, 365(6453):570–574, 2019.

[174] Chao Song, Kai Xu, Hekang Li, Yu-Ran Zhang, Xu Zhang, Wuxin Liu, Qiujiang Guo, Zhen Wang, Wenhui Ren, Jie Hao, et al. Generation of multicomponent atomic Schrödinger cat states of up to 20 qubits. *Science*, 365(6453):574–577, 2019.

[175] Michael A Nielsen. Cluster-state quantum computation. *Rep. Math. Phys.*, 57(1):147–161, 2006.

[176] Kishor Bharti, Alba Cervera-Lierta, Thi Ha Kyaw, Tobias Haug, Sumner Alperin-Lea, Abhinav Anand, Matthias Degroote, Hermanni Heimonen, Jakob S. Kottmann, Tim Menke, Wai-Keong Mok, Sukin Sim, Leong-Chuan Kwek, and Alán Aspuru-Guzik. Noisy intermediate-scale quantum algorithms. *Rev. Mod. Phys.*, 94(1):015004, February 2022.

[177] Michael P. Zaletel, Roger S. K. Mong, Christoph Karrasch, Joel E. Moore, and Frank Pollmann. Time-evolving a matrix product state with long-ranged interactions. *Phys. Rev. B*, 91(16):165112, April 2015.

[178] Johannes Hauschild and Frank Pollmann. Efficient numerical simulations with tensor networks: Tensor Network Python (TeNPy). *SciPost Phys. Lect. Notes*, page 5, 2018. Code available from https://github.com/tenpy/tenpy.

[179] Sebastian Deffner and Steve Campbell. Quantum speed limits: from Heisenberg's uncertainty principle to optimal quantum control. *J. Phys. A: Math. Gen.*, 50(45):453001, 2017.

[180] Data for Orozco-Ruiz et al. "Quantum control without quantum states", 2024. DOI: 10.5281/zenodo.8298203.

[181] David Joseph, Adam Callison, Cong Ling, and Florian Mintert. Two quantum ising algorithms for the shortest-vector problem. *Phys. Rev. A*, 103:032433, Mar 2021.

[182] Tad Hogg. Adiabatic quantum computing for random satisfiability problems. *Phys. Rev. A*, 67(2):022314, 2003.

[183] N. Goldman and J. Dalibard. Periodically driven quantum systems: Effective Hamiltonians and engineered gauge fields. *Phys. Rev. X*, 4:031027, Aug 2014.

[184] André Eckardt and Egidijus Anisimovas. High-frequency approximation for periodically driven quantum systems from a floquet-space perspective. *New J. Phys.*, 17(9):093039, sep 2015.

[185] Ady Stern and Netanel H Lindner. Topological quantum computation—from basic concepts to first experiments. *Science*, 339(6124):1179–1184, 2013.

[186] Adam Paetznick, Christina Knapp, Nicolas Delfosse, Bela Bauer, Jeongwan Haah, Matthew B Hastings, and Marcus P da Silva. Performance of planar Floquet codes with Majorana-based qubits. *PRX Quantum*, 4(1):010310, 2023.

[187] Craig Gidney, Michael Newman, Austin Fowler, and Michael Broughton. A fault-tolerant honeycomb memory. *Quantum*, 5:605, 2021.

[188] Basudha Srivastava, Anton Frisk Kockum, and Mats Granath. The XYZ^2 hexagonal stabilizer code. *Quantum*, 6:698, 2022.

[189] Takanori Maehara and Kazuo Murota. Algorithm for error-controlled simultaneous block-diagonalization of matrices. *SIAM J. Matrix Anal. Appl.*, 32(2):605–620, 2011.

[190] Pieter W Claeys, Mohit Pandey, Dries Sels, and Anatoli Polkovnikov. Floquet-engineering counterdiabatic protocols in quantum many-body systems. *Phys. Rev. Lett.*, 123(9):090602, 2019.

[191] Paul Manuel Schindler and Marin Bukov. Counterdiabatic driving for periodically driven systems. *arXiv preprint arXiv:2310.02728*, 2023.

[192] Jiahao Yao, Lin Lin, and Marin Bukov. Reinforcement learning for many-body ground-state preparation inspired by counterdiabatic driving. *Phys. Rev. X*, 11(3):031070, 2021.

[193] Ieva Čepaitė, Anatoli Polkovnikov, Andrew J Daley, and Callum W Duncan. Counterdiabatic optimized local driving. *PRX Quantum*, 4(1):010312, 2023.

[194] Albert Verdeny, Łukasz Rudnicki, Cord A Müller, and Florian Mintert. Optimal control of effective Hamiltonians. *Phys. Rev. Lett.*, 113(1):010501, 2014.

[195] Albert Verdeny, Joaquim Puig, and Florian Mintert. Quasi-periodically driven quantum systems. *Z. Naturforsch. A*, 71(10):897–907, 2016.

[196] Mogens Dalgaard and Felix Motzoi. Fast, high precision dynamics in quantum optimal control theory. *J. Phys. B: At. Mol. Opt. Phys.*, 55(8):085501, 2022.

[197] Shai Machnes, Elie Assémat, David Tannor, and Frank K Wilhelm. Tunable, flexible, and efficient optimization of control pulses for practical qubits. *Phys. Rev. Lett.*, 120(15):150401, 2018.

[198] Göran Wendin. Quantum information processing with superconducting circuits: a review. *Rep. Prog. Phys.*, 80(10):106001, 2017.

[199] Sepehr Ebadi, Tout T Wang, Harry Levine, Alexander Keesling, Giulia Semeghini, Ahmed Omran, Dolev Bluvstein, Rhine Samajdar, Hannes Pichler, Wen Wei Ho,

et al. Quantum phases of matter on a 256-atom programmable quantum simulator. *Nature*, 595(7866):227–232, 2021.

[200] Jose Carrasco, Andreas Elben, Christian Kokail, Barbara Kraus, and Peter Zoller. Theoretical and Experimental Perspectives of Quantum Verification. *PRX Quantum*, 2(1):010102, March 2021.

[201] David G Cory, M. D. Price, W Maas, Emanuel Knill, Raymond Laflamme, Wojciech H Zurek, Timothy F Havel, and Shyamal S Somaroo. Experimental quantum error correction. *Phys. Rev. Lett.*, 81(10):2152, 1998.

[202] John Chiaverini, Dietrich Leibfried, Tobias Schaetz, Murray D Barrett, RB Blakestad, Joseph Britton, Wayne M Itano, John D Jost, Emanuel Knill, Christopher Langer, et al. Realization of quantum error correction. *Nature*, 432(7017):602–605, 2004.

[203] Frederic Sauvage and Florian Mintert. Optimal quantum control with poor statistics. *PRX Quantum*, 1(2):020322, 2020.

[204] Christopher Monroe, Robert Raussendorf, Alex Ruthven, Kenneth R Brown, Peter Maunz, L-M Duan, and Jungsang Kim. Large-scale modular quantum-computer architecture with atomic memory and photonic interconnects. *Phys. Rev. A*, 89(2):022317, 2014.

[205] Bjoern Lekitsch, Sebastian Weidt, Austin G Fowler, Klaus Mølmer, Simon J Devitt, Christof Wunderlich, and Winfried K Hensinger. Blueprint for a microwave trapped ion quantum computer. *Sci. Adv.*, 3(2):e1601540, 2017.

[206] G-D Lin, S-L Zhu, Rajibul Islam, Kihwan Kim, M-S Chang, Simcha Korenblit, Christopher Monroe, and L-M Duan. Large-scale quantum computation in an anharmonic linear ion trap. *Europhys. Lett.*, 86(6):60004, 2009.

[207] Joseph W Britton, Brian C Sawyer, Adam C Keith, C-C Joseph Wang, James K Freericks, Hermann Uys, Michael J Biercuk, and John J Bollinger. Engineered two-dimensional ising interactions in a trapped-ion quantum simulator with hundreds of spins. *Nature*, 484(7395):489–492, 2012.

[208] DTC Allcock, JA Sherman, DN Stacey, AH Burrell, MJ Curtis, G Imreh, NM Linke, DJ Szwer, SC Webster, AM Steane, et al. Implementation of a symmetric surface-electrode ion trap with field compensation using a modulated Raman effect. *New J. Phys.*, 12(5):053026, 2010.

[209] David J Wineland, Christopher Monroe, Wayne M Itano, Dietrich Leibfried, Brian E King, and Dawn M Meekhof. Experimental issues in coherent quantum-state manipulation of trapped atomic ions. *J. Res. Natl. Inst. Stand. Technol.*, 103(3):259, 1998.

[210] Quentin A Turchette, BE King, D Leibfried, DM Meekhof, CJ Myatt, MA Rowe, CA Sackett, CS Wood, WM Itano, C Monroe, et al. Heating of trapped ions from the quantum ground state. *Phys. Rev. A*, 61(6):063418, 2000.

[211] Ryan Bowler, John Gaebler, Yiheng Lin, Ting Rei Tan, David Hanneke, John D Jost, JP Home, Dietrich Leibfried, and David J Wineland. Coherent diabatic ion transport and separation in a multizone trap array. *Phys. Rev. Lett.*, 109(8):080502, 2012.

[212] H. Ralph Lewis Jr. Classical and quantum systems with time-dependent harmonic-oscillator-type Hamiltonians. *Phys. Rev. Lett.*, 18(13):510, 1967.

[213] J-F Schaff, X-L Song, Pablo Capuzzi, Patrizia Vignolo, and Guillaume Labeyrie. Shortcut to adiabaticity for an interacting Bose-Einstein condensate. *EPL*, 93(2):23001, 2011.

[214] Jing Li, Xi Chen, and Andreas Ruschhaupt. Fast transport of Bose–Einstein condensates in anharmonic traps. *Philos. Trans. R. Soc. A*, 380(2239):20210280, 2022.

[215] Chris Whitty, Anthony Kiely, and Andreas Ruschhaupt. Robustness of enhanced shortcuts to adiabaticity in lattice transport. *Phys. Rev. A*, 105(1):013311, 2022.

[216] Christiane P Koch, Ugo Boscain, Tommaso Calarco, Gunther Dirr, Stefan Filipp, Steffen J Glaser, Ronnie Kosloff, Simone Montangero, Thomas Schulte-Herbrüggen, Dominique Sugny, et al. Quantum optimal control in quantum technologies. Strategic report on current status, visions and goals for research in Europe. *EPJ Quant. Technol.*, 9(1):19, 2022.

[217] George T Gilbert. Positive definite matrices and Sylvester's criterion. *Am. Math. Mon.*, 98(1):44–46, 1991.

[218] John Preskill. Quantum computing and the entanglement frontier. *arXiv preprint arXiv:1203.5813*, 2012.

[219] Sukhpal Singh Gill, Adarsh Kumar, Harvinder Singh, Manmeet Singh, Kamalpreet Kaur, Muhammad Usman, and Rajkumar Buyya. Quantum computing: A taxonomy, systematic review and future directions. *Softw. Pract. Exper.*, 52(1):66–114, 2022.

[220] Antonio D Córcoles, Abhinav Kandala, Ali Javadi-Abhari, Douglas T McClure, Andrew W Cross, Kristan Temme, Paul D Nation, Matthias Steffen, and Jay M Gambetta. Challenges and opportunities of near-term quantum computing systems. *Proc. IEEE*, 108(8):1338–1352, 2019.

[221] Simone Montangero, Tommaso Calarco, and Rosario Fazio. Robust optimal quantum gates for Josephson charge qubits. *Phys. Rev. Lett.*, 99(17):170501, 2007.

[222] Felix Motzoi, Jay M Gambetta, Patrick Rebentrost, and Frank K Wilhelm. Simple pulses for elimination of leakage in weakly nonlinear qubits. *Phys. Rev. Lett.*, 103(11):110501, 2009.

[223] Yuri Alexeev, Dave Bacon, Kenneth R Brown, Robert Calderbank, Lincoln D Carr, Frederic T Chong, Brian DeMarco, Dirk Englund, Edward Farhi, Bill Fefferman, et al. Quantum computer systems for scientific discovery. *PRX Quantum*, 2(1):017001, 2021.

[224] Pablo M Poggi, Gabriele De Chiara, Steve Campbell, and Anthony Kiely. Universally robust quantum control. *Phys. Rev. Lett.*, 132(19):193801, 2024.

[225] Anupam Mitra, Michael J Martin, Grant W Biedermann, Alberto M Marino, Pablo M Poggi, and Ivan H Deutsch. Robust Mølmer-Sørensen gate for neutral atoms using rapid adiabatic Rydberg dressing. *Phys. Rev. A*, 101(3):030301, 2020.

[226] John P Gaebler, Ting Rei Tan, Yiheng Lin, Y Wan, Ryan Bowler, Adam C Keith, Scott Glancy, Kevin Coakley, Emanuel Knill, Dietrich Leibfried, et al. High-fidelity universal gate set for $^{9}Be^{+}$ ion qubits. *Phys. Rev. Lett.*, 117(6):060505, 2016.

[227] TP Harty, MA Sepiol, DTC Allcock, CJ Ballance, JE Tarlton, and DM Lucas. High-fidelity trapped-ion quantum logic using near-field microwaves. *Phys. Rev. Lett.*, 117(14):140501, 2016.

[228] Jan Benhelm, Gerhard Kirchmair, Christian F Roos, and Rainer Blatt. Towards fault-tolerant quantum computing with trapped ions. *Nat. Phys.*, 4(6):463–466, 2008.

[229] Joseph Aidan Delf Randall. *High-fidelity entanglement of trapped ions using long-wavelength radiation*. PhD thesis, Imperial College London, 2015.

[230] CH Valahu, Iason Apostolatos, Sebastien Weidt, and WK Hensinger. Quantum control methods for robust entanglement of trapped ions. *J. Phys. B: At. Mol. Opt. Phys.*, 55(20):204003, 2022.

[231] Farhang Haddadfarshi and Florian Mintert. High fidelity quantum gates of trapped ions in the presence of motional heating. *New J. Phys.*, 18(12):123007, 2016.

[232] VM Schäfer, CJ Ballance, K Thirumalai, LJ Stephenson, TG Ballance, AM Steane, and DM Lucas. Fast quantum logic gates with trapped-ion qubits. *Nature*, 555(7694):75–78, 2018.

[233] Taeyoung Choi, Shantanu Debnath, TA Manning, Caroline Figgatt, Z-X Gong, L-M Duan, and Christopher Monroe. Optimal quantum control of multimode couplings between trapped ion qubits for scalable entanglement. *Phys. Rev. Lett.*, 112(19):190502, 2014.

[234] Yao Lu, Shuaining Zhang, Kuan Zhang, Wentao Chen, Yangchao Shen, Jialiang Zhang, Jing-Ning Zhang, and Kihwan Kim. Global entangling gates on arbitrary ion qubits. *Nature*, 572(7769):363–367, 2019.

[235] Hartmut Häffner, Wolfgang Hänsel, CF Roos, Jan Benhelm, D Chek-al Kar, M Chwalla, T Körber, UD Rapol, M Riebe, PO Schmidt, et al. Scalable multiparticle entanglement of trapped ions. *Nature*, 438(7068):643–646, 2005.

[236] Kihwan Kim, M-S Chang, Rajibul Islam, Simcha Korenblit, L-M Duan, and Christopher Monroe. Entanglement and tunable spin-spin couplings between trapped ions using multiple transverse modes. *Phys. Rev. Lett.*, 103(12):120502, 2009.

[237] Kevin A Landsman, Yukai Wu, Pak Hong Leung, Daiwei Zhu, Norbert M Linke, Kenneth R Brown, Luming Duan, and Christopher Monroe. Two-qubit entangling gates within arbitrarily long chains of trapped ions. *Phys. Rev. A*, 100(2):022332, 2019.

[238] G Zarantonello, H Hahn, J Morgner, M Schulte, A Bautista-Salvador, RF Werner, K Hammerer, and C Ospelkaus. Robust and resource-efficient microwave near-field entangling $^9Be^+$ gate. *Phys. Rev. Lett.*, 123(26):260503, 2019.

[239] Alistair R Milne, Claire L Edmunds, Cornelius Hempel, Federico Roy, Sandeep Mavadia, and Michael J Biercuk. Phase-modulated entangling gates robust to static and time-varying errors. *Phys. Rev. Appl.*, 13(2):024022, 2020.

[240] Mahdi Sameti, Jake Lishman, and Florian Mintert. Strong-coupling quantum logic of trapped ions. *Phys. Rev. A*, 103(5):052603, 2021.

[241] Jamie David Wong-Campos, Steven A Moses, Kale Gifford Johnson, and Christopher Monroe. Demonstration of two-atom entanglement with ultrafast optical pulses. *Phys. Rev. Lett.*, 119(23):230501, 2017.

[242] Anna E Webb, Simon C Webster, S Collingbourne, David Bretaud, Adam M Lawrence, Sebastian Weidt, Florian Mintert, and Winfried K Hensinger. Resilient entangling gates for trapped ions. *Phys. Rev. Lett.*, 121(18):180501, 2018.

[243] CH Baldwin, BJ Bjork, M Foss-Feig, JP Gaebler, D Hayes, MG Kokish, C Langer, JA Sedlacek, D Stack, and G Vittorini. High-fidelity light-shift gate for clock-state qubits. *Phys. Rev. A*, 103(1):012603, 2021.

[244] Anders Sørensen and Klaus Mølmer. Entanglement and quantum computation with ions in thermal motion. *Phys. Rev. A*, 62(2):022311, 2000.

[245] Data for Orozco-Ruiz et al. "Generally noise-resilient quantum gates for trapped-ions", 2024. DOI:10.5281/zenodo.10908290.

[246] Willis E Lamb Jr and Robert C Retherford. Fine structure of the hydrogen atom by a microwave method. *Phys. Rev.*, 72(3):241, 1947.

[247] Guido Pagano, PW Hess, HB Kaplan, WL Tan, Phil Richerme, Patrick Becker, Antonis Kyprianidis, Jiehang Zhang, Eric Birckelbaw, MR Hernandez, et al. Cryogenic trapped-ion system for large scale quantum simulation. *Quantum Sci. Technol.*, 4(1):014004, 2018.

[248] Sabine Wölk and Christof Wunderlich. Quantum dynamics of trapped ions in a dynamic field gradient using dressed states. *New J. Phys.*, 19(8):083021, 2017.

[249] Daniel FV James. Quantum dynamics of cold trapped ions with application to quantum computation. Technical report, 1998.

[250] David J Wineland, Murray Barrett, Joseph Britton, J Chiaverini, B DeMarco, Wayne M Itano, B Jelenković, Christopher Langer, Dietrich Leibfried, V Meyer, et al. Quantum information processing with trapped ions. *Philos. Trans. R. Soc. Lond. A*, 361(1808):1349–1361, 2003.

[251] Ferdinand Schmidt-Kaler, Hartmut Häffner, Mark Riebe, Stephan Gulde, Gavin PT Lancaster, Thomas Deuschle, Christoph Becher, Christian F Roos, Jürgen Eschner, and Rainer Blatt. Realization of the Cirac–Zoller controlled-NOT quantum gate. *Nature*, 422(6930):408–411, 2003.

[252] Giuseppe Vitagliano, Arnau Riera, and José I. Latorre. Volume-law scaling for the entanglement entropy in spin-1/2 chains. *New J. Phys.*, 12(11):113049, 2010.

[253] Giovanni Ramírez, Javier Rodríguez-Laguna, and Germán Sierra. Entanglement over the rainbow. *J. Stat. Mech. Theory Exp.*, 2015(6):P06002, 2015.

[254] Ernst Hairer. Solving differential equations on manifolds. *Lect. Notes*, 2011.

[255] Tommaso Caneva, Tommaso Calarco, and Simone Montangero. Chopped random-basis quantum optimization. *Phys. Rev. A*, 84(2):022326, 2011.

[256] William H Press. *Numerical recipes 3rd edition: The art of scientific computing.* Cambridge University Press, 2007.

[257] Katta G Murty and Feng-Tien Yu. *Linear complementarity, linear and nonlinear programming*, volume 3. Citeseer, 1988.

[258] Roger Fletcher. *Practical methods of optimization.* John Wiley & Sons, 2000.

[259] Pierre de Fouquieres, Sophie G Schirmer, Steffen J Glaser, and Ilya Kuprov. Second order gradient ascent pulse engineering. *J. Magn. Reson.*, 212(2):412–417, 2011.

[260] AI Konnov and Vadim F Krotov. Deterministic systems-on global methods of successive improvement of controlled processes. *Autom. Remote Control.*, 60(10):1427–1436, 1999.

[261] Daniel M Reich, Mamadou Ndong, and Christiane P Koch. Monotonically convergent optimization in quantum control using Krotov's method. *J. Chem. Phys.*, 136(10), 2012.

[262] Jörg Liesen and Zdenek Strakos. *Krylov subspace methods: principles and analysis*. Numerical Mathematics and Scie, 2013.

[263] Commandant Benoit. Note sur une méthode de résolution des équations normales provenant de l'application de la méthode des moindres carrés à un système d'équations linéaires en nombre inférieur à celui des inconnues (procédé du Commandant Cholesky). *Bull. Géod.*, 2(1):67–77, 1924.

[264] Gene H Golub and Charles F Van Loan. *Matrix computations*. JHU Press, 2013.

[265] Aaron Meurer, Christopher P Smith, Mateusz Paprocki, Ondřej Čertík, Sergey B Kirpichev, Matthew Rocklin, AMiT Kumar, Sergiu Ivanov, Jason K Moore, Sartaj Singh, et al. SymPy: symbolic computing in Python. *PeerJ Comput. Sci.*, 3:e103, 2017.

[266] J Robert Johansson, Paul D Nation, and Franco Nori. QuTiP: An open-source Python framework for the dynamics of open quantum systems. *Comput. Phys. Commun.*, 183(8):1760–1772, 2012.

Appendix A

Relevant Mathematical Relations

This Section contains the proofs of important mathematical relations that are referenced throughout the thesis.

A.1 Differentiation of the matrix exponential map

Consider the exponential map defined by

$$\exp(A(t)) = \sum_{n=0}^{\infty} \frac{1}{n!} A^n(t) \ , \tag{A.1}$$

where $A(t)$ is an operator that may depend on a scalar t. To compute the derivative with respect to t, we differentiate term by term using the product rule

$$\frac{\partial}{\partial t} \exp(A) = \sum_{n=0}^{\infty} \frac{1}{n!} \frac{\partial A^n}{\partial t} = \sum_{n=0}^{\infty} \frac{1}{n!} \sum_{k=0}^{n-1} A^{n-k-1} \dot{A} A^k \ , \tag{A.2}$$

where $\dot{A} = \frac{\partial A}{\partial t}$. Next, we exchange the order of summation. It is convenient to introduce a new index $j = n - k - 1$, so that $n = j + k + 1$. With this change of variables, the sum becomes

$$\frac{\partial}{\partial t} \exp(A) = \sum_{j,k=0}^{\infty} \frac{1}{(j+k+1)!} A^j \dot{A} A^k \ . \tag{A.3}$$

To separate the sums over j and k, we use a standard integral representation that expresses the factorial in the denominator in terms of an integral. Specifically, the Beta-function identity reads

$$\frac{1}{(j+k+1)!} = \frac{1}{j!k!} \int_0^1 d\alpha \ \alpha^j (1-\alpha)^k \ . \tag{A.4}$$

Inserting this representation into the sum yields

$$\frac{\partial}{\partial t}\exp(A) = \int_0^1 d\alpha \sum_{j,k=0}^{\infty} \frac{\alpha^j (1-\alpha)^k}{j!k!} A^j \dot{A} A^k \ . \tag{A.5}$$

Recognize that the sums over j and k are just the power-series definitions of exponential functions, leading to the desired expression for the derivative of the exponential map

$$\begin{aligned}\frac{\partial}{\partial t}\exp(A) &= \int_0^1 d\alpha \ e^{\alpha A}\dot{A}e^{(1-\alpha)A} \\ &= \left(\int_0^1 d\alpha \ e^{\alpha A}\dot{A}e^{-\alpha A}\right) e^{A} \ .\end{aligned} \tag{A.6}$$

A.2 Integral of the matrix exponential map

Consider the exponential map $e^{\alpha A}$ as defined in Eq. (A.1) for a generic operator A, which is given by the power series expansion

$$e^{\alpha A} = \sum_{n=0}^{\infty} \frac{\alpha^n}{n!} A^n \ . \tag{A.7}$$

Our goal is to evaluate the integral

$$\int_0^1 d\alpha \ e^{\alpha A} \ . \tag{A.8}$$

Integrating term by term, we obtain

$$\begin{aligned}\int_0^1 d\alpha \ e^{\alpha A} &= \sum_{n=0}^{\infty} \int_0^1 d\alpha \ \frac{\alpha^n}{n!} A^n \\ &= \sum_{n=0}^{\infty} \frac{\alpha^{n+1}}{(n+1)!}\Big|_0^1 A^n \\ &= \sum_{n=0}^{\infty} \frac{1}{(n+1)!} A^n .\end{aligned} \tag{A.9}$$

To simplify this expression, we rewrite the sum as

$$\begin{aligned}\sum_{n=0}^{\infty} \frac{1}{(n+1)!} A^n &= \mathbb{I} + A^{-1} \sum_{n=1}^{\infty} \frac{1}{(n+1)!} A^{n+1} \\ &= \mathbb{I} + A^{-1}\left(\sum_{n=0}^{\infty} \frac{1}{n!} A^n - \mathbb{I} - A\right) \\ &= \mathbb{I} + A^{-1}e^{A} - A^{-1} - \mathbb{I} \ ,\end{aligned}$$

which simplifies to

$$\int_0^1 d\alpha\; e^{\alpha A} = A^{-1}\left(e^A - \mathbb{I}\right). \tag{A.10}$$

A.3 Similarity transformation via the adjoint action

A similarity transformation of the operator X under the exponential map generated by A is given by

$$Y(\alpha) \equiv e^{\alpha A} X e^{-\alpha A}\ , \tag{A.11}$$

where α is a scalar parameter, and A and X are operators. By construction, $Y(0) = X$ and X does not depend on α. Our goal is to derive a closed-form expression for this map in terms of the adjoint action of A.

Differentiating $Y(\alpha)$ using the product rule yields the differential equation

$$\begin{aligned}
\frac{\partial Y(\alpha)}{\partial \alpha} &= \frac{\partial e^{\alpha A}}{\partial \alpha} X e^{-\alpha A} + e^{\alpha A} X \frac{\partial e^{-\alpha A}}{\partial \alpha} \\
&= A e^{\alpha A} X e^{-\alpha A} - e^{\alpha A} X e^{-\alpha A} A \\
&= \left[A, e^{\alpha A} X e^{-\alpha A}\right] \\
&= [A, Y(\alpha)]\ .
\end{aligned} \tag{A.12}$$

To solve this differential equation, let us expand $Y(\alpha)$ in power series in α,

$$Y(\alpha) = \sum_{n=0}^{\infty} Y_n \alpha^n\ , \tag{A.13}$$

where the boundary condition imposes $Y_0 = X$. Differentiating term by term gives

$$\frac{\partial Y(\alpha)}{\partial \alpha} = \sum_{n=0}^{\infty} n Y_n \alpha^{n-1}\ , \tag{A.14}$$

which, when substituted into the differential equation, leads to the relation

$$\sum_{n=0}^{\infty} n Y_n \alpha^{n-1} = \sum_{n=0}^{\infty} \alpha^n [A, Y_n]\ . \tag{A.15}$$

Matching powers of α on both sides, we obtain the recurrence relations

$$Y_1 = [A, Y_0]\ , \tag{A.16a}$$

$$2Y_2 = [A, Y_1]\ , \tag{A.16b}$$

$$\vdots \tag{A.16c}$$

$$nY_n = [A, Y_{n-1}]\ . \tag{A.16d}$$

Since $Y_0 = X$, we explicitly compute the first few terms

$$Y_1 = [A, X] \ , \tag{A.17a}$$

$$Y_2 = \frac{1}{2}[A, [A, X]] \ , \tag{A.17b}$$

$$Y_2 = \frac{1}{6}[A, [A, [A, X]]] \ , \tag{A.17c}$$

$$\vdots \tag{A.17d}$$

$$Y_n = \frac{1}{n!}\underbrace{[A, [\cdots, [A, X]]]}_{n \text{ commutators}} = \frac{1}{n!}\mathrm{ad}_A^n(X) \ , \tag{A.17e}$$

where $\mathrm{ad}_A^n(X)$ denotes the n-fold nested commutator with A. Thus, summing over all orders, we obtain

$$e^{\alpha A} X e^{-\alpha A} = \sum_{n=0}^{\infty} \frac{\alpha^n}{n!}\mathrm{ad}_A^n(X) = \exp(\alpha \mathrm{ad}_A)(X) \ , \tag{A.18}$$

which expresses the similarity transformation in terms of the adjoint action of A.

A.4 Directional derivative of an operator function

The directional derivative of an operator function quantifies how the function changes when its argument is perturbed in a specific direction. For an operator function $F(\Omega)$, the directional (Gâteaux) derivative at Ω in the direction A is defined as

$$D_A F(\Omega) \equiv \lim_{\epsilon \to 0} \frac{F(\Omega + \epsilon A) - F(\Omega)}{\epsilon} \ . \tag{A.19}$$

Since a first-order expansion gives

$$F(\Omega + \epsilon A) = F(\Omega) + \epsilon \frac{\partial F(\Omega)}{\partial \Omega} A + \mathcal{O}(\epsilon^2) \ , \tag{A.20}$$

where $\frac{\partial F(\Omega)}{\partial \Omega}$ is the Fréchet derivative of F at Ω. Substituting this into the definition of the directional derivative, we obtain

$$D_A F(\Omega) = \left(\frac{\partial F(\Omega)}{\partial \Omega}\right) A \ . \tag{A.21}$$

A particularly instructive example is the case $F(\Omega) = \Omega^k$, for which

$$D_A \Omega^k = \lim_{\epsilon \to 0} \frac{(\Omega + \epsilon A)^k - \Omega^k}{\epsilon} = \left(\frac{\partial \Omega^k}{\partial \Omega}\right) A \ . \tag{A.22}$$

Expanding $(\Omega + \epsilon A)^k$ to first order in ϵ using the product rule (and noting that operators may not commute) gives

$$(\Omega + \epsilon A)^k = \Omega^k + \epsilon \left(A\Omega^{k-1} + \Omega A \Omega^{k-2} + \cdots + \Omega^{k-2} A \Omega + \Omega^{k-1} A \right) + \mathcal{O}(\epsilon^2) \tag{A.23}$$

Substituting in Eq. (A.22) yields

$$\left(\frac{\partial \Omega^k}{\partial \Omega}\right) A = A\Omega^{k-1} + \Omega A \Omega^{k-2} + \cdots + \Omega^{k-2} A \Omega + \Omega^{k-1} A \ . \tag{A.24}$$

In the special case where Ω and A commute, *i.e.*, $[\Omega, A] = 0$, every term in the sum is identical, and the expression reduces to $\left(\frac{\partial \Omega^k}{\partial \Omega}\right) A = k\Omega^{k-1} A$, which is analogous to the familiar result for scalar functions. However, when Ω do not commute, the order of multiplication is crucial, and the full sum must be retained.

A.5 Adjoint representation for derivatives of operator powers

Given an operator Ω, the derivative of its k-th power with respect to Ω is defined in Eq. (A.24). One can rewrite Eq. (A.24) in a more convenient form involving only powers of Ω and nested commutators of Ω and A. For that, it is convenient the following relation

$$\Omega[\Omega, A] = [\Omega, A]\Omega + [\Omega, [\Omega, A]] \ . \tag{A.25}$$

By applying this identity recursively, Eq. (A.24) can be rewritten in a compact form. For instance, for $k = 2$ and $k = 3$, one obtains

$$A\Omega + \Omega A = 2A\Omega + [\Omega, A] \ , \tag{A.26a}$$

$$A\Omega^2 + \Omega A \Omega + \Omega^2 A = 3\Omega A \Omega + [\Omega, [\Omega, A]] = 3A\Omega^2 + 3[\Omega, A]\Omega + [\Omega, [\Omega, A]] \ , \tag{A.26b}$$

respectively. The general expression for arbitrary integer $k \geq$ then reads

$$\begin{aligned}\left(\frac{\partial \Omega^k}{\partial \Omega}\right) A &= \sum_{j=0}^{k-1} \binom{k}{j+1} \underbrace{[\Omega, [\cdots, [\Omega, A]]]}_{j \text{ commutators}} \Omega^{k-j-1} \\ &= \sum_{j=0}^{k-1} \binom{k}{j+1} \mathrm{ad}_\Omega^j(A) \Omega^{k-j-1} \ ,\end{aligned} \tag{A.27}$$

where we define $\mathrm{ad}_\Omega^0(A) = \underbrace{[\Omega, [\cdots, [\Omega, A]]]}_{0 \text{ commutators}} \equiv A$, and for $j \geq 1$, $\mathrm{ad}_\Omega^j(A) = \Big[\Omega, \mathrm{ad}_\Omega^{j-1}(A)\Big]$.

From Eq. (A.27), one can derive the derivative of the matrix exponential $\exp(\Omega)$ with respect ot Ω, *i.e.*, $\frac{\partial \exp(\Omega)}{\partial \Omega}$. Using the series expansion of the exponential function (Eq. (A.7)), the derivative reads

$$\begin{aligned}\left(\frac{\partial \exp(\Omega)}{\partial \Omega}\right) A &= \sum_{k=0}^{\infty} \frac{1}{k!} \sum_{i=0}^{k-1} \binom{k}{i+1} \underbrace{[\Omega, [\cdots, [\Omega, A]]]}_{j \text{ commutators}} \Omega^{k-i-1} \\ &= \sum_{k=1}^{\infty} \sum_{j=0}^{k-1} \frac{1}{(j+1)!(k-j-1)!} \underbrace{[\Omega, [\cdots, [\Omega, A]]]}_{j \text{ commutators}} \Omega^{k-j-1} \\ &= \left(A + \frac{1}{2!}[\Omega, A] + \frac{1}{3!}[\Omega, [\Omega, H]] + \cdots\right) \left(\mathbb{I} + \Omega + \frac{1}{2}\Omega^2 + \frac{1}{3!}\Omega^3 + \cdots\right) \ .\end{aligned} \tag{A.28}$$

Using convenient notation, we define the linear operator

$$d\exp_\Omega(A) \equiv \sum_j \frac{1}{(j+1)!} \underbrace{[\Omega, [\cdots, [\Omega, A]]]}_{j \text{ commutators}} , \tag{A.29}$$

so that the derivative of the exponential simplifies to

$$\left(\frac{\partial \exp(\Omega)}{\partial \Omega}\right) A = d\exp_\Omega(A) \exp(\Omega) \ . \tag{A.30}$$

The operator $d\exp_\Omega$ in Eq. (A.29) is invertible in a neighborhood of $\Omega = 0$, and more generally, in any region where ad_Ω has no nonzero eigenvalues equal to integer multiples of $2\pi i$. A sufficient condition for invertibility is

$$\|\mathrm{ad}_\Omega\| < 2\pi \ , \tag{A.31}$$

which is guaranteed, for instance, when $\|\Omega\| < \pi$ (in operator norm). For a detailed discussion, see [41, 42, 254].

In this case, the inverse of the differential of the exponential map, $d\exp_\Omega^{-1}$, admits the formal series expansion

$$d\exp_\Omega^{-1}(A) = \sum_j \frac{B_j}{j!} \underbrace{[\Omega, [\cdots, [\Omega, A]]]}_{j \text{ commutators}} , \tag{A.32}$$

where B_j are the Bernoulli numbers, defined via the generating function

$$\sum_{j=0}^{\infty} \frac{B_j}{j!} x^j = \frac{x}{e^x - 1} \ . \tag{A.33}$$

This identity plays a central role in the construction of the Magnus expansion, particularly in the derivation leading to Eq. (2.49).

Appendix B

Dynamical Pictures in Quantum Mechanics

In quantum mechanics, there are three fundamental dynamical pictures, also referred to as representations, that offer distinct perspectives on the time evolution of quantum systems. Each picture provides a different approach to describing how quantum systems change over time. This Section outlines the key features and differences of these representations.

B.1 Schrödinger picture

In the Schrödinger picture, the quantum state of a system evolves dynamically over time, while operators representing observables remain static unless they possess *explicit time dependence*. For example, consider an operator $O_S(t)$ designed to transition between measuring spin along the z-axis at $t = 0$ and the y-axis at $t = T$. Such an operator can be explicitly time-dependent, as illustrated by

$$O_S(t) = \left(1 - \frac{t}{T}\right)\sigma_z + \frac{t}{T}\sigma_y \ , \tag{B.1}$$

where σ_y and σ_z are fixed Pauli operators. Here, $O_S(t)$ evolves *explicitly* due to its parametric dependence on time, even though the underlying spin operators themselves remain constant in this picture.

The time evolution of a quantum state $|\psi(t)\rangle$, on the other hand, is governed by the Schrödinger equation

$$i\frac{\partial}{\partial t}|\psi(t)\rangle = H(t)\,|\psi(t)\rangle \ , \tag{B.2}$$

where $H(t)$ is the Hamiltonian of the system, which may itself be time-dependent. Solving this equation for an initial state $|\psi(0)\rangle$ yields the time-evolved state

$$|\psi(t)\rangle = U(t)\,|\psi(0)\rangle \ , \tag{B.3}$$

where $U(t)$ is the time-evolution operator.

B.2 Heisenberg picture

In the Schrödinger picture, quantum states $|\psi(t)\rangle$ evolve dynamically over time, while operators (representing observables) remain static unless they have explicit time dependence. Conversely, in the Heisenberg picture, states remain fixed at their initial value $|\psi(0)\rangle$, and operators evolve instead. The two pictures are related via the time-evolution operator $U(t)$ associated with the Hamiltonian $H(t)$. Specifically, a Heisenberg-picture operator $O_H(t)$ is connected to its Schrödinger-picture counterpart $O_S(t)$ by

$$O_H(t) = U^\dagger(t) O_S(t) U(t) \ , \tag{B.4}$$

where $U(t)$ solves the Schrödinger equation $i\partial_t U(t) = H(t)U(t)$.

The physical equivalence of the two pictures is ensured by matching expectation values at all times. At $t = 0$, the boundary condition $O_H(0) = O_S(0)$ guarantees agreement. For any later time t, the expectation value of an observable must satisfy

$$\langle\psi(t)|_S \, O_S(t) \, |\psi(t)\rangle_S = \langle\psi(0)| \, U^\dagger(t) O_S(t) U(t) \, |\psi(0)\rangle = \langle\psi(0)| \, O_H(t) \, |\psi(0)\rangle \ , \tag{B.5}$$

where $|\psi(t)\rangle_S = U(t) \, |\psi(t)\rangle$ (Schrödinger picture) and $|\psi(t)\rangle_H = |\psi(0)\rangle$ (Heisenberg picture). This equivalence underscores that measurable outcomes are picture-independent.

From these relations, we can find the equation of motion for the operators $O_H(t)$ in the Heisenberg picture. Differentiating Eq. (B.4) yields

$$\frac{\partial O_H(t)}{\partial t} = \frac{\partial U^\dagger(t)}{\partial t} O_S(t) U(t) + U^\dagger(t) \frac{\partial O_S(t)}{\partial t} U(t) + U^\dagger(t) O_S(t) \frac{\partial U(t)}{\partial t} \ . \tag{B.6}$$

Substituting $i\partial_t U(t) = H(t)U(t)$ and $-i\partial_t U^\dagger(t) = U^\dagger(t)H(t)$, we simplify the expression to

$$\frac{\partial O_H(t)}{\partial t} = iU^\dagger(t)H(t)O_S(t)U(t) + U^\dagger(t) \frac{\partial O_S(t)}{\partial t} U(t) - iU^\dagger(t)O_S(t)H(t)U(t) \ . \tag{B.7}$$

Recognizing $H_H(t) = U^\dagger(t)H(t)U(t)$ and $O_H(t) = U^\dagger(t)O_S(t)U(t)$, we rewrite this as

$$\frac{\partial O_H(t)}{\partial t} = iH_H(t)O_H(t) + U^\dagger(t) \frac{\partial O_S(t)}{\partial t} U(t) - iO_H(t)H_H(t) \ . \tag{B.8}$$

Thus, we obtain the equation of motion for $O_H(t)$ in the Heisenberg picture

$$\frac{\partial O_H(t)}{\partial t} = i[H_H, O_H] + U^\dagger(t) \frac{\partial O_S(t)}{\partial t} U(t) \ , \tag{B.9}$$

which represents the general form of the Heisenberg equation of motion.

In some simpler cases, Eq. (B.9) can be further simplified. For instance, many observables O_S in the Schrödinger picture are time-independent, such as the position or momentum

operators. Additionally, if the Hamiltonian $H(t)$ and propagator $U(t)$ commute at any time t, the equation simplifies to

$$\frac{\partial O_H(t)}{\partial t} = i[H, O_H] \ . \tag{B.10}$$

B.3 Interaction picture

The interaction picture provides an intermediate framework between the Schrödinger and Heisenberg pictures, proving particularly useful when the Hamiltonian comprises two distinct components. One component, the *bare* Hamiltonian, $H_0(t)$), represents a well-understood term (typically time-independent, but more generally a Hamiltonian with a known time-evolution operator), such as harmonic oscillator states or atomic internal states. The other component, $H_I(t)$, is a time-dependent term, typically more challenging to analyze, that can have arbitrary magnitude (and therefore does not admit a perturbative treatment), such as a coupling between the two components or a coupling to external motion. The total Hamiltonian is given by

$$H(t) = H_0(t) + H_I(t) \ . \tag{B.11}$$

In the interaction picture, the goal is to isolate the effects of the bare Hamiltonian from those of the time-dependent perturbation $H_I(t)$. To achieve this, consider a state initialized in $|\psi(t_0)\rangle_S$ in the Schrödinger picture. This state evolves to $|\psi(t)\rangle_S$ according to the usual Schrödinger equation (Eq. (2.29)) with $H(t)$.

To isolate the effect of $H_I(t)$, a new state vector is defined

$$|\psi(t)\rangle_R = U_R(t) \, |\psi(t)\rangle_S \ , \tag{B.12}$$

where $U_R(t)$ is a time-dependent unitary transformation that defines a new dynamical frame. The choice of this rotation operator $U_R(t)$ is crucial for decomposing the dynamics induced by the bare Hamiltonian from those of the perturbation $H_I(t)$.

Differentiating the above expression yields

$$\begin{aligned} i\frac{\partial \, |\psi(t)\rangle_R}{\partial t} &= i\Big(\frac{\partial U_R(t)}{\partial t} \, |\psi(t)\rangle_S + U_R(t)\frac{\partial \, |\psi(t)\rangle_S}{\partial t}\Big) \\ &= i\frac{\partial U_R(t)}{\partial t} \, |\psi(t)\rangle_S + U_R(t)H(t) \, |\psi(t)\rangle_S \\ &= \Big(i\frac{\partial U_R(t)}{\partial t}U_R^\dagger(t) + U_R(t)H(t)U_R^\dagger(t)\Big) \, |\psi(t)\rangle_R \ . \end{aligned} \tag{B.13}$$

This shows that $|\psi(t)\rangle_R$ obeys the Schrödinger with a modified Hamiltonian $\tilde{H}(t)$

$$\tilde{H}(t) = i\frac{\partial U_R(t)}{\partial t}U_R^\dagger(t) + U_R(t)H(t)U_R^\dagger(t) \ . \tag{B.14}$$

A particularly useful choice for $U_R(t)$ in the interaction picture is $U_R(t) = U_0^\dagger(t)$, *i.e.* the

Hermitian conjugate of the time-evolution operator associated with the bare Hamiltonian $H_0(t)$. Substituting this into the first term of Eq. (B.14) and using Eq. (2.28) yields

$$i\frac{\partial U_0^\dagger(t)}{\partial t}U_0(t) = -U_0^\dagger(t)H_0(t)U_0(t)\ . \tag{B.15}$$

Consequently, the modified Hamiltonian simplifies to

$$\begin{aligned}\tilde{H}(t) &= U_0^\dagger(t)\Big(H(t) - H_0(t)\Big)U_0(t)\\ &= U_0^\dagger(t)H_I(t)U_0(t)\ ,\end{aligned} \tag{B.16}$$

which corresponds to the perturbation Hamiltonian $H_I(t)$ in the rotated frame. This transformation effectively *removes* the dynamics generated by the bare Hamiltonian, which is often analytically solvable and considered less relevant, leaving only the transformed perturbation term $H_I(t)$. Notably, if the perturbation induces trivial dynamics (*i.e.*, $H_I(t) = \mathbb{I}$), the transformed Hamiltonian reduces to the identity, $\tilde{H}(t) = \mathbb{I}$, as expected when the bare evolution is completely removed.

An important property that greatly simplifies the computation of the transformed Hamiltonian is the ability to systematically transform composite operators. Consider a perturbative Hamiltonian expressed as a product of operators

$$H_I(t) = \sum_{i,j} a_j b_k P^j Q^k = \left(a_0\mathbb{I} + a_1 P + a_2 P^2 + \cdots\right)\left(b_0\mathbb{I} + b_1 Q + b_2 Q^2 + \cdots\right)\ , \tag{B.17}$$

where P^j and Q^k are operators acting in the Hilbert space associated with H_I raised to the powers of j and k respectively, and a_j and b_k are scalar coefficients. The transformed Hamiltonian under the unitary transformation $U_0^\dagger(t)$ can be written as

$$\begin{aligned}\tilde{H}(t) &= U_0^\dagger(t)\sum_{j,k} a_j b_k P^j Q^k U_0(t)\\ &= \sum_{j,k} a_j b_k \left(U_0^\dagger(t)P^j U_0(t)\right)\left(U_0^\dagger(t)Q^k U_0(t)\right)\ .\end{aligned} \tag{B.18}$$

Using the relation $U_0^\dagger(t)P^j U_0(t) = U_0^\dagger(t)PU_0(t)U_0^\dagger(t)P^{j-1}U_0(t)$, yields

$$\begin{aligned}\tilde{H}(t) &= \sum_{j,k} a_j b_k \left[\left(U_0^\dagger(t)PU_0(t)\right)^j\left(U_0^\dagger(t)QU_0(t)\right)^k\right]\\ &= \sum_{j,k} a_j b_k \tilde{P}^j(t)\tilde{Q}^k(t)\ ,\end{aligned} \tag{B.19}$$

where

$$\tilde{P}(t) = U_0^\dagger(t)PU_0(t), \quad \tilde{Q}(t) = U_0^\dagger(t)QU_0(t) \tag{B.20}$$

are the transformed operators in the interaction picture.

This result highlights that transforming any polynomial or product of operators reduces to transforming the individual operators. Consequently, only the transformations of the fundamental operators, P and Q, need to be computed, significantly simplifying the analysis.

An essential observation is that operators which are time-independent in the Schrödinger picture may acquire explicit time dependence in the interaction picture due to the time evolution of the unitary transformation $U_0(t)$. To derive the time evolution of a transformed operator, one computes the time derivative of $\tilde{P}$

$$\begin{aligned}\frac{\partial \tilde{P}}{\partial t} &= \frac{\partial \tilde{U}_0^\dagger(t)}{\partial t} P U_0(t) + U_0^\dagger(t) \frac{\partial P}{\partial t} U_0(t) + U_0^\dagger(t) P \frac{\partial U_0(t)}{\partial t} \\ &= i U_0^\dagger(t) H_0(t) P U_0(t) + U_0^\dagger(t) \frac{\partial P}{\partial t} U_0(t) - i U_0^\dagger(t) P H_0(t) U_0(t) \\ &= i \tilde{H}_0(t) \tilde{P} + U_0^\dagger(t) \frac{\partial P}{\partial t} U_0(t) - \tilde{P} \tilde{H}_0(t) \ , \end{aligned} \tag{B.21}$$

which yields the equation of motion

$$\frac{\partial \tilde{P}}{\partial t} = i \Big[\tilde{H}_0(t), \tilde{P} \Big] + U_0^\dagger(t) \frac{\partial P}{\partial t} U_0(t) \ . \tag{B.22}$$

Crucially, the time derivative on the left-hand side applies to the transformed operator $\tilde{P}$, whereas the derivative on the right-hand side is performed over the operator in the original (Schrödinger) picture. Furthermore, the transformed bare Hamiltonian, $\tilde{H}_0(t)$, matches its Schrödinger form if H_0 is time-independent, as demonstrated by the relation $e^{itH_0} H_0 e^{-itH_0} = H_0$. This equivalence, however, does not generally hold when H_0 is time-dependent.

Appendix C

Methods for Quantum Control

In this Section, we provide an overview of the most widely used methods in quantum control: CRAB, GRAPE, and Krotov. These approaches are particularly relevant to the control problems discussed in this thesis, especially in relation to the method developed in Chapter 5. These techniques are designed to optimize control functions $\{u_j(t)\}$ in the control Hamiltonian, which takes the general form

$$H(t) = H_0 + \sum_{j=1}^{N_h} u_j(t)\mathfrak{h}_j \ , \tag{C.1}$$

where H_0 is the system's intrinsic Hamiltonian, $\mathfrak{h}_j$ are control operators, and $u_j(t)$ are time-dependent control fields. By tailoring $u_j(t)$, these methods enable precise manipulation of quantum systems, making them indispensable tools for solving a wide range of quantum control problems.

C.1 The CRAB algorithm

The core principle of the Chopped RAndom Basis (CRAB) algorithm [63, 255] is to utilize a sufficiently complex parametrization for the control fields $u_j(t)$ to enable solutions to complex optimization problems. The method involves decomposing each control field, $u_j(t)$, into a set of basis functions, typically chosen randomly, in order to capture the necessary time-dependence required for optimization. The algorithm starts with an initial guess $u_j^{(0)}(t)$ for the control fields and iteratively generates refined solutions of the form $f_j(t) \cdot u_j^{(0)}(t)$, where $f_j(t)$ are correction functions that adjust the time-dependence of the controls to minimize the loss functional $\mathcal{L}$. These corrective functions $f_j(t)$ are expanded in a simple function basis, such as a Fourier series, with parameters Ω_{jk} that characterize the expansion. Formally, the correction function for the j-th control field can be expressed as

$$f_j(t) = \sum_k c_{jk} \cdot g_{jk}(\Omega_{jk}, t) \tag{C.2}$$

where $g_{jk}(\Omega_{jk}, t)$ are the basis functions, and c_{jk} are the corresponding coefficients. In the specific case of a Fourier series, g_{jk} would encompass sinusoidal and cosinusoidal components, while Ω_{jk} would represent both the frequencies and the amplitudes of each frequency component. To facilitate the exploration of the parameter space and accelerate the convergence process, the CRAB algorithm introduces a randomization scheme. This involves introducing a random variable, r_{jk}, which perturbs the parameters of the basis functions. Specifically, the parameters Ω_{jk} are modified as

$$\Omega_{jk} \to \Omega_{jk}(1 + r_{jk}) \ , \tag{C.3}$$

where $0 \leq r_{jk} \leq 1$. This random perturbation effectively introduces variability in the shape and characteristics of the basis functions, broadening the search space. This randomness serves to enhance the algorithm's ability to avoid local minima and accelerate the search for an optimal solution by introducing variability into the function space spanned by the basis functions.

The optimization problem within the CRAB framework then translates to minimizing a multivariable cost function $\mathcal{L}$ with respect to the parameters c_{jk} and the total evolution time T. This process requires evaluating $\mathcal{L}$ for specific choices of c_{jk} and determining the optimal values of these coefficients that minimize the cost function. To do so, the state $|\psi(T)\rangle$ at the final time T must be constructed, which entails numerically solving the Schrödinger equation — because the time-evolution operator $U(t)$ cannot be computed exactly. As a result, only a numerical estimate of $\mathcal{L}$ is available, making the optimization problem inherently numerical. To identify the optimal solution, numerical methods are employed to explore the parameter space. These include gradient-based techniques such as conjugate gradient, steepest descent or direct search methods [256], or direct search methods that do not require any estimate of the gradient, such as Nelder-Mead or Simplex algorithms [257].

C.2 The GRAPE algorithm

The GRadient Ascent Pulse Engineering (GRAPE) algorithm [26] operates by iteratively refining control parameters $u_j(t)$ through gradient descent. Specifically, GRAPE seeks to minimize the cost function $\mathcal{L}$ by adjusting the control parameters in the direction of its gradient $\partial\mathcal{L}/\partial u_j(t)$. The core principle of GRAPE lies in its efficient computation and utilization of these gradients, enabling the identification of optimal control solutions.

To facilitate the computation of the time evolution and the associated gradients, GRAPE assumes that the control parameters $u_j(t)$ within the system Hamiltonian are piecewise constant. This approximation is often a good representation of real experimental setups where control signals are inherently discretized or can be approximated by step functions. Under this assumption, the total evolution time T is divided into M intervals (usually of

equal duration), during which the control amplitude remains constant, *i.e.*

$$\begin{aligned} u_j(t) &= u_{j0} \text{ for } 0 \leq t < t_1 \ , \\ u_j(t) &= u_{j1} \text{ for } t_1 \leq t < t_2 \ , \\ &\vdots \\ u_j(t) &= u_{j(M-1)} \text{ for } t_{M-1} \leq t < t_M = T \ . \end{aligned} \tag{C.4}$$

This discretization translates the continuous control problem into a finite-dimensional optimization over the set of u_{jk}, where j indexes the control fields, and k indexes the time intervals. Within the piecewise-constant framework, the Hamiltonian at time t_k is given by

$$H(t_k) = H_0 + \sum_{j=1}^{N_h} u_{jk} \mathfrak{h}_j \ . \tag{C.5}$$

The time evolution of the system over each interval $[t_k, t_{k-1}]$ is then described by the propagator

$$U(t_k; t_{k-1}) = e^{-i\Delta_k H(t_k)} \ , \tag{C.6}$$

with $\Delta_k = t_k - t_{k-1}$, and the total evolution from $t = t_0 = 0$ to t_k is obtained by sequentially multiplying these propagators

$$U(t_k; 0) = \prod_{m=k}^{1} U(t_m; t_{m-1}) = e^{-i\Delta_k H(t_k)} e^{-i\Delta_{k-1} H(t_{k-1})} \cdots e^{-i\Delta_1 H(t_1)} \ . \tag{C.7}$$

This structure enables efficient numerical computation of the forward-evolved states, $|\psi(t_k)\rangle = U(t_k; 0)\,|\psi(0)\rangle$, and the backward-evolved states, $|\psi(0)\rangle = U^\dagger(t_k; 0)\,|\psi(t_k)\rangle$, a crucial aspect for accurately estimating the gradients.

The gradient of the cost function $\mathcal{L}$ with respect to the control parameters u_{jk} guides the search for optimal control sequences. In the piecewise-constant framework where each control is discretized into M steps, this translates to optimizing over a $(N_h \cdot M)$-dimensional space. The exact expression for the gradient of $\mathcal{L}$ with respect to u_{jk} depends on the specific forms of the cost term $\mathcal{C}$ and the regularization term $\mathcal{R}$. While an analytical expression for the gradient is often desirable, it may not always be feasible, particularly for complex or non-smooth functionals. In such cases, numerical methods such as finite-difference approximations or quasi-Newton methods (*e.g.*, the Broyden–Fletcher–Goldfarb–Shanno (BFGS [258]) algorithm) can be employed to estimate the gradient and facilitate the optimization process.

To illustrate the computation of the gradient, consider the scenario where the cost term $\mathcal{C}$ is defined as the state infidelity, $\mathcal{C} = 1 - |\langle\psi_F|\psi(T)\rangle|^2$, and no additional regularization is applied ($\mathcal{R} = 0$). Since the final state $|\psi(T)\rangle$ is related to the initial state $|\psi(0)\rangle$ via

$|\psi(T)\rangle = U(T;0)\,|\psi(0)\rangle$, the gradient of $\mathcal{L}$ with respect to u_{jk} is given by

$$\frac{\partial \mathcal{L}}{\partial u_{jk}} = -\langle\psi_F|\,\frac{\partial U(T;0)}{\partial u_{jk}}\,|\psi(0)\rangle\langle\psi(0)|\,\frac{\partial U^\dagger(T;0)}{\partial u_{jk}}\,|\psi_F\rangle \ , \tag{C.8}$$

where the derivative of the propagator with respect to u_{jk} can be expressed as

$$\frac{\partial U(T;0)}{\partial u_{jk}} = \prod_{m=M}^{k+1} U(t_m;t_{m-1}) \frac{\partial U(t_k;t_{k-1})}{\partial u_{jk}} \prod_{m=k-1}^{1} U(t_m;t_{m-1}) \ , \tag{C.9a}$$

$$\frac{\partial U^\dagger(T;0)}{\partial u_{jk}} = \prod_{m=1}^{k-1} U(t_{m-1};t_m) \frac{\partial U(t_{k-1};t_k)}{\partial u_{jk}} \prod_{m=k+1}^{M} U(t_{m-1};t_m) \ , \tag{C.9b}$$

with the adjoint property $U^\dagger(t_k;t_{k-1}) = U(t_{k-1};t_k)$ applied in the second line. For the derivative of the single-interval propagator, the matrix exponential expansion for non-commuting operators [259] yields

$$\begin{aligned}\frac{\partial U(t_k;t_{k-1})}{\partial u_{jk}} = U(t_k;t_{k-1})\Big(&- i\Delta_k \mathfrak{h}_j + \frac{\Delta_k^2}{2}[H(t_k),\mathfrak{h}_j] + \frac{i\Delta_k^3}{6}[H(t_k),[H(t_k),\mathfrak{h}_j]] \\ &+ \mathcal{O}(\Delta_k^4)\Big) \ .\end{aligned} \tag{C.10}$$

Defining the forward-evolved state as $|\psi(t_{k-1};0)\rangle = \prod_{m=k-1}^{1} U(t_m;t_{m-1})\,|\psi(0)\rangle$ and the backward-propagated target state as $\langle\psi_F(t_{k-1})| = \langle\psi_F|\prod_{m=M}^{k} U(t_m;t_{m-1})$, the gradient simplifies to

$$\begin{aligned}\frac{\partial \mathcal{L}}{\partial u_{jk}} = -\Bigg| \langle\psi_F(t_{k-1})| \Bigg(&- i\Delta_k \mathfrak{h}_j + \frac{\Delta_k^2}{2}[H(t_k),\mathfrak{h}_j] \\ &+ \frac{i\Delta_k^3}{6}[H(t_k),[H(t_k),\mathfrak{h}_j]] + \mathcal{O}(\Delta_k^4)\Bigg) |\psi(t_{k-1};0)\rangle \Bigg|^2 \ .\end{aligned} \tag{C.11}$$

This expression captures the overlap between the forward-evolved state (up to t_{k-1}) and the backward-propagated target state (from T to t_{k-1}), linked via the operator encoding the propagator's control dependence. The gradient expression essentially quantifies how the control parameters should be adjusted to align these states perfectly, ensuring optimal connectivity between the forward-evolved and backward-propagated trajectories.

Finally, the control parameters are iteratively updated from iteration $i-1$ to iteration i as

$$u_{jk}^{(i)} = u_{jk}^{(i-1)} + \alpha \frac{\partial \mathcal{L}}{\partial u_{jk}} \ , \tag{C.12}$$

where α is the learning rate controlling the update step size.

C.3 The Krotov algorithm

The Krotov's method [260, 261] follows a similar approach to GRAPE in seeking the optimality of the control parameters $u_j(t)$. Likewise, the core idea is to iteratively refine the control fields using both forward and backward propagations of the quantum system, ensuring efficient convergence toward the desired solution. Starting with an initial guess for the control fields, denoted $u_j^{(0)}(t)$, the fields are updated at each iteration i according to the update rule

$$u_j^{(i)}(t) = u_j^{(i-1)}(t) + \Delta u_j^{(i)}(t) \ , \tag{C.13}$$

where $\Delta u_j^{(i)}(t)$ represents the calculated adjustment to the control fields at the i-th iteration. The main difference between Krotov's method and GRAPE lies in the construction of $\Delta u_j^{(i)}(t)$. In Krotov's method, the update is not based on the gradient of the cost function $\mathcal{L}$ with respect to the control parameters, but rather on the derivative of the Hamiltonian with respect to the control field. This guarantees a monotonic reduction of the cost function in each iteration by directly updating the control pulses using a deterministic update rule derived from the variational principle. In contrast, GRAPE guarantees convergence only when second-order or higher expansions of the derivative $\partial U/\partial u_{jk}$ (Eq. (C.10)) are included.

In Krotov's method, the forward-propagated state $|\psi(t)\rangle$ is obtained by numerically integrating the time-dependent Schrödinger equation (*e.g.*, using the Runge-Kutta or Crank-Nicholson method) with the updated controls from iteration i, $u_j^{(i)}(t)$,

$$i\frac{\partial\,|\psi(t)\rangle}{\partial t} = H^{(i)}(t)\,|\psi(t)\rangle \ , \tag{C.14}$$

where the superindex (i) indicates that the Hamiltonian employs the controls $u_j^{(i)}(t)$, and the initial condition is $|\psi(0)\rangle = |\psi_I\rangle$. Similarly, the backward-propagated state $|\chi(t)\rangle$ evolves backward in time using the optimal controls from iteration $(i-1)$ as

$$i\frac{\partial\,|\chi(t)\rangle}{\partial t} = -H^{(i-1)}(t)\,|\chi(t)\rangle \ , \tag{C.15}$$

with the boundary condition

$$|\chi(T)\rangle = -\frac{\partial \mathcal{C}}{\partial\,\langle\psi(T)|}\Big|_{(i-1)} \ . \tag{C.16}$$

Here, the right-hand side is evaluated for the state $|\psi(T)\rangle$, which results from the forward propagation of the initial state $|\psi(0)\rangle = |\psi_I\rangle$ with the optimal controls from the previous iteration $(i-1)$. In the case where the cost function is $\mathcal{C} = 1 - |\langle\psi(T)|\psi_T\rangle|^2$, the boundary condition simplifies to

$$|\chi(T)\rangle = \Big(\,\langle\psi_T|\psi(T)\rangle\,\Big)\Big|_{(i-1)}\,|\psi_T\rangle \ , \tag{C.17}$$

which is the target state $|\psi_T\rangle$ scaled by the overlap with the state at final time T with the current optimal controls.

With these definitions, the update rule reads [261]

$$\Delta u_j^{(i)}(t) = \frac{S_j(t)}{\alpha} \mathrm{Im}\left(\langle \chi(t)| \frac{\partial H^{(i)}(t)}{\partial u_j(t)} |\psi(t)\rangle \right) , \tag{C.18}$$

where $S_j(t)$ is a scaling factor that determines the magnitude of the update at each iteration, α is the learning rate, and $\frac{\partial H^{(i)}(t)}{\partial u_j(t)}$ is the partial derivative of the system Hamiltonian $H(t)$ with respect to the control u_j. Using the expression for the Hamiltonian in Eq. (3.1), this simplifies to $\frac{\partial H^{(i)}(t)}{\partial u_j(t)} = \mathfrak{h}_j$. The imaginary part guarantees that the update $\Delta u_j^{(i)}(t)$ is real.

Intuitively, the overlap $\langle \chi(t)| \frac{\partial H^{(i)}(t)}{\partial u_j(t)} |\psi(t)\rangle$ measures how much the action of a specific control $u_j(t)$ can push the current forward-evolved state $|\psi(t)\rangle$ towards the backward-evolved state $|\chi(t)\rangle$ (which contains information about how changes in the final state depend on earlier parts of the trajectory). When the forward and backward states exhibit high overlap, the system is already evolving near-optimally. In this case, the action of the Hamiltonian term $\mathfrak{h}_j$ associated with control $u_j(t)$ is likely to diminish the overlap between these states. This implies that the optimal adjustment to the control $\Delta u_j^{(i)}(t)$ will be relatively small. Conversely, when the forward and backward states are significantly different, a substantial modification to the control $u_j(t)$ is often necessary. If the action of $\mathfrak{h}_j(t)$ increases the overlap between these states, it suggests that this control should be adjusted accordingly.

Appendix D

Mathieu Equation

This Section presents a detailed solution to the multi-dimensional Mathieu equation (Eq. (4.9)), which models the behavior of particles in traps, such as Paul traps. The coupled system of Mathieu equations is given by

$$\frac{d^2\vec{r}}{d\tau^2} + \Big(\mathbf{P} - 2\cos(2\tau)\mathbf{Q}\Big)\vec{r} = 0 \ , \tag{D.1}$$

where $\mathbf{P}$ and $\mathbf{Q}$ re symmetric matrices with dimensionless elements defined as

$$P_{ij} = \frac{4Z|e|V_{DC}M_{ij}}{m\omega_{rf}^2 r_0^2} \ , \qquad Q_{ij} = \frac{-2Z|e|V_{RF}N_{ij}}{m\omega_{rf}^2 r_0^2} \ . \tag{D.2}$$

Note that the minus sign in $\mathbf{Q}$ is consistent with the formulation in Eq. (4.9) due to extra sign in Eq. (D.1).

In order to solve Eq. (D.1), it is convenient to define the *ansatz*

$$\vec{r}(\tau) = \sum_{n=-\infty}^{\infty} \vec{C}_{2n}\Big(be^{i(2n+\nu)\tau} + ce^{-i(2n+\nu)\tau}\Big) \ , \tag{D.3}$$

with real vectors $\vec{C}_{2n}$, real phases ν and complex coefficients b, c that are determined by the initial conditions. Substituting in Eq. (D.1) yields the recursive relation

$$\mathbf{R}_{2n}\vec{C}_{2n} - \mathbf{Q}(\vec{C}_{2n-2} + \vec{C}_{2n+2}) = 0 \ , \tag{D.4}$$

with the compact matrix form

$$\mathbf{R}_{2n} = \mathbf{P} - (2n+\nu)^2\mathbb{I} \ . \tag{D.5}$$

From Eq. (D.4), it follows a recursive relation that specifies the coefficients $\vec{C}_{2n}$ in terms of the anterior and posterior terms $\vec{C}_{2n-2}$ and $\vec{C}_{2n+2}$, respectively, namely

$$\vec{C}_{2n} = \mathbf{R}_{2n}^{-1}\mathbf{Q}\left(\vec{C}_{2n-2} + \vec{C}_{2n+2}\right) \ . \tag{D.6}$$

Similarly, setting $n = 1$ in Eq. (D.4), yields

$$\mathbf{Q}\vec{C}_0 = \mathbf{R}_2\vec{C}_2 - \mathbf{Q}\vec{C}_4 \ . \tag{D.7}$$

Substituting recursively Eq. (D.6) into Eq. (D.7) yields

$$\mathbf{Q}\vec{C}_0 = \Big(\mathbf{R}_2 - \mathbf{Q}\mathbf{R}_4^{-1}\mathbf{Q} - \mathbf{Q}\mathbf{R}_4^{-1}\mathbf{Q}\mathbf{R}_6^{-1}\mathbf{Q}\mathbf{R}_4^{-1}\mathbf{Q} - \cdots\Big)\vec{C}_2 \ , \tag{D.8}$$

which allows finding an expression for $\vec{C}_2$ in terms of the matrices $\mathbf{Q}, \mathbf{R}_{2n}$ and $\vec{C}_0$

$$\vec{C}_2 = \Big(\mathbf{R}_2 - \mathbf{Q}\mathbf{R}_4^{-1}\mathbf{Q} - \mathbf{Q}\mathbf{R}_4^{-1}\mathbf{Q}\mathbf{R}_6^{-1}\mathbf{Q}\mathbf{R}_4^{-1}\mathbf{Q} - \cdots\Big)^{-1}\mathbf{Q}\vec{C}_0 \ . \tag{D.9}$$

This expression generalizes for any $\vec{C}_{2n}$. In order to determine the exponents ν in Eq. (D.3), it is convenient to use a different arrangement of Eq. (D.4) an evaluate for $n = 0$, which results in $\mathbf{Q}\vec{C}_2 = \mathbf{R}_0\vec{C}_0 - \mathbf{Q}\vec{C}_{-2}$ and, hence, allows finding an alternative formulation for $\vec{C}_2$, namely

$$\vec{C}_2 = \mathbf{Q}^{-1}\Big(\mathbf{R}_0 - \mathbf{Q}\mathbf{R}_{-2}^{-1}\mathbf{Q} - \mathbf{Q}\mathbf{R}_{-2}^{-1}\mathbf{Q}\mathbf{R}_{-4}^{-1}\mathbf{Q}\mathbf{R}_{-2}^{-1}\mathbf{Q} - \cdots\Big)\vec{C}_0 \ . \tag{D.10}$$

Comparing Eqs. (D.9) and (D.10), yields the relation

$$\begin{aligned}\mathbf{W} \equiv \mathbf{Q}&\left[\mathbf{R}_2 - \mathbf{Q}\mathbf{R}_4^{-1}\mathbf{Q} - \mathbf{Q}\mathbf{R}_4^{-1}\mathbf{Q}\mathbf{R}_6^{-1}\mathbf{Q}\mathbf{R}_4^{-1}\mathbf{Q} - \cdots\right]^{-1}\mathbf{Q} \\ &- \left[\mathbf{R}_0 - \mathbf{Q}\mathbf{R}_{-2}^{-1}\mathbf{Q} - \mathbf{Q}\mathbf{R}_{-2}^{-1}\mathbf{Q}\mathbf{R}_{-4}^{-1}\mathbf{Q}\mathbf{R}_{-2}^{-1}\mathbf{Q} - \cdots\right] = \mathbf{0} \ .\end{aligned} \tag{D.11}$$

The values of the frequencies ν in Eq. (D.3) thus correspond to the solutions to

$$\det(\mathbf{W}) = 0 \ , \tag{D.12}$$

and are thus given in terms of the dimensionless variables in Eq. (D.2).

Solving Eq. (D.12) and subsequently determining the coefficients $\vec{C}_{2n}$ (Eq. (D.10)) that characterize the ion trajectory requires constructing an infinite series. To simplify the analysis, a common approximation truncates this series at the lowest order (*i.e.*, $n = \pm 1$), assuming $\vec{C}_{\pm 4}, \vec{C}_{\pm 6}, \cdots \approx \vec{0}$, resulting in a finite expansion. This approach typically provides an accurate estimate of the ion's trajectory, $\vec{r}(t)$, which depends on the specific values of the parameters in Eq. (D.2).

Not all parameter combinations yield bounded solutions and stable dynamics. Stable orbits occur when the field parameters satisfy $P_{ij}, Q_{ij} \ll 1$. These conditions require a sufficiently high ω_{rf} to ensure that the rapidly oscillating field reverses polarity fast enough to prevent the ion from escaping along the transiently anti-confining direction. This rapid oscillation creates a time-averaged potential well that effectively confines the ion in all three dimensions, leading to the solutions in Eq. (4.11) of the Main text.

Appendix E

Classical Electrodynamics

This Section provides an overview of the key equations describing electromagnetic fields, which are essential for understanding the light-matter interactions discussed throughout this thesis.

The fundamental equations of classical electrodynamics govern the interaction between charged particles and electromagnetic fields. Maxwell's equations establish the relationships between the electric and magnetic fields as follows [111]

$$\vec{\boldsymbol{\nabla}} \cdot \vec{E}(\vec{r},t) = \frac{1}{\epsilon_0}\rho(\vec{r},t) \ , \tag{E.1a}$$

$$\vec{\boldsymbol{\nabla}} \cdot \vec{B}(\vec{r},t) = 0 \ , \tag{E.1b}$$

$$\vec{\boldsymbol{\nabla}} \times \vec{E}(\vec{r},t) = -\frac{\partial \vec{B}(\vec{r},t)}{\partial t} \ , \tag{E.1c}$$

$$\vec{\boldsymbol{\nabla}} \times \vec{B}(\vec{r},t) = \frac{1}{c^2}\frac{\partial \vec{E}(\vec{r},t)}{\partial t} + \frac{1}{\epsilon_0 c^2}\vec{J}(\vec{r},t) \ , \tag{E.1d}$$

where $\rho(\vec{r},t)$ is the charge density, $\vec{J}(\vec{r},t)$ is the current density, $\vec{E}(\vec{r},t)$ is the electric field, and $\vec{B}(\vec{r},t)$ is the magnetic field. The electromagnetic fields can be expressed in terms of a scalar potential $U(\vec{r},t)$ and a vector potential $\vec{A}(\vec{r},t)$, which are related to the fields by

$$\vec{E}(\vec{r},t) = -\frac{\partial \vec{A}(\vec{r},t)}{\partial t} - \vec{\boldsymbol{\nabla}} U(\vec{r},t) \ , \tag{E.2a}$$

$$\vec{B}(\vec{r},t) = \vec{\boldsymbol{\nabla}} \times \vec{A}(\vec{r},t) \ . \tag{E.2b}$$

The potentials $\{\vec{A}(\vec{r},t), U(\vec{r},t)\}$ are not uniquely defined, as different pairs of potentials can produce the same electromagnetic fields. Such pairs are related through a gauge transformation [111]

$$\vec{A}'(\vec{r},t) = \vec{A}(\vec{r},t) + \vec{\boldsymbol{\nabla}} F(\vec{r},t) \ , \tag{E.3a}$$

$$U'(\vec{r},t) = U(\vec{r},t) - \frac{\partial F(\vec{r},t)}{\partial t} \ , \tag{E.3b}$$

where $F(\vec{r},t)$ is an arbitrary scalar field. The freedom associated with the potentials can be constrained by imposing specific gauge conditions. Common choices include the Lorentz gauge, the Coulomb gauge, and the dipole gauge. For the purposes of this analysis, the Coulomb gauge is adopted, characterized by the condition

$$\vec{\boldsymbol{\nabla}} \cdot \vec{A}(\vec{r},t) = 0 \ . \tag{E.4}$$

Assuming a charge-free region (*i.e.* $\rho = 0$, $\vec{J} = 0$), Eqs. (E.1d) and (E.2b) yield the following relation

$$\frac{1}{c^2}\frac{\partial \vec{E}(\vec{r},t)}{\partial t} = \vec{\boldsymbol{\nabla}} \times \vec{B}(\vec{r},t) = \vec{\boldsymbol{\nabla}} \times \Big(\vec{\boldsymbol{\nabla}} \times \vec{A}(\vec{r},t)\Big) \ . \tag{E.5}$$

Using the vector identity for the curl of a curl, one obtains

$$\vec{\boldsymbol{\nabla}} \times \Big(\vec{\boldsymbol{\nabla}} \times \vec{A}(\vec{r},t)\Big) = \vec{\boldsymbol{\nabla}} \cdot \Big(\vec{\boldsymbol{\nabla}} \cdot \vec{A}(\vec{r},t)\Big) - \vec{\boldsymbol{\nabla}}^2 A(\vec{r},t) \ . \tag{E.6}$$

Imposing the Coulomb gauge (Eq. (E.4)), implies

$$\frac{1}{c^2}\frac{\partial \vec{E}(\vec{r},t)}{\partial t} = -\vec{\boldsymbol{\nabla}}^2 A(\vec{r},t) \ . \tag{E.7}$$

Substituting this into the equation for the electric field $\vec{E}(\vec{r},t)$ from Eq. (E.2a), the equation of motion for the vector potential $\vec{A}(\vec{r},t)$ is obtained

$$\frac{1}{c^2}\frac{\partial^2 \vec{A}(\vec{r},t)}{\partial t^2} = \vec{\boldsymbol{\nabla}}^2 A(\vec{r},t) \ . \tag{E.8}$$

This is a wave equation with a plane wave solution in charge-free space, given by

$$\vec{A}(\vec{r},t) = A_0 \vec{\epsilon} \exp\Big(i(\vec{k}^T \cdot \vec{r} - \omega t)\Big) + A_0^* \vec{\epsilon} \exp\Big(-i(\vec{k}^T \cdot \vec{r} - \omega t)\Big) \ . \tag{E.9}$$

where $A_0 = |A_0| e^{i\phi}$ denotes the amplitude of the vector potential, $\vec{\epsilon}$ is a unit vector representing the polarization direction of the wave, $\vec{k}$ is the wave vector indicating the direction of propagation, and ω is the wave frequency. These quantities satisfy the dispersion relation

$$\|\vec{k}\| = \frac{\omega}{c} \ . \tag{E.10}$$

From the vector potential (Eq. (E.9)), the electromagnetic fields $\vec{E}(\vec{r},t)$ and $\vec{B}(\vec{r},t)$ can be derived as

$$\vec{E}(\vec{r},t) = |E_0| \vec{\epsilon} \cos\Big(\vec{k}^T \cdot \vec{r} - \omega t + \phi\Big) \ , \tag{E.11a}$$

$$\vec{B}(\vec{r},t) = |B_0| \vec{b} \cos\Big(\vec{k}^T \cdot \vec{r} - \omega t + \phi\Big) \ , \tag{E.11b}$$

where the identity

$$\vec{\boldsymbol{\nabla}} \times \Big(\phi \vec{v}\Big) = \Big(\vec{\boldsymbol{\nabla}} \phi\Big) \times \vec{v} + \phi \Big(\vec{\boldsymbol{\nabla}} \times \vec{v}\Big) \tag{E.12}$$

was employed, and defined the following quantities

$$E_0 = 2i\omega A_0 \ , \qquad B_0 = 2i\|\vec{k}\|A_0 \ , \tag{E.13}$$

where the magnetic field polarization vector $\vec{b}$ is given by

$$\vec{b} = \frac{\vec{k} \times \vec{\epsilon}}{\|\vec{k}\|} \ . \tag{E.14}$$

Appendix F

Supplementary Information for Chapter 5

In this Section, we provide further details on various aspects related to Chapter 5, including proofs of key claims, additional insights into numerical optimization, and examples demonstrating the applicability of the method.

F.1 Absence of symmetries in the system Hamiltonian

We will show here that there is no symmetry in the Hamiltonian

$$H(t) = \sum_{j=1}^{n} f_j(t) Z_j + g \sum_{j=1}^{n-1} X_j X_{j+1} + \sum_{j \in \{1,n\}} w_j(t) X_j \tag{F.1}$$

for $g \neq 0$ and general time-dependent functions $f_j(t)$ and $w_j(t)$, *i.e.*

> there is no n-qubit operator A^n (besides multiples of the identity) that commutes with each of the operators $Z_1, Z_2, \ldots, Z_n$, X_1, X_n and $\sum_{j=1}^{n} X_j X_{j+1}$.

The requirement to commute with each of the operators $Z_1, Z_2, \ldots, Z_n$ implies that A^n can be expanded in terms of tensor-products of $\mathbb{1}$ and Z terms only.

The requirement to also commute with X_1 and X_n then implies that A_n is of the form

$$A^n = \mathbb{1} \otimes D^n \otimes \mathbb{1} \ , \tag{F.2}$$

with an $n-2$-qubit operator D^n that can be expanded in terms of tensor-products of $\mathbb{1}$ and Z terms, or more explicitly as

$$A^n = \mathbb{1}_1 \otimes F^n \otimes \mathbb{1}_{n-1} \otimes \mathbb{1}_n + \mathbb{1}_1 \otimes G^n \otimes Z_{n-1} \otimes \mathbb{1}_n \ , \tag{F.3}$$

with $n-3$-qubit operators F_n and G_n that can be expanded in terms of tensor-products of $\mathbb{1}$ and Z terms,

In order to address commutativity with

$$\sum_{j=1}^{n-1} X_j X_{j+1} = H_x^n \ , \tag{F.4}$$

it is instructive to express H_x^n as

$$H_x^n = H_x^{n-1} \otimes \mathbb{1}_n + \mathbb{1}_{1\ldots n-1} \otimes X_{n-1} \otimes X_n \ . \tag{F.5}$$

The commutator $[A^n, H_x^n]$ thus reads

$$\begin{aligned} [A^n, H_x^n] &= [\mathbb{1}_1 \otimes G^n \otimes Z_{n-1}, H_x^{n-1}] \otimes \mathbb{1}_n & \text{(F.6)} \\ &+ 2i\mathbb{1}_1 \otimes G^n \otimes Y_{n-1} \otimes X_n & \text{(F.7)} \\ &+ [\mathbb{1}_1 \otimes F^n \otimes \mathbb{1}_{n-1}, H_x^{n-1}] \otimes \mathbb{1}_n \ . & \text{(F.8)} \end{aligned}$$

Since the term in (F.7) is the only term with a factor X_n, the commutator can vanish only if G^n vanishes. If this is the case, however, then also the right-hand-side in (F.6) vanishes, such that the commutator reduces to

$$[A^n, H_x^n] = [\mathbb{1}_1 \otimes F^n \otimes \mathbb{1}_{n-1}, H_x^{n-1}] \otimes \mathbb{1}_n \ , \tag{F.9}$$

with an operator

$$A^{n-1} = \mathbb{1}_1 \otimes F^n \otimes \mathbb{1}_{n-1} \ , \tag{F.10}$$

that is exactly of the form of Eq. (F.2), but for $n-1$ instead of n qubits.

The result to be proven thus holds for an n-qubit system, provided that it holds for an $n-1$ qubits system, and since one can readily verify it explicitly for a 2 qubits system, the proof is completed by induction.

F.2 More details on numerical optimisation

Computing infidelity and gradient

In the numerical optimizations of Chapter 5, we employ the GRAPE (Gradient Ascent Pulse Engineering) methodology (see Appendix C) to optimize the control fields of the system Hamiltonian. GRAPE is chosen primarily for its efficient gradient computation, which accelerates convergence in high-dimensional optimization problems. However, other optimization methods, such as those described in Appendix C, are equally compatible and could be used depending on the specific requirements of the problem.

The time-dependent Hamiltonian $H(t)$ (Eq. (5.3)) is decomposed into two parts: a constant, non-controllable component H_0 and a controllable part $\sum_{j=1}^{N_h} u_j(t) H_j$, where N_h is

the number of control terms. We assume the control parameters $u_j(t)$ are piecewise constant, with the total pulse duration T divided into M intervals of equal length Δt. Within each interval, the driving amplitude $u_j(t)$ is held constant, simplifying the numerical implementation.

The optimization process aims to minimize the infidelity, defined by Eq. (5.19) or Eq. (5.34), by tuning the set of control amplitudes $\{u_{jl} : 1 \leq j \leq N_h, 1 \leq l \leq M\}$ and the total duration T. To facilitate efficient evaluation of the infidelity during optimization, the operator basis elements $\{\mathfrak{a}_j\}$ are normalized such that $\mathrm{Tr}(\mathfrak{a}_j \mathfrak{a}_k) = \delta_{jk}$. This normalization simplifies the propagation of operators according to Eq. (5.10) and the computation of the overlap between the target coefficient vector $\boldsymbol{a}_T$ and the final coefficient vector $\boldsymbol{a}(T)$, obtained from an initial condition $\boldsymbol{a}(0)$.

Within the IQC framework, the control problem is thus formulated as finding the final coefficient vector $\boldsymbol{a}(T)$ that minimizes the infidelity given in Eq. (5.20) for state preparation, or Eq. (5.35) for quantum gate implementation. The evolution of $\boldsymbol{a}(t)$ is governed by the adjoint representation matrix $K(t)$ of the system Hamiltonian $H(t)$, which can be written as

$$K(t) = K_0 + \sum_j u_j(t) K_j \ , \tag{F.11}$$

where K_0 and K_j are the adjoint representations of H_0 and H_j, respectively (see Eq. (5.11)). For a piecewise-constant control, the solution to $\dot{\boldsymbol{a}}(t) = K(t)\boldsymbol{a}(t)$ is given by

$$\boldsymbol{a}(T) = \mathcal{U}(t_M; t_{M-1}) \cdots \mathcal{U}(t_2; t_1)\mathcal{U}(t_1; t_0)\boldsymbol{a}(0) = \prod_{l=M}^{1} \mathcal{U}(t_l; t_{l-1})\boldsymbol{a}(0) \ , \tag{F.12}$$

for $t_l \in \{t_0 = 0, \cdots, t_M = T\}$, and where the time-evolution operator in each interval $[t_{l-1}, t_l]$ is simply

$$\mathcal{U}(t_l; t_{l-1}) = e^{\Delta t\left(K_0 + \sum_k u_{kl} K_k\right)} \ . \tag{F.13}$$

Importantly, since $K(t)$ is anti-hermitian, $\mathcal{U}(t_l; t_{l-1})$ is unitary.

To illustrate the computation of gradients, we focus on the cost function $\mathcal{J}$ from Eq. (5.20), as the result generalizes to Eq. (5.35) for gates. Following standard GRAPE (see Appendix C), we define the forward and backward propagated vectors

$$\begin{aligned} \boldsymbol{a}(t_m) &= \mathcal{U}(t_m; t_{m-1})\mathcal{U}(t_{m-1}; t_{m-2}) \ldots \mathcal{U}(t_1; t_0)\boldsymbol{a}(0) \ , \\ \boldsymbol{b}^\dagger(t_m) &= \boldsymbol{a}_T^\dagger \mathcal{U}(t_M; t_{M-1})\mathcal{U}(t_{M-1}; t_{M-2}) \ldots \mathcal{U}(t_{m+1}; t_m) \ . \end{aligned}$$

These vectors represent the operator $\mathcal{I}(t)$ and its time-reversed counterpart $\mathcal{I}_T(T-t)$ at $t = m\Delta t$ in the vector space of the basis elements.

The gradient of $\mathcal{J}$ with respect to c_{kl} can be computed similarly to Eq. (C.8), yielding

$$\begin{aligned}\frac{\partial \mathcal{J}}{\partial u_{kl}} &= -\left|\boldsymbol{a}_T \frac{\partial \mathcal{U}(T;0)}{\partial c_{kl}} \boldsymbol{a}(0)\right|^2 \\ &= -\left|\boldsymbol{a}_T \prod_{m=M}^{l+1} \mathcal{U}(t_m;t_{m-1}) \frac{\partial \mathcal{U}(t_l;t_{l-1})}{\partial u_{kl}} \prod_{m=l-1}^{1} \mathcal{U}(t_m;t_{m-1}) \boldsymbol{a}(0)\right|^2 \\ &= -\left|\boldsymbol{b}^\dagger(t_l) \frac{\partial \mathcal{U}(t_l;t_{l-1})}{\partial u_{kl}} \boldsymbol{a}(t_{l-1})\right|^2 . \end{aligned} \tag{F.14}$$

The derivative $\partial \mathcal{U}(t_l;t_{l-1})/\partial u_{kl}$ is approximated by the 2nd-order method [259], which is derived by retaining the first two terms of the expansion in Eq. (C.10) and replacing each Hamiltonian term $-iH_k$ with its corresponding adjoint K_k,

$$\frac{\partial \mathcal{U}(t_l;t_{l-1})}{\partial u_{kl}} = \mathcal{U}(t_l;t_{l-1}) \left(\Delta t K_k - \frac{\Delta t^2}{2} \left[K_0 + \sum_p u_{pl} K_p, K_k \right] \right) + \mathcal{O}(\Delta t^3) , \tag{F.15}$$

resulting in the gradient of the objective function

$$\frac{\partial \mathcal{J}}{\partial u_{kl}} = -\left| \boldsymbol{b}^\dagger(t_{l-1}) \left(\Delta t K_k - \frac{\Delta t^2}{2} \left[K_0 + \sum_p u_{pl} K_p, K_k \right] \right) \boldsymbol{a}(t_{l-1}) \right|^2 , \tag{F.16}$$

which is efficiently computed using matrix-vector multiplication. The most computationally demanding step is the multiplication of a matrix exponential with a vector to obtain $\boldsymbol{a}(t_m)$ and $\boldsymbol{b}^\dagger(t_m)$, but it can be done efficiently with the Krylov subspace method [262] owing to the sparsity of $K(t)$.

Since the optimization relies on numerically exact integration of Eq. (5.10), it is not constrained by adiabaticity. Consequently, the control protocol duration T can be minimized, limited only by the physical constraints of the system.

To compute the derivative of $\mathcal{J}$ with respect to the duration T, $\mathcal{J}$ is evaluated again for a slightly perturbed duration $T + dT$, while keeping the control amplitudes c_{kl} fixed. The derivative is then approximated as

$$\frac{\partial \mathcal{J}}{\partial T} \approx \frac{\mathcal{J}(T + dT) - \mathcal{J}(T)}{dT} . \tag{F.17}$$

Navigating the optimization landscape

Given suitably chosen initial and final conditions $\{\mathcal{I}(0), \mathcal{I}_T\}$ (or multiple pairs for quantum simulation tasks), the goal in IQC is to optimize the system Hamiltonian $H(t)$ such that it drives $\mathcal{I}(0)$ to $\mathcal{I}_T$. This is accomplished by minimizing a cost function $\mathcal{J}$, which quantifies the deviation from the desired target. The control parameters in $H(t)$ are fine-tuned iteratively to minimize $\mathcal{J}$, guided by the gradient-based optimization strategy derived in the previous Sec. F.2.

To efficiently navigate the optimization landscape, we analytically compute the gradient

of $\mathcal{J}$ with respect to the control parameters. Additionally, to accelerate convergence and improve stability, we approximate the Hessian of $\mathcal{J}$ using the L-BFGS method, which provides a reliable estimate of the curvature of the optimization landscape while maintaining low memory requirements, making it particularly suitable for large-scale problems. Once both the gradient and Hessian are determined, they are supplied to Matlab's *fmincon* function, which optimizes the control parameters and refines the system evolution toward the desired target.

In most cases, this optimization strategy succeeds after testing a few initial guesses for the controls. However, certain problems require more careful handling and a tailored approach. These challenging cases typically arise when the target Hamiltonian involves an effective interaction that scales with system size—such as the n-body operator $\prod_k Z_k$ in U_G. As n increases, the optimization landscape becomes more complex, characterized by numerous shallow local minima and extended plateaus, making convergence significantly more difficult.

To systematically overcome these challenges, we employ a three-step procedure. First, we impose the inherent symmetry of the control problem onto the control variables, ensuring that the optimization starts from a structured, physically meaningful ansatz

$$H_1^c(t) = g\sum_{j=1}^{n-1} X_j X_{j+1} + f_1(t)\sum_{j=1}^{n} Z_j + f_2(t)(Z_1 + Z_n) + w(t)(X_1 + X_n) \ , \tag{F.18}$$

which maintains symmetry across the chain except at the boundaries. This choice ensures consistency with the control targets and simplifies the optimization landscape. The optimization is performed sequentially for increasing system sizes, from $n = 5$ to $n = 50$ in steps of five, using the optimal control from $n - 5$ as the initial guess for n.

Once a solution is obtained for $H_1^c(t)$, we refine it by optimizing with a system Hamiltonian that preserves only inversion symmetry

$$H_2^c(t) = g\sum_{j=1}^{n-1} X_j X_{j+1} + \sum_{j=1}^{\lfloor (n+1)/2 \rfloor} f_j(t)(Z_j + Z_{n+1-j}) + w(t)(X_1 + X_n) \ , \tag{F.19}$$

allowing for more flexibility in the control landscape while retaining some symmetry constraints. The final control from the previous step serves as the initial guess. Finally, we remove all symmetry constraints and optimize using the fully general control Hamiltonian

$$H_3^c(t) = g\sum_{j=1}^{n-1} X_j X_{j+1} + \sum_{j=1}^{n} f_j(t) Z_j + \sum_{j\in\{1,n\}} w_j(t) X_j \ . \tag{F.20}$$

This step provides the highest degree of flexibility, enabling the control parameters to adapt freely to the optimization landscape. Each optimisation step is done with a maximum of 1000 function-and-gradient evaluations. To further enhance convergence and avoid local traps, we introduce small random perturbations to the initial guess at every step and

explore 12 nearby solutions in parallel. In many cases, the target infidelity is already reached with $H_1^c(t)$ or $H_2^c(t)$, eliminating the need for the fully unconstrained optimization.

As explained in Chapter 5, IQC not only optimizes the control parameters of $H(t)$, but also allows for the optimization of the total time T required for the task. The optimal time T is thus system-dependent, and we have found the following results: for the optimizations of H_G, H_C, $T \approx n\pi/2g$; for H_D, $T \approx n\pi/g$ for H_D. In all three cases, the number of time bins in the piecewise control pulse is $M = 10n$. For U_C and U_D, $T \approx 2\pi g$ and $M = 10n$. For U_G, $T \approx 2n\pi/g$ and $M = 20n$.

F.3 Relation between the state infidelity bound and the operator infidelity

Given the system Hamiltonian $H(t)$ (Eq. (5.36)), the initial condition $\mathcal{I}(0) = \sum_j Z_j$ and a control target $\mathcal{I}_T$ that coincides with the target Hamiltonian H_T (which includes the cases of H_G and H_C defined in Sec. 5.3.1), the bound

$$\mathcal{B} = \frac{\langle\Psi(T)|\, H_T\, |\Psi(T)\rangle - E_0}{E_1 - E_0} \tag{F.21}$$

in the state infidelity defined in Eq. (5.29) depends on the operator infidelity $\mathcal{J}$ via the linear relation

$$\mathcal{B} = \frac{n\mathcal{J} - s}{E_1 - E_0}\ , \tag{F.22}$$

with a term s that, under assumptions on typicality, becomes vanishingly small in the limit $n \to \infty$. This is proven in the following.

Given the requirement that $\mathcal{I}_T = H_T$, the expectation value in Eq. (F.21) satisfies the equality

$$\langle\Psi(T)|\, H_T\, |\Psi(T)\rangle = \langle\Psi(0)|\, \tilde{\mathcal{I}}(T)\, |\Psi(0)\rangle\ , \tag{F.23}$$

where $\tilde{\mathcal{I}}(T) = U^\dagger(T)\mathcal{I}_T U(T)$, $|\Psi(0)\rangle$ is the ground state of $\mathcal{I}(0)$, and E_0 the ground energy of both H_T and $\mathcal{I}(0)$. Using the relations

$$\mathrm{tr}(\mathcal{I}(T)\mathcal{I}_T) = \mathrm{tr}(U(T)\mathcal{I}(0)U^\dagger(T)\mathcal{I}_T) = \mathrm{tr}(\mathcal{I}(0)\tilde{\mathcal{I}}(T)) \tag{F.24}$$

and $\mathrm{tr}(\mathcal{I}_T^2) = \mathrm{tr}(\mathcal{I}^2(0))$, the operator infidelity in Eq. (5.19) can be expressed as

$$\mathcal{J} = 1 - \frac{\mathrm{tr}(\mathcal{I}(0)\tilde{\mathcal{I}}(T))}{\mathrm{tr}(\mathcal{I}^2(0))}\ . \tag{F.25}$$

If the control target is reached exactly, the identity $\tilde{\mathcal{I}}(T) = \mathcal{I}(0)$ holds, and any imperfec-

tion of the optimal control solution can be captured by the deviation

$$\Delta\mathcal{I} = \mathcal{I}(0) - \tilde{\mathcal{I}}(T) \ . \tag{F.26}$$

The deviation $\Delta\mathcal{I}$ can be expanded in terms of the operators $\mathfrak{a}_j$ (Eqs. (5.37)) as $\Delta\mathcal{I} = \sum_j c(\mathfrak{a}_j)\mathfrak{a}_j$, with expansion coefficients

$$c(\mathfrak{a}_j) = \frac{\mathrm{Tr}(\mathfrak{a}_j \ \Delta\mathcal{I})}{\mathrm{Tr}\left(\mathfrak{a}_j^2\right)} \ . \tag{F.27}$$

The operator infidelity can be expressed as

$$\mathcal{J} = \frac{\mathrm{tr}(\mathcal{I}(0)\Delta\mathcal{I})}{\mathrm{tr}(\mathcal{I}^2(0))} \ . \tag{F.28}$$

With $\mathcal{I}(0) = \sum_j Z_j$, $\mathrm{tr}(\mathcal{I}^2(0)) = n2^n$, and the overlaps $\mathrm{tr}(\mathcal{I}(0)Z_j) = 2^n$, and $\mathrm{tr}(\mathcal{I}(0)\mathfrak{a}_j) = 0$ for all operators $\mathfrak{a}_j$ that are not single-spin Z operators (*i.e.* Eqs. (5.37b) to (5.37j)), the operator infidelity reduces to

$$\mathcal{J} = \frac{\sum_j c(Z_j)}{n} \ , \tag{F.29}$$

in terms of the expansion coefficients $c(Z_j)$ defined in Eq. (F.27).

Given the ground state energy $\langle\Psi(0)|\,\mathcal{I}(0)\,|\Psi(0)\rangle = E_0$, the bound $\mathcal{B}$ can be expressed as

$$\mathcal{B} = -\frac{\langle\Psi(0)|\,\Delta\mathcal{I}\,|\Psi(0)\rangle}{E_1 - E_0} \ . \tag{F.30}$$

With $\Delta\mathcal{I}$ expanded in terms of the operators $\mathfrak{a}_j$ (Eqs. ((5.37)) and the expectation values $\langle\Psi(0)|\,Z_j\,|\Psi(0)\rangle = -1$, $\langle\Psi(0)|\prod_j Z_j\,|\Psi(0)\rangle = (-1)^n$, and $\langle\Psi(0)|\,\mathfrak{a}_j\,|\Psi(0)\rangle = 0$ for all other cases (*i.e.* Eqs. (5.37b) to (5.37i)), this yields

$$\mathcal{B} = \frac{\sum_j c(Z_j) - s}{E_1 - E_0} \ , \tag{F.31}$$

where $s = (-1)^n c(\prod_j Z_j)$, and the expansion coefficient $c(\prod_j Z_j)$ is defined in Eq. (F.27). Together with Eq. (F.29), this results in Eq. (F.22).

While it is conceivable that $\Delta\mathcal{I}$ is proportional to the operator $\prod_j Z_j$, one would expect that, typically, $\Delta\mathcal{I}$ would have contributions from all operators $\mathfrak{a}_j$ in Eq. (5.37). In estimating the magnitude of s, we will thus assume the expansion coefficients $c(\mathfrak{a}_j)$ to be random with each coefficient resulting from a distribution with zero mean and standard deviation δ. The typical magnitude of the term

$$n\mathcal{J} = \sum_{j=1}^{n} c(Z_j) \tag{F.32}$$

is then given by its standard deviation, *i.e.* by $\sqrt{n}\delta$. The typical magnitude of $c\left(\prod_j Z_j\right)$,

on the other hand, is given by δ. The term s thus becomes negligible as compared to the term $n\mathcal{J}$ for large systems.

Fig. F.1 depicts the deviation of the actual results of Fig. 5.2a from the linear dependence $\mathcal{B} = \frac{n\mathcal{J}}{E_1 - E_0}$ as a function of the system size n. The figure shows that the deviation decays rapidly with n. The actual results thus follow the linear dependence in good approximation.

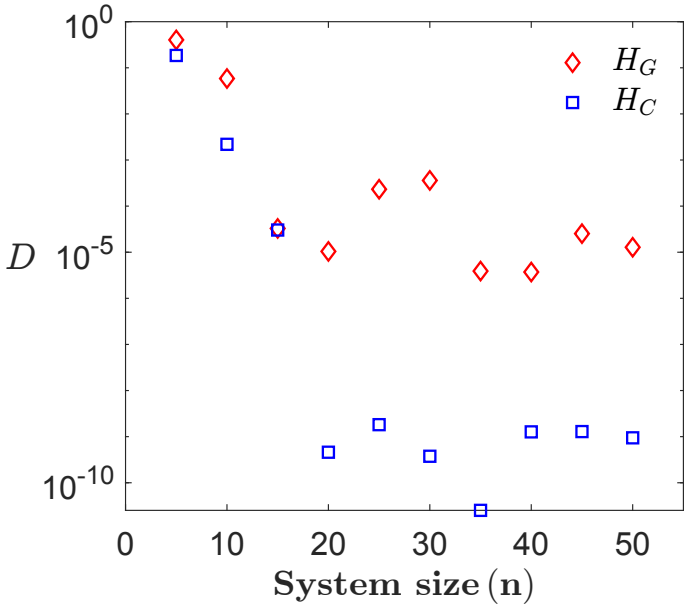

Figure F.1: Deviation $D = |1 - (E_1 - E_0)\mathcal{B}/n\mathcal{J}| = |s|/n\mathcal{J}$, in log-scale, from the linear relation between the bound $\mathcal{B}$ on state infidelity and operator infidelity $\mathcal{J}$ that is expected to hold in the limit $n \to \infty$ following Eq. (F.22). The deviation obtained from the data shown in Fig. 5.2a decays rapidly with n, consistently with Eq. (F.22).

F.4 Lie algebra of the hexagonal spin ladder

In this Section, we construct the Lie algebra generated by the operators in Eq. (5.64) for the spin ladder depicted in Fig. 5.7 and determine its scaling with the number of qubits n. Specifically, we show that the dimension of the Lie algebra grows as $(25n^2 - 40n + 12)/32$ for a system of $n = 4n_h + 2$ spins, where n_h is the number of hexagons.

To derive this scaling, we begin by analyzing two non-interacting spin chains. The Lie algebra for the top chain is generated by the operators in Eqs. (5.64a) and (5.64b). Introducing the shorthand notation $X_{jk} = \prod_{i=1}^{k} X_{i+j}^1$, we define the following operators

$$\overline{YZ}_{jk} = Y_j^1 X_{jk} Z_{j+k+1}^1 \,, \tag{F.33a}$$

$$\overline{ZY}_{jk} = Z_j^1 X_{jk} Y_{j+k+1}^1 \,, \tag{F.33b}$$

$$\overline{YY}_{jk} = Y_j^1 X_{jk} Y_{j+k+1}^1 \,, \tag{F.33c}$$

$$\overline{ZZ}_{jk} = Z_j^1 X_{jk} Z_{j+k+1}^1 \,, \tag{F.33d}$$

where j and k are indices specifying the positions and lengths of the operators. The Lie algebra is then spanned by the operators γ_{jk}, with $j \in [1, m-1]$ and $k \in [0, m-j-1]$, defined as

$$\gamma_{jk} = \begin{cases} \overline{YZ}_{jk}, & \text{for odd } j \text{ and odd } k \ , \\ \overline{YY}_{jk}, & \text{for odd } j \text{ and even } k \ , \\ \overline{ZY}_{jk}, & \text{for even } j \text{ and odd } k \ , \\ \overline{ZZ}_{jk}, & \text{for even } j \text{ and even } k \ . \end{cases} \tag{F.34}$$

The Lie algebra for the bottom chain is generated by Eqs. (5.64c) and (5.64d), and it includes (besides Eqs. (5.64c) and (5.64d))

$$X^2_{2j} Y^2_{2j+1} X^2_{2j+2} \ , \tag{F.35}$$

with $j \in [1, (m-3)/2]$. With $s \in \{-1, 1\}$, $j \in [1, (m-1)/2]$, $k \in [0, m-j-1]$, and with Γ_{2j} adopting the four different values

$$\Gamma_{2j} = \begin{cases} X^2_{2j-1} X^2_{2j} \ , \\ Y^2_{2j-1} \mathbb{1}^2_{2j} \ , \end{cases} \tag{F.36}$$

for $s = -1$,

$$\Gamma_{2j} = \begin{cases} X^2_{2j} Z^2_{2j+1} \ , \\ \mathbb{1}^2_{2j} Y^2_{2j+1} \ , \end{cases} \tag{F.37}$$

for $s = 1$, the Lie algebra generated by the full set of operators in Eq. (5.64) contains the additional terms

$$X^1_{2j+s} \Gamma_{2j} \ , \tag{F.38a}$$
$$\overline{ZY}_{2j+s,k} \Gamma_{2j} \ , \tag{F.38b}$$
$$\overline{ZY}_{2j-1-k+s,k} \Gamma_{2j} \ , \tag{F.38c}$$

for even k, and

$$\overline{ZZ}_{2j+s,k} \Gamma_{2j} \ , \tag{F.38d}$$
$$\overline{ZY}_{2j+s,k} \Gamma_{2j} Y^2_{2j+k+s+1} \ , \tag{F.38e}$$
$$\overline{ZY}_{2j+s,k} \Gamma_{2j} X^2_{2j+k+s} Z^2_{2j+k+s+1} \ , \tag{F.38f}$$
$$\overline{ZY}_{2j+s,k} \Gamma_{2j} X^2_{2j+k+s+1} Z^2_{2j+k+s+2} \ , \tag{F.38g}$$
$$\overline{YY}_{2j-1-k+s,k} \Gamma_{2j} \ , \tag{F.38h}$$
$$\overline{ZY}_{2j-1-k+s,k} Y^2_{2j-1-k+s} \Gamma_{2j} \ , \tag{F.38i}$$
$$\overline{ZY}_{2j-1-k+s,k} X^2_{2j-2-k+s} Z^2_{2j-1-k+s} \Gamma_{2j} \ , \tag{F.38j}$$
$$\overline{ZY}_{2j-1-k+s,k} X^2_{2j-1-k+s} X^2_{2j-k+s} \Gamma_{2j} \ , \tag{F.38k}$$

for odd k.

Given that Eqs. (5.64c)-(5.64d) contain $(n-2)/2$ elements, Eq. (F.34) includes $(n^2/8-n/4)$ elements (encompassing Eqs. (5.64a) and (5.64b)), Eq. (F.35) contributes with $(n-6)/4$ elements, and Eq. (F.38) adds $(21n^2-56n+92)/32$ operators, the size of the Lie algebra grows as $(25n^2-40n+12)/32$ with the number of qubits $n=2+4n_h$ defined in terms of the number of hexagons n_h.

For $k=1$, $s=1$ and $\Gamma_{2j}=X^2_{2j}Z^2_{2j+1}$, the operator in Eq. (F.38i) reduces to the 6-body plaquette operators $P_j=Z^1_{2j-1}X^1_{2j}Y^1_{2j+1}Y^2_{2j-1}X^2_{2j}Z^2_{2j+1}$ in Eq. (5.65).

Appendix G

Supplementary Information for Chapter 6

In this Section, we provide additional details regarding Chapter 6, focusing on the parametrizations used to determine the optimal form of the invariant operator $\mathcal{I}(t)$ in Eq. (3.57). These parametrizations are designed to achieve ion shuttling with no motional excitation while satisfying additional optimality conditions.

G.1 Parametrization for invariant-based shuttling

Designing a control Hamiltonian $H(t)$ of the form given in Eq. (3.52) to transport an ion from the ground state of an initial Hamiltonian to the ground state of a final Hamiltonian requires appropriately defining the matrix $\boldsymbol{M}(t)$ and vector $\vec{F}(t)$. These are determined by their relationship with the invariant's defining quantities: the matrix $\boldsymbol{R}(t)$ and the vector $\vec{r}_c(t)$. Notably, for any arbitrary selection of $\boldsymbol{R}(t)$ and $\vec{r}_c(t)$, the corresponding $\boldsymbol{M}(t)$ and $\vec{F}(t)$ will yield valid shuttling protocols that guarantee ground-state-to-ground-state transport.

This inherent flexibility in the choice of $\boldsymbol{R}(t)$ and $\vec{r}_c(t)$ not only ensures the desired state transfer but also provides valuable degrees of freedom for optimizing additional criteria. These criteria may include minimizing the ion's displacement from the trap center, reducing energy consumption, or enhancing robustness against experimental imperfections. By strategically tailoring these parameters, one can systematically construct protocols that achieve a desirable balance between theoretical efficiency and practical feasibility.

In this Section, we explore a specific parametrization for $\boldsymbol{R}(t)$ and $\vec{r}_c(t)$ that effectively leverages this inherent freedom.

As outlined in the Main text, we introduce a set of $N_a + 1$ basis functions $\{\vec{z}_i(t)\}_{i=0}^{N_a}$ and $N_b + 1$ basis matrices $\{\boldsymbol{R}_i(t)\}_{i=0}^{N_b}$ to express these quantities as

$$\vec{r}_c(t) = \vec{z}_0(t) + \sum_{i=1}^{N_a} a_i \vec{z}_i(t) \ , \tag{G.1a}$$

$$\boldsymbol{R}(t) = \boldsymbol{R}_0(t) + \sum_{i=1}^{N_b} b_i \boldsymbol{R}_i(t) \ . \tag{G.1b}$$

The functions $\vec{z}_0(t)$ and $\boldsymbol{R}_0(t)$ are chosen to satisfy the boundary conditions specified in Eq. (6.6), meaning that setting $\vec{r}_c(t) = \vec{z}_0(t)$ and $\boldsymbol{R}(t) = \boldsymbol{R}_0(t)$ would already provide a valid solution. However, to enhance the flexibility of the parametrization, we introduce the remaining vectors $\vec{z}_{i>0}(t)$ and matrices $\boldsymbol{R}_{i>0}(t)$. These functions are designed to vanish at the boundaries, along with their first and second time derivatives, ensuring that they satisfy homogeneous boundary conditions. As a result, they influence the dynamics exclusively within the interior of the time interval without perturbing the prescribed boundary behavior.

The vector $\vec{z}_0(t)$ can be conveniently chosen as the lowest-degree polynomial that satisfies the associated boundary equations for each component. Specifically, each component of $\vec{z}_0(t)$ can be parametrized by the following function

$$f(\tau) = C_I + 10(C_F - C_I)\tau^3 - 15(C_F - C_I)\tau^4 + 6(C_F - C_I)\tau^5 \ , \tag{G.2}$$

where C_I and C_F refer to the initial and final values, respectively, and $\tau = t/T$ denotes the normalized time.

If additional constraints beyond the boundary conditions are imposed, higher-order polynomials become necessary. For instance, if the function is required to satisfy an intermediate constraint such as $f(\tau = 1/2) = C_J$, the polynomial must be modified accordingly to incorporate this condition while simultaneously preserving the original boundary requirements. One such suitable parametrization is given by

$$\begin{aligned} f(\tau) = C_I &+ 2(-11C_F - 21C_I + 32C_J)\tau^3 + (81C_F + 111C_I - 192C_J)\tau^4 \\ &+ 2(-45C_F - 51C_I + 96C_J)\tau^5 + 32(C_F + C_I - 2C_J)\tau^6 \ . \end{aligned} \tag{G.3}$$

The remaining functions $\vec{z}_{i>0}(t)$ are required to satisfy the homogeneous boundary conditions. While a similar polynomial expansion can be employed for each component of $\vec{z}_{i>0}(t)$, the following parametrization is often more suitable for problems involving fast dynamics

$$g(\tau) = \sin(\pi(1 + 2\omega_1)\tau) - \frac{1 + 2\omega_1}{1 + 2\omega_2} \sin(\pi(1 + 2\omega_2)\tau) \ , \tag{G.4}$$

where the coefficients $\omega_1, \omega_2 \in \mathbb{Z}$ are free parameters. Since $g(0) = g(1) = \dot{g}(0) = \dot{g}(1) = \ddot{g}(0) = \ddot{g}(1) = 0$, the function $g(\tau)$ indeed satisfies the homogeneous boundary conditions.

As in the case of $\vec{z}_0$,it may also be necessary to impose additional constraints on the function $g(\tau)$ for specific control problems. Of particular interest is the condition $g(\tau = 1/2) = 0$. To satisfy both the homogeneous boundary conditions and this additional constraint, a suitable set of functions is given by

$$\tilde{g}(\tau) = \frac{\omega_2 S_3 - \omega_3 S_2}{\omega_1 S_2 - \omega_2 S_1} \sin(\pi\omega_1\tau) + \frac{-\omega_1 S_3 + \omega_3 S_1}{\omega_1 S_2 - \omega_2 S_1} \sin(\pi\omega_2\tau) + \sin(\pi\omega_3\tau), \tag{G.5}$$

where we introduced the notation $S_i \equiv \sin(\pi\omega_i/2)$ and consider integer frequencies $\omega_1, \omega_2, \omega_3 \in \mathbb{Z}$ subject to $\omega_1 \neq \omega_2$.

Similarly, matrix $\mathbf{R}_0(t)$ that satisfies the boundary conditions in Eq. (6.6) can be conveniently expressed as

$$\mathbf{R}_0(\tau) = \begin{pmatrix} f_1(t) & 0 & 0 \\ 0 & f_2(t) & 0 \\ \vdots & \ddots & \vdots \\ 0 & \cdots & f_d(t) \end{pmatrix}, \tag{G.6}$$

where the functions $f_i(t)$ are polynomials of degree p that remain positive for all t. The boundary conditions are given by

$$f_i(0) = M_{I,ii}^{-1/4}\,, \quad f_i(T) = M_{F,ii}^{-1/4}\,, \tag{G.7a}$$

$$\dot{f}_i(0) = \ddot{f}_i(0) = \dot{f}_i(T) = \ddot{f}_i(T) = 0\,, \tag{G.7b}$$

where $M_{I,ii}$ and $M_{F,ii}$ denote the diagonal elements of the curvature matrices $\boldsymbol{M}_I$ and $\boldsymbol{M}_F$, which define the boundary conditions of the control problem.

These conditions are fulfilled by the control function defined in Eq. (G.2). Note that the non-negativity is also guaranteed because $C_I, C_F > 0$ and the control function in Eq. (G.2) has no minimum for $\tau \in (0, 1)$.

The matrices $\mathbf{R}_{i>0}(t)$ can be chosen following two different approaches. In the first approach, each matrix $\mathbf{R}_i(t)$ is constructed with entries comprising functions that individually satisfy the homogeneous boundary conditions. Subsequently, the positive definiteness of $\mathbf{R}(t)$ can be numerically verified at every instant of time using various methods, including eigenvalue analysis, the Sylvester criterion [217], or the calculation of moments.

Alternatively, each matrix $\mathbf{R}_{i>0}(t)$ can be decomposed using the *Cholesky decomposition* [263, 264] as

$$\mathbf{R}_i(t) = \mathbf{L}_i \mathbf{L}_i^\dagger\,, \tag{G.8}$$

where $\mathbf{L}_i$ is a lower-triangular matrix given by

$$\mathbf{L}_i(\tau) = \begin{pmatrix} g_{11}(t) & 0 & 0 \\ g_{21}(t) & g_{22}(t) & 0 \\ \vdots & \ddots & \vdots \\ g_{d1} & \cdots & g_{dd}(t) \end{pmatrix} . \tag{G.9}$$

Thus, it is sufficient to impose homogeneous boundary conditions on all functions $g_{ij}(t)$ to ensure that $\mathbf{L}_i\mathbf{L}_i^\dagger$ satisfies them as well.

For $\mathbf{L}_i\mathbf{L}_i^\dagger$ to be positive semi-definite, its diagonal elements must remain non-negative throughout the time domain [264]. This condition is automatically satisfied if the off-diagonal functions are selected from Eq. (G.4) and the diagonal elements are parameterized with $g^2(\tau)$, where each $g(\tau)$ is taken to correspond to a function of the form in Eq. (G.4). Ensuring that the expansion coefficients b_i are positive guarantees that $\mathbf{R}(t)$ remains positive semi-definite for all t.

Note that, although this method guarantees the positivity of $\boldsymbol{R}(t)$ at any time t, also limits the spectrum of valid solutions.

Appendix H

Supplementary Information for Chapter 7

This Section presents additional proofs, numerical evidence, and further explanations to complement the content of Chapter 7.

H.1 Power requirements

To assess the practicality of the entanglement generation control scheme presented in Chapter 7, we must consider its power consumption. This Section will compare the power requirements of our method with those of traditional approaches.

In the standard MS gate, spin-spin coupling is achieved by driving the first sideband transition of a designated central mode with a Rabi frequency Ω_{MS} that is independent of the coupling strength η_{jl} and satifies $(\Omega_{MS}/\delta)^2 = \Phi_T/8\pi$. This Rabi frequency thus specifies the maximum required power.

In the present scheme, the Rabi frequencies are determined by solving Eq. (7.38) and, thus, depend on the ion-mode coupling strengths η_{jl} of each ion j and motional mode l. The solutions are given by

$$\frac{\Omega}{\delta} = \frac{\pm 1}{2\sqrt{15}} \sqrt{\frac{10 + 5\zeta \pm \sqrt{25(2+\zeta)^2 - 240\vartheta\Phi_T/\pi}}{\vartheta}} \tag{H.1}$$

where $\vartheta = \sum_j \eta_{j1}^2$, $\zeta = \sum_{j,l} \eta_{jl}^2$. Typically, the solution that minimizes $|\Omega|$ is chosen.

In the limit of vanishing couplings, $\eta_{jl} \to 0$, the Rabi frequency becomes $\Omega/\delta = \sqrt{\Phi_T/5\pi}$, which corresponds to a factor of $|\Omega/\Omega_{MS}| = 2\sqrt{2/5} \approx 1.26$ relative to the MS Rabi frequency. As the spin-motion coupling strength increases (larger ϑ and ζ in Eq. (H.1)), the required Ω diminishes. This can be attributed to the fact that higher-order processes, emerging from the expansion of the displacement operators (Eq. (7.7)), contribute to entanglement generation, with their effect becoming more pronounced as the coupling strengths

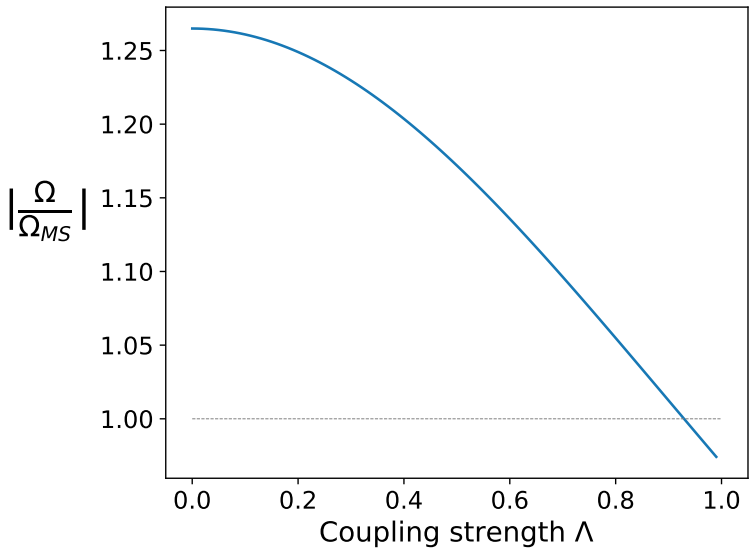

Figure H.1: Ratio $|\Omega/\Omega_{MS}|$ of the Rabi frequency for the robust gate Ω to that of the MS scheme Ω_{MS}, plotted as a function of the coupling strength Λ for a two-ion system.

η_{jl} increase. Fig. H.1 illustrates this behavior for a two-ion system. For weak coupling, the Rabi frequency ratio $|\Omega/\Omega_{MS}|$ is indeed around 1.26. As the coupling strength Λ grows, however, the required Rabi frequency decreases. In strong coupling regimes, the Rabi frequency of the proposed solution can even become smaller than the MS Rabi frequency.

While the peak power demand for the MS implementation coincides with the Rabi frequency, this is not the case for the present scheme. Here, the peak power is determined by the maximum amplitude of the driving functions specified in Eq. (7.37). First-order sideband transitions (Eq. (7.37a)) require time-varying drive amplitudes, reaching a maximum of $\frac{5}{2}|\Omega|$. Second-order sideband transitions (Eqs. (7.37b), (7.37c)), on the other hand, require constant drive amplitudes $\sim |\Omega|$.

Hence, while the proposed solution requires a modest increase in drive amplitudes compared to MS implementation (a factor of $\sqrt{10}$ for first-order sideband transitions), as well as including second-order sidebands of comparable power to the first-order sidebands of the MS gate, this is far outweighed by the substantial performance gains. In fact, stronger spin-motion coupling can further alleviate these requirements, reducing the maximum power for first-order sideband transitions to $\sim 5/2\Omega_{MS}$.

H.2 Highly excited thermal states

While Fig. 7.2 in the Main text showcases the performance of the proposed gate for various ion chain sizes and scenarios including ideal conditions or motional heating, the results are limited to motional Fock states $|n_1, \cdots, n_M\rangle$ with occupation numbers of up to $n_l = 10$.

Fig. H.2 depicts the infidelity of a two-ion system for thermal states with thermal excitation of up to $\bar{n}_l = 100$ and different spin-motion coupling strengths Λ. The figure demonstrates

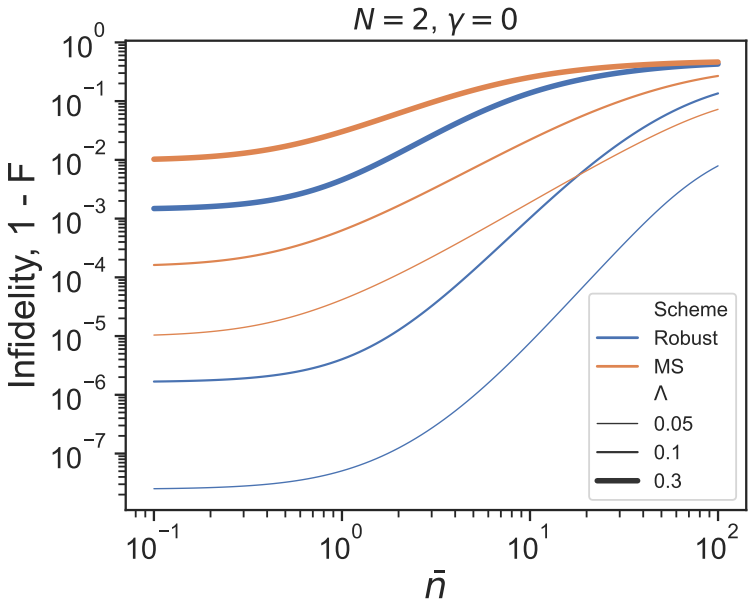

Figure H.2: Infidelity $1 - F$ for $N = 2$ qubits as a function of the mean occupation $\bar{n}$ (with $\bar{n}_1 = \bar{n}_2 = \bar{n}$) of a thermal state (on log scale). Increasing line thickness represents increasing values of the coupling parameter Λ (defined in the Main text), while the color line distinguishes between the conventional MS approach (orange) and the present robust gate scheme (blue). No motional heating or detuning errors are considered.

that the proposed scheme outperforms the standard MS approach for any value of $\bar{n}_l$ and Λ. Remarkably, fidelities exceeding 99% are achieved with spin-motion couplings Λ of 0.05, a value commonly encountered in experiments, which represents more than an order of magnitude improvement compared to the standard MS approach.

H.3 Analytical derivations and numerical simulations of trapped ion gates

The symbolic computation package SymPy [265] was employed to derive high-order expansions of the system Hamiltonian, calculate the time-dependent propagator using the Magnus expansion, determine the exact form of transformed jump operators in the master equation Eq. (7.28), and calculate the control solutions Eq. (7.37).

Numerical simulations of the gate dynamics were performed using the Qutip package [266]. Both unitary (dissipation-free) and dissipative dynamics were simulated using Qutip's *mesolve* function. For unitary dynamics, the time-evolved quantum states were obtained by numerically solving the Schrödinger equation. For dissipative dynamics, the density matrix was constructed using the Lindblad master equation. In both cases, strict numerical tolerances were employed: an absolute tolerance of 10^{-12} and a relative tolerance of 10^{-12}. The finite difference evolution was performed using 10^6 time steps.

The Hilbert space dimension used in the simulations was adjusted to include all relevant

states that could be populated during the dynamics. For an initial motional Fock state $|n\rangle$, a dimension of at least $d = n+50$ was used for each mode. For two-ion gates, where initial Fock states up to $|250\rangle^{\otimes 2}$ were simulated, the truncated Hilbert space had a dimension of up to $d = 300^2$. For the 4-ion gate, with initial Fock states up to $|10\rangle^{\otimes 4}$, the motional Hilbert space dimension was set to $d = 60^4$. The validity of these choices was confirmed by observing negligible changes in fidelity upon further increasing the Hilbert space dimension or expanding the set of initial states.

H.4 Hamiltonian expansion with off-resonant contributions

To align with the perturbative framework in Chapter 7, which truncates the Lamb-Dicke expansion at third order in η, we expand the Hamiltonian in Eq. (7.12) to the same order, exposing residual off-resonant interactions from higher-order sideband processes.

$$
\begin{aligned}
H^{(j)} = -i\sigma_+^{(j)} \sum_{p=0}^{M} \mathfrak{f}_p^{(j)} \Bigg\{ & \mathbb{I} + i \sum_{l'=1}^{M} \eta_{jl'} \left(e^{i\nu_{l'}t} a_{l'}^\dagger + e^{-i\nu_{l'}t} a_{l'} \right) - \frac{1}{2} \sum_{l'=1}^{M} \eta_{jl'}^2 \left(e^{2i\nu_{l'}t} a_{l'}^{\dagger 2} + e^{-2i\nu_{l'}t} a_{l'}^2 \right) \\
& - \frac{i}{6} \sum_{l'=1}^{M} \eta_{jl'}^3 \left(e^{3i\nu_{l'}t} a_{l'}^{\dagger 3} + e^{-3i\nu_{l'}t} a_{l'}^3 \right) \\
& - \sum_{l',l''=1}^{M} \eta_{jl'} \eta_{jl''} \Big[e^{i(\nu_{l'}+\nu_{l''})t} a_{l'}^\dagger a_{l''}^\dagger + e^{-i(\nu_{l'}+\nu_{l''})t} a_{l'} a_{l''} \\
& \quad + e^{i(\nu_{l'}-\nu_{l''})t} a_{l'}^\dagger a_{l''} + e^{-i(\nu_{l'}-\nu_{l''})t} a_{l'} a_{l''}^\dagger \Big] \\
& - \frac{i}{2} \sum_{l',l''=1}^{M} \eta_{jl'} \eta_{jl''}^2 \Big[e^{i(\nu_{l'}+2\nu_{l''})t} a_{l'}^\dagger a_{l''}^{\dagger 2} + e^{-i(\nu_{l'}-2\nu_{l''})t} a_{l'} a_{l''}^{\dagger 2} \\
& \quad + e^{-i(\nu_{l'}+2\nu_{l''})t} a_{l'} a_{l''}^2 + e^{i(\nu_{l'}-2\nu_{l''})t} a_{l'}^\dagger a_{l''}^2 \Big] \\
& - \frac{i}{2} \sum_{l',l''=1}^{M} \eta_{jl'}^2 \eta_{jl''} \Big[e^{i(2\nu_{l'}+\nu_{l''})t} a_{l'}^{\dagger 2} a_{l''}^\dagger + e^{-i(2\nu_{l'}-\nu_{l''})t} a_{l'}^{\dagger 2} a_{l''} \\
& \quad + e^{-i(2\nu_{l'}+\nu_{l''})t} a_{l'}^2 a_{l''} + e^{i(-2\nu_{l'}+\nu_{l''})t} a_{l'}^2 a_{l''}^\dagger \Big] \\
& - i \sum_{l',l'',l'''=1}^{M} \eta_{jl'} \eta_{jl''} \eta_{jl'''} \Big[e^{i(\nu_{l'}+\nu_{l''}+\nu_{l'''})t} a_{l'}^\dagger a_{l''}^\dagger a_{l'''}^\dagger + e^{i(\nu_{l'}+\nu_{l''}-\nu_{l'''})t} a_{l'}^\dagger a_{l''}^\dagger a_{l'''} \\
& \quad + e^{i(\nu_{l'}-\nu_{l''}+\nu_{l'''})t} a_{l'}^\dagger a_{l''} a_{l'''}^\dagger + e^{i(-\nu_{l'}+\nu_{l''}+\nu_{l'''})t} a_{l'} a_{l''}^\dagger a_{l'''}^\dagger \\
& \quad + e^{i(\nu_{l'}-\nu_{l''}-\nu_{l'''})t} a_{l'}^\dagger a_{l''} a_{l'''} + e^{i(-\nu_{l'}+\nu_{l''}-\nu_{l'''})t} a_{l'} a_{l''}^\dagger a_{l'''} \\
& \quad + e^{i(-\nu_{l'}-\nu_{l''}+\nu_{l'''})t} a_{l'} a_{l''} a_{l'''}^\dagger + e^{i(-\nu_{l'}-\nu_{l''}-\nu_{l'''})t} a_{l'} a_{l''} a_{l'''} \Big] \Bigg\} + \text{h.c.}
\end{aligned}
\tag{H.2}
$$

where

$$
\mathfrak{f}_0^{(j)} = \frac{F_{1,1}^{(j)} e^{-i\nu_1 t} - F_{1,1}^{*(j)} e^{i\nu_1 t}}{\eta_{j1}} , \quad \mathfrak{f}_p^{(j)} = \frac{F_{p,2}^{(j)} e^{-2i\nu_p t} + F_{p,2}^{*(j)} e^{i2\nu_p t}}{\eta_{jp}} , \quad 1 \le p \le M . \tag{H.3}
$$

System Size (N)	ν_1/ν	ν_2/ν	ν_3/ν	ν_4/ν	ν_5/ν	ν_6/ν	ν_7/ν	ν_8/ν	ν_9/ν	ν_{10}/ν
2	1	$\sqrt{3}$	-	-	-	-	-	-	-	-
3	1	$\sqrt{3}$	2.408319	-	-	-	-	-	-	-
4	1	$\sqrt{3}$	2.410381	3.050959	-	-	-	-	-	-
5	1	$\sqrt{3}$	2.41199	3.054857	3.670809	-	-	-	-	-
6	1	$\sqrt{3}$	2.413296	3.058092	3.676123	4.27384	-	-	-	-
7	1	$\sqrt{3}$	2.414388	3.060842	3.680698	4.280253	4.863726	-	-	-
8	1	$\sqrt{3}$	2.41532	3.063224	3.684702	4.285907	4.871014	5.44292	-	-
9	1	$\sqrt{3}$	2.41613	3.065319	3.688254	4.290956	4.87755	5.450923	6.013165	-
10	1	$\sqrt{3}$	2.416842	3.067182	3.69144	4.295509	4.883469	5.458192	6.021762	6.575752

Table H.1: Frequencies of normal modes, ν_l, obtained from the normal mode decomposition of a chain of ions confined in a harmonic trap. Each ν_l is expressed as a fraction of the characteristic trap frequency ν, for system sizes ranging from 2 to 10 ions.